



**Core-Shell Nanoparticle Models for *in-situ* SERS  
Measurements of Carbonate Dissolution Under  
Environmentally Realistic Conditions**

**Charles Stuart Davis**

*In partial fulfilment of the requirement for the degree*

*Doctor of Philosophy in Chemistry*

**Cardiff University, July 2015**

## Dedication

I would like to dedicate this PhD thesis to my father and inspiration

Peter John Davis (1949 – 2010)

# Acknowledgements

---

I would like to express my special appreciation and thanks to my supervisors Prof. Philip Davies, Prof. Gary Attard and Dr. Stephen Barker, you have been fantastic mentors.

I would especially like to thank Prof. Philip Davies for your untiring support and encouragement throughout my time at Cardiff, you have been a tremendous mentor, your energy and drive in the face of obstacles was infectious. You're always going above and beyond any level of support I expected concerning both academic and personal matters, thank you. I would also like to thank Dr. David Morgan for all of his help and expertise in the interpretation of XPS data, as well as always having an extremely friendly and approachable demeanour.

Thanks to all of the numerous technical staff in the department, who have always been welcoming and only too happy to help. I would particularly like to thank Alun Davies and Steven Morris, you have both taught me so much about engineering and electronics. Your speed of work and expertise meant that even the worst of technical difficulties experienced, resulted in swift and exceptional fixes. Without your continued aid this thesis would not have been possible. I would also like to thank all my friends and colleagues in the department for making the environment inclusive, encouraging and supportive.

I would especially like to thank my family. Words cannot express how grateful I am to my mum for all of the sacrifices that you've made on my behalf, thank you. I would also like to thank all of my friends for not disowning me over the course of this research, always happy to listen to me vent about various troubles. Finally I would like to pay special thanks to Rebecca McVicker, your love, support and encouragement has been paramount to my completion of this work. For you I save the last recognition, thank you.

# Contents

---

## 1 Introduction

<b>1.1 Paleocyanography</b> .....	1
1.1.1 Mg/Ca Thermometry .....	2
<b>1.2 Calcium Carbonate</b> .....	4
1.2.1 Deposition and Dissolution .....	6
<b>1.3 Nanoparticles</b> .....	7
1.3.1 Introduction.....	7
1.3.2 Synthesis .....	8
1.3.3 Physical Properties and Application .....	9
1.3.4 Core-Shell Nanoparticles .....	10
<b>1.4 Aim</b> .....	12

## 2 Theoretical Background

<b>2.1 Surface Structure</b> .....	17
<b>2.2 Cyclic Voltammetry</b> .....	18
2.2.1 Faradaic Processes .....	19
2.2.2 Non-Faradaic Processes .....	22
<b>2.3 Microscopy</b> .....	23
2.3.1 Scanning Electron Microscopy .....	24
2.3.2 Transmission Electron Microscopy.....	26
2.3.3 Scanning Tunnelling Microscopy.....	28
<b>2.4 Spectroscopy</b> .....	32
2.4.1 The Absorption Process.....	33
2.4.2 Light Scattering .....	35
2.4.3 Raman Spectroscopy.....	35
2.4.4 Surface Enhanced Raman Spectroscopy .....	37
2.4.4 X-Ray Photoelectron Spectroscopy.....	38

2.4.4.1 The Photoelectric Effect .....	38
2.4.4.2 Koopmans' Theorem .....	39
2.4.4.3 Initial and Final State Effects.....	40
2.4.4.4 Work Function .....	40
2.4.4.5 Surface Sensitivity .....	42
2.4.4.6 Quantification of Surface Species .....	43
2.4.5 Energy Dispersive X-Ray Spectroscopy.....	43
<b>3 Experimental</b>	
<b>3.1 The Milli-Q Pure Water System.....</b>	<b>48</b>
<b>3.2 In Situ Raman analysis; Probing the Deposition and Dissolution of Calcium Carbonate.....</b>	<b>48</b>
3.2.1 The Spectro-electrochemical Flowcell.....	49
3.2.2 Typical Experimental Procedure.....	52
3.2.3 Preparation of Pure Calcium Carbonate.....	53
<b>3.3 Nanoparticle Synthesis and Coating.....</b>	<b>54</b>
3.3.1 Synthesis of Citrate Stabilised Gold Nanoparticles.....	54
3.3.2 Synthesis of Thiol Stabilised Gold Nanoparticles.....	54
3.3.3 Coating Methods.....	55
3.3.4 Coating of Particles by Exposure to Ammonium Carbonate.....	55
3.3.5 Coating of Particles by the Bubbling of High Purity CO <sub>2</sub> .....	56
<b>3.4 Platinum Single Crystal Production, Electrochemical Cleaning and Gold Coating.....</b>	<b>57</b>
3.4.1 The Electrochemical Cell.....	57
3.4.2 Preparing the Platinum Working Electrode.....	59
3.4.3 Electrolyte.....	61
3.4.4 Metal Preparation and Coating.....	61
<b>3.5 Ultra High Vacuum Studies of Carbonates on Gold Single Crystals.....</b>	<b>63</b>
3.5.1 Ultra High Vacuum Systems.....	63
3.5.2 Ultra-High Vacuum Apparatus.....	64

3.5.3 Sample Analysis.....	65
3.5.3.1 XPS Analysis.....	65
3.5.3.2 STM Analysis.....	66
3.5.4 Sample Preparation.....	67
3.5.4.1 Metal Vapour Deposition.....	67
3.5.4.2 Gaseous Exposure.....	68
<b>4 In-situ Raman Analysis and Particle Synthesis</b>	
<b>4.1 Deposition of Calcium Carbonate for SERS Studies.....</b>	<b>70</b>
4.1.1 Production of Pure Precipitates of Calcium Carbonate.....	70
4.1.1.1 Precipitated Calcite.....	70
4.1.1.2 Precipitated Vaterite.....	72
4.1.1.3 Precipitated Aragonite.....	74
4.1.2 In situ Electrochemical Raman Analysis of Calcium Carbonate.....	75
4.1.2.1 Investigation of the Deposition and Dissolution of Calcium Carbonate Thin Films.....	75
4.1.3 Raman/SERS Analysis of Calcium Carbonate Growth.....	77
<b>4.2 Nanoparticle Synthesis and Coating.....</b>	<b>82</b>
4.2.1 Citrate Stabilised Gold Nanoparticles.....	82
4.2.1.1 Calcium Carbonate Deposition on Citrate Stabilised Gold Nanoparticles.....	85
4.2.1.2 Addition of Nanoparticles to Solution of Calcium Chloride.....	86
4.2.2 Thiol Stabilised Gold Nanoparticles.....	89
4.2.2.1 Analysis of p-Mercaptophenylboronic Acid.....	89
4.2.2.2 Analysis of p-Mercaptobenzoic Acid.....	91
4.2.3 Coating of Thiol Stabilised Gold Nanoparticles.....	94
4.2.3.1 Coating of Nanoparticles via Exposure to Ammonium Carbonate.....	94
4.2.3.2 Investigation of the Effect of Ca Concentration.....	98
4.2.3.3 Initial Coating of Thiol Stabilised Particles by the Bubbling Method.....	113
4.2.4 Synthesis of Gold@Carbonate Core Shell Nanoparticles.....	115
<b>4.3 Discussion.....</b>	<b>119</b>

## **5 Epitaxial Growth of Calcium Carbonate on Gold Single Crystals**

<b>5.1 Introduction</b> .....	123
<b>5.2 Preliminary Investigations on Au(h,k,l)</b> .....	126
5.2.1 Deposition in the Absence of an Applied Potential.....	126
5.2.2 Ultra-Pure Water (-1000 mV, 10 mins).....	128
<b>5.3 Epitaxial Growth on Au(111)</b> .....	129
<b>5.3 Epitaxial Growth on Au(110)</b> .....	136
<b>5.4 Epitaxial Growth on Au(100)</b> .....	138
<b>5.5 Discussion</b> .....	139

## **6 Carbonate Formation on Au(111) Under UHV Conditions**

<b>6.1 Introduction</b> .....	142
<b>6.2 Clean Au Surface, Stability of Clean Surface, Effect of CO<sub>2</sub> Exposure</b> .....	143
<b>6.3 Calibration of Cs Coating and Stability of Cs Layer in Vacuum</b> .....	145
6.3.1 Caesium Coating Calibration.....	145
6.3.2 Caesium Stability in Vacuum.....	146
<b>6.4 Investigating Alloy Formation on Cs Coated Au(111) Surface</b> .....	148
6.4.1 Sputtered Surface.....	148
6.4.2 Partially Annealed Surface.....	149
6.4.3 Annealed Surface.....	151
<b>6.5 Formation of Cs<sub>2</sub>CO<sub>3</sub> on Au(111)</b> .....	152
<b>6.6 Thermal Stability of Caesium Carbonate</b> .....	157
6.6.1 Caesium Carbonate Formation and Thermal Stability at ~1 ML Coverage.....	158
6.6.2 Caesium Carbonate Formation and Thermal Stability at ~2 ML Coverage.....	163
<b>6.7 Exposure of CsAu Surface to a 1:1 CO<sub>2</sub>/O<sub>2</sub> mixture</b> .....	166
<b>6.8 Discussion</b> .....	167
6.8.1 Effect of Heating.....	169
<b>7 Conclusions</b> .....	171

# Chapter 1 Introduction

---

## 1.1 Paleoceanography

Paleoceanography investigates how the oceanic environment has changed throughout history, it involves the study of oceanic sedimentary records, documenting; glacial changes and temperature changes linked to climatic change and tectonic plate movements. Information is gleaned about the past oceanic environment via proxies and the relationship between present sedimentation patterns and past environmental factors. With the continued anthropogenic emission of carbon dioxide linked to accelerated changes in our climate, it is vital that we understand how Earth's oceans have reacted and adapted to past climatic changes. The better our understanding of these past changes, the more accurate predictions can be made relating to how the oceans will change in the future in response to rising temperatures, rising atmospheric carbon dioxide levels and ocean acidification [1, 2].

Biominalisation is the process in which calcium carbonate is formed naturally, either by sedimentation or by micro-organisms which build shells of calcium carbonate, in nature there is great control over the phase, morphology and crystal shapes which are produced [3-5]. These marine carbonates makes up a large proportion of the global carbon cycle and the dissolution of such marine carbonates has a direct link with atmospheric levels of carbon dioxide. Over the past century the continued emission of anthropogenic carbon dioxide has increased the relative pressure of the gas in the atmosphere and this in turn has had direct effects on the oceanic carbonate behaviour.

The study of the mechanisms surrounding the nucleation, growth and dissolution of calcium carbonate from saturated solutions has recently attracted much attention [4, 6]. This is due to the growing number of applications such as in paleo-oceanic temperature estimations [1, 2, 7, 8], industrial scale prevention [9-11] and more recently as additives in specialised materials such as papers, paints and plastics [12-14]. The latter two applications require specific morphologies or mixtures of morphologies of calcium carbonate to be produced in a controlled manor, hence the continued need to understand the mechanisms of nucleation and growth.

When dissolved into the ocean, carbon dioxide can exist as one of four inorganic forms: dissolved carbon dioxide; carbonic acid; bicarbonate and carbonate. The former two species exist only in very small concentrations at the pH of oceanic waters, bicarbonate is by far the most dominant species followed by carbonate. Another effect of the increased levels of carbon dioxide being dissolved by the ocean is a phenomena known as ocean acidification, which is

effectively lowering the pH of oceanic waters which results in the lowering of the saturation state in respect of carbonate, preventing the precipitation and sedimentation of carbonate in favour of higher levels of dissolved bicarbonate (Figure 1-1).

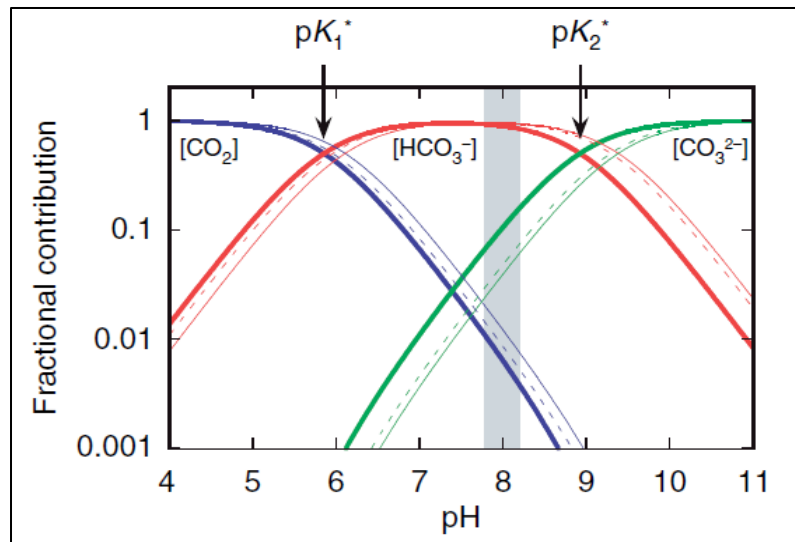


**Figure 1-1** Bjerrum plot of the relative concentration of oceanic carbonate forms [1].

Another application for the better understanding of the parameters which affect the rate of formation and dissolution of calcium carbonate is that of Mg/Ca thermometry. The discovery in 1954, of the temperature dependence of the Mg/Ca ratio in calcite deposits, led to the suggestion in 1981 of using the minor elemental composition variation in such deposits, as a means to gain useful information of paleoclimatic estimations. Mg/Ca thermometry arises from this technique.

### 1.1.1 Mg/Ca Thermometry

Mg/Ca thermometry is a proxy for paleoceanographic temperature estimations, which utilises the temperature dependence of the inclusion of magnesium in calcium carbonate deposits. This is made possible as small organisms in the ocean build a layer of calcium carbonate as “tests” or shells (Figure 1-2). Some of the calcifying organisms include foraminifera, ostracods and coccoliths, there are many more.



**Figure 1-2** SEM image of a planktonic foraminifera (*Hantkenina alabamensis*) measuring 0.8mm spine tip to spine tip

There are a plethora of other proxies which are more long standing than Mg/Ca thermometry which yield paleotemperature information such as faunal counting or alkenones. However Mg/Ca thermometry has some major advantages over other approaches. First and foremost, the Mg/Ca ratio of the bulk oceans has a vast residence time somewhere in the region of  $10^6$ - $10^7$  years, a time scale that is longer than that of glacial/interglacial time scales. Therefore the concentration of both magnesium and calcium in oceanic water can be thought of as constant which substantially reduces the uncertainty in the paleotemperature estimations. Another advantage of the use of Mg/Ca thermometry over other proxies is that it can yield other useful information.

Potentially the most advantageous uses of this proxy is that the Mg/Ca deposits are obtained from living organisms. This is extremely useful as different species of foraminifera and other calcifying organisms have specific habitats in various oceanic areas and at a variety of ocean column depths. Therefore the collection and analysis of a variety of species, both living and fossilised, will lead to the construction of detailed paleotemperature 'maps' of the ocean spanning large time scales. It is this multi-faceted aspect which makes this approach the proxy of choice.

Finally foraminiferal carbonate contains some fractional composition of  $^{18}\text{O}$  which follows the isotopic composition of the sea water, which in turn is influenced by the local salinity of sea water and the global volume of ice. Therefore the observed  $\delta^{18}\text{O}$  in foraminiferal carbonate will give an indication of these parameters. The  $\delta^{18}\text{O}$  is a percentage calculated using the

isotopic composition of a sample compared to that of a reference, and is expressed as follows.

$$\delta^{18}O = \left[ \frac{\left(\frac{^{18}O}{^{16}O}\right)_{sample}}{\left(\frac{^{18}O}{^{16}O}\right)_{ref}} - 1 \right] * 1000$$

Equation 1-1

However the  $\delta^{18}O$  composition of these deposits is also temperature dependant making useful predictions difficult, but since in this case, both temperature and the  $\delta^{18}O$  composition are obtained from the same source, the temperature dependence is eliminated and useful information regarding the local salinity and global ice volume can be obtained through the determination of the isotopic composition of the sea water over time.

This new proxy using Mg/Ca thermometry is not without issue, many factors affect the rate of dissolution of calcium carbonate such as acidity, localised acidity variation in oceanic aquifers, temperature and pressure. The largest uncertainty comes from that of pressure and how it effects the deposition, dissolution and partial dissolution of calcium carbonate. This leads to an overall uncertainty in the region of  $10^3$  years for paleoceanographic temperature estimations. Therefore this study aims to lower this uncertainty by developing a Raman probe which would be able to be used to study the effects of these parameters on the dissolution rates of various morphologies of calcium carbonate.

## 1.2 Calcium Carbonate

Calcium carbonate forms three anhydrous polymorphs, calcite, aragonite and vaterite. Each polymorph can exhibit different crystal morphologies, calcite predominantly forms rhombohedra, aragonite predominantly forms orthorhombic needle structures and vaterite has numerous morphologies; flowers, kernels, spherules and octahedral structures.

Calcite is the most stable phase, aragonite and vaterite are both considered meta-stable, as in solution they will transform to calcite. Vaterite is the least stable and will transform to calcite at low temperatures and to aragonite at high temperatures ( $> 80^{\circ}C$ ). Although the most abundant natural form of calcium carbonate is calcite, aragonite and vaterite are also found naturally, stabilised by the inclusion of other ions in mineral deposits, and with protein directed deposition in biomineralisation. When precipitation occurs from saturated solutions amorphous calcium carbonate (ACC) forms quickly, followed by the phase transformation to vaterite spheres followed by the eventual transformation to calcite or aragonite [6, 10]. However the inclusion of other ions [10, 15, 16], alcohols [17], magnetic fields [18-20] and the

Ca/CO<sub>3</sub> ratio can effect this mechanism greatly [6]. For a detailed historic perspective the reader is directed to [4].

Calcite exhibits a rhombohedral crystal structure, the most stable and hence dominant surface is the  $[10\bar{1}4]$  plane, which consists of layers of both Ca and CO<sub>3</sub> groups; the surface is terminated with O atoms. In the absence of water the surface undergoes a relaxation whereby the carbonate groups rotate to lie flat and exist in two different but equivalent orientations. This causes strain at the crystal edges and small  $[10\bar{1}1]$  facets appear (Figure 1-3), the hydrated surface is more stable, and the relaxation does not occur and thus the  $[10\bar{1}1]$  face is not observed under these conditions. Bulk calcium atoms are coordinated to 6 oxygen atoms, this is the lowest coordination number of the three anhydrous crystal phases, which leads to the strongest lattice interactions and hence most stable crystal [21].

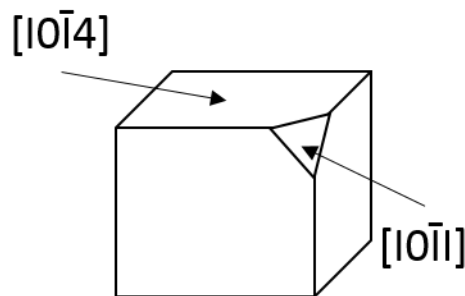


**Figure 1-3** Schematic of a rhombohedra of calcite.

Aragonite has a differing crystal structure to that of calcite with orthorhombic crystal structure, leading to the development of spike or needle structures. In the lattice structure each Ca atom is coordinated to 9 O atoms. Due to the crystal nature of aragonite there are many different crystal faces terminating the structure. Finally vaterite has a complex crystal structure which is hard to define, due to the instability of the crystal, high number of defects and the number of morphologies it can express. Vaterite exhibits hexagonal crystal growth, with great disorder with respect to the orientation of the carbonate groups, more information can be found on the surface crystal structure here [21-26].

### 1.2.1 Deposition and Dissolution

The deposition and dissolution of calcium carbonate is important for the reasons previously mentioned. To understand the mechanisms and conditions which are required to form certain polymorphs and morphologies of calcium carbonate is of utmost importance if one wishes to control the production of calcium carbonate, whether that be to prevent precipitation to avoid industrial scale build up, to precipitate desired polymorphs for pipe corrosion protection, for specific shapes as specialised additives in composite materials, or as models to help understand biomineralisation. The majority of work performed has been on bulk calcium carbonate, further it is usually the deposition that is of interest, with far fewer studies concerning the dissolution of calcium carbonate and fewer still addressing the very initial stages of dissolution specifically at high pressure.

Dandeu and Carteret first showed how Raman and more specifically the fingerprint Raman region ( $<500\text{ cm}^{-1}$ ) could be used to differentiate the different polymorphs of calcium carbonate using the unique lattice vibrations which are present in this region, for the identification of polymorphic mixtures in industrial scale deposits [27]. Building on this they have shown how temperature and time effect the observed polymorphism [28]. The culmination of the work supports that previously known in the literature that amorphous calcium carbonate forms before transformation to an anhydrous form, followed by the eventual transformation of the meta-stable anhydrous phases to calcite.

A large volume of work has been presented by Gabrielli's group in the field of electrochemical deposition and analysis using Raman spectrometry, the majority of this work has focused on bulk deposition, and the parameters effecting the deposition rate and polymorphism. Initial work involved the use of Raman to determine the structure of pure vaterite [29] and the fingerprint Raman to determine the structure of three calcium carbonate hydrates [30]. The former used only the main Raman region and the lattice vibrations were not fully determined until Carteret's work [28]. Much electrochemical, optical and SEM work was carried out to understand the effect of reduction potential and pH [31], super saturation [32], ionic effects [33] and extensive effects of the inclusion of  $\text{Mg}^{2+}$  [34].

## 1.3 Nanoparticles

### 1.3.1 Introduction

The field of nanoscience is being divided into an ever increasingly large number of subdivisions, with the recent emergence of nanoelectrochemistry, nanoparticles, self-assembled monolayers (SAM's), nanoengineering and nanoreactors.

The synthesis of gold nanoparticles is a field that has emerged as a subdivision of the wide area of colloids. Gold has been an area of immense interest dating far back in history, with the yearly extraction of gold exceeding 10 tonnes per annum from Egypt alone as far back as the 13<sup>th</sup> century BC although aesthetics were its main attraction then. Great interest in the production of ruby gold was popularised by the Lycurgus cup (Figure 1-4), thought to be produced by the Romans in the 4<sup>th</sup> century AD. The green colour arising from reflected light and the red from transmitted light attributed to the inclusion of colloidal gold/silver nanoparticles [35]

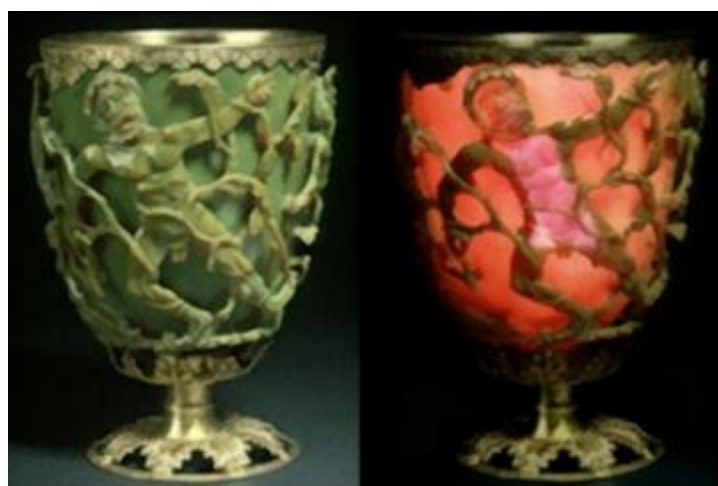


**Figure 1-4** Image of the Lycurgus cup

Colloidal gold was also used extensively for early curative medicine including treatments for heart conditions, epilepsy, tumours and in the diagnosis of syphilis, of which the latter was in use until the early 20<sup>th</sup> century. Early findings by Antonii (1618) and Kunckel (1676) in the 17<sup>th</sup> century noted in detail some of the curative applications of colloidal gold, including successful case studies in their findings [36]. The first person to propose that the colour of gold was size dependent was Richters (1818), who stated that small subdivisions of gold appear to be red, while the yellow colour was caused by agglomeration to large sizes. This came shortly before Faraday's synthesis of gold nanoparticles in 1857 which involved the two-phase reduction of chloroauric acid with phosphorus in carbon disulphide, as well as his extensive workings into

the optical properties of gold colloids and thin films, and was the first to document the effects of quantum size, well before the theory behind this was understood [36, 37], although it was not until a few years later in 1861 that Graham popularised the word colloid. In recent years the amount of research involving the use of nanoparticles has increased dramatically. The properties of gold nanoparticles are vastly different from that of bulk gold highlighting the interesting world of quantum particles, with a particular interest in gold nanoparticles due to their very varied application, interesting quantum properties and relative stability.

### 1.3.2 Synthesis

Various methods for the synthesis of gold nanoparticles developed in the 20<sup>th</sup> century, with great control over their physical properties through the size specific syntheses. These have led to their use as probes for exploring many areas including, electron transfer theory, catalysis and bio-labelling, it is because of this multidisciplinary spanning of physical, chemical and biological applications that this area has grown so rapidly.

Two of the major routes to synthesis are the Turkevich and Brust methods. Turkevich's synthesis [38], derived in the early 1950's involved the reduction of aqueous chloroauric acid with sodium citrate. Thanks to the then recent development of the electron microscope, although still in the developmental stages, Turkevich was able to show that the average size and distribution of particles could be controlled by altering the concentration of gold and the time taken for the addition of reductant, furthermore, the finding that the nucleation and growth stages succeeded each other and could be separated and analysed individually gave the ability to also predict the kinetics of the process, making this an extremely powerful synthesis still used today [38-40].

However due to the fact that citrate only stabilises the particles electrostatically, only particles over ~20 nm can be produced this way, the higher energy that smaller particles possess, over comes the stabilising power of the citrate and the particles will agglomerate until a more stable size range has been reached. This occurs as smaller particles have a much higher surface area to bulk ratio than larger particles. This means that the particle possess a high degree of surface energy and hence will agglomerate to lower this ratio and reduce the surface energy. As a result of these effects particles are hard to isolate out of aqueous solution and are sensitive to the presence of other charged particles which could potentially destabilise the gold citrate interactions causing further aggregation, leading to the precipitation of bulk gold. In the 1970's Frens modified the synthesis further, altering the concentration of citrate in the hope of controlling the size of the particles produced and was able to reliably produce large particles of a narrow average size distribution and of sizes ranging from 16-150 nm [36, 37], although particles of a smaller diameter were still unobtainable.

The method Brust first employed in the early 1990's [41, 42], involved the reduction of chloroauric acid in the presence of a stabilising agent, with a reducing agent in an organic solvent. This contrasts with the Turkevich method which uses a combined stabilising and reducing agent. A range of thiols were used for first syntheses, leading to the ability to produce nanoparticles with size ranges from 2-8 nm, the stabilisation of these smaller particles has been attributed to the nature of the associated thiol. Sulphur's great affinity for gold results in the stabilising agent being bound covalently rather than electrostatically to the nanoparticle which leads to the greater stabilisation of the particle, and makes the synthesis of smaller, higher energy particles possible. More recently it has been found that rather than simple sulphur-gold bonds occurring, it is more complex with direct sulphur to gold bonds, bridging sulphur interactions, and some gold sites left free, and angled stabilising agents with other moieties of the molecule partaking in the stabilising effect [42-45].

Finally, another benefit of using nanoparticles is their flexibility post synthesis. Not only can one control the extent of agglomeration, as well as other minor physical attributes, it is also possible to adjust the nanoparticles further such as modifying the stabilising agent or coating the nanoparticles leading to applications such as antennas or core-shell coatings respectively. It is also possible, to exchange the supporting agent if differing chemical requirements are desired such as extra stability or different functionality.

### **1.3.3 Physical Properties and Application**

Nanoparticles are an intermediate between atomic or simple collections of molecules and that of a bulk material. As a result the properties of these materials are highly tuneable and their properties are of considerable interest. Nanoparticles in the 1-20 nm diameter range are predicted to possess physical properties that are neither that of the bulk or atomic/molecular material and highly dependent upon size, shape, the supporting agent and interparticle distances. When the de Broglie wavelength of the surface or valence electrons is of the same magnitude as the size of the particle in which they lie they can behave as quantum dots, whereby their electronic properties behave as if they were zero-dimensional point charges. Differing from bulk materials, when nanoparticles are smaller than a certain diameter ~10 nm, or more specifically for gold ~3 nm, an energy gap occurs between the valence and conduction bands, the energy of this band gap is again very dependent upon the size of the particle, leading to the ability to tune the degree to which a particle exhibits conducting, semi-conducting or insulating properties. As nanoparticles are considered point charges or quantum dots, the surface electrons are trapped possessing size specific oscillation frequencies. Collectively, nanoparticles of the same size will result in a plasma resonance due to this effect

and it is this plasma resonance which can be excited by electromagnetic radiation resulting in a surface plasmon resonance, “SPR”.

SPR was first described by Mie in 1908. The theory states that ‘the total cross section composed of the surface plasmon absorption and scattering is given as a summation over all electric and magnetic oscillations’. The surface plasmon resonances were later described by Maxwell’s equations for spherical particles. In Mie theory it is the dipole oscillations of the electrons lying in the conduction band that are responsible for the surface plasmon band of spherical particles. However experimental results are rarely identical, as any influence due to the stabilising ligand is not accounted for, although this can be used as an advantage for a means to estimate the extent of ligand influence on said particles. Due to quantum size effects there is also a lower size limit (<3 nm) below which the nanoparticles are no longer able to support surface plasmon resonances due to the formation of a band gap in the metal structure [46, 47].

The fact that gold nanoparticles are relatively stable, have immensely diverse and tuneable properties not to mention their post synthesis flexibility, means that they find application in an enormously diverse range of technologies. Examples include cell imaging, biolabelling, catalysis, nonlinear optics, spectral enhancement and electrochemical redox catalysis, but this list only scratches the surface of possible applications [36, 37, 44, 48, 49].

Therefore by synthesising stabilised gold nanoparticles ~50 nm, able to support surface plasmons, followed by the subsequent coating of nanoparticles in a shell of calcium carbonate it should be possible to analyse the layer utilising the plasmon induced enhancement, in order to better understand the initial rate of carbonate dissolution with the ability to see how the rates differ when other parameters such as morphology, pH, temperature, pressure or concentrations of other ions are altered.

#### **1.3.4 Core-Shell Nanoparticles**

Shortly after the rise in interest in simple colloidal systems came the interest in composite nano-materials, core-shell nanoparticles, alloyed nanoparticles etc. These materials were of great interest as the properties they exhibit can greatly differ from that of the component materials alone and have applications as semiconductors, catalysts, optoelectronics, photonics, biomedical and pharmaceuticals.

Nanoparticles of various shapes and sizes have been investigated as even minor changes in these parameters can have substantial effects on reactivity. The most common structure and the one of interest here, is that of spherical core-shell (core@shell) nanoparticles, whereby the core consists of one material for example, gold. The shell then consisting of another

material of interest. Here our focus is calcium carbonate, however other materials are used for numerous reasons, such as the coating of a cheap abundant metal with more precious ones. Another application could be the coating of gold nanoparticles with silica for SERS applications, these particles are known as shiners [50], and benefit from the chemically inert silica protecting the gold core from contamination yet allowing the electric field enhancement to proliferate. However the domain of core-shell particles is not limited to spherical particles and many have been investigated, Figure 1-5.

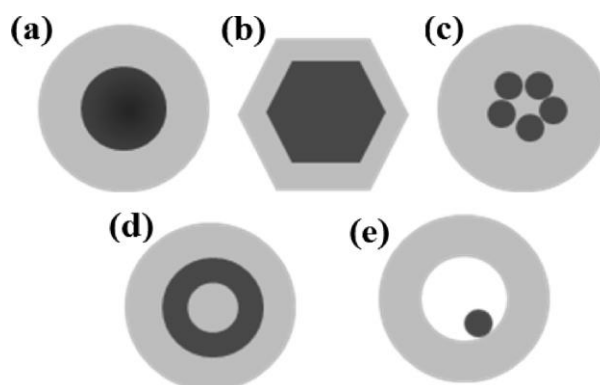


**Figure 1-5** Schematic of different core-shell nanoparticles: (a) spherical core-shell nanoparticles, (b) hexagonal core-shell nanoparticles, (c) multiple small core materials coated by single shell material (d) multiple shell nanoparticles, (e) movable core within hollow shell material [51].

The form of core-shell nanoparticles can be categorised dependent upon the type of material the core and shell are made from, the materials can generally be thought of as organic or inorganic and thus inorganic/inorganic, inorganic/organic, organic/inorganic and organic/organic systems are possible. The most widely used of these systems is that of inorganic/inorganic. For an in depth review of the routes to synthesis of core-shell particles, characterisation and applications the reader is directed to reference [51].

## 1.4 Aims

For the reasons mentioned above there has been much research into the rates of dissolution of calcium carbonate and the factors influencing it. Much of this research has been focused on bulk precipitation and dissolution whereas the research to be undertaken herein will be focused on the precipitation and dissolution at a molecular level, looking at the very initial stages.

An *in situ* Raman probe will be developed which utilises the surface plasmons of gold nanoparticles known as surface enhanced Raman spectroscopy (SERS).

Calcium carbonate can form in a number of morphologies (calcite, vaterite and aragonite) each of which has unique lattice vibrational modes and hence it is possible to differentiate between them using the fingerprint Raman region analysis. However the Raman effect is very weak and the utilisation of SERS is essential. SERS is capable of enhancing signals to the order of  $10^{10}$ , which makes it possible to study associated species down to the monolayer and sub-monolayer concentrations. Using this method it should be possible to monitor the deposition and subsequent dissolution of calcium carbonate as well differentiating between the morphologies present.

Calcium carbonate growth normally involves nucleation of individual crystals followed by growth. The extent of nucleation after this initial stage is minimised in the subsequent stage [32-34, 52, 53]. However the presence of the gold nanoparticles mimics that of a roughened surface giving a surface comprised of numerous nucleation sites. For this reason it was hoped that the nucleation of many crystals all over the surface would lead to the formation of thin films.

The first goal will be to use the Raman spectra in conjunction with TEM analysis to measure the layer thickness of calcium carbonate deposited on a gold nanoparticle coated polycrystalline platinum working electrode. This will be achieved by monitoring the level of the intensity of the carbonate peaks in the Raman spectra followed by detailed TEM analysis to find the exact thickness of the shell. It is expected that as the calcium carbonate is deposited the Raman spectra will appear more intense until a maxima is reached after which the signal will become less intense until it has returned to what would be expected for bulk calcium carbonate. This will not only prove useful as a means of knowing the thickness of the shell produced but will also yield information as to the optimum thickness for maximum SERS enhancement and the penetration depth of the enhancement. The next step will be to achieve morphological control of the calcium carbonate produced by alteration of the ratio of calcium and carbonate in the solutions used.

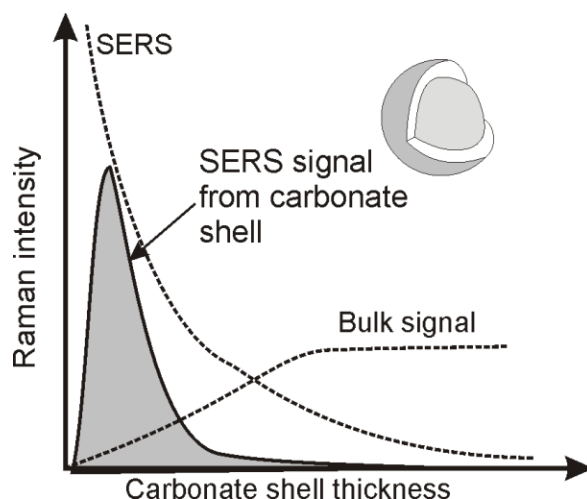


**Figure 1-5** Raman intensity as a function of carbonate layer thickness

The gold nanoparticles produced for the above analysis are in the region of 50 nm in diameter and are citrate stabilised, the particles are then deposited onto a Pt working electrode before analysis. It may be possible to coat the particles simply by flowing the saturated solutions over the surface of the electrode, however if this is not possible electrochemical deposition can be achieved by applying a reducing potential to encourage the deposition of calcium carbonate over the nanoparticles. Parallel to this investigation will be the synthesis of core-shell gold calcium carbonate nanoparticles. If possible it will be performed on the citrate stabilised particles however due to the lower stability of these particles thiol stabilised particles will be employed as they are inherently more stable due to the high affinity of sulphur for gold. It is hoped it will be possible to control the morphology and shell thickness in a similar manner to that which will be achieved electrochemically.

Spherical nanoparticles are not uniform in surface structure and are in fact composed of different single crystal surfaces, each with a slightly different surface atomic arrangement. This difference in surface structure leads to a difference in reactivity. Therefore single crystal surfaces will also be investigated for calcium carbonate growth. These physical studies on single crystals will involve looking at the epitaxial growth of calcium carbonate on the gold basal planes. The epitaxial studies will feedback useful information to aid in the synthesis of core-shell type nanoparticles for SERS enhancement.

## References

1. Barker, S., et al., *Planktonic foraminiferal Mg/Ca as a proxy for past oceanic temperatures: a methodological overview and data compilation for the Last Glacial Maximum*. Quaternary Science Reviews, 2005. **24**(7-9): p. 821-834.
2. Eggins, S., P. De Deckker, and J. Marshall, *Mg/Ca variation in planktonic foraminifera tests: implications for reconstructing palaeo-seawater temperature and habitat migration*. Earth and Planetary Science Letters, 2003. **212**(3-4): p. 291-306.
3. Meldrum, F.C., *Calcium carbonate in biomineralisation and biomimetic chemistry*. International Materials Reviews, 2003. **48**(3): p. 187-224.
4. Morse, J.W., R.S. Arvidson, and A. Lutge, *Calcium carbonate formation and dissolution*. Chemical Reviews, 2007. **107**(2): p. 342-381.
5. Dharmi, N.K., M.S. Reddy, and A. Mukherjee, *Bionninerlization of calcium carbonates and their engineered applications: a review*. Frontiers in Microbiology, 2013. **4**: p. 13.
6. Colfen, H., *Precipitation of carbonates: recent progress in controlled production of complex shapes*. Current Opinion in Colloid & Interface Science, 2003. **8**(1): p. 23-31.
7. Erez, J., *The source of ions for biomineralization in foraminifera and their implications for paleoceanographic proxies*, in *Biomineralization*, P.M. Dove, J.J. DeYoreo, and S. Weiner, Editors. 2003, Mineralogical Soc America: Washington. p. 115-149.
8. Schiebel, R., et al., *Planktic foraminiferal dissolution in the twilight zone*. Deep-Sea Research Part II-Topical Studies in Oceanography, 2007. **54**(5-7): p. 676-686.
9. Kitamura, M., *Controlling factor of polymorphism in crystallization process*. Journal of Crystal Growth, 2002. **237**: p. 2205-2214.
10. Liu, Y.Y., et al., *Phase Transformation of Magnesium Amorphous Calcium Carbonate (Mg-ACC) in a Binary Solution of Ethanol and Water*. Crystal Growth & Design, 2013. **13**(1): p. 59-65.
11. Suda, S., et al., *Morphology of calcium carbonate coating on amorphous silicate powder*. Journal of Materials Science, 2000. **35**(12): p. 3023-3028.
12. Niu, T., J.B. Xu, and J.G. Huang, *Growth of aragonite phase calcium carbonate on the surface of a titania-modified filter paper*. Crystengcomm, 2014. **16**(12): p. 2424-2431.
13. Drummond, D.K., *Electrolytic purification of calcium carbonate*. 2001, Minerals Technologies Inc., Bethlehem, PA, USA.
14. Boyjoo, Y., V.K. Pareek, and J. Liu, *Synthesis of micro and nano-sized calcium carbonate particles and their applications*. Journal of Materials Chemistry A, 2014. **2**(35): p. 14270-14288.
15. Bots, P., et al., *The role of SO<sub>4</sub> in the switch from calcite to aragonite seas*. Geology, 2011. **39**(4): p. 331-334.
16. Kitamura, M., *Crystallization and transformation mechanism of calcium carbonate polymorphs and the effect of magnesium ion*. Journal of Colloid and Interface Science, 2001. **236**(2): p. 318-327.
17. Dickinson, S.R. and K.M. McGrath, *Switching between kinetic and thermodynamic control: calcium carbonate growth in the presence of a simple alcohol*. Journal of Materials Chemistry, 2003. **13**(4): p. 928-933.
18. Alimi, F., et al., *Influence of magnetic field on calcium carbonate precipitation*. Desalination, 2007. **206**(1-3): p. 163-168.
19. Alimi, F., et al., *Effect of magnetic water treatment on calcium carbonate precipitation: Influence of the pipe material*. Chemical Engineering and Processing, 2009. **48**(8): p. 1327-1332.
20. Gabrielli, C., et al., *Magnetic water treatment for scale prevention*. Water Research, 2001. **35**(13): p. 3249-3259.
21. de Leeuw, N.H. and S.C. Parker, *Surface structure and morphology of calcium carbonate polymorphs calcite, aragonite, and vaterite: An atomistic approach*. Journal of Physical Chemistry B, 1998. **102**(16): p. 2914-2922.

22. Andersson, M.P. and S.L.S. Stipp, *How acidic is water on calcite?* Journal of Physical Chemistry C, 2012. **116**(35): p. 18779-18787.
23. Bano, A.M., P.M. Rodger, and D. Quigley, *New Insight into the Stability of CaCO<sub>3</sub> Surfaces and Nanoparticles via Molecular Simulation.* Langmuir, 2014. **30**(25): p. 7513-7521.
24. Fenter, P., et al., *Is the Calcite-Water Interface Understood? Direct Comparisons of Molecular Dynamics Simulations with Specular X-ray Reflectivity Data.* Journal of Physical Chemistry C, 2013. **117**(10): p. 5028-5042.
25. Wang, J.W. and U. Becker, *Structure and carbonate orientation of vaterite (CaCO<sub>3</sub>).* American Mineralogist, 2009. **94**(2-3): p. 380-386.
26. Wolthers, M., et al., *Calcite growth kinetics: Modeling the effect of solution stoichiometry.* Geochimica Et Cosmochimica Acta, 2012. **77**: p. 121-134.
27. Dandeu, A., et al., *Raman spectroscopy - A powerful tool for the quantitative determination of the composition of polymorph mixtures: Application to CaCO<sub>3</sub> polymorph mixtures.* Chemical Engineering & Technology, 2006. **29**(2): p. 221-225.
28. Carteret, C., et al., *Polymorphism Studied by Lattice Phonon Raman Spectroscopy and Statistical Mixture Analysis Method. Application to Calcium Carbonate Polymorphs during Batch Crystallization.* Crystal Growth & Design, 2009. **9**(2): p. 807-812.
29. Gabrielli, C., et al., *In situ Raman spectroscopy applied to electrochemical scaling. Determination of the structure of vaterite.* Journal of Raman Spectroscopy, 2000. **31**(6): p. 497-501.
30. Tlili, M.M., et al., *Characterization of CaCO<sub>3</sub> hydrates by micro-Raman spectroscopy.* Journal of Raman Spectroscopy, 2002. **33**(1): p. 10-16.
31. Tlili, M.M., et al., *Influence of the interfacial pH on electrochemical CaCO<sub>3</sub> precipitation.* Journal of the Electrochemical Society, 2003. **150**(11): p. C765-C771.
32. Devos, O., et al., *Nucleation-growth process of scale electrodeposition - Influence of the supersaturation.* Journal of the Electrochemical Society, 2003. **150**(7): p. C494-C501.
33. Tlili, M.M., et al., *Study of electrochemical deposition of CaCO<sub>3</sub> by in situ Raman spectroscopy - II. Influence of the solution composition.* Journal of the Electrochemical Society, 2003. **150**(7): p. C485-C493.
34. Devos, O., et al., *Nucleation-growth process of scale electrodeposition - influence of the magnesium ions.* Journal of Crystal Growth, 2009. **311**(18): p. 4334-4342.
35. Freestone, I., et al., *The Lycurgus Cup - A Roman nanotechnology.* Gold Bulletin, 2007. **40**(4): p. 270-277.
36. Sardar, R., et al., *Gold Nanoparticles: Past, Present, and Future.* Langmuir, 2009. **25**(24): p. 13840-13851.
37. Daniel, M.C. and D. Astruc, *Gold nanoparticles: Assembly, supramolecular chemistry, quantum-size-related properties, and applications toward biology, catalysis, and nanotechnology.* Chemical Reviews, 2004. **104**(1): p. 293-346.
38. Turkevich, J., P.C. Stevenson, and J. Hillier, *A study of the nucleation and growth processes in the synthesis of colloidal gold.* Discussions of the Faraday Society, 1951(11): p. 55-58.
39. Enustun, B.V. and J. Turkevich, *Coagulation of colloidal gold.* Journal of the American Chemical Society, 1963. **85**(21): p. 3317.
40. Turkevich, J., P.C. Stevenson, and J. Hillier, *The formation of colloidal gold.* Journal of Physical Chemistry, 1953. **57**(7): p. 670-673.
41. Brust, M., et al., *Synthesis and reactions of functionalized gold nanoparticles.* Journal of the Chemical Society-Chemical Communications, 1995(16): p. 1655-1656.
42. Brust, M., et al., *Synthesis of thiol-derivatized gold nanoparticles in a 2-phase liquid-liquid system.* Journal of the Chemical Society-Chemical Communications, 1994(7): p. 801-802.
43. Gofberg, I. and D. Mandler, *Preparation and comparison between different thiol-protected Au nanoparticles.* Journal of Nanoparticle Research, 2010. **12**(5): p. 1807-1811.

44. Kuther, J., et al., *Mercaptophenol-protected gold colloids as nuclei for the crystallization of inorganic minerals: Templated crystallization on curved surfaces*. Chemistry of Materials, 1999. **11**(5): p. 1317-1325.
45. Kuther, J. and W. Tremel, *Stabilization of aragonite on thiol-modified gold surfaces: effect of temperature*. Chemical Communications, 1997(21): p. 2029-2030.
46. Gouesbet, G., *Generalized Lorenz-Mie theories, the third decade: A perspective*. Journal of Quantitative Spectroscopy & Radiative Transfer, 2009. **110**(14-16): p. 1223-1238.
47. Heller, W., J.N. Epel, and R.M. Tabibian, *Experimental verification of the mie theory of light scattering .1*. Journal of Chemical Physics, 1954. **22**(10): p. 1777-1778.
48. Bell, S.E.J. and M.R. McCourt, *SERS enhancement by aggregated Au colloids: effect of particle size*. Physical Chemistry Chemical Physics, 2009. **11**(34): p. 7455-7462.
49. Jansen, M., *The chemistry of gold as an anion*. Chemical Society Reviews, 2008. **37**(9): p. 1826-35.
50. Hu, Y.J., et al., *Scalable Preparation of Ultrathin Silica-Coated Ag Nanoparticles for SERS Application*. ACS Applied Materials & Interfaces, 2013. **5**(21): p. 10643-10649.
51. Chaudhuri, R.G. and S. Paria, *Core/Shell Nanoparticles: Classes, Properties, Synthesis Mechanisms, Characterization, and Applications*. Chemical Reviews, 2012. **112**(4): p. 2373-2433.
52. Devos, O., C. Gabrielli, and B. Tribollet, *Nucleation-growth process of scale electrodeposition - Influence of the mass transport*. Electrochimica Acta, 2006. **52**(1): p. 285-291.
53. Gabrielli, C., et al., *Study of the electrochemical deposition of CaCO<sub>3</sub> by in situ Raman spectroscopy - I. Influence of the substrate*. Journal of the Electrochemical Society, 2003. **150**(7): p. C478-C484.

# Chapter 2 Theoretical background

---

## 2.1 Surface Structure

The surface structure of metals is a valuable tool in the armoury of surface science; pure metals arrange in ordered matrices and most metals adhere to one bulk structural form. The arrangement of the atoms of most metals can be described using one of the three crystal systems; face centred cubic (fcc), body centred cubic (bcc) and hexagonal close packed (hcp) (Figure 2-1).

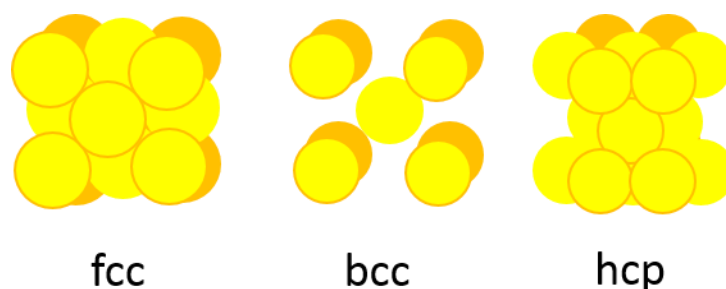


**Figure 2-1** Crystallographic structure of metals; Face centred cubic (fcc), body centred cubic (bcc), hexagonal close packed (hcp)

In the work described here we are predominately interested in the fcc structure as this is the structure of gold, exhibiting a close packed arrangement of atoms in the bulk, with a coordination number of 12. However, the closely related hcp structure must also be considered with gold, as some surfaces of gold exhibit both fcc and hcp structuring [1]. When a metal is cut to expose a surface, different atomic arrangements will be exposed depending on the orientation of the metal and the direction of the cutting plane. Miller indices are used to describe the orientation of the cut surface to the bulk unit cell.

Miller indices simply describe the way in which a metal is cut so that the atomic arrangement of the surface can be predicted. The different surfaces and the differing atomic arrangements they exhibit lead to unique physical electronic characteristics and subsequent differences in chemical reactivity when exposed to the same reactive species. It is for this reason that metal single crystals are of interest here and the parallels drawn to the structure of nanoparticle surfaces.

The arrangement of the atoms on the exposed single crystal surfaces are described by defining the most basic repeating structure on the surface known as the unit cell. For more

information on surface electronic structure, Miller indices and unit cells the reader is directed to references [1-3].

## 2.2 Cyclic Voltammetry

Cyclic voltammetry is an example of a potential sweep technique, where a potential is swept first in one direction, then back in the opposite direction. The resulting current is monitored and reveals useful information about the reactivity of the species being studied. It can also give extremely sensitive qualitative information about the structure of the electrode surface and any species present. It is used to ensure a good single crystal surface is produced ready for experimentation while also giving an indication of any contaminants present.

Cyclic voltammetry involves the measurement of current density with respect to an applied voltage. A voltage is applied to the working electrode with respect to that of the reference electrode. The potential is swept, at a constant rate,  $V s^{-1}$ , from an initial potential to a final potential, known as the potential limits ( $E_1 - E_2$ ), this simple potential sweep is known as linear sweep voltammetry. For cyclic voltammetry when the potential reaches  $E_2$  it is simply reversed and the potential is swept in the opposite direction back to  $E_1$ , resulting in a saw-tooth waveform. It is this reversibility that makes this technique excellent for studying redox reactions. The use of a potentiostat during experiments allows the current generated at the working electrode to be controlled and monitored and ensures that the current passes through the counter electrode, this is important as if any current reaches the reference electrode it could cause error in the measured current or potential, this is discussed further in Section 3.4.1. Figure 2-2 shows the resulting saw-tooth waveform that is produced during a cyclic voltammetry experiment.

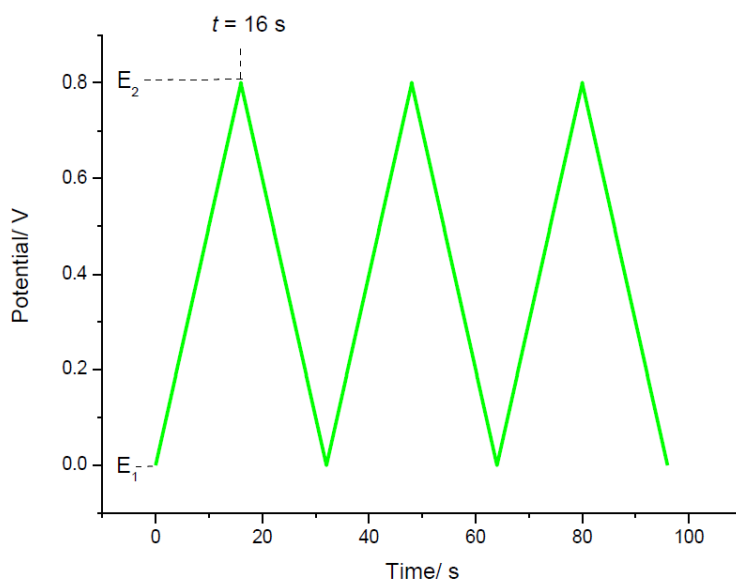


**Figure 2-2** Saw-tooth potential applied for cyclic voltammetry, sweep rate  $0.05 \text{ V s}^{-1}$ , between 0 - 0.80 V

The current that is measured during these potential sweep experiments is typically expressed as current density, which is the current normalised to the surface area of the working electrode. Therefore a cyclic voltammogram may be expressed as current density ( $j$ ) vs potential ( $E$ ).

At a stationary electrode there are two main types of processes to consider that result in the production of current, those where the applied potential causes electron transfer to or from species in solution, an example of this would be a simple one electron charge transfer redox reaction e.g.  $\text{Fe}^{3+}_{(\text{aq})} + \text{e}^- = \text{Fe}^{2+}_{(\text{aq})}$ , this type of process is known as a Faradaic process. The second type involves the adsorption and desorption of ions on the electrode surface without any charge transfer occurring, this is a non-Faradaic process, an example of which is the charging of the double layer, seen in most voltammograms. The electrical double layer is a model describing the interaction and structure of ions at the interface of materials, in this case the electrode surface and the electrolyte[3].

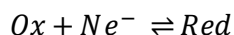
### 2.2.1 Faradaic Processes

Faradaic processes involve the transfer of electrons across the electrode/electrolyte interface resulting in redox reactions taking place. The current produced through this process is known as Faradaic current,  $I_F$ , as it obeys Faraday's Law:

$$I_F = \frac{dQ}{dt} = n_e F \frac{dN}{dt} = n_e F A v$$

Equation 2-1

Where the charge  $Q$ , is seen to be related to the concentration of reactant  $N$ , the Faraday constant  $F$  and the number of electrons transferred  $n_e$ . As such a direct correlation exists between the reaction rate  $v$  for a given electrode surface area  $A$ . A simple redox reaction is considered:



Equation 2-2

A typical voltammogram for the above reversible redox reaction occurring at the electrode during this reaction is shown in Figure 2-3.

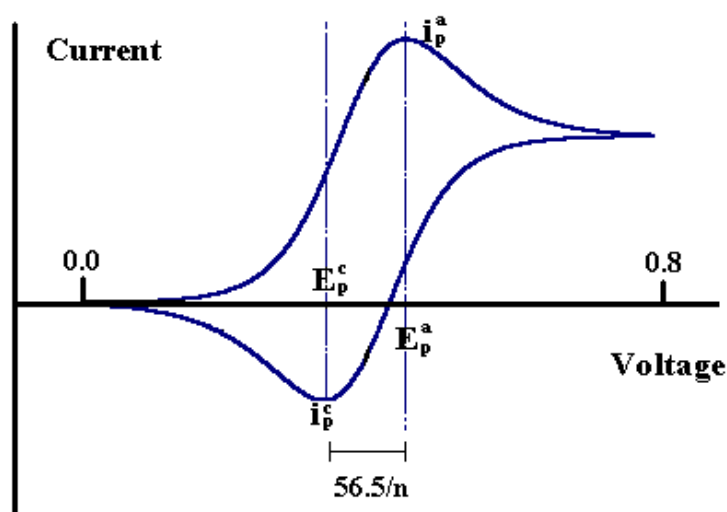


**Figure 2-3** Cyclic voltammogram of a reversible reaction

In the voltammogram the scan begins from left to right, and current starts to flow as more of the species are oxidised, at some point the number of available reactants in the double layer is reduced and the current drops off again, as the voltage is then swept in the opposite direction the species are reduced before once again returning to  $E_1$ . The rate of electron transfer is very fast when compared to that of the voltage sweep rate, therefore the concentration of species at the electrode surface is governed by the Nernst equation (Equation 2-3).

$$E = E_0 + \frac{RT}{nF} \ln \frac{[Ox]}{[Red]}$$

Equation 2-3

Where  $E$  is the applied potential,  $E_0$  the standard equilibrium potential both in V,  $R$  is the universal gas constant ( $8.314 \text{ J K}^{-1} \text{ mol}^{-1}$ ),  $T$  is the temperature in K,  $n$  is the number of

electrons transferred,  $F$  is the Faraday constant ( $96487 \text{ C mol}^{-1}$ ). Finally  $[Ox]$  and  $[Red]$  are the concentrations of the species at the electrode surface. It can be seen from this equation that the basis to all voltammetry is the variation of the ratio of the oxidised and reduced species as a function of potential. For a reversible reaction at 298 K the peak current,  $i_p$  (A), should be of the same magnitude for both the forward and reverse sweeps and can be calculated using the Randles-Sevcik equation (Equation 2-4).

$$i_p = (2.69 \times 10^5) n^{\frac{3}{2}} A D^{\frac{1}{2}} C v^{\frac{1}{2}}$$

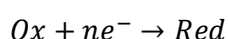
Equation 2-4

Whereby  $n$  is the electron stoichiometry,  $A$  is the area of the electrode ( $\text{cm}^2$ ),  $D$  is the diffusion coefficient ( $\text{cm}^2 \text{ s}^{-1}$ ),  $C$  is the concentration of the bulk electrolyte ( $\text{mol cm}^{-3}$ ) and  $v$  is the scan rate ( $\text{V s}^{-1}$ ). Immediately it can be seen that the peak current is proportional to the concentration and the square root of the scan rate, hence as the scan rate increases so to should the observed current peak height. The number of electrons transferred in a reversible reaction, such as that shown in Figure 2-3, can be calculated from the separation between the anodic and cathodic peaks (Equation 2-5).

$$\Delta E_p = E_p^a - E_p^c \approx \frac{0.057}{n}$$

Equation 2-5

It is worth noting that when the rate of electron transfer is slow compared to that of the scan rate, the above does not hold true and cannot be described by the Nernst equation, these reactions are known as quasi-reversible or irreversible reactions.



Equation 2-6

In a simple irreversible reaction (Equation 2-6) the applied voltage will not give the correct concentrations of species of interest at the electrode surface, this is due to the breakdown of the Nernst equation as an equilibria is not formed rapidly enough compared to the scan rate. For irreversible reactions the electrode potential becomes dependent upon the scan rate since an equilibria for the system is not reached, while the peak current remains proportional to the square root of the scan rate [3], in this case Equation 2-7 and 2-8 take prevalence for the peak current  $i_p$ , and the electrode potential  $E_p$ .

$$i_p = (3.01 \times 10^5) n \sqrt{\frac{2.3RT}{bF}} D^{\frac{1}{2}} C v^{\frac{1}{2}}$$

Equation 2-7

$$E_p = E_{\frac{1}{2}} - b \left[ 0.52 - \frac{1}{2} \log \frac{b}{D} - \log k_s + \frac{1}{2} \log v \right]$$

Equation 2-8

To enable the calculation of peak current or electrode potential a Tafel plot is required to deduce  $b$ , the gradient from a Tafel slope ( $\log_e i$  vs  $E$ ) in  $V^{-1}$ .  $K_s$  is the specific rate constant at the standard potential found from a plot of  $E_p$  vs  $\log v$ .

### 2.2.2 Non-Faradaic Processes

A current also arises from the double layer, as a result of non-faradaic processes. The current results from adsorption and desorption of species at the electrode surface, in the absence of electron transfer i.e. no chemical reaction occurs as no electrons cross the electrode/electrolyte interface. An applied negative potential at the electrode builds charge, to balance this charge ions in solution move toward or away from the charge, causing a change in the electrochemical double layer. The subsequent charging of the double layer can be given by Equation 2-9.

$$I_{DL} = AC_{DL}v$$

Equation 2-9

Where  $I_{DL}$  (A) is the double layer current, it is observed to be proportional to the electrode surface area  $A$  ( $\text{cm}^2$ ), the capacitance of the double layer  $C_{DL}$  (F) and the scan rate. This non-faradaic current generated from the charging of the double layer appears in CV measurements and must be subtracted from CV peak current data before any calculations are performed for the determination of charge transfer data. The focus of this study is primarily on Faradaic processes.

## 2.3 Microscopy

Electron microscopes work in a similar manner to that of light microscopes, however they utilise magnetic fields instead of glass lenses and electrons rather than photons to illuminate a sample for analysis.

The resolution limit of a light microscope was defined by Ernst Abbe and known as the Abbe diffraction limit [1];

$$d = \frac{\lambda}{2n \sin\theta}$$

Equation 2-10

Where  $d$  is the resolution limit,  $\lambda$  is the wavelength of light, and the denominator  $n\sin\theta$ , also known as the numerical aperture, is a dimensionless number that describes the range of angles that an objective lens of a system can emit or accept light, modern optics can reach about 1.4-1.6, this means the above expression can be simplified

$$d = \frac{\lambda}{2.8}$$

Equation 2-11

Therefore the diffraction limited resolution of a light microscope using 500 nm light would be ~ 200 nm.

Electron microscopes are also diffraction limited as they rely upon the wave nature of the electron beam. However a considerable improvement in resolution is achieved with electron microscopes as they use electrons with wavelengths much shorter than that of photons of visible light. An electrons wavelength  $\lambda$  is known as its de Broglie wavelength:

$$\lambda = \frac{h}{p} = \frac{h}{\sqrt{2m_e E_b}}$$

Equation 2-12

Where  $h$  is Planck's constant and  $p$  is the linear momentum of the electron. Hence the greater the momentum of an electron the shorter the resulting de Broglie wavelength and the greater the achievable resolution limit. The momentum is dependent upon the resting mass of the electron  $m_e$  a fundamental physical constant and  $E_b$  the energy of the electron beam. Therefore as the electron beam energy increases the de Broglie wavelength decreases.

### 2.3.1 Scanning Electron Microscopy

Electron microscopy began with the development of electron optics in 1926 when Busch studied how a magnetic field affected the trajectories of electrons and realised the capabilities of this as means of focusing electron beams [5]. At almost the same time wave-particle duality was proposed by De Broglie and hence a frequency and wavelength could be attributed to particles and for this purpose, electrons. It was these two discoveries which opened up the field of electron optics and lead to the realisation of electron microscopy [6]. Relatively soon after, at the beginning of the 1930's, Knoll and Ruska calculated the higher resolution of electron microscopy to light microscopy and in 1931 the world's first transmission electron microscope (TEM) was constructed.

The development of this technique over shadowed that of the developing scanning electron microscopy (SEM) due to its greater resolution. However, the first SEM was constructed in 1935 by Knoll although the resolution of this machine was relatively poor somewhere in the region of 100  $\mu\text{m}$ . Over the next few decades improvements were made and the capability of SEM to scan large areas and to produce three dimensional topographical images was understood and more prototypes were constructed by Zworykin (1942)[7], Oatley (1948)[5], Smith (1956)[8] and Everhart & Thornley (1960)[9]. However it was not until 1963 that Pease and Nixon combined all of these improvements into one machine and constructed what we would now recognise as an SEM machine [5, 6, 10].

Fundamentally Scanning Electron Microscopy (SEM) involves the combined analysis of electrons and X-ray photons resulting from the interaction of a beam of electrons with a surface. An electron beam, usually operating between 1 and 50 keV, is concentrated using successive electromagnetic condenser lenses and focused by the objective lens onto the sample. The electron beam is rastered over the surface, using the magnetic field created by a pair of deflector coils (Figure 2-4).

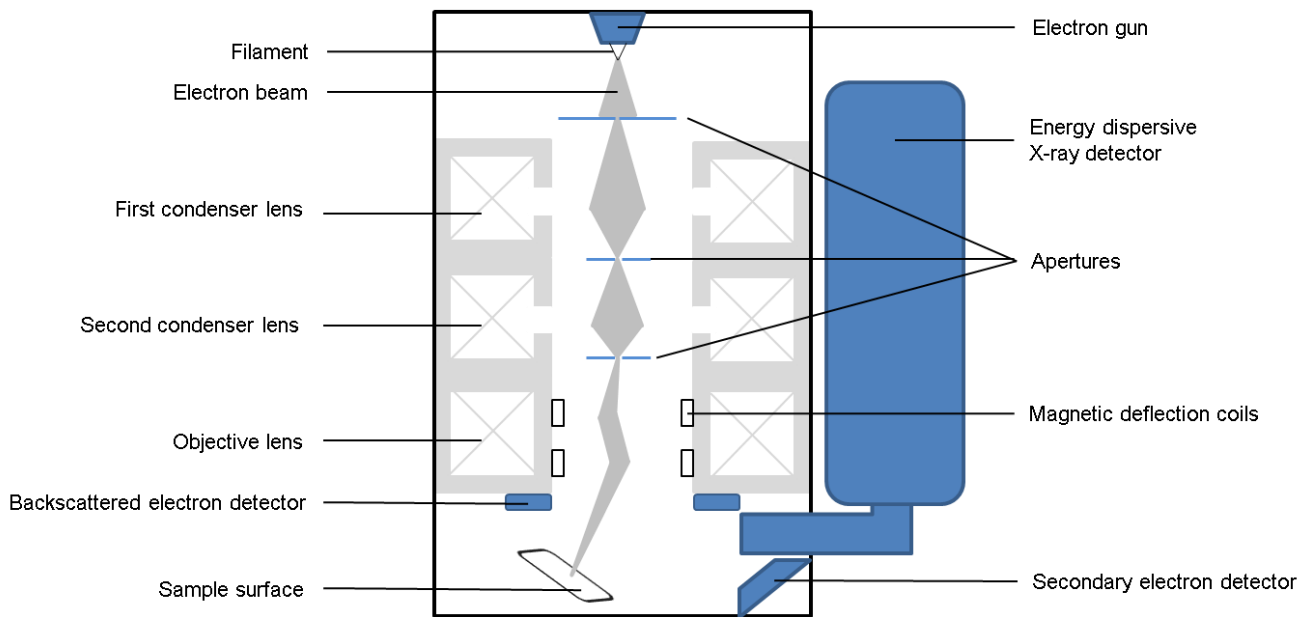


**Figure 2-4** Schematic of scanning electron microscope

The incident electron beam penetrates the sample surface leading to the emission of various electron and X-ray photons. For the purpose of imaging in this work only three are considered: Primary or backscattered electrons and secondary electrons which are both used for imaging and X-ray photons for elemental analysis. The incident beam can interact with the sample atoms in an elastic or inelastic manner; elastic scattering occurs when an incident electron interacts with an atomic nucleus, the resulting electron's energy remains predominantly unchanged. These electrons are known as primary electrons and are collected to form the backscattered images that show contrast between atoms of high and low atomic number  $Z$ . A higher atomic number and hence larger atomic nucleus tends to scatter electrons more effectively and therefore results in a brighter image compared to smaller nuclei. This is particularly useful when looking at a sample where there is a large difference in atomic number, for example carbon and gold. Inelastic scattering, on the other hand, occurs when the incident electron transfers some of its energy to an electron in the sample, if the energy transferred is sufficient, the electron will be emitted and detected at lower energies than the primary electrons. When these electrons poses less than 50 eV they are known as secondary electrons and are detected using a cathode ray tube, giving rise to high resolution images. The third type of interaction involves a primary electron colliding with and ejecting a core electron from the sample, the resulting excited atom then drops to a lower energy state emitting either a characteristic X-ray photon (the basis of X-ray fluorescence spectroscopy) or an Auger electron, (Auger spectroscopy) allowing information to be garnered on the chemical composition of the surface. It is the combined analysis of interactions that make the SEM a vital analytical instrument.

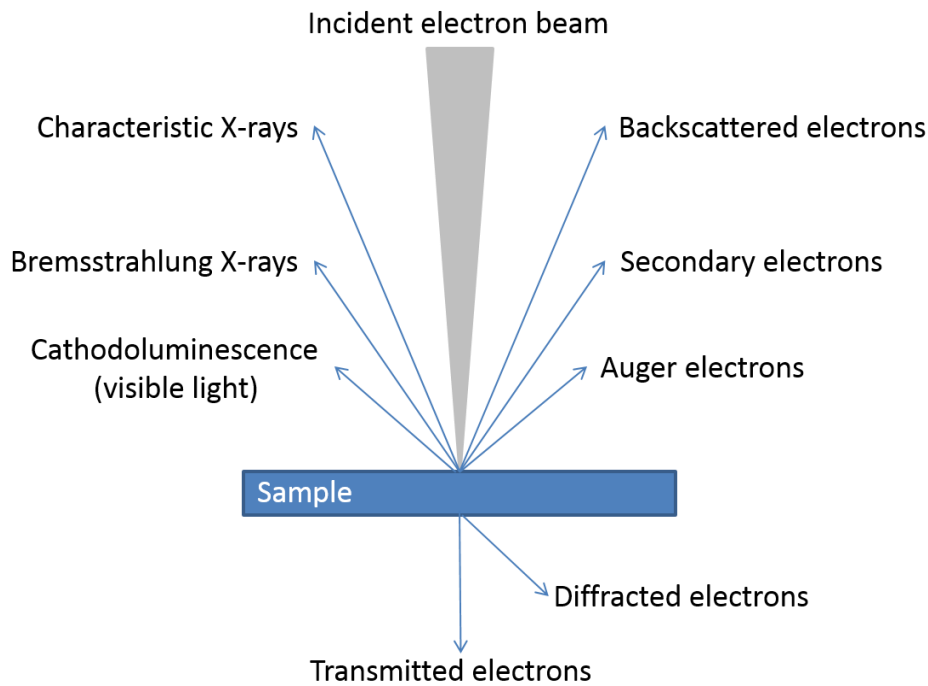


**Figure 2-5** Schematic of electron beam interactions

The limit of resolution for a scanning electron microscope is dependent upon the wavelength  $\lambda$  of the electrons in the incident beam and the numerical aperture NA. The wavelength, (as discussed above) varies depending on the energy of the beam, and the numerical aperture varies from system to system and can usually be found engraved on the system. Thus R, the resolution limit is defined as:

$$R = \frac{\lambda}{2NA}$$

Equation 2-13

### 2.3.2 Transmission Electron Microscopy

Transmission electron microscopy, like SEM, involves the analysis of electrons and X-rays resulting from the interaction of a beam of electrons with a sample as illustrated in Figure 2-5. The key difference is that much higher energy electrons are used and the image is composed of electrons that are transmitted through the sample and collected on a phosphorescing screen. It is the higher energy electrons which are key to the TEM, firstly higher energy electrons are required to penetrate a sample, secondly and more fundamentally higher energy electrons have shorter wavelengths and hence higher resolution is achievable.

Typically electrons are accelerated to 100 keV, but can be accelerated to as much as 1 MeV depending on sample thickness. Condenser lenses are used to concentrate the electron beam onto and through a thin sample. Deflected electrons, photo electrons and X-rays are collected in the same way as SEM and the un-deflected electrons are collected on a phosphorous screen used to help focus the image, then the screen is moved to reveal a charge-coupled device (CCD) camera, which enables the image to be viewed via a computer monitor. The main advantage of TEM is that much smaller samples can be imaged and that diffraction measurements are also possible. However, due to the need for transmitted electrons samples can only be up to a few hundred nanometres in thickness.

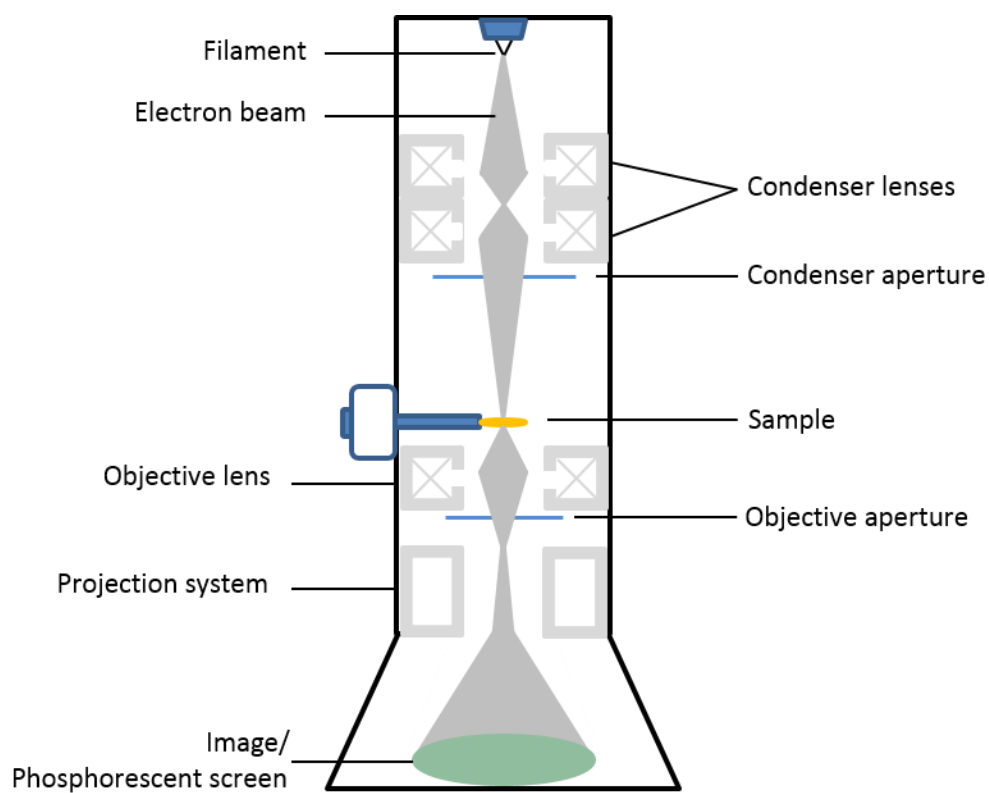


**Figure 2-6** Schematic of transmission electron microscope

### 2.3.3 Scanning Tunnelling Microscopy

Scanning tunnelling microscopy (STM) was first invented in 1981 by Gerd Binnig and Heinrich Rohrer at the IBM Zurich research laboratories in Switzerland, for which they were awarded the Nobel Prize in physics in 1986.

Scanning tunnelling microscopy is a technique that allows for atomic resolution of samples making it an extremely useful probe when investigating the interactions of single atoms or single molecules on a surface and is based on a phenomenon, which arises from a quantum mechanical effect, known as electron or quantum tunnelling.

Quantum mechanics shows that particles and waves are not separate entities and that they can have shared properties, this theory is known as wave-particle duality. Therefore when a particle such as an electron encounters a potential barrier whose height is greater than its own kinetic energy there is in fact a non-zero probability that the particle crosses the barrier, this is contrary to classical mechanics which describes the particle having a zero probability of crossing the potential barrier. Therefore when two conductors are brought very close together, an electron from one conductor can escape and enter the separating vacuum, before appearing on the other side of the barrier in the second conductor. The associated wavefunctions can be expressed as follows:

$$\Psi(d) = \Psi(0)e^{-kz}$$

Equation 2-14

Where  $k$  is described in Equation 2-17, and  $z$  is the distance between the two conductors. In the presence of an applied potential when the wavefunctions overlap and tunnelling occurs a current will result,  $I$ , known as the tunnelling current.

$$I \propto e^{-2kz}$$

Equation 2-15

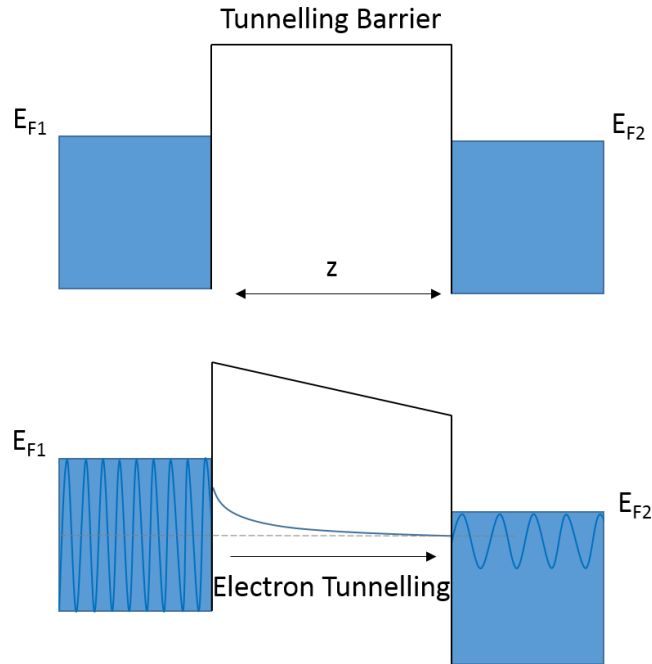


**Figure 2-7** One dimensional model of electron tunnelling, a) in the absence of an applied potential (no tunnelling) and b) in the presence of an applied bias  $V$  (tunnelling occurs).

Similarly in a typical STM, when a conducting tip which has had an applied potential bias, is brought close to the surface of a metal or semi-conductor, the extended wavefunctions of the electrons in the tip and surface will overlap and quantum tunnelling can occur. Tunnelling is the movement of an electron from the tip to the surface or visa versa depending on the polarity of the applied bias. For tunnelling to proceed the extended wavefunctions of the electrons in the tip and surface must overlap as well as having a sufficiently strong applied potential bias (Figure 2-7). The tunnelling current,  $I$ , for an STM is given by:

$$I = C\rho_t\rho_s e^{-zk^2}$$

Equation 2-16

Where  $C$  is a constant dependent upon the applied voltage,  $\rho_t$  is the electronic structure of the tip,  $\rho_s$  is the electronic structure of the sample surface,  $z$  is the distance between the tip and the surface and  $k$  is given as follows:

$$k = \frac{\sqrt{2m(V - E)}}{h}$$

Equation 2-17

Where  $m$  is the mass of an electron ( $9.11 \times 10^{-31}$  kg),  $V$  is the potential of the barrier or vacuum,  $E$  is the energy of the tunnelling electron and  $h$  is Planck's constant ( $6.626 \times 10^{-34}$  J s).

From Equation 2-16 it can be seen that there is an exponential relationship between the tunnelling current and the tip-surface distance, it is this that enables the practical use of STM as a very small change in distance (0.1 nm) results in an order of magnitude change in the tunnelling current.

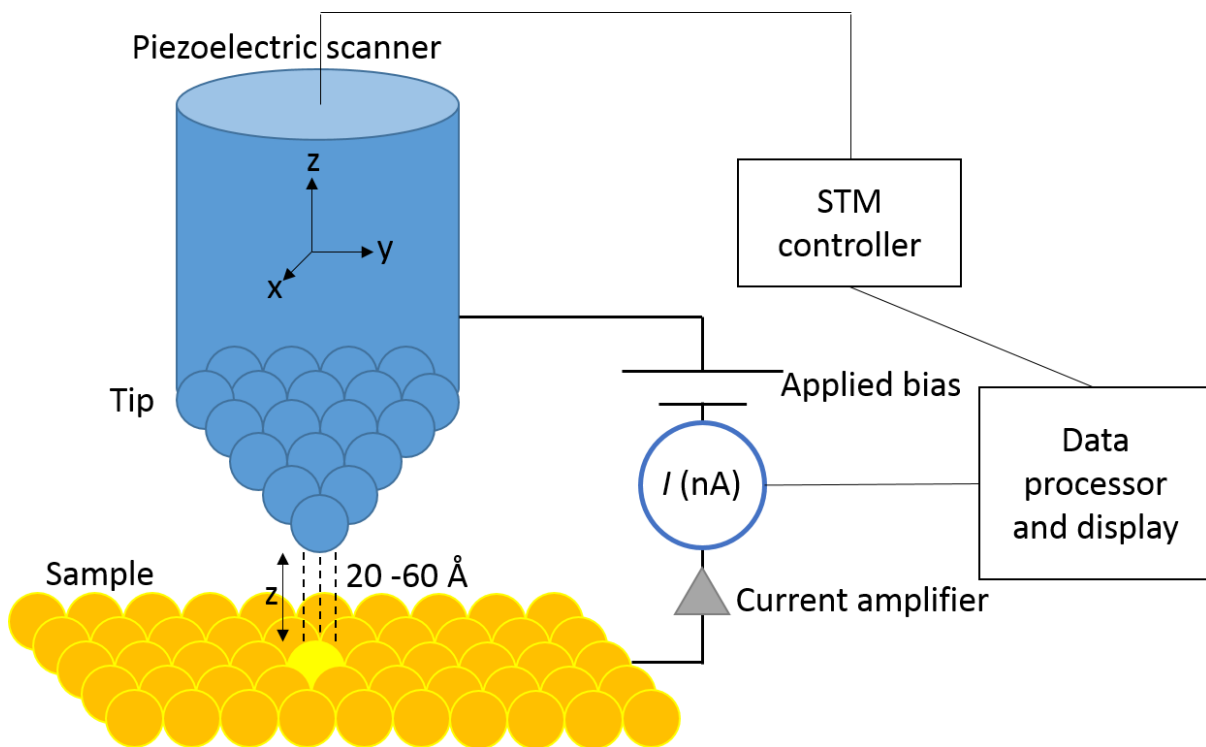


**Figure 2-8** Schematic of scanning tunnelling microscope

The tips used here are of tungsten and in practice, the tip is positioned above the sample surface with a typical tip-surface distance of between 0.2 – 0.6 nm. Piezoelectric arrays enable the tip to be moved very accurately in the x,y and z directions, with a limit to resolution of 0.01 nm and 0.002 nm respectively. During operation when the tip is scanning the surface, the height of the tip is continually monitored and adjusted to ensure that the tunnelling current remains constant. The tip position is recorded and used to create the three dimensional topographic atomic resolution images.

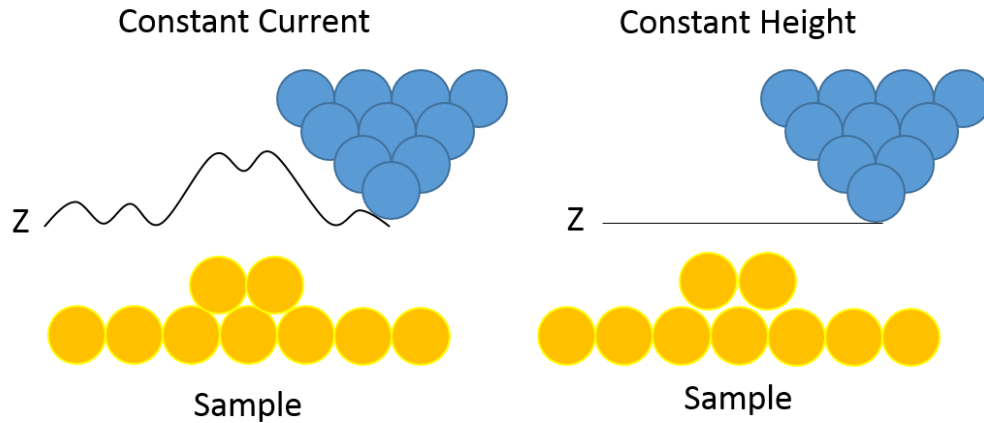


**Figure 2-9** Different modes of operation for the STM. Left constant current, right constant height.

Commonly STM is operated in one of two modes, constant current mode or constant height mode (Figure 2-9). In constant current mode the tunnelling current and voltage bias are kept constant by altering the tip-surface distance, this results in an image that directly correlates to the electron density profiles at the surface. Constant height mode requires the tip-surface distance and voltage bias to remain constant while changes in the tunnelling current are recorded. This method enables quicker scan times but risks the occurrence of tip-surface crash incidents if the surface being scanned is not very atomically flat. In the Omicron STM systems the software uses a blend of these two approaches by allowing the operator to control the extent of the feedback response of the tip. At large scan dimensions the tip scans the surface in constant height mode allowing for more rapid scan speeds of larger areas  $\sim 500 \text{ nm}^2$ . When smaller images are sought, the feedback mechanism lends more toward constant current mode and higher resolution scans are achieved at the expense of speed.

An interesting twist in the dawning of the STM was its struggle to become accepted as the formidable analysis technique it has now become. This was due to the already developed invention of the topographer which academics at the time saw as useless; STM was viewed as a reincarnation of the older technique. However due to younger researchers at IBM persisting with this technique and considering the rise of surface science studies, they realised that for studies under high vacuum and with much greater vibration protection this technique could excel and the first atomic resolved image was born, that of the  $7 \times 7$  reconstructed silicon surface [11].

## 2.4 Spectroscopy

Fundamentally spectroscopy involves the analysis of absorbed and emitted electromagnetic (EM) radiation upon interaction with matter (an analyte). In its infancy spectroscopy involved the splitting of visible light through a prism and the analysis of the individual colours representing the discrete wavelengths of visible light, it can be imagined how this led to the UV-Vis spectroscopy we know today. Spectroscopy now utilises much more of the EM spectrum and is used extensively in all aspects of science and technology.

In classical physics electromagnetic radiation is described as a wave that is able to propagate through space, at the speed of light, made up of two perpendicular alternating waves, one electronic wave vector and one magnetic wave vector.

However EM radiation also has some particle characteristics as explained by quantum mechanics, hence a particular wavelength of EM radiation possesses a discrete quanta of energy, the particles associated with EM radiation are known as photons and their energy is dependent upon the frequency of the wave and hence the energy,  $E$  (eV), can be calculated:

$$E = \frac{hc}{\lambda} = h\nu$$

Equation 2-18

Where  $h$  is Planck's constant (J s),  $c$  is the speed of light ( $2.99 \times 10^8$  m s<sup>-1</sup>) and  $\lambda$  is the wavelength (m) of the EM radiation, the link between the speed of light and the wavelength can be seen in this expression leading to the frequency,  $\nu$ , (s<sup>-1</sup>) of the EM radiation.

The electric field,  $E$ , (V m<sup>-1</sup>) is a vector quantity and its strength is dependent upon its magnitude and direction, hence at any given time ( $t$ ) its strength is related to both its amplitude ( $E_0$ ) and frequency.

$$E = E_0 \cos 2\pi \nu t$$

Equation 2-19

Rather than quoting wavelengths when presenting data it is often presented in wavenumbers  $\bar{\nu}$  (m<sup>-1</sup>), this symbol represents a wavenumber for a wave travelling through a vacuum, when travelling through a medium it is more commonly expressed as  $\sigma$ , with units of cm<sup>-1</sup>. The wavenumber is merely the number of waves present over a certain distance, when wavelength is presented in metres, wavenumber is simply its reciprocal.

$$\bar{\nu} = \frac{\nu}{c} = \frac{1}{\lambda}$$

Equation 2-20

As mentioned previously the EM radiation used now in spectroscopy is not limited to that of the visible light region, the range of EM radiation is presented below with the associated type of radiation and its source. The present study utilises, UV-vis, IR and X-ray.

Electromagnetic radiation	wavelength (m)	Source of radiation
Gamma ray	$10^{-10} - 10^{-14}$	Rearrangement of nuclei, atomic decay
X-Ray	$10^{-8} - 10^{-12}$	Inner level electron transitions within atoms or molecules
Ultraviolet	$10^{-7} - 10^{-9}$	Valence level electron transitions within atoms and molecules
Visible	$10^{-6} - 10^{-7}$	
Infrared	$10^{-3} - 10^{-6}$	Vibrational level transitions
Micro wave	$10^{-1} - 10^{-3}$	Rotational level transitions
Radio wave	$10^4 - 10^{-3}$	Nuclear (magnetic) and electronic (spin) resonance

### 2.4.1 The Absorption Process

For the absorption of electromagnetic radiation to occur, the energy of the incident radiation must be quantised and the quanta of energy must be equal to the difference in energy between the ground state and an excited state. Electronic transitions are usually excited by UV-Vis radiation and result in the molecule becoming excited from the ground to the first electronic excited state. Vibrational spectroscopy involves the transition of electrons between vibrational states of the same electronic state, this is usually the transition between the ground ( $v = 0$ ) and an excited state ( $v = 1$ ). At room temperature most molecules exist in the ground electronic state, this is described by the Boltzmann distribution.

$$\frac{N_{Ex}}{N_{Gr}} = \frac{g_{Ex}}{g_{gr}} \exp \left[ \frac{-(E_{Ex} - E_{Gr})}{kT} \right]$$

Equation 2-21

This is a probability distribution describing the position of electrons in a molecule in its natural unexcited state at a given temperature. Where  $N_{Ex}$  is the number of molecule in the excited state and  $N_{Gr}$  is the number in the ground state,  $g$  is the degeneracy of the state,  $E$  is the energy of the state,  $k$  the Boltzmann constant ( $1.3806 \times 10^{-23} \text{ m}^2 \text{ kg s}^{-2} \text{ K}^{-1}$ ) and  $T$  the temperature. It can be seen from this formula that as the temperature rises so too will the population of the higher vibrational states.

For a covalently bound molecule to absorb Infrared radiation it must possess a changing dipole moment,  $\mu$ . Defined as a vector whose magnitude of charge ( $\delta$ ) is multiplied by the charge separation distance, ( $l$ ), measured in coulomb-metres (C m). The first scientist to extensively study dipole moments was Peter Debye and hence are sometimes expressed in Debye units ( $1 \text{ D} = 3.34 \times 10^{-30} \text{ C m}$ ).

$$\mu = \delta l$$

Equation 2-22

When a transition occurs there must be a non-zero change in the dipole moment, that is when a transition occurs the resulting dipole must have experienced some change, the transition dipole moment  $M_{01}$  is described in Equation 2-23.

$$M_{01} = \int_{-\infty}^{\infty} \psi_1 \mu_x \psi_0 dx$$

Equation 2-23

Whereby  $\psi$  represents the wavefunctions of the excited (1) and ground (0) states,  $dx$  represents the change in the vector length and  $\mu_x$  is the dipole moment. During a transition (a vibration in this case) there will be a change in  $dx$ , therefore for  $M_{01}$  to be non-zero and an absorption event to take place so too must  $\mu_x$  be non-zero. Similarly vectors in the  $y$  and  $z$  directions are considered, and the vibration will be Infrared active if there is a change in the dipole moment in any of these directions during a vibration event.

The intensity of a peak is defined by its specific absorbance ( $A$ ), the degree of absorbance is dependent upon the concentration of the absorbing species and is defined by the well-known Beer-Lambert law (Equation 2-24).

$$A = \epsilon cl$$

Equation 2-24

Whereby the concentration of the absorbing species is  $c$  (M), the path length  $l$  (cm) and the molar extinction coefficient  $\epsilon$  ( $M^{-1} \text{ cm}^{-1}$ ). The molar extinction coefficient is a constant for a given species and is a measure of the probability of the electronic transition occurring.

### 2.4.2 Light Scattering

For absorption to occur the frequency of the oscillating dipole moment of the molecule must be in resonance with the frequency of the incident light. If the frequency is not the same, the EM field of the incident light can still interact with the electron cloud surrounding the molecule causing the cloud to distort in shape. The distortion is a polarisation of the electron cloud with an induced dipole  $P$ :

$$P = E\alpha$$

Equation 2-25

The induced dipole moment is dependent upon two factors, the strength of the electric field  $E$  (Equation 2-19) and the polarisability ( $\alpha$ ), which is the susceptibility of the electron cloud to become polarised. When the induced dipole and the incident light oscillate at the same frequency a virtual state is formed. This excited state will relax by emitting photons, returning the complex to the ground state. The photons are emitted in random directions and hence the effect is known as scattering. This process is similar to fluorescence in as far as it is a two photon process, and differs in that no absorption takes place. For this reason it is also a much quicker event lasting just  $10^{-12}$  seconds. In fact, the time frame for the scattering event occurs so rapidly that the nuclei do not have time to adjust to the excited virtual state and the resulting scattered photon will possess the same energy as the incident photon. This process leads to the inelastic Rayleigh scattering and explains why the inelastic Raman scattering is such a weak effect.

### 2.4.3 Raman Spectroscopy

Raman spectroscopy began in the late 1920's with the discovery by physicist Sir C.V Raman, for whom the phenomenon was named [12]. His investigations concerned the way light interacts with liquids and particularly what gave sea water its colour; he was convinced it was not merely reflection of light. Using photographic filters to produce monochromatic light, and secondary crossed filters to block the monochromatic light after interaction with the water he was able to show that the light emanating from the water was able to pass through the second filter and therefore a change in wavelength had occurred. For this discovery he was awarded

the Nobel Prize in 1930 [13, 14]. The Raman Effect gives a very weak signal in comparison to the elastic Rayleigh scattering and it was not until high powered lasers were introduced that the Raman Effect could be effectively utilised.

Raman spectroscopy is a vibrational spectroscopy that relies on the scattering of photons upon interaction with the electron cloud of an analyte molecule, causing a change in the virtual vibrational energy state of the molecule. The emitted photons are collected and analysed, yielding information about the nature of the vibrational level from which they originated [1].

When monochromatic light interacts with a molecule two interactions are observed; elastic Rayleigh scattering and inelastic Raman scattering, of which two forms can exist Stokes and Anti-Stokes (Figure 2-9).

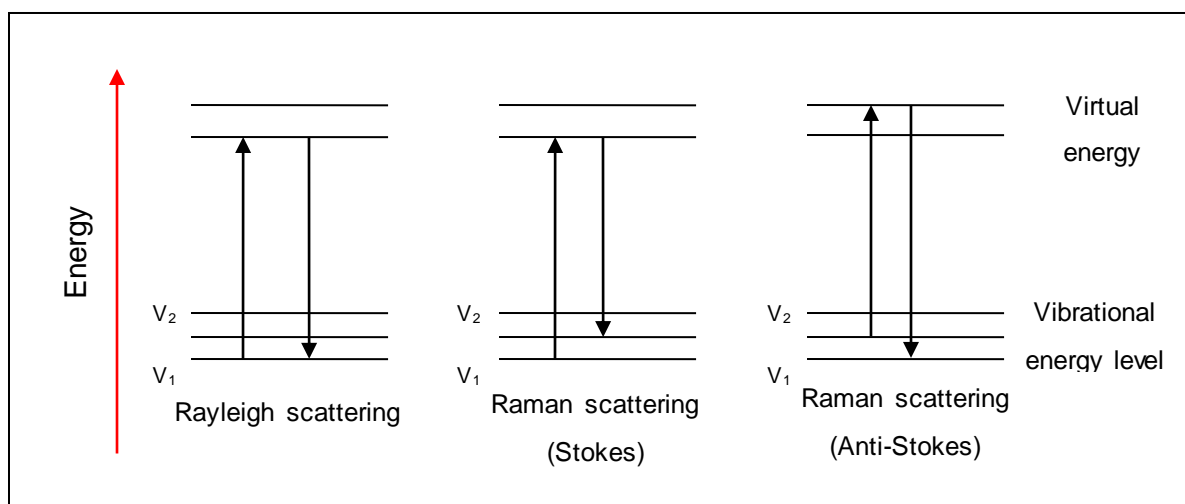


**Figure 2-9** Energy diagram of light scattering interactions of light with matter

When incident light interacts with the analyte the molecular bond will be excited to a higher vibrational energy level, also known as a virtual vibrational state. Upon relaxation, the majority of the emitted photons will possess the same frequency, depicted above as Rayleigh scattered photons. The Stokes scattering process seen above is a Raman process and occurs when the emitted photon has a lower frequency than the incident radiation. The anti-Stokes scattering of photons is a weaker process than that of the Stokes scattering and is temperature dependant as it occurs when an incident photon interacts with a molecule which is already thermally excited and hence a higher frequency photon is emitted upon relaxation.

The Raman effect is an extremely weak process constituting only about 1 photon in every 10 million Rayleigh scattered photons. High powered lasers have gone some way to improve the intensity of observed spectra, however very high powered lasers are likely to affect or even

destroy the analyte. It is for this reason that the development of an enhanced form of the Raman Effect was sought, and this led to the discovery of Surface Enhanced Raman Spectroscopy (SERS). This field has now broadened to Surface-Enhanced Vibrational Spectroscopy and encompasses numerous enhancement techniques for both Raman and Infrared spectroscopy [15].

### 1.1 Surface Enhanced Raman Spectroscopy

Surface Enhanced Raman Spectroscopy (SERS) was first discovered by Fleischmann in 1974 [16] who measured the highly enhanced spectra of pyridine on a roughened silver electrode. The roughened silver electrode was initially employed as it was expected that the higher surface area would result in enhanced spectra of the monolayer of substrate. However, the enhancement of the resultant spectra was so great it could not have been due to the increased surface area alone. A few years later Duynes and Creighton simultaneously described that the high degree of enhancement was due to some surface interaction with the substrate [17, 18].

Ever since this discovery much work has gone into describing a definitive mechanism for the observed enhancement although thus far no single mechanism can describe all of the observed enhancements. Two main schools of thought exist, one focusing on the electromagnetic enhancement and the other on a chemical enhancement with the former generally being considered to be the dominant effect [19]. The electromagnetic effect is attributed to a number of effects but the main contributor is considered to be from localised surface Plasmon excitation. When a metal surface is roughened with imperfections such as protrusions and step edges, or when metal nanoparticles whose size is smaller than the wavelength of the incident radiation are present, surface plasmons can occur, which are the collective motion of conduction electrons. The surface plasmons oscillate coherently with the oscillations of the incident radiation causing the surface plasmon resonances and the resultant observed electric field enhancement [20].

The chemical theory of enhancement focuses on the interactions between the metal surface and the adsorbate, with the most dominant of these effects being the photon induced charge transfer. The metal can mediate charge transfer of incident radiation from the metal to the adsorbate leading to the observed enhancement [21]. The key difference between these two mechanisms is that the chemical mechanism only holds true when the adsorbate is chemisorbed to the metal surface whereas the electromagnetic mechanism holds true whether the adsorbate is chemisorbed or physisorbed to the surface. The entanglement of these two mechanisms makes it hard to study them in isolation, however, recent advancements in the use of graphene which does not undergo enhancement by the electrochemical mechanism has opened up the isolated study of the chemical mechanism [22].

#### 2.4.4 X-Ray Photoelectron Spectroscopy

X-ray photoelectron spectroscopy (XPS) is a solid surface analysis technique, yielding highly valuable information about the elemental composition of surfaces, both quantitatively and qualitatively. Making it a vital technique in modern day analytical chemistry. Its origins date back to the turn of the last century with the discovery of the photoelectric effect on which XPS is based. German physicist H. Hertz noted this effect in 1887, by observing that a charged metal (electrode) would emit electrons, in the form of a spark, more easily when irradiated with ultraviolet light. This experimental observation was explained by Einstein in 1905, who proposed that a beam of light could be thought of as a collection of discrete packets of energy, known as photons, rather than simply as a wave propagating through space, this paved the way for wave-particle duality and the formation of quantum theory, for this contribution Einstein was awarded the Noble Prize in 1921. However it was not until the 1950's that the first X-ray photoelectron spectrometer was first designed, emerging in 1954 from a Swedish research group headed by notable scientist Prof. K. Siegbahn, one of the first ever spectra from an XPS spectrometer was that of solid sodium chloride, showing the characteristic peaks identifying the elemental composition of the surface. Shortly after this the same group published in 1956 that XPS could also be used to identify chemical shifts of non-metals and oxidation states of metals. It is these combined attributes that make XPS such a powerful technique, leading Siegbahn to be awarded the Nobel Prize in 1981. The group continued the progression of XPS and alongside Hewlett-Packard released the first commercial monochromatic XPS spectrometer in 1969. Today this technique is used widely with applications in chemical analysis, materials science, microelectronics, heterogeneous catalysis and polymer science, it is likely to remain at the forefront of analytical science with progression coming in the form of higher energy synchrotron radiation for the production of photoelectrons leading to better resolution, angle resolved XPS for layer by layer analysis of surfaces and the newly realised ability of XPS as a form of microscopy giving spatial resolution of analyte surfaces [23, 24].

##### 2.4.4.1 The Photoelectric Effect

The photoelectric effect describes the emission of an electron from an energy level or shell of an atom as the result of the absorption of a photon of electromagnetic radiation. This process is referred to as photoemission, and the electron which is emitted is known as a photoelectron. Two common techniques that utilise this photoelectric effect are that of ultraviolet photoelectron spectroscopy (UPS) and X-ray photoelectron spectroscopy (XPS). UPS uses lower energy ultraviolet radiation causing photoemission from valence levels, XPS uses high energy X-rays resulting in the photoemission of core level electrons.

An incident photon must possess energy equal to or greater than that of the ionisation energy of the electron for an emission event to occur. The resulting photoelectron will have a kinetic energy (KE) equal to that of the incident radiation and the electrons ionisation energy. In an XPS experiment both the photoelectrons kinetic energy (KE) and the energy of the incident photons ( $h\nu$ ) are measured. Hence the ionisation or binding energy ( $E_B$ ) can be calculated.

$$E_B = h\nu - KE$$

Equation 2-26

The binding energy of an electron is characteristic to the energy level and hence atom from which it was emitted, this is because the binding energy depends upon the nuclear charge of the atom, it is this that provides the elemental identification. A smaller effect is felt by the nature of the atoms bonding to neighbouring atoms, it is from this that information about the chemical state of the atom such as oxidation state can be identified.

#### 2.4.4.2 Koopmans' Theorem

Koopmans' theorem firstly defines the  $E_B$  of an emitted photoelectron, which is defined as the energy difference between the final electron state ( $E_f(n-1)$ ) and the initial electron state ( $E_i(n)$ ). That is the difference between the state of an atom before and after photoemission (Equation 2-27).

$$E_B = E_f(n-1) - E_i(n)$$

Equation 2-27

Koopmans' theorem therefore shows that the binding energy is equal to the negative of the orbital energy ( $\varepsilon_k$ ) from which the photoelectron was removed (Equation 2-28). This however is only an approximation as it assumes there is no electronic rearrangement in response to the photoemission.

$$E_B = -\varepsilon_k$$

Equation 2-28

The assumption that when photoemission occurs there is no rearrangement of electronic structure in the atom that has been ionised does not hold true and hence the above breaks down. In response to the creation of a 'core hole' the electrons will undergo some form of rearrangement to minimise the energy of the ionised atom, this is known as a relaxation process. The binding energy can now be more accurately calculated.

$$E_B = -\varepsilon_f - E_r(k) - \delta\varepsilon_{corr} - \delta E_{rel}$$

Equation 2-29

Additionally to the consideration of the relaxation energy ( $E_r(k)$ ), the differential correlation ( $\delta\varepsilon_{corr}$ ) and relativistic energies ( $\delta\varepsilon_{rel}$ ) are also included, although they are corrective terms and are typically small.

#### 2.4.4.3 Initial and Final State Effects

Initial state (or ground state) effects are those which cause a change in the initial energy state of the atom, prior to photoemission. This change in the binding energy is known as a chemical shift. An example of this would be the formal oxidation state of the atom, a change to the charge of an atom would cause a change in the measured binding energy, as the oxidation state increases so too will the binding energy.

Final state effects are those which occur after photoemission has taken place. Referring to the rearrangement of electrons in an attempt to minimise the energy of the remaining 'core hole'. This relaxation process results in a lowering of the binding energy. Two types of relaxation process can occur, atomic and interatomic relaxation. An atomic relaxation is one that occurs with the rearrangement of the outer valence electrons of the atom which bates the 'core hole'. Due to the higher energies associated with the movement of inner core electrons, little to no relaxation occurs involving the movement of such electrons. Interatomic relaxation occurs when electrons from neighbouring atoms contribute to the relaxation process. For conducting materials electrons from the outer shells of neighbouring atoms can move to the atom with the core hole and aid in shielding. For non-conducting materials where electrons are not free to move, the surrounding atoms can become polarised by the charge of the remaining core to aid with relaxation.

#### 2.4.4.4 Work Function

A final process that will affect the measured binding energy is that of the work function of the system. There are two aspects of work function to consider, that of the spectrometer and that of the sample. For conducting samples that are connected via an earth to the spectrometer the Fermi levels will be of the same magnitude and so for the purpose of calculation of the binding energy it is only necessary to know the work function of the spectrometer (Figure 2-10). The work function of the spectrometer is an instrumental correction value which is adjustable and different from system to system, it is to compensate for the energy loss experienced by the photoelectron as it is absorbed by the detector.

$$E_B = h\nu - KE - \varphi$$

Equation 2-30

Here  $E_B$  is referenced to the Fermi level ( $E_f$ ), which is the highest occupied energy level and  $\varphi$  is the work function of the system. The work function is defined as the energy taken to remove an electron from the Fermi level into the vacuum level ( $E_{vac}$ ).

$$\varphi = E_f - E_{vac}$$

Equation 2-31

Typically the work function for a system should not change and should remain constant, however it is possible to calibrate an instrument if needs must, this is done using standard reference materials such as Au or Cu. When considering non-conducting samples, the photoemission process will lead to accumulation of positive charge at the sample, for the above to hold true when calculating the binding energy, a source of electrons must be supplied to the sample so that no considerable charge build up is able to occur. A low energy electron source can be applied so that a constant stream of electrons are able to neutralise any positive charge build up.

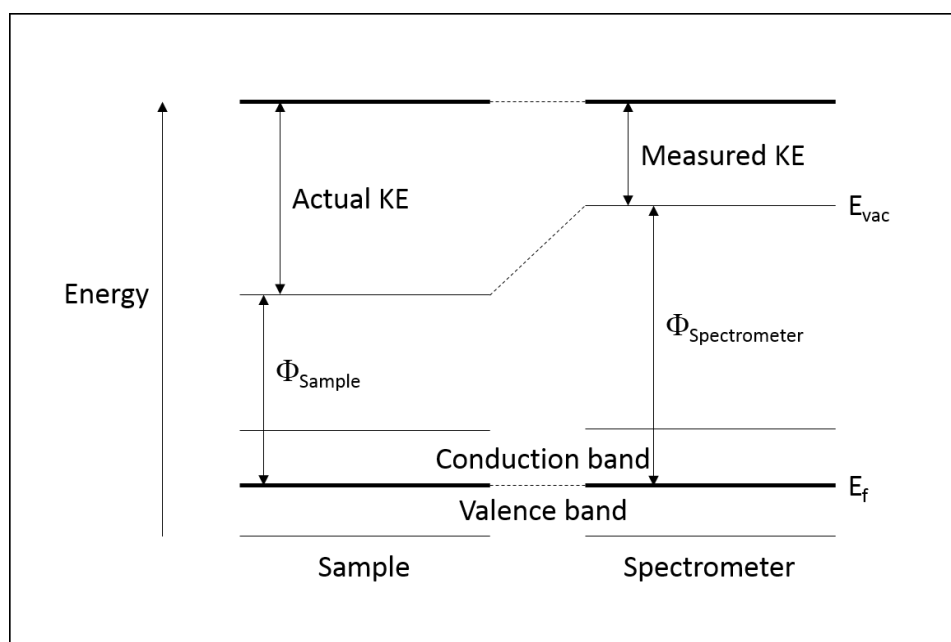


**Figure 2-10** Energy level diagram of a conducting sample earthed to a spectrometer, with equivalent Fermi levels, highlighting the calculable sample workfunction

#### 2.4.4.5 Surface Sensitivity

When considering the surface sensitivity of XPS it is the distance that the photoelectrons can travel through the sample that is the limiting factor and not the penetration depth of the incident X-ray radiation. The X-ray radiation can penetrate the sample over the micron range, however the photoelectrons can only travel a few nanometres through a sample. The surface sensitivity is more accurately described by the sampling depth.

The sampling depth is defined as the distance an electron can travel without suffering from any loss of energy, this is more formally known as the inelastic mean free path length (IMFP,  $\lambda$ ) of an electron. It is only the electrons which escape the surface without any loss of energy that are of interest for the determination of binding energy, any electrons that do experience a loss of energy and are still able to escape simply make up part of the background signal.

$$I_k = I_0 e^{\left(-\frac{d}{\lambda \cos\theta}\right)}$$

Equation 2-32

Here  $I_k$  is the intensity of the incident photoelectrons,  $I_0$  is the intensity of the transmitted photoelectrons,  $d$  is the depth of the matter and  $\lambda$  is the IMFP. This expression describes the intensity loss of transmitted photoelectrons which is not the case for XPS, as the sample thickness is usually much greater than the IMFP of the photoelectrons and is concerned with emitted photoelectrons. It is also often the case that the sample being analysed will have additional surface species such as oxide or deposited thin film overlayers. Therefore the above equation is modified to account for these effects of the substrate (sub) and overlayer (OL) (Equation 2-33 and 2-34).

$$I_{k\ sub} = I_{0\ sub} e^{\left(-\frac{d}{\lambda \cos\theta}\right)}$$

Equation 2-33

$$I_{k\ OL} = I_{0\ OL} \left[ 1 - e^{\left(-\frac{d}{\lambda \cos\theta}\right)} \right]$$

Equation 2-34

#### 2.4.4.6 Quantification of Surface Species

The peaks observed in an XPS spectrum are characteristic of the element from which they emerged, further the area underneath the peaks is proportional to the amount of each element present. More specifically it is possible to calculate the concentration of surface atoms present on a bulk sample by using the equation described by Carley & Roberts [25].

$$\sigma_a = \frac{I_a}{I_s} \times \frac{\mu_{s'}}{\mu_{a'}} \times \rho_s \times \frac{N_A}{RM_s} \times (\lambda \cos \theta) \times \frac{KE_a}{KE_s}$$

Equation 2-35

Where  $\sigma$  is the surface concentration (atoms  $\text{cm}^{-2}$ ),  $I$  is the measured peak area,  $\mu$  is the photoionisation cross-section,  $\rho$  is density ( $\text{g cm}^{-3}$ )  $N_A$  is Avogadro's number,  $RM$  is the relative mass ( $\text{g mol}^{-1}$ ),  $\lambda$  is the IMFP (cm),  $\theta$  is the beam-sample-analyser angle and  $KE$  is the kinetic energy (eV). Finally the subscripts s and a represent the substrate and adsorbate respectively. This expression assumes that the surface is homogeneous and that the beam-sample-analyser angle is known.

#### 2.4.5 Energy Dispersive X-Ray Spectroscopy

Often coupled to electron microscopy, as is the case here, energy dispersive X-ray spectroscopy (EDS) utilises the characteristic X-rays emitted from matter that has been excited by a beam of electrons. It is for this reason that it is often coupled to electron microscopy for the source of electrons is already apparent. EDS is both qualitative, producing spectral lines that are characteristic of an element, and quantitative, giving atomic percentages of elements detected. EDS is able to detect elements with an atomic number ( $Z$ ) greater than 4 (Boron onwards), with a quantitative limit of 1-2 wt%.

An electron beam is focussed upon the sample, the incident beam interacts with both the electrons and nuclei of the sample atoms. This results in the emission of two types of X-ray from two distinct interactions. Characteristic X-rays are emitted as a result of the interactions with the electrons and bremsstrahlung X-rays are emitted as a result of interaction with the atomic nuclei, these are often referred to as background or continuum X-rays.

Bremsstrahlung X-rays are produced by the interaction of the incident electron beam with the atomic nuclei of the sample atoms. A primary incident electron interacts with the positive charge of the nucleus, causing an inelastic scattering event. This inelastic scattering causes a change in the electron energy, the energy lost is emitted in the form of X-ray radiation. During the scattering event the incident electron can give up any amount of energy, depending on the degree of the inelastic scattering event, therefore the distribution of the

emitted X-rays is continuous and it is this that gives rise to the background continuum of Bremsstrahlung radiation. The closer the incident electron comes to the nucleus the greater the interaction and hence the greater the energy loss (Figure 2-11).

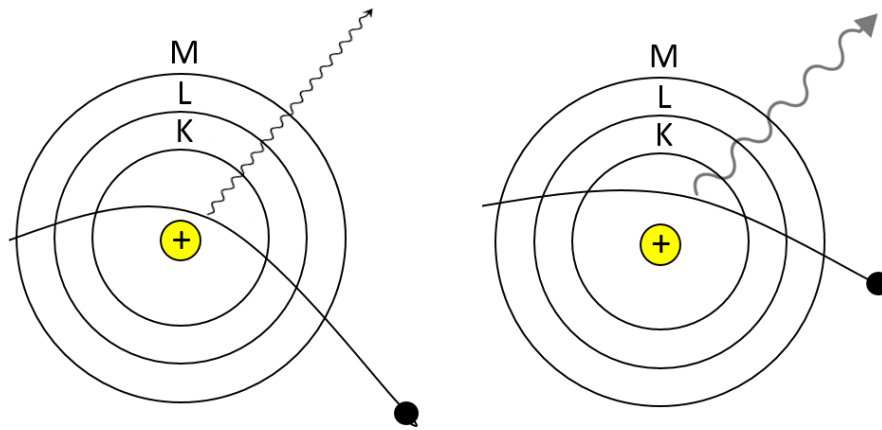


**Figure 2-11** Schematic of Bremsstrahlung X-ray production; left strong interaction, right weaker interaction

When an incident electron interacts with an inner atomic level electron it can be ejected, the resulting atom is left in an excited state. For the ejection of a core electron to occur the incident electron must possess energy greater than that binding the electron to its nucleus. The excited atom then goes through a relaxation process whereby an electron from an outer energy level 'drops' down to the vacant inner level. This process can involve more than one electron transition (Figure 2-12). Each electron transition of the relaxation process will result in an X-ray or an electron being emitted, each X-ray has a unique energy corresponding to the difference in energy between the vacant level and the level donating its electron. The energy of X-ray emitted is therefore unique to the element it arose from and hence a characteristic X-ray.

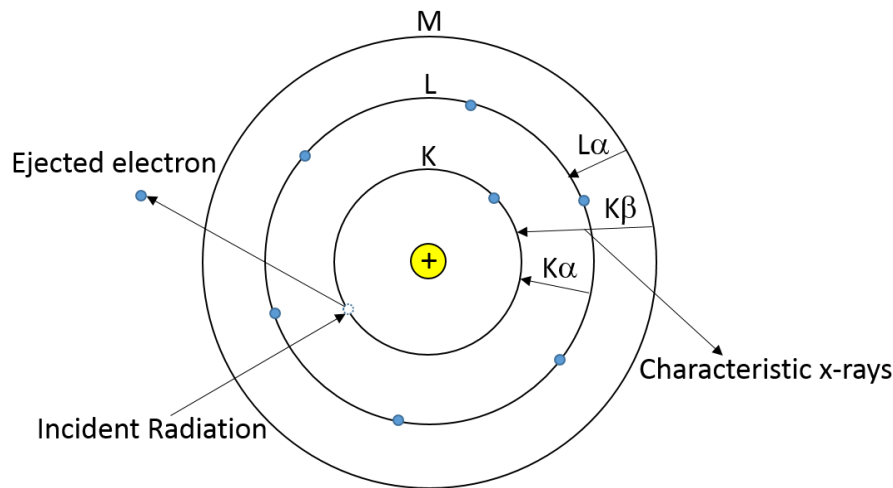


**Figure 2-12** Schematic of X-ray production resulting from core electron hole production for energy dispersive X-ray spectroscopy

The spectral lines/peaks that appear in a typical EDS spectrum are named according to the transition from which they arose. For example if the vacancy occurred in a K shell and the donated electron came from the adjacent L shell it is known as a  $K\alpha$  X-ray. If the same vacancy was filled from the next shell, the M shell, the emitted X-ray would be dubbed a  $K\beta$  X-ray (Figure 2-12).

A characteristic X-ray's energy is closely linked to the atomic number of the atom from which it emerged, it is this that makes the elemental identification possible and its relationship is described by Moseley's Law (Equation 2-36).

$$E = A(Z - B)^2$$

Equation 2-36

Where  $E$  is the energy of the emitted X-ray,  $A$  and  $B$  are constants dependent upon the transition that occurred ( $K\alpha$ ,  $K\beta$ ,..) and  $Z$  is the atomic number of the atom from which the X-ray emerged. Thus for a given transition (e.g.  $K\alpha$ ), as the X-ray energy increases so too will the corresponding atomic number.

The X-rays are collected using an energy dispersive detector. The detector comprises of a crystal (often silicon), which absorbs the incoming X-rays creating an electrical current plus, the magnitude of the electric pulses correspond to the characteristic X-rays. This information is displayed as a spectrum of X-ray intensity (counts per second) versus the energy of the X-ray. Hence both elemental identification and quantification are obtained. The limits of this

quantification differ dependent upon the electron beam energy, with SEM having an accurate limit of 1-2 wt% and TEM with the higher energy more focused beam leading to a better limit of detection of 0.01-0.1 wt%.

## References

1. Cao, G., *Nanostructures & Nanomaterials: Synthesis, Properties & Applications*. 2004, London: Imperial College Press. 433.
2. Gary Attard, C.B., *Surfaces*. Oxford Chemistry Primers. 1998: OUP Oxford. 96.
3. Fisher, A.C., *Electrode Dynamics*. Oxford Chemistry Primers. 1996, Oxford: Oxford University Press. 83.
4. Cremer, C. and B.R. Masters, *Resolution enhancement techniques in microscopy*. European Physical Journal H, 2013. **38**(3): p. 281-344.
5. Oatley, C.W., *The early history of the scanning electron microscope*, in *Advances in Imaging and Electron Physics*, Vol 133. 2004, Elsevier Academic Press Inc: San Diego. p. 7-34.
6. Bogner, A., et al., *A history of scanning electron microscopy developments: Towards "wet-STEM" imaging*. Micron, 2007. **38**(4): p. 390-401.
7. Hillier, J., R.F. Baker, and V.K. Zworykin, *A diffraction adapter for the electron microscope*. Journal of Applied Physics, 1942. **13**(9): p. 571-577.
8. Smith, C.L., *A simple microscope protractor*. Copeia, 1956. **1956**((4)): p. 250.
9. Everhart, T.E. and R.F.M. Thornley, *Wide-band detector for micro-microampere low-energy electron currents*. Journal of Scientific Instruments, 1960. **37**(7): p. 246-248.
10. Ruska, E., *The development of the electron-microscope and of electron-microscopy*. Uspekhi Fizicheskikh Nauk, 1988. **154**(2): p. 243-259.
11. Baird, D. and A. Shew, *Probing the history of scanning tunneling microscopy*. Discovering the Nanoscale, ed. D. Baird, A. Nordmann, and J. Schummer. 2004, Amsterdam: los Press. 145-156.
12. RAMAN, S.C.V., *The molecular scattering of light*, in *The colour of the sea*. 1930: Nobel Lecture. p. 267-275.
13. Singh, R., *C. V. Raman and the discovery of the Raman effect*. Physics in Perspective, 2002. **4**(4): p. 399-420.
14. Singh, R., *80 years ago - the discovery of the Raman effect at the Indian Association for the Cultivation of Science, Kolkata, India*. Indian Journal of Physics and Proceedings of the Indian Association for the Cultivation of Science, 2008. **82**(8): p. 969-985.
15. Aroca, R., *Surface-Enhanced Vibrational Spectroscopy*. 2007, Chichester, West Sussex: John Wiley and Sons, Ltd. 233.
16. Fleischm.M, P.J. Hendra, and McQuilla.Aj, *Raman-spectra of pyridine adsorbed at a silver electrode*. Chemical Physics Letters, 1974. **26**(2): p. 163-166.
17. Jeanmaire, D.L. and R.P. Vanduyne, *Surface raman spectroelectrochemistry .1. heterocyclic, aromatic, and aliphatic-amines adsorbed on anodized silver electrode*. Journal of Electroanalytical Chemistry, 1977. **84**(1): p. 1-20.
18. Albrecht, M.G. and J.A. Creighton, *Anomalous intense raman-spectra of pyridine at a silver electrode*. Journal of the American Chemical Society, 1977. **99**(15): p. 5215-5217.
19. Lin, X.M., et al., *Surface-enhanced Raman spectroscopy: substrate-related issues*. Analytical and Bioanalytical Chemistry, 2009. **394**(7): p. 1729-1745.
20. Tong, L., T. Zhu, and Z. Liu, *Approaching the electromagnetic mechanism of surface-enhanced Raman scattering: from self-assembled arrays to individual gold nanoparticles*. Chemical Society Reviews, 2011. **40**(3): p. 1296-1304.

21. Hurst, S.J., et al., *Utilizing Chemical Raman Enhancement: A Route for Metal Oxide Support-Based Biodetection*. Journal of Physical Chemistry C, 2011. **115**(3): p. 620-630.
22. Yu, X.X., et al., *Tuning Chemical Enhancement of SERS by Controlling the Chemical Reduction of Graphene Oxide Nanosheets*. ACS Nano, 2011. **5**(2): p. 952-958.
23. Alov, N.V., *Fifty years of X-ray photoelectron spectroscopy*. Journal of Analytical Chemistry, 2005. **60**(3): p. 297-300.
24. Bonzel, H.P. and C. Kleint, *On the history of photoemission*. Progress in Surface Science, 1995. **49**(2): p. 107-153.
25. Carley, A.F. and M.W. Roberts, *X-ray photoelectron spectroscopic study of interaction of oxygen and nitric-oxide with aluminum*. Proceedings of the Royal Society of London Series a-Mathematical Physical and Engineering Sciences, 1978. **363**(1714): p. 403-424.

# Chapter 3 Experimental

---

## 3.1 The Milli-Q Pure Water System

A Milli-Q plus water system (Millipore, Watford Hertfordshire) produced ultra-pure water used for all electrochemical work, cleaning of glassware, preparation of electrolyte solutions and particle syntheses. The system was capable of producing water with a resistivity of 18.2 M $\Omega$  cm, and a total organic content (TOC) of less than 10 ppb.

The system consisted of a number of stages for the total purification: Initial purification of the mains water occurs in a Milli-RO 10 plus system consisting of a semipermeable reverse osmosis membrane able to remove inorganic matter, colloids and bacteria. The water is then passed through a pre-treatment pack made up of activated carbon for the removal of chloride, organic compounds and particulates greater than 5  $\mu$ m. A large tank containing anti-scaling compounds stores this water before it is passed into the Milli-Q system for further purification, finally the water is passed through a microporous membrane to remove micro-organisms and particulates less than 0.22  $\mu$ m in size. The resistivity of the water at the outlet is constantly measured and monitored to ensure pure water always flows [1].

## 3.2 *In Situ* Raman Analysis; Probing the Deposition/Dissolution of Calcium Carbonate

Raman spectroscopic measurements were performed using a LabRam HR confocal Raman Microscope (Horiba JobinYvon Ltd), fitted with a He-Ne laser ( $\lambda$  633 nm, output power 16 mW). Collection and analysis of the data was performed on the proprietary LabSpec software (Horiba JobinYvon).

The detector was cooled by a Peltier device (thermoelectric cooler) to a constant -75 °C. Minor temperature variations in the ambient surroundings could cause apparent shifts in spectral peak positions, caused by the temperature dependence of the zero coefficient of the spectrometer. Therefore the laboratory housing the spectrometer was air conditioned to maintain a constant 18 °C. Auto-calibration of the detector was run daily and the LabSpec program was calibrated against a well-defined Raman shift. A single crystal silicon wafer with a reliable crystal lattice vibration at 520.7 cm<sup>-1</sup> was used for this purpose and the result saved and archived for future reference.

The sample was secured on the X-Y stage and positioned in front of the objective lens. The objective lens, stage and flow cell were encased in an emission guard whenever the laser was switched on to prevent laser emission in the laboratory, and to prevent ambient light contamination from within the laboratory reaching the detector. A white focusing light was switched on and a beam splitter set to direct light from the objective lens to a video camera and the image focused using the X-Y stage manipulator. Once the surface was focused the light source was switched off and the beam splitter raised to direct the scattered laser light to the detector. Unless otherwise stated, standard conditions for acquisition were: accumulation time 10 seconds, number of accumulations 10, shutter filter 10%, frequency range 100 – 1200  $\text{cm}^{-1}$ . A typical schematic of the experimental set up can be seen in figure 3-1.

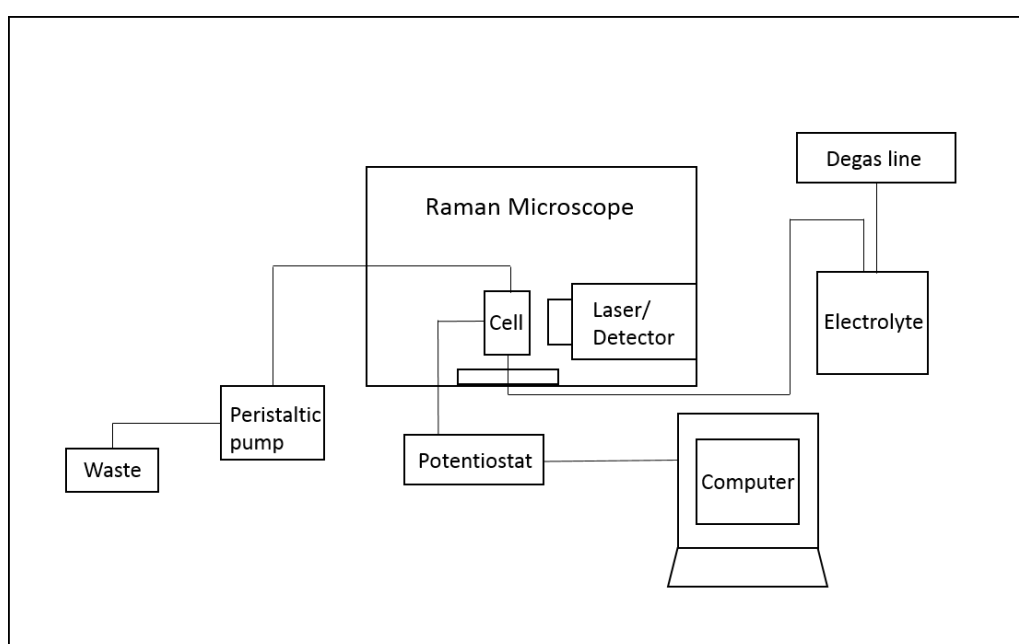


**Figure 3-1** Diagram of the full electrochemical Raman apparatus

### 3.2.1 The Spectro-electrochemical Flowcell

The spectro-electrochemical flowcell allows for Raman and more specifically SERS to be taken *in situ* while also electrochemically controlling the potential at the electrode of interest. The body of the flowcell was tailored to the experiments undertaken and built in house using a PTFE block. The block was drilled to incorporate a 3 electrode system in a flow channel measuring 12 x 30 x 1 mm. To seal the channel a 24 x 50 mm borosilicate glass window (Sigma-Aldrich, cover glass) was sandwiched between two hand-cut Viton® gaskets, secured in place using an aluminium screen and clamped securely using brass screw thread clamps. PTFE inlet and outlet tubes (1.58 mm outer diameter, 0.8 mm internal diameter) were secured to the main block using Supelco® HPLC fittings and sealed with ferrules. Occasionally the

ferrules were not sufficient to make an air tight seal, UHU® white tack was used to enhance the sealing at the external tube - Supelco® fitting interface (Figure 3-2).

Before conducting experiments the PTFE flowcell, Vitron® rubber gaskets and glass screen were all immersed in green acid (98% sulphuric acid with a few grains of potassium permanganate added stepwise until the solution became translucent green in colour) for a period of at least an hour. The green acid solution was then neutralised and disposed of in the appropriate manner. All components were then thoroughly rinsed, boiled for 30 minutes and finally rinsed again, all using ultra-pure water.

The platinum polycrystalline working electrode employed was flame annealed using a high Bunsen flame, the electrode was heated until glowing cherry red, the heating was stopped once the Bunsen flame burnt blue indicating any impurities has been removed [2, 3]. The gold counter electrode was also flame annealed, however this was achieved using a lower temperature flame as that of the Bunsen flame would exceed the melting point of gold (1064 °C). When the electrodes had stopped glowing hot they were immersed in ultra-pure water to cool them and keep them free of impurities before being sealed into the flowcell. To ensure a good seal between the electrodes and the flowcell Klingerflon® PTFE thread tape was wrapped around the electrodes prior to insertion. The working electrode was positioned so that it was flush with the channel of the flowcell, reducing the chance of fluid turbulence in the stream of electrolyte flowing through the channel. Finally, to further seal the flowcell high purity paraffin wax was melted and dripped onto the back of the flowcell ensuring no air could penetrate the flowcell-electrode seals during operation. A palladium reference electrode was electrochemically charged with hydrogen until a Pd-H  $\beta$ -hydride phase was formed and used as the reference electrode, the electrode was installed upstream of the working electrode to reduce potential Ohmic drop. Similarly but conversely the gold counter electrode was positioned downstream of the working electrode to ensure any possible electrochemical products formed at the counter electrode would not impinge upon the working electrode. The electrical circuit was completed using a potentiostat, whereby crocodile clips and clips specially designed to prevent movement of the electrode upon connection were connected using colour coded cables (red CE, white RE and green WE).

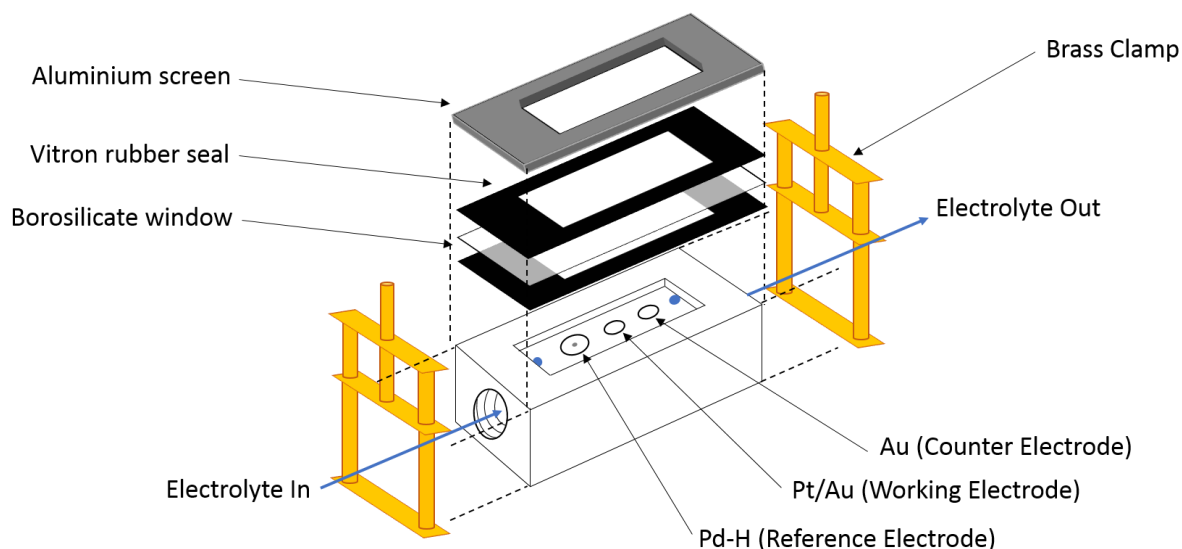


**Figure 3-2** Diagram of the electrochemical flowcell

Due to the potential issue of ‘rogue signals’ first reported by Etchegoin and assigned to the interaction of dissolved dioxygen in the electrolyte solution with the metal surface [4], all electrolyte solutions were degassed thoroughly with argon, except for that of  $\text{CaCO}_3$  solutions due to acidification via  $\text{CO}_2$  bubbling which would have been adversely effected by argon degassing.

Solutions were drawn through the cell and into an appropriate waste container using a peristaltic pump (Cole Parmer, Masterflex C/L) capable of producing flow rates of between  $1.5$  and  $7.2 \text{ mL min}^{-1}$ . The partial vacuum created by the peristaltic pump drawing solution through the cell helped to both seal the cell and highlight any potential leaks by applying a negative pressure on the gaskets and resulting in the formation of air bubbles within the flowcell. If bubbles appeared the cell was removed from the spectrometer and the paraffin wax was removed and reapplied as described above. The reason for the immediate removal and re-waxing was due to the potential issue caused by air bubbles entering the cell, not only would this cause a possible route for contaminants to enter but could also break the electronic connection between the electrodes if a bubble resided between two electrodes cutting off electrolyte flow.

The hydrodynamics of the flow-cell had been tested to ensure analyte delivery and removal was suitably effective. This was achieved by alternating between solutions of  $0.1 \text{ M KCl}$  and  $10 \text{ mM K}_3\text{Fe}(\text{CN})_6$  whilst the working electrode was held at a potential at which the ferricyanide would be reduced ( $-0.436 \text{ mV}$ ) [5]. Figure 3-3 shows the resulting ‘concentration transient’ for the moderate flow rates used herein. This showed that there was minor mixing of the solutions, which was attributed to the depth of the channel and in particular the depth of the channel in the entry to the flow-cell. This finding was not crucial for the present study, as electrolyte

solutions were not changed during experimenting, however the cell could be redesigned for future studies where changing solutions would be necessary and hence mixing would need to be kept to a minimum.

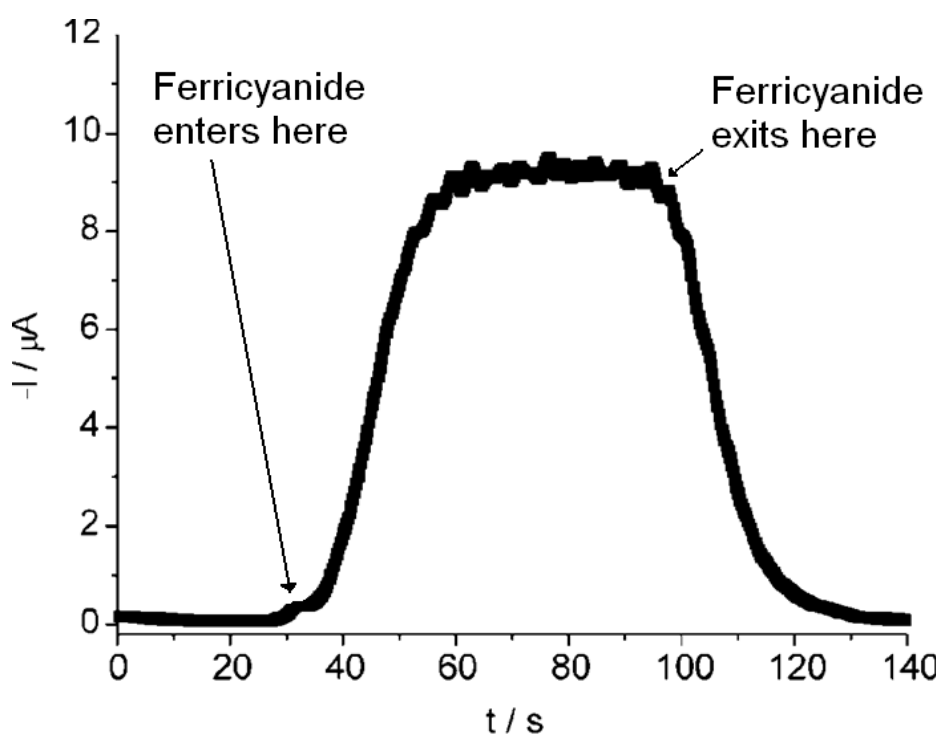


**Figure 3-3** Current vs. time plot to determine fluid dynamics of the flow cell, as ferricyanide is passed through the cell, reprinted from [5].

### 3.2.2 Typical Experimental Procedure

For the *in situ* Raman analysis, gold nanoparticles were utilised for their SERS activity. Gold nanoparticles with diameters of  $\sim 55$  nm were used for this purpose, the nanoparticles (synthesis described below) were centrifuged (10 mL, 5500 RPM, 15 min). The particles collected at the bottom of the centrifuge tube, the remaining solution was carefully removed without disturbing the nanoparticles, they were then re-dispersed with UPW (ultra-pure water), centrifuged and again the remaining solution was carefully removed leaving a few drops ( $< 1$  mL) of purified concentrated nanoparticles.

A polycrystalline Pt working electrode was prepared for nanoparticle application. The Pt electrode was flamed as described above, the electrode surface was then sanded with coarse and then, fine, glass paper (800 and 400  $\mu\text{m}$ ). The electrode was finally polished with diamond sprays, 4  $\mu\text{m}$  then  $\frac{1}{4}$   $\mu\text{m}$ .

The Pt electrode was carefully positioned vertically in a vacuum desiccator, a drop of the concentrated nanoparticles was pipetted onto the clean and polished electrode before being vacuumed to dryness, this process was repeated once more before the electrode was sufficiently loaded with nanoparticles and ready to be placed inside the flowcell.

Once the flowcell had been set up (Section 3.2.1) the nanoparticles were electrochemically cleaned to remove the stabilising agent and any impurities. This was achieved by alternating between  $\text{H}_2\text{SO}_4$  (0.1 M, 10 min,  $2.5 \text{ mL min}^{-1}$ ) and NaOH (0.1 M, 10 min,  $2.5 \text{ mL min}^{-1}$ ) while cycling across the potential range between -200 mV and 600 mV. The cell was now set up, clean and ready to pass the electrolytes of interest through.

The rate and phase of deposition of calcium carbonate was explored by varying the concentrations, substituent components, substituent ratios, pH, temperature and reducing potential of the electrolyte. Subsequently, when calcium carbonate had been deposited, the dissolution phase was monitored while UPW or dilute  $\text{H}_2\text{SO}_4$  was passed through the flowcell. The deposition and subsequent dissolution was monitored *in situ* with both Raman spectroscopy and optical microscopy.

### 3.2.3 Preparation of Pure Calcium Carbonate

Pure polymorphs of calcium carbonate were prepared for the determination of bulk carbonate characteristics for comparison with the thin films deposited electrochemically. Methods were taken from a preparation devised by Dandeu [6, 7], for the formation of pure calcite, vaterite or aragonite, the precipitates obtained were analysed using Raman and SEM.

### 3.3 Nanoparticle Synthesis and Coating

Gold nanoparticles were produced using a method similar to the Turkevich method [8-10], whereby citrate was used as both the reductant and stabilising agent. This method accurately produced stable 55 nm sized particles with a satisfactory size distribution monitored by UV-Vis spectroscopy. These particles were utilised for their superior SERS activity and hence for all SERS experiments including core-shell particle production and as precursors to novel thiol stabilised particles.

Prior to synthesis all glassware was soaked in aqua regia (nitric acid, hydrochloric acid, 1:3) for at least 1 hr, the aqua regia was carefully decanted back into the stock solution for future use. The aqua regia was only neutralised and disposed of when a colour change occurred indicating it was no longer of high strength. All glassware was rinsed once with UPW, this solution, still rich in aqua regia was then disposed of appropriately; subsequently the glassware was rinsed thoroughly with UPW (>10 times).

#### 3.3.1 Synthesis of Citrate Stabilised Gold Nanoparticles

HAuCl<sub>4</sub> (1g, 2.9 mM) was weighed and dissolved in UPW (18.2 mL, 100 mL) to give a 1 % stock solution. HAuCl<sub>4</sub> stock solution (1 %wt, 1 mL) was diluted to 100 mL to give a 0.01 % solution which was heated over a silicon oil bath (112 °C). Sodium citrate (0.57 g, 2.2 mM) was dissolved in a minimal volume of UPW, dissolution was encouraged with sonication before dilution to 100 mL. An aliquot (600 µL) was added slowly to the hot gold solution and refluxed (30 min, 112 °C). Over the 30 minute reflux the solution quickly turned from yellow to dark brown/black, then slowly to a dark red/brown. When light was shone through this solution it appeared bright red, indicative of the production of nanoparticles in the region of 55 nm [11]. Particle size was confirmed via UV-Vis spectroscopy and more accurately determined with TEM.

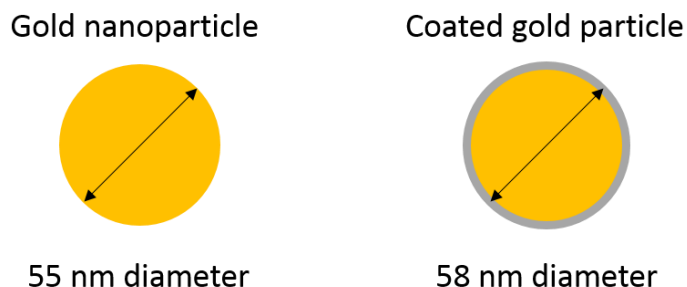
#### 3.3.2 Synthesis of Thiol Stabilised Gold Nanoparticles

For the purpose of achieving core-shell type Au@CaCO<sub>3</sub> nanoparticles it was found that for some coating techniques employed, citrate was not a strong enough stabilising agent. For this reason a simple and novel technique for exchanging the citrate ligand with stronger stabilising compounds was designed. Ligands were required to stabilise the gold particles to a greater degree than citrate and must also facilitate the deposition of calcium carbonate. Linear thiol stabilising agents with either carboxylic acid or hydroxyl moieties were employed [12-15] which would bond more strongly with the gold than the citrate and, through the OH or CO<sub>2</sub>H functional groups would be expected to promote nucleation of calcium carbonate.

Adapted from a synthesis by Kuther [14], citrate stabilised particles (100 mL) were rapidly stirred using a large magnetic stirrer. Equimolar quantities of stabilising thiols (10-12 mg) were added to the solution under rapid stirring. NaOH (0.1 M) was added drop wise to prevent the precipitation of the newly stabilised particles; the pH was monitored for a period of 3 – 4 hrs and kept between pH 10 – 12. As more of the added thiol dissolved the solution slowly became more acidic hence the reason for this prolonged monitoring. Once the pH had stabilised, the solution was kept under rapid stirring for 8 – 12 hrs. Upon completion the solution had changed colour from red/brown to various shades of purple. This colour change was attributed to the change in the surface plasmon energy of the gold nanoparticles due to the new thiol ligand. The particle solutions were analysed using UV-Vis, TEM and Raman.

### 3.3.3 Coating Methods

To synthesise the calcium carbonate coating required the addition of  $\text{CaCl}_2$  followed by exposure to a source of carbonate. Two sources were used for the latter:  $(\text{NH}_4)_2\text{CO}_3$ , and  $\text{CO}_2(\text{g})$ . Concentrations were varied to encourage deposition and, more specifically, the deposition of desired morphologies of calcium carbonate. Theoretical quantities of the reagents needed for the formation of a thin 2-3 nm shell were calculated using the following model:



1. Calculate number of 55 nm gold nanoparticles in sample,
2. Calculate volume of  $\text{CaCO}_3$  needed for 3 nm shell on 55 nm particle,
3. Multiply volume of  $\text{CaCO}_3$  by number of nanoparticles,
4. Convert volume to concentration and hence weight.

This calculation makes a number of assumptions about the physical properties of the thin films, predominantly that they exhibit the same physical properties of bulk calcium carbonate, for example, density. Assumptions about the nanoparticles are also made, for example, that all particles are exactly the same diameter.

### 3.3.4 Coating of Particles by Exposure to Ammonium Carbonate

5 mL of nanoparticle (Au 0.1 wt %) solution was added to solutions of  $\text{CaCl}_2$  (10 mL, 1-10 mmol) and placed in a closed desiccator containing ammonium carbonate and exposed for

various times (0.5, 1, 2, 3 hrs). Ammonium carbonate decomposes to give gaseous ammonia and carbon dioxide, the increased carbon dioxide partial pressure will increase the dissolved hydrogen carbonate and carbonate ions in the solution inducing the precipitation of calcium carbonate.



This method was used for the exposure of citrate, p-mercaptophenol, p-mercaptobenzoic acid, p-mercaptophenylboronic acid, mercaptosuccinic acid and mercaptopropionic acid stabilised particles. For SEM analysis the particles were collected in a number of ways. Carbon SEM sample slides were placed in the bottom of the sample vials to collect the particles. After exposure the sample slides were removed dried under nitrogen and analysed using SEM. Similar methods were used to a) analyse samples in which the nanoparticles were evaporated onto the sample slide before immersion in the calcium chloride solution, b) with a droplet of concentrated particles added, c) when  $\text{CaCl}_2$  was added to nanoparticle solutions and d) in the presence of no nanoparticles as a control measure, all were analysed using SEM. A typical experimental set up can be seen in figure 3-4.

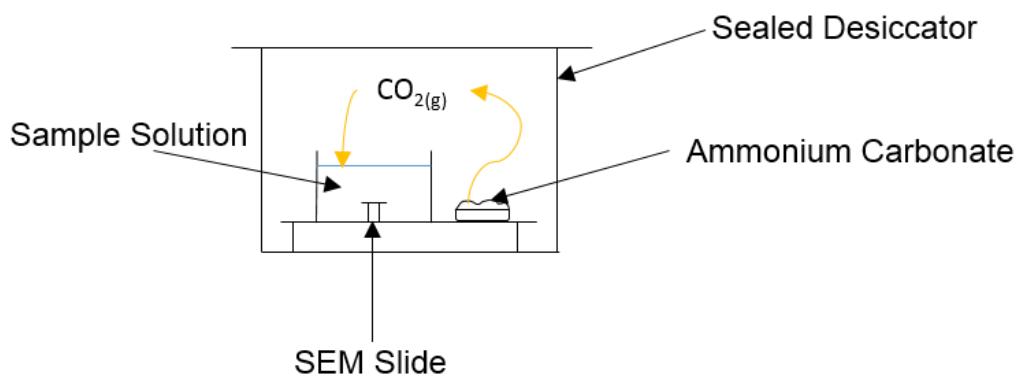


**Figure 3-4** Diagram of the coating apparatus for all particles coated through exposure to ammonium carbonate

### 3.3.5 Coating of Particles by the Bubbling of High Purity $\text{CO}_2$

Another technique used for coating was the bubbling method adapted from a common method for the formation of precipitated calcium carbonate. A solution containing a source of calcium is bubbled with high purity  $\text{CO}_2$  or mixtures of  $\text{CO}_2$  and other gases, leading to some control over the morphology of the polymorphs of calcium carbonate [16, 17].

Calcium chloride (12-14 mg) was added to thiol stabilised gold nanoparticles (25 mL), the solution was then bubbled with high purity CO<sub>2</sub> (10-20 min). The bubbling was stopped, a droplet of the solution was carefully pipetted onto a TEM slide and left in a desiccator to encourage evaporation and analysed using TEM. This method was used to coat the citrate stabilised particles, and solutions of CaCl<sub>2</sub> to which nanoparticles were added.

## **3.4 Platinum Single Crystal Production, Electrochemical Cleaning and Gold Coating**

### **3.4.1 The Electrochemical Cell**

The electrochemical cell comprised of a two compartment Pyrex glass cell containing three electrodes; the first electrode was the working electrode which was a platinum single crystal. The second, the reference electrode was palladium/hydrogen. The third was the counter electrode which was a platinum mesh, the counter electrode was placed downstream of the working electrode in a Luggin capillary to minimise Ohmic drop, its function was to ensure current passed effectively between it and the working electrode, this was paramount to ensure current did not pass to the reference electrode as this would change its potential and cause error. A potentiostat was used to control and monitor the current passing between the three electrodes.

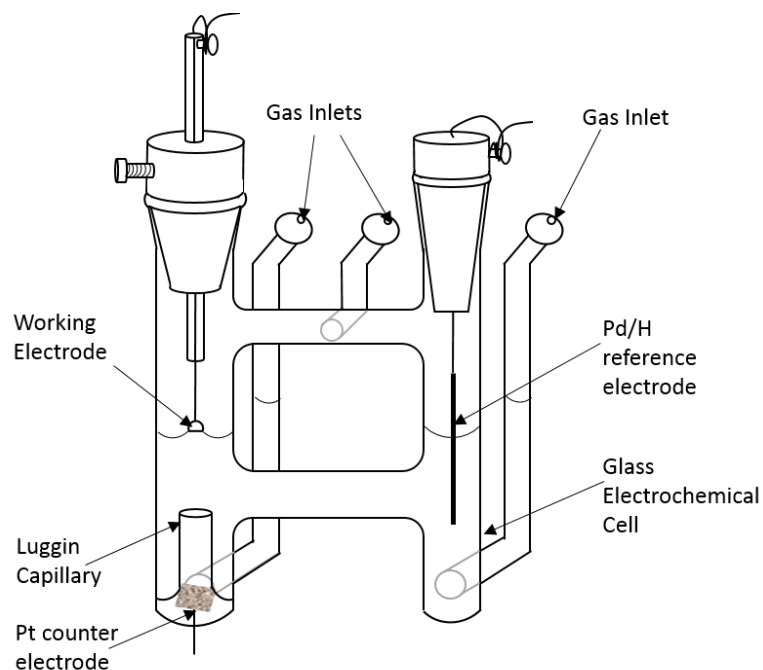


**Figure 3-5** Schematic of the two compartment, three electrode, electrochemical cell

The palladium/hydrogen reference electrode consisted of a high purity palladium wire (99.999% purity, Goodfellows Ltd) spot welded to a platinum wire sealed in a glass stopper. To clean and charge the electrode it was heated in a Bunsen flame until the flame burnt orange indicating any surface contaminants had been oxidised and removed [3], was placed in a glass bubbler (Figure 3-6) filled with ultra-pure water and high purity hydrogen gas was bubbled through the glass vessel over the electrode (30-40 min) forming a stable  $\beta$ -hydride phase over the surface of the palladium. This electrode system can hold a constant potential of +50 mV vs SHE for several hours, the benefit of this reference electrode is that does not require constant hydrogen bubbling compared to the SHE and avoids the risk of contamination associated with chloride from a silver/silver chloride reference electrode.

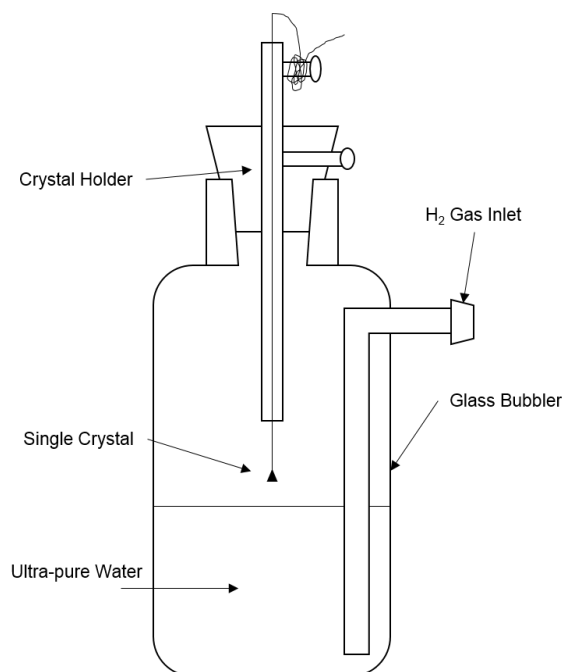


**Figure 3-6** Schematic of hydrogen gas bubbling apparatus

To minimize contamination all glassware was thoroughly cleaned before every experiment; the cell was rinsed in ultra-pure water 10 times before being steam cleaned and again rinsed 10 times. Smaller glassware such as stoppers were boiled in a beaker, and rinsed thoroughly. When the glassware was not in use it was filled or covered with ultra-pure water and sealed to minimise contamination.

### 3.4.2 Preparing the Platinum Working Electrode

The platinum single crystal of interest was coiled with a copper wire, the wire was threaded through a glass capillary tube and then fastened into a purpose built Teflon stopper. It should be noted that the copper wire must only touch the very tip of the stem of the working electrode and be well inside the capillary, further the capillary itself must never touch the electrolyte, as either could result in the contamination of the cell. The capillary tube was secured in the stopper via a Teflon screw which enabled the ease of movement of the capillary and electrode inside the cell, the working electrode was carefully positioned with tweezers so that the surface was parallel with the electrolyte, aiding the formation of a good meniscus, vital for accurate surface measurements.

The platinum electrode was first annealed in a Bunsen flame, the crystal was positioned in the hottest part of the flame producing a bright white hot light, while also ensuring that the metal does not get hot enough to glow near the entrance to the capillary as this could cause

contamination from the copper wire over time. This annealing process ensured that all contaminants were oxidised and removed from the surface and that a well ordered surface could be achieved [2, 3]. The crystal was quickly transferred to a hydrogen bubbler, this step was crucial as the more the crystal cooled in air the more contaminants adsorb and the more disordered the resulting surface, however if placed in the bubbler when the crystal is too hot it will cause the hydrogen to ignite making a light popping noise, then the process must be repeated. It was noted the best surfaces were obtained when the crystal was placed in the hydrogen quick enough that it started to glow hotter for a split second before continuing to cool.

Once cool (30 – 60 sec) the crystal was dipped under the surface of the hydrogen rich ultra-pure water to quench it and a droplet allowed to form covering the crystal surface upon removal, minimizing contamination from air during the transfer from hydrogen bubbler to the electrochemical cell. In the cell the working electrode was positioned just under the electrolyte surface while nitrogen was bubbling through, the nitrogen bubbling helped to dissipate the droplet of water from the bubbler into the electrolyte, without this there may be a concentration variation near the crystal surface leading to error. The nitrogen gas was then transferred to a different inlet line so that it was no longer bubbling through the electrolyte as this would prevent the formation of a meniscus due to surface disturbance, the nitrogen flow was increased to ensure that no air would get in to the cell during the removal and replacement of the working electrode and that a sufficient flow was still present over the electrolyte surface.

A good meniscus was formed by immersing the working electrode just under the surface of the electrolyte and raising it up away from the solution, as previously mentioned a good meniscus was achieved by accurate positioning of height and ensuring the electrode surface was parallel to the electrolyte. The Teflon screw was subsequently tightened and the position fixed. A cyclic voltammogram measurement was then performed to assess the cleanliness and crystallinity of the electrode surface. A large sharp peak centred around +0.74 V (Pd/H) was used to monitor the quality of the single crystal surface from contamination from the transfer and the electrolyte (Figure 3-7). If the peak was observed to reduce in size during the course of a measurement it implied high levels of contamination requiring a change of electrolyte. All measurements of this kind were measured at a sweep rate of 50 mV s<sup>-1</sup>.

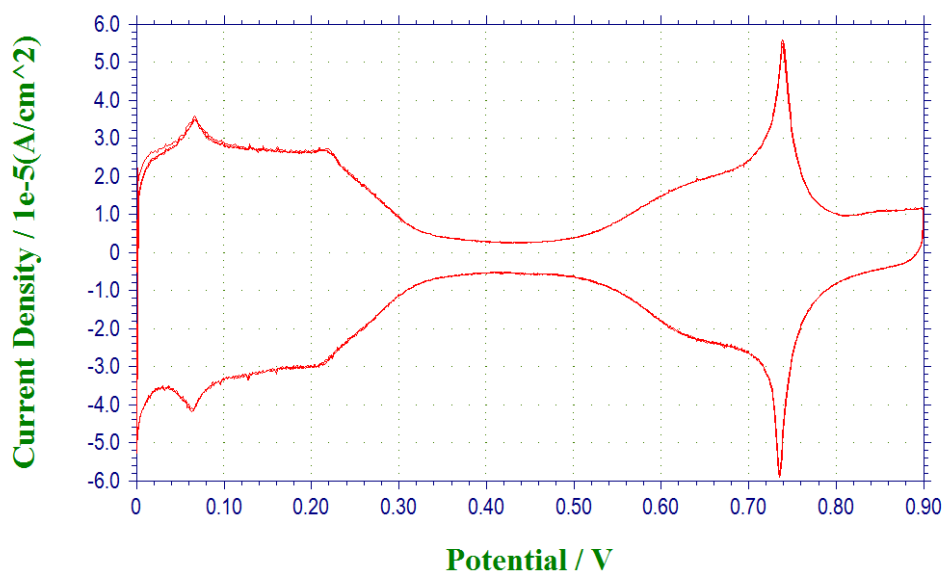


**Figure 3-7** Cyclic Voltammogram of the clean Pt(111) single crystal working electrode

### 3.4.3 Electrolyte

For the high level of purity required for single crystal studies very high quality reagents (Aristar) were used to make all electrolyte solutions. Concentrated perchloric acid was diluted using ultra-pure water (0.1 M) for all experiments conducted in the two compartment electrochemical cell. The cell was bubbled with nitrogen (20-25 min) to remove dissolved oxygen from the electrolyte, then the nitrogen was moved to another inlet to ensure a positive nitrogen pressure was kept at all times to reduce oxygen contamination.

### 3.4.4 Metal Preparation and Coating

Solutions of  $\text{Au}^{3+}_{(\text{aq})}$  were prepared from chloroauric acid (Johnson Matthey 99.99% pure), a tiny aliquot was drawn into a pipette using capillary action and placed into a cleaned glass vial containing ultra-pure water ( $<10^{-5}$  M).

To coat the working electrode, the Pt single crystal was removed from the cell, taking care to ensure a good droplet was covering the surface to reduce contamination during transfer. It was then dipped into the gold solution and drawn up to form a meniscus and left for 10 – 15 seconds. The meniscus formed when dipping was important to prevent the unnecessary coating of gold on the sides of the Pt single crystal, causing age related alloying to occur more quickly. The single crystal was removed again ensuring a droplet had formed on the surface, before transfer to the hydrogen bubbler and left to reduce (10-15 seconds). The crystal was

removed and rinsed with ultra-pure water before being replaced in the cell. A voltammogram was taken and the observed reduction in the intensity of the strong peak at 0.74 mV can be attributed to the blocking of Pt sites with Au, this process was repeated until only the double layer remained (Figure 3-8).

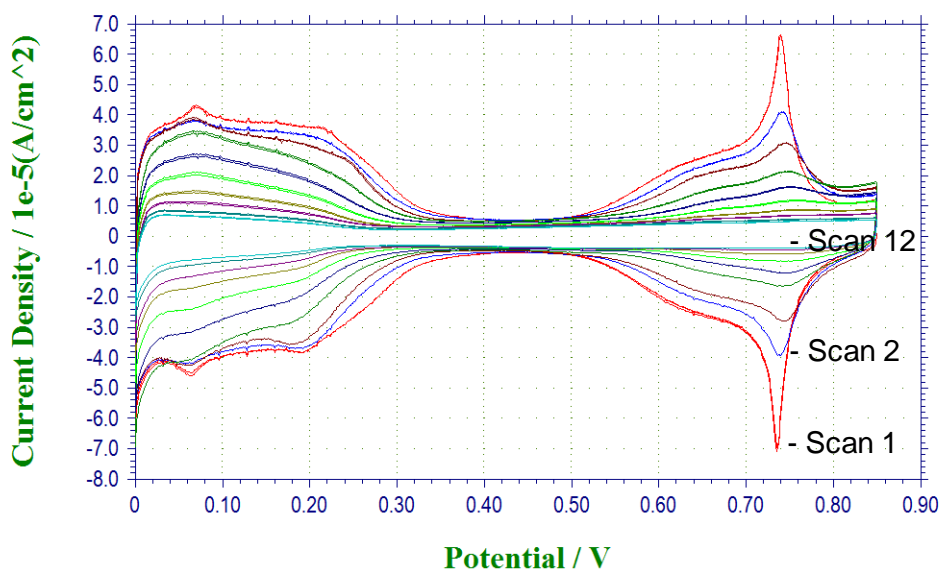


**Figure 3-8** Cyclic voltammogram of the Au coating of the Pt(111) single crystal working electrode

Figure 3-8 only indicates that the Pt sites have all been blocked however no information about the single crystallinity of the ad-layer of gold can be drawn from this, therefore for each single crystal electrode a test was carried out after coating to confirm if this method of coating was in fact leading to epitaxial growth. The following method to probe the structure of the gold surface was irreversible and hence was only done once to confirm the method worked and subsequent coatings for experimental studies were not tested in this manner. Once coating was complete and only the double layer was observed it was possible to change the parameters of the acquisition of the voltammogram so that a greater positive potential was swept leading to the oxidation of the Au. A successful coating was achieved when finite peaks were observed in the Au oxidation region (*ca.* +1.4 mV) indicating the oxidation of an ordered surface (Figure 3-9). If the coating of the Pt single crystal had not lead to a well ordered Au ad-layer then the observed voltammogram would show a broad peak with no sharp features.

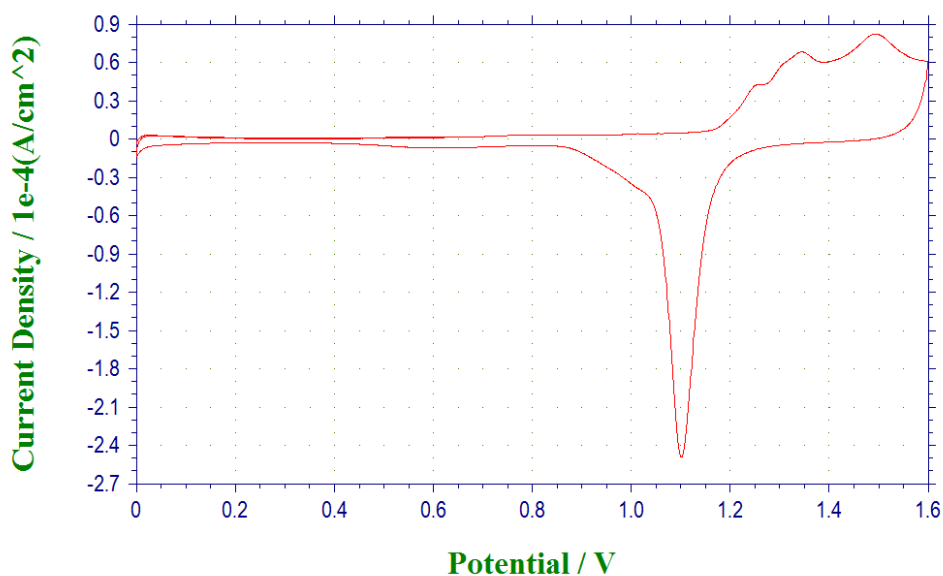


**Figure 3-9** Cyclic voltammogram of the coated Pt, Au(111) single crystal surface

## 3.5 Ultra High Vacuum Studies of Carbonates on Gold Single Crystals

### 3.5.1 Ultra High Vacuum Systems

For the surface structure and reactivity of carbonate formation on gold surfaces ultra-high vacuum (UHV) conditions were utilised. The surfaces studied were analysed using STM and XPS, the following section describes the experimental set up and procedure for these types of studies.

Ultra-high vacuum conditions are required to ensure that a very clean analyte surface is present. At a pressure of  $10^{-6}$  mbar, and assuming a sticking probability “S” of  $\sim 1$ , the number of impacts of gas phase molecules with the surface is sufficient to form a monolayer in  $< 1$  second. Although S is usually much less than one for metals such as gold and silver, nevertheless working pressures of  $< 10^{-9}$  mbar are generally required to ensure the surface remains clean throughout the experiment. At this low pressure the mean free path of a gas phase molecule is in the order of kilometres.

Gas phase molecules must also be in a low enough concentration so that the photoelectrons emitted from the surface (in XPS) have a sufficiently long mean free path length to reach the analyser.

The mean free path  $\lambda$ , can be calculated as follows

$$\lambda = \frac{kT}{1.414P\sigma}$$

Equation 3-1

Whereby  $k$  is the Boltzmann constant ( $1.38 \times 10^{-23} \text{ J K}^{-1}$ ),  $T$  is the temperature,  $P$  is the pressure of the system and  $\sigma$  is the collision cross section, which is a value dependent upon the radius of the atoms involved in a model gas phase collision.

### 3.5.2 Ultra-High Vacuum Apparatus

The UHV system itself is made from stainless steel with glass windows to enable the operator to see into the chambers of the machine. Where radiation could be emitted, for example in front of an X-ray source the glass viewports are covered with a protective glass window to absorb any potentially harmful radiation. These types of machines can be comprised of a single chamber or multiple chambers linked together. To ensure a good vacuum is achieved a combination of pumps are utilised, these pumps are summarised as follows:

- Rotary pumps: a mechanical pump capable of pressures up to  $10^{-3}$  mbar, a series of rotary pumps are used to 'rough' the system (remove the bulk of the air) and to aid the turbo pump.
- Turbo pump: a compression pump capable of pressures up to  $10^{-9}$  mbar, the turbo pump is designed to achieve and maintain the high vacuum.
- Ion pump: ionises chemically active gas molecules and removes them from the system, this pump allows the system to reach ultra-high vacuum pressures  $10^{-11}$  mbar.
- Titanium sublimation pump: a chamber whose walls are coated with a reactive thin film of titanium, able to collect gas phase molecules upon collision and form stable products. The titanium film is replenished periodically to maintain good performance.

Sometimes it was necessary to expose a system to atmosphere when maintenance or repairs were required, whenever junctions or flanges were opened the copper gaskets sealing them were replaced, this was vital to ensure a good seal was maintained and low pressures were achievable. Once a system had been opened to atmosphere it was important to bake the machine while all of the pumps were working to attain a high vacuum, this required encasing the machine with insulating metal walls and heating (425 K), this process removed contaminants from the inner walls of the chamber and enables much greater vacuum and lower contaminant levels post cooling.

To monitor the vacuum levels within the chamber a number of gauges had to be employed as no single gauge could measure over the whole pressure ranges experienced within the chamber.

To monitor near atmospheric and medium pressures Pirani gauges were used. Pirani gauges use the variation in thermal conductivity of gases in order to measure pressure. The gauge consists of a metal filament exposed to the chamber or area of interest, a current is passed through the filament, as the current flows through the thin filament resistance causes the filament to give off heat to the surrounding gas molecules, this process is known as thermal conductivity and is highly dependent upon the pressure of the surrounding gas molecules.

When the system is at lower pressures Bayard Alpert type "Ion gauges" are used to monitor the pressure. A heated filament thermionically emits electrons, these electrons are accelerated towards an anode and if they come into contact with gas phase molecules they will be ionised, the ionised gas particles are then collected. Ion gauges utilise the ionisation of gas molecules resulting in a measureable current upon detection, the resulting current is proportional to the number of gas molecules in the chamber and hence the pressure.

### **3.5.3 Sample Analysis**

To probe the chemical state of the surface and any surface species XPS is utilised for elemental identification, oxidation state measurements as well as concentration of surface species. Subsequent STM analysis reveals the organisation and structure of the surface and any species present on the surface.

#### **3.5.3.1 XPS Analysis**

The X-ray gun used, involves the bombardment of high energy electrons (10 keV) upon a target anode creating core holes. When electrons fall to fill these core holes the anode emits low energy fluorescence X-rays of a characteristic energy (Al source, 1487 eV), these X-rays are directed toward the sample where they cause the production of photoelectrons and Auger electrons which are then collected and analysed. There are numerous possible anodes for X-ray emission on modern spectrometers or multi-anode systems, two common anodes and the two available on the spectrometer used for this investigation were Al and Mg, of which the Al was used exclusively. When the anode was in operation it was water cooled at all times, this was paramount to the safe operation of the X-ray gun as the production of electrons causes a significant amount of heat. The end of the gun was fitted with a thin aluminium foil that minimised contributions from electron flux, Bremsstrahlung radiation and any heat emitted from the source during operation. To reduce the chance of contamination from the X-ray source an ion pump similar to those discussed previously was used to evacuate the internals

of the gun and prevent contaminants associated with the X-ray production from reaching the chamber. To further improve the quality of the X-ray signal monochromators can be used to ensure that the X-rays reaching the sample possess a single energy and prevent the occurrence of satellite peaks from X-ray energy variation.

The photoelectrons emitted from the sample are collected by a magnetic lens and more importantly reduced the kinetic energy of the electrons to match that of the pass energy of the analyser. The analyser consists of two concentric stainless steel hemispheres, the hemispheres both have a negative applied bias with a central line through the hemispheres possessing a potential known as the pass energy. The photoelectrons enter the hemisphere and pass through along the trajectory of the pass energy created by the negative bias, the energy and number of photoelectrons are then detected and counted using a 5 channel (multichannel) detector. This data was then collated and presented using Omicron Matrix 3.2 XPS software, exported and analysed using CasaXPS 2.3.17dev6.4k.

### 3.5.3.2 STM Analysis

For STM analysis the sample was transferred to the STM sample holder, this procedure was performed with a mechanical claw on the STM chamber of the UHV system, this was done with utmost precaution for two reasons, firstly if the sample was dropped during transfer it would likely event in the system having to be vented and opened to atmosphere, secondly the STM sample holder is within a few mm of the STM tip, even the smallest collision between sample and tip would critically damage the tip. During use the chamber was sealed via pneumatic gate valves so that the rotary and turbo pumps could be switched off, this was essential to reduce vibration in the room which would interfere greatly with operation. Briefly the microscope comprises of a tip, coarse and piezoelectric scanners, tip-sample controls and a suspended stage for vibration reduction. The tip was tungsten that had been etched to atomic sharpness, the tip was held in an Omicron magnetic tip holder that enabled the easy changing of tips within the UHV system. The magnetic holder attached to the piezodrive, which consisted of three piezoelectric transducer towers which changed shape in the presence of an applied electric field resulting in movement in the x,y and z directions. The motion of the x,y plane is controlled by the application of a sawtooth voltage to the x transducer, and a voltage ramp applied to the y transducer, together providing the movement in this plane. The z transducer enables the approach of the tip to the surface, this is controlled by eye (magnified through a camera) initially then the software encroaches the surface in a sub nm step by step manner until a distance is reached where the electron wavefunctions overlap and a tunnelling current achieved. The tip is then scanned across the surface in the x,y plane, sensing of both height and electron density leads to the production of the STM image.

Tips were etched in house from tungsten wire using the lamella method [18]. A cathode ring was dipped into a solution of NaOH (2 M) creating a lamella, a tungsten wire (0.38 mm) connected to the anode was lowered into the lamella, a voltage was applied sufficient to etch the tip. Lower voltages take longer to etch but form great sharpness of the tip, and fast voltages cause a less sharp tip hence a voltage is found where a suitable tip is etched in a timely fashion. After a period of 8-12 minutes the wire would break leaving two atomically sharp tips, the tips were collected, cleaned, crimped into the tip holders and placed into the UHV system.

### 3.5.4 Sample Preparation

Experiments were carried out on a Au(111) single crystal disc, the disc was initially secured with silver adhesive, the sample was further secured with wafers of tantalum, spot welded to the sample plate, this ensured the risk of detachment was minimal during transfer to the STM as the sample had to be inverted inside the chamber (Figure 3-11).



**Figure 3-11** Image of Au(111) crystal attached to sample plate using spot welded tungsten foil

Preparation usually involved cycles of argon ion bombardment to sputter impurities from the surface, and annealing the sample. The annealing process provided two functions, to a dirty sample it would encourage subsurface impurities to the surface which could then be removed via the following sputtering cycle. Annealing the surface also ensured a good single crystal surface was produced for experimentation, heating makes the surface atoms more mobile, upon cooling the surface should form long range ordered surfaces in the crystal phase it was cut. If the sample had not been sufficiently cleaned before this final annealing step the surface would likely be disordered due to the presence of impurities on the surface either due to an inadequate vacuum causing contamination of from impurities still being drawn out from the sample itself.

#### 3.5.4.1 Metal Vapour Deposition

To coat the surface of the single crystal with metals of interest, getters were used. For caesium deposition a SAES AMD getter was used, this alkali metal dispenser (AMD) contained a

common getter material known as St 101 (Zr 84 %, Al 16 %). This material not only releases caesium when a current is passed through the getter, it is also able to irreversibly sorb any contaminants released during the reduction process, ensuring that a very high purity metal is released contaminant free. The reduction rate and hence emission of metal is dependent upon the voltage applied to the device, therefore the amount of caesium deposited was controlled with both applied voltage and time. Before initial use, and first application upon exposure of the system to air the getter was degassed by applying a higher voltage than that used for coating, this ensured any contaminants were removed before sample coatings were attempted further reducing the risk of contamination.

#### 3.5.4.2 Gaseous Exposure

To expose the chamber to gases, firstly the ion pump was isolated using a mechanical gate valve, then gases could be introduced to the system through a variety of gas lines and leak valves able to introduce pure gases or mixture of pure gases. The level of exposure was controlled with gas pressure and exposure time. Common gases used were O<sub>2</sub> and CO<sub>2</sub>, although HCl, CO and Ar were also available on the gas apparatus.

## References

1. Systems, M.-Q.I.W., *User Manual*. Millipore, 2015.
2. Clavilier, J., *Role of anion on the electrochemical-behavior of a (111) platinum surface - unusual splitting of the voltammogram in the hydrogen region*. Journal of Electroanalytical Chemistry, 1980. **107**(1): p. 211-216.
3. Clavilier, J., et al., *Preparation of Mono-Crystalline Pt Microelectrodes and Electrochemical Study of the Plane Surfaces cut in the Direction of the (111) and (110) Planes*. Journal of Electroanalytical Chemistry, 1980. **107**(1): p. 205-209.
4. Etchegoin, P., et al., *A novel amplification mechanism for surface enhanced Raman scattering*. Chemical Physics Letters, 2002. **366**(1-2): p. 115-121.
5. Taylor, R., *A study on the surface adsorbates of an enantioselective, heterogeneously catalysed, hydrogenation reaction*. 2010.
6. Carteret, C., et al., *Polymorphism Studied by Lattice Phonon Raman Spectroscopy and Statistical Mixture Analysis Method. Application to Calcium Carbonate Polymorphs during Batch Crystallization*. Crystal Growth & Design, 2009. **9**(2): p. 807-812.
7. Dandeu, A., et al., *Raman spectroscopy - A powerful tool for the quantitative determination of the composition of polymorph mixtures: Application to CaCO<sub>3</sub> polymorph mixtures*. Chemical Engineering & Technology, 2006. **29**(2): p. 221-225.
8. Enustun, B.V. and J. Turkevich, *Coagulation of colloidal gold*. Journal of the American Chemical Society, 1963. **85**(21): p. 3317-20
9. Turkevich, J., P.C. Stevenson, and J. Hillier, *The formation of colloidal gold*. Journal of Physical Chemistry, 1953. **57**(7): p. 670-673.
10. Turkevich, J., P.C. Stevenson, and J. Hillier, *A study of the nucleation and growth processes in the synthesis of colloidal gold*. Discussions of the Faraday Society, 1951(11): p. 55-61.

11. Sardar, R., et al., *Gold Nanoparticles: Past, Present, and Future*. Langmuir, 2009. **25**(24): p. 13840-13851.
12. Kuang, M., D.Y. Wang, and H. Mohwald, *Fabrication of Au@CaCO<sub>3</sub> nanoparticles by in situ mineralization in hydrogel microspheres*. Chemistry of Materials, 2006. **18**(5): p. 1073-1075.
13. Kuther, J., et al., *Templated growth of calcite, vaterite and aragonite crystals on self-assembled monolayers of substituted alkylthiols on gold*. Journal of Materials Chemistry, 1998. **8**(3): p. 641-650.
14. Kuther, J., et al., *Mercaptophenol-protected gold colloids as nuclei for the crystallization of inorganic minerals: Templated crystallization on curved surfaces*. Chemistry of Materials, 1999. **11**(5): p. 1317-1325.
15. Kuther, J. and W. Tremel, *Stabilization of aragonite on thiol-modified gold surfaces: effect of temperature*. Chemical Communications, 1997(21): p. 2029-2030.
16. Boyjoo, Y., V.K. Pareek, and J. Liu, *Synthesis of micro and nano-sized calcium carbonate particles and their applications*. Journal of Materials Chemistry A, 2014. **2**(35): p. 14270-14288.
17. Han, Y.S., et al., *Factors affecting the phase and morphology of CaCO<sub>3</sub> prepared by a bubbling method*. Journal of the European Ceramic Society, 2006. **26**(4-5): p. 843-847.
18. Schmidt, U., et al., *Characterization of stm tips by fim with an organic image gas*. Surface Science, 1992. **266**(1-3): p. 249-252.

# Chapter 4 *In-situ* Raman Analysis and Particle Synthesis

---

## 4.1 Deposition of Calcium Carbonate for SERS Studies

For a systematic study of dissolution, stable repeatable layers of calcium carbonate must be deposited, ideally with control over the phase or polymorph of calcium carbonate. As the carbonate monolayers build over the nanoparticle surface a significant increase in the intensity of the Raman signal would be expected which would then decline as the layers build beyond the penetration depth of the SERS enhancement. It should be possible for the intensity of the Raman signal to be correlated to the thickness of the calcium carbonate layer and this would then provide the necessary information to underpin an in-situ probe for carbonate dissolution under various conditions.

### 4.1.1 Production of Pure Precipitates of Calcium Carbonate

For the determination of accurate peak positions for the different polymorphs of calcium carbonate, particularly the lattice vibrations, polymorphic pure precipitated calcium carbonate was produced for analysis with the same Raman apparatus used for the dissolution experiments. This would also aid in the discrimination of the bulk carbonate signals obtained from pure precipitates and those associated with the thin films produced and the associated SERS enhancement.

#### 4.1.1.1 Precipitated Calcite

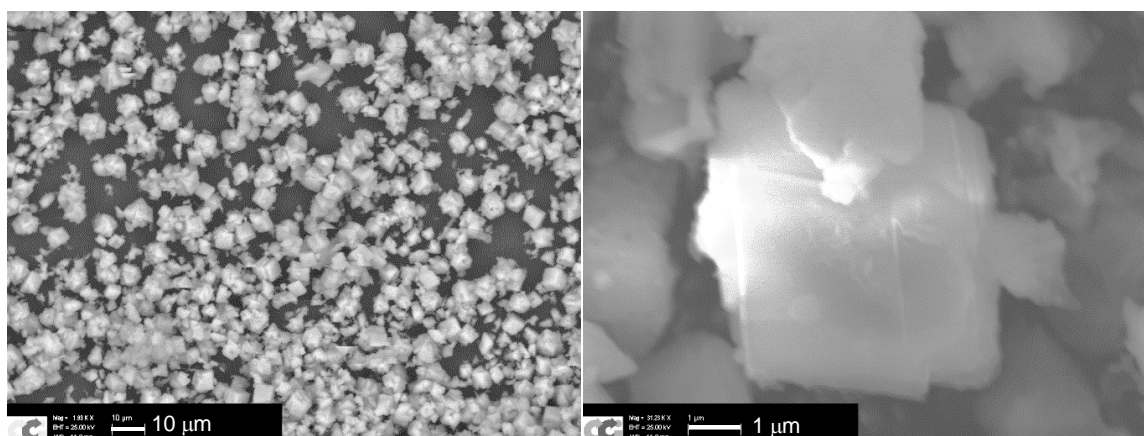


**Figure 4-1** SEM images of deposited precipitated calcium carbonate for the formation of calcite

The SEM images of the precipitated calcium carbonate (Figure 4-1) show clusters which largely exhibit rhombohedral structure as expected for calcite [1]. However, when this image is studied in more detail it is clear that some of the precipitated calcium carbonate is not rhombohedral, this could suggest another polymorph is present in the precipitate.

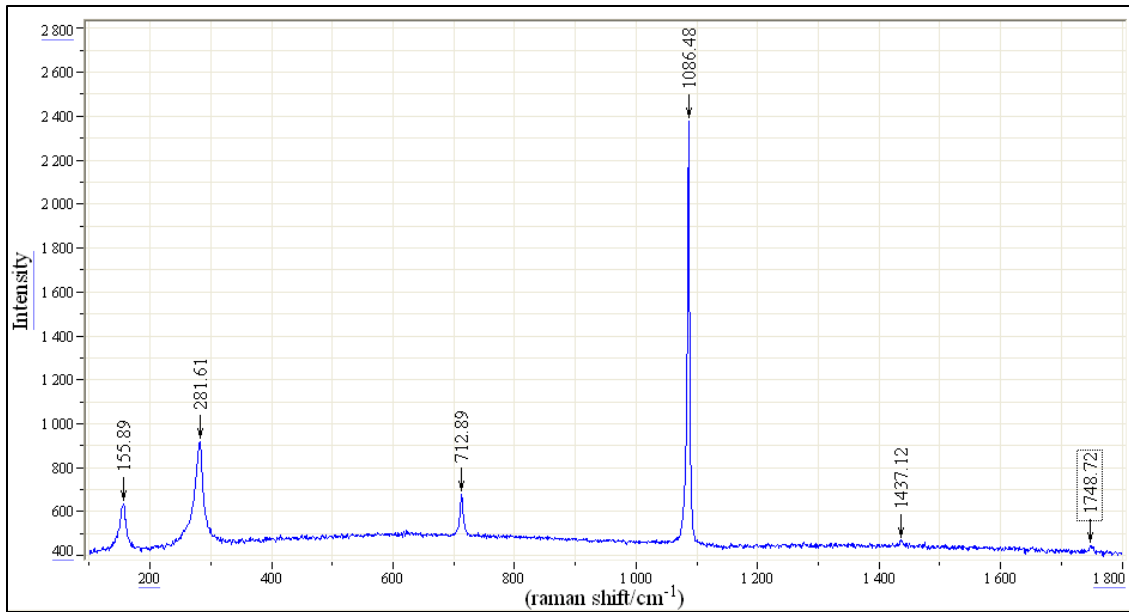


**Figure 4-2** Raman spectrum of precipitated calcium carbonate during the production of calcite

Figure 4-2 a Raman spectrum of the precipitate, shows a very clean calcite spectrum, a large intensity peak is observed at  $1086.5 \text{ cm}^{-1}$ , this is assigned to the strong  $\nu_1$  symmetric C-O stretching mode. A weaker peak is observed at  $712.9 \text{ cm}^{-1}$ , attributed to the  $\nu_4$  O-C-O in plane bending mode. The former is common to the other morphologies of calcium carbonate and hence cannot be used for morphological determination, the latter at  $712.9 \text{ cm}^{-1}$  is very weak and is also common to aragonite; again preventing any morphological scrutiny. The Raman spectrum also shows two sharp peaks of medium intensity in the low frequency region, an area in which lattice mode vibrations occur. These tend to be unique to each morphology, and peaks at  $155.9 \text{ cm}^{-1}$  and  $281.6 \text{ cm}^{-1}$  are expected for calcite [2, 3]. Therefore the presence of non-rhombohedral in the observed SEM is likely due to the mechanical breaking of calcite rhombohedra during sample preparation and not due to the precipitation of other polymorphs as they would have been visible in this region of the Raman analysis.

#### 4.1.1.2 Precipitated Vaterite

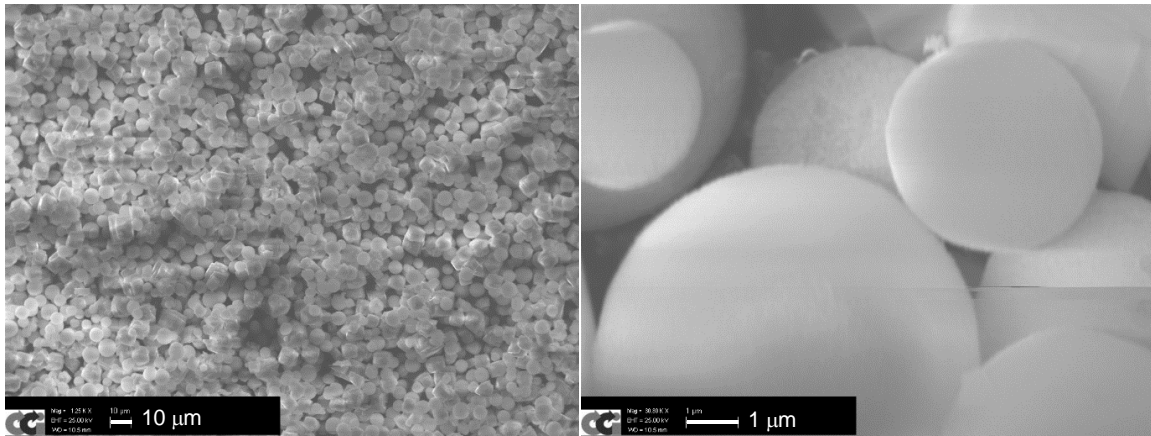


**Figure 4-3** SEM images of precipitated calcium carbonate during the production of pure vaterite

Figure 4-3 shows the SEM images of the precipitate collected for the pure vaterite sample, it can be seen that the vaterite present is in the form of spherules, one of the many forms which vaterite exhibits [2, 4-7]. There are also a number of rhombohedral looking particles which are likely to be due to the presence of calcite. Calcite is the more thermodynamically stable form of calcium carbonate and hence pure vaterite or aragonite are much harder to attain than calcite. Furthermore, there is some evidence that over time, precipitated vaterite in contact with the solution will reform as calcite [8-10]. However, it is unlikely that this has happened here as the solutions were filtered and dried shortly after precipitation occurred. The formation of these different morphologies can be highly dependent upon the temperature, ratio and concentration of substituents [11-18]; the change in concentration during precipitation could have been sufficient for calcite to form in the latter stages of precipitation. This could easily be tested by performing the precipitation again and leaving it for some time before filtering and drying, if more calcite was present it would suggest that the formation was due to the conversion of vaterite to calcite in solution, however for the present study this was not paramount.

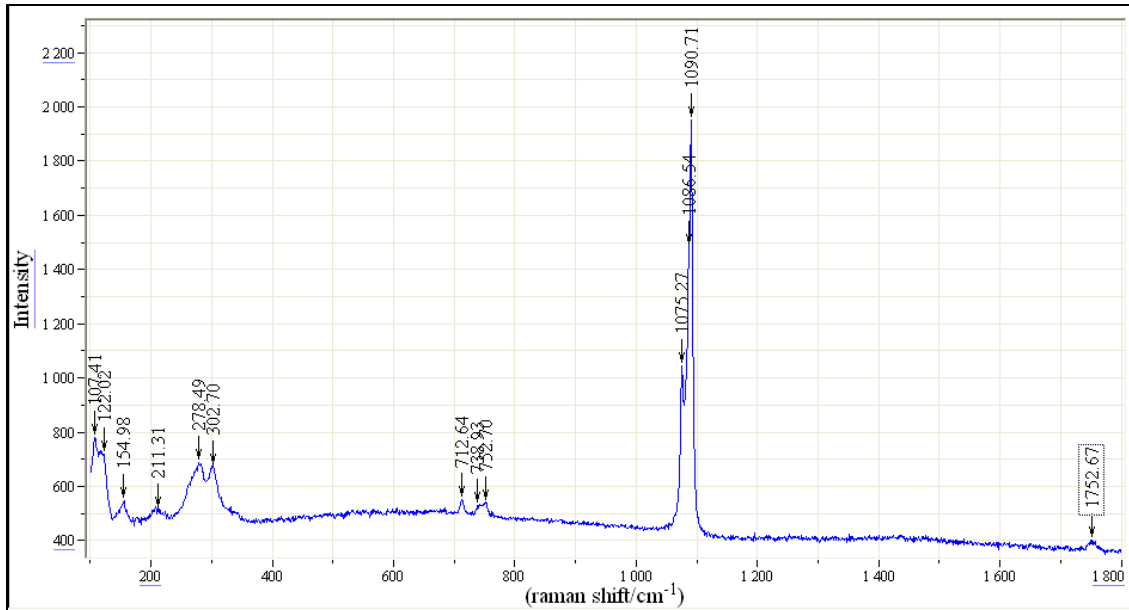


**Figure 4-4** Raman spectrum of the precipitate of pure vaterite

The Raman spectrum for the pure vaterite sample (Figure 4-4) confirms that the rhombohedra observed are indeed of calcite and not an abnormal morphology of vaterite. The large doublet at 1075.3  $\text{cm}^{-1}$ , 1090.7  $\text{cm}^{-1}$  is as expected for vaterite but the shoulder on the 1090.7  $\text{cm}^{-1}$  peak at  $\sim 1086 \text{ cm}^{-1}$  can be attributed to calcite. This spectrum highlights how the intensity observed in this region cannot be used for definitive identification of phase. In contrast, the weak signals seen around 700  $\text{cm}^{-1}$  can identify the two different phases: the weak peak at 712.6  $\text{cm}^{-1}$  for example can be attributed to the  $\nu_4$  bending mode of the carbonate in calcite, whereas the multiplet at 730  $\text{cm}^{-1}$  can be attributed to that of vaterite [19]. However these weak signals could easily be obscured by any impurity in a real system, furthermore aragonite also has a vibration mode for carbonate at 712.6  $\text{cm}^{-1}$  and hence this peak is not a definitive means of identifying morphologies in the presence of calcite. Again, it is the lattice mode vibrations in the low frequency range which are of interest. The two peaks at 155.0 and 278.5  $\text{cm}^{-1}$  can be attributed to the lattice mode vibrations of the minor calcite phase, whereas the peaks at 102.4, 122.0, 211.3, 270 and 302.7  $\text{cm}^{-1}$  are all attributed to the vaterite phase [3]. The presence of aragonite can be excluded as there is no evidence of a small peak around 706  $\text{cm}^{-1}$ , further aragonite shares a lattice vibrational mode with calcite at 154  $\text{cm}^{-1}$  which would be stronger if aragonite were present.

#### 4.1.1.3 Precipitated Aragonite

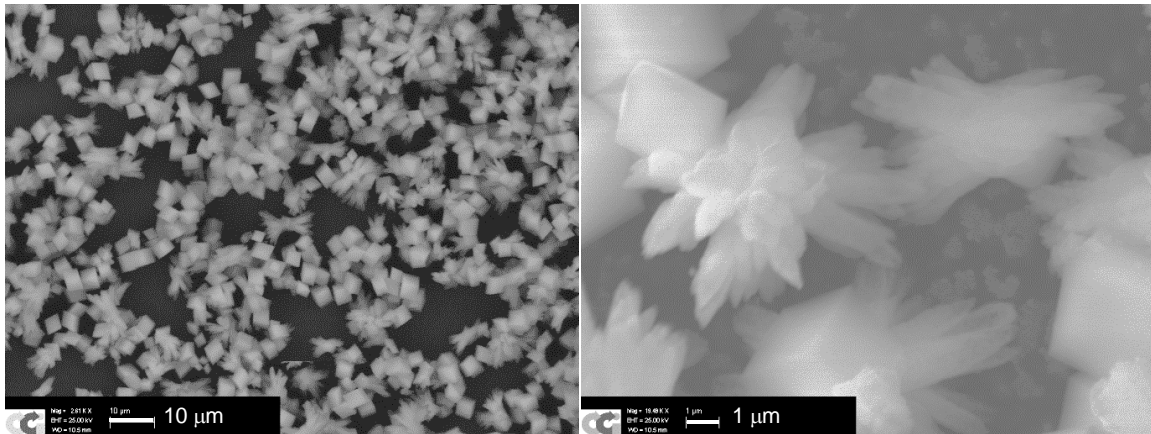


**Figure 4-5** SEM image of precipitated calcium carbonate during the production of pure aragonite

Aragonite can be hard to form without the inclusion of sulphate or magnesium to encourage this phase. As clear Raman spectra are required any inclusion of other species would hinder the analysis, therefore the precipitation of aragonite was performed at elevated temperatures [10, 20-22]. Figure 4-5 shows SEM images of the aragonite formed. The aragonite appears as small clusters of needles and was produced in a minor phase, with calcite the dominant precipitate, as shown by the presence of the characteristic calcite rhombohedra.

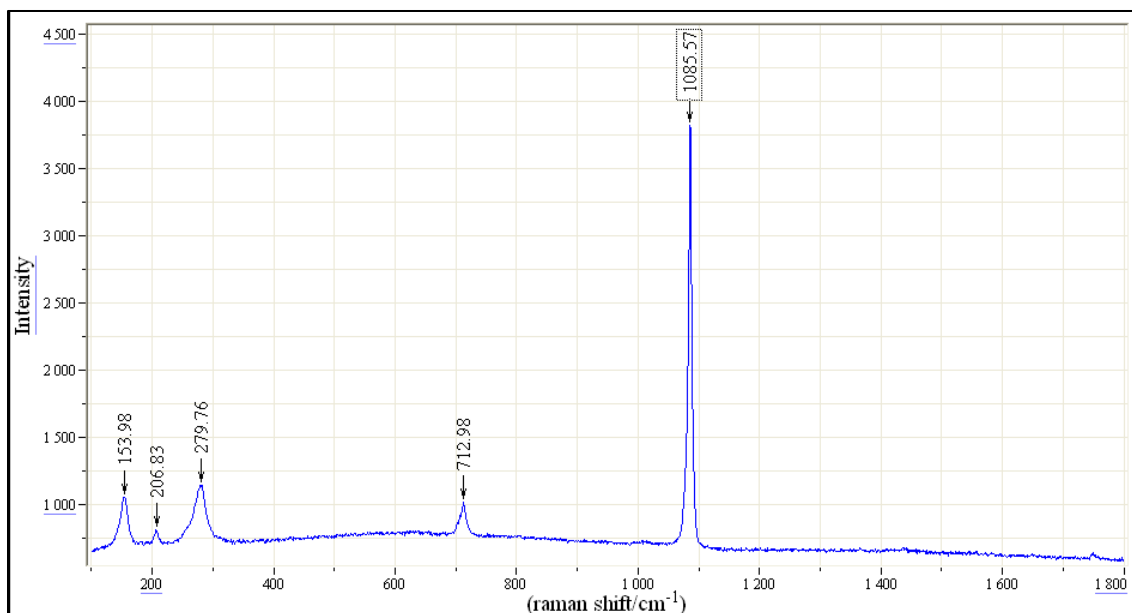


**Figure 4-6** Raman spectrum of the precipitate formed during the production of pure aragonite

Aragonite and calcite share many similar Raman features and so the differentiation of the two phases can be difficult. They both have the same main intensity for the  $\nu_1$  carbonate internal vibrational mode at  $1085.6\text{ cm}^{-1}$ . The weaker internal vibration at  $713.0\text{ cm}^{-1}$  is also shared by the two morphologies, although the aragonite peak is expected at a slightly lower frequency. The latter can be seen in Figure 4-6 as a shoulder and clear widening of the peak when compared to that of the pure calcite in Figure 4-2. The distinguishing peak for aragonite can be seen as a very weak signal at  $206.8\text{ cm}^{-1}$ . Finally when the two main lattice vibrations are observed they are of different intensities, the low frequency band being smaller in calcite and larger in aragonite, this can clearly be seen when comparing the lattice vibrations of calcite (Figure 4-2) and aragonite (Figure 4-6). These findings highlight the difficulty of forming very pure phases of calcium carbonate from saturated solutions and emphasises the need for better understanding and control.

#### **4.1.2 In Situ Electrochemical Raman Analysis of Calcium Carbonate**

##### **4.1.2.1 Investigation of the Deposition and Dissolution of Calcium Carbonate Thin Films**

Considerable efforts were taken to find suitable conditions for observable, phase controlled, deposition. It was found that reliable deposition of calcite was achieved with calcium chloride (10 mmol) and sodium hydrogen carbonate (20 mmol), with the unique lattice vibrations for calcite clearly visible ( $281\text{ cm}^{-1}$  and  $155\text{ cm}^{-1}$ ) and with no presence of other lattice vibrations representing the other polymorphs of calcium carbonate or any sign of impurity (Figure 4-7). Other sources of calcium were investigated, however no repeatable control over deposition was found with any other sources (calcium chloride hydrate, calcium nitrate hydrate). Further, various reduction potentials (open, -200, -400, -600, -800, -1000, -1200 and -1400 mV) were used to encourage phase and deposition control.

A large number of variables were explored in determining favourable conditions for the deposition of phase pure calcite. It was found that calcium chloride was the only source tested that led to reliable deposition. Interestingly, calcium chloride hydrate appeared not to lead to the same results as the anhydrous form, no clear deposition was ever observed with this reagent. This observation is unusual as both the anhydrous and hydrated forms were dissolved in UPW, in equimolar (of Ca) quantities. Although calcium nitrate facilitated the deposition of calcium carbonate, the nitrate ion shares a vibrational frequency with the lattice vibration of calcium carbonate and since the nitrate signal is stronger and broader than that of the carbonate, completely overwhelmed the  $280\text{ cm}^{-1}$  lattice vibration. For this reason the nitrate salt was not investigated any further as a suitable source of calcium.

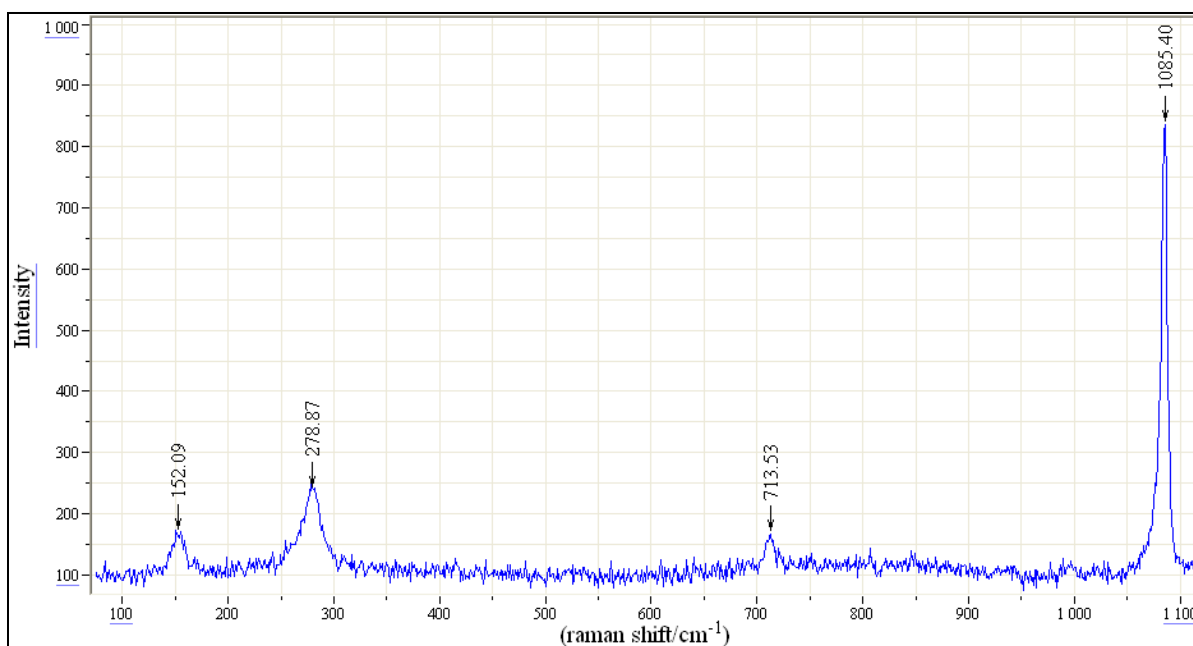


**Figure 4-7** Raman spectra of calcite grown from electrolyte solution ( $\text{CaCl}_2$  10 mmol and  $\text{NaHCO}_3$  20 mmol) held at -1000mV

In initial experiments, the potential was held at -1600 mV. This often led to the rapid deposition of calcite, however at this very negative potential hydrogen was produced at the surface of the electrode leading to  $\text{H}_2$  gas bubbles being produced. If the bubbles grew large enough they could cut off the circuit between the electrodes in the flow cell, causing error in potential measurements. Furthermore, if a bubble, even very small, grew at the focal point of the Raman laser it immediately caused loss of intensity. Signal intensity, being paramount to the investigation other experimental conditions were investigated.

A variable applied potential strategy was investigated in which the potential was initially held low, -1600 mV, to encourage the nucleation of calcite. Then, as soon as peaks started to appear in the Raman spectrum, the potential was raised to above that where hydrogen is produced (-0.800 mV). This meant that initial nucleation could be spurred by the potential and subsequent growth occurred at higher potentials. This method led to more reproducible results, however there was still great disparity between repeat experiments of how long the initial nucleation took to occur.

Interestingly, once the initial nucleation had occurred at the lower potential, it seemed the subsequent growth was not affected by the potential. Experiments at various negative potentials above -800 mV all led to similar patterns in growth after the initial deposition had occurred. It was necessary to have a slightly negative potential held at the electron surface; if

no potential was present, large broad peaks appeared in the region of the spectrum associated with the lattice vibrations blocking the identification of the calcium carbonate polymorph (Figure 4-8). The broad signal was due to Pt-O interactions between the working electrode and the electrolyte water molecules [23].

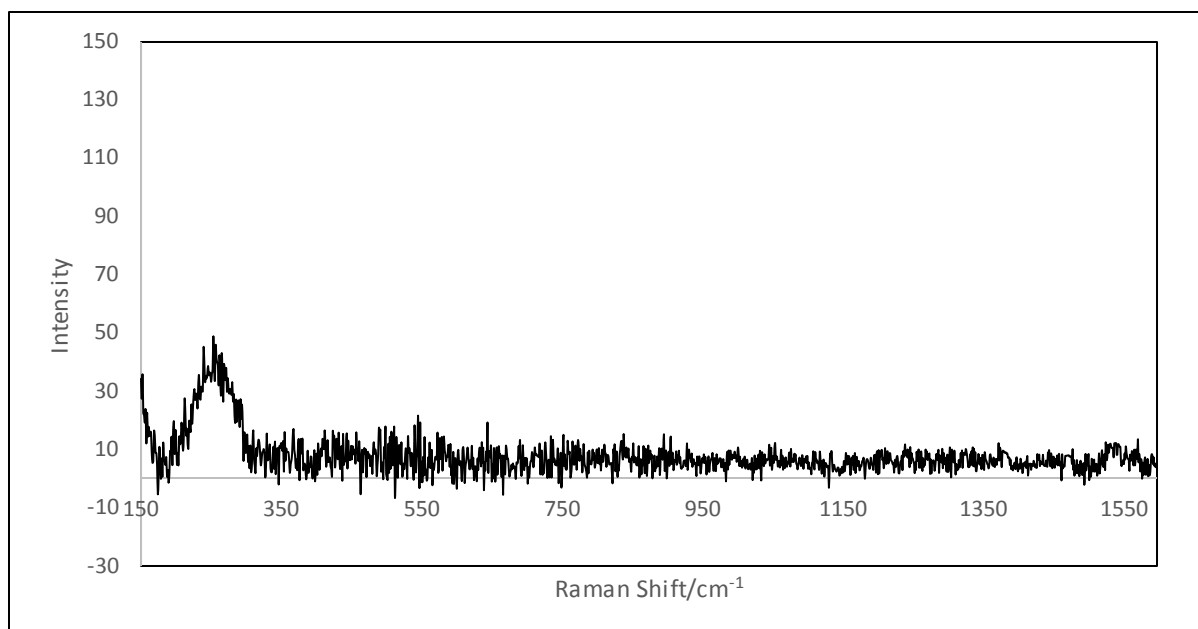


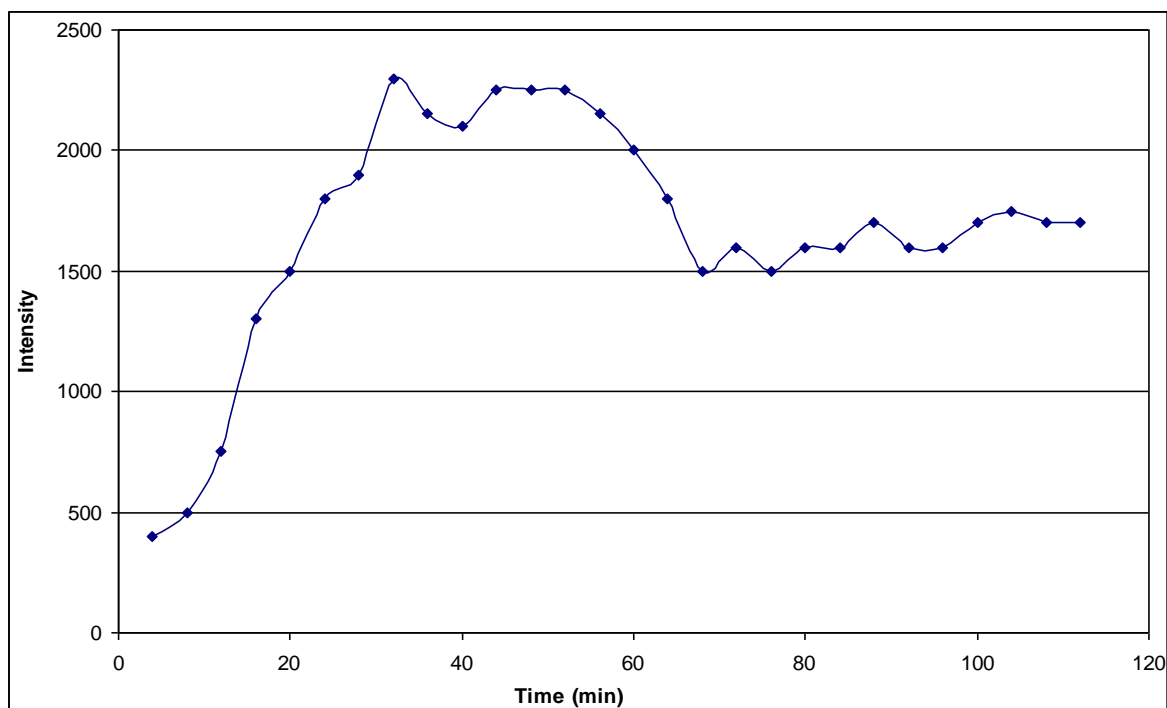
**Figure 4-8** Raman spectrum monitoring calcite growth ( $\text{CaCl}_2$  6 mmol,  $\text{NaHCO}_3$  4 mmol) with open potential evidence of Pt-O blocking lattice vibration region

Not only was the growth seemingly independent of the potential, so too was the polymorph of calcium carbonate with calcite being the dominant structure in all of the experiments. The deposition of specific polymorphs of calcium carbonate has been shown to be highly dependent upon the composition of the electrolyte [13-17]. This is further supported here, showing that the effects of the composition of the electrolyte dominate any stemming from the electrochemical potential. In all experiments the variation of potential did not affect the polymorph deposited. When the solution composition was changed ( $\text{Ca}:\text{CO}_3$ ) in favour of vaterite, minor phases were obtained with the majority phase of calcite.

#### 4.1.3 Raman/SERS Analysis of Calcium Carbonate Growth

Where calcite can be reliably deposited, without the appearance of any other polymorphs or interference from any impurities, the intensity of the  $1085\text{ cm}^{-1}$   $\nu_1$  vibrational mode can be used to track calcite growth over time.

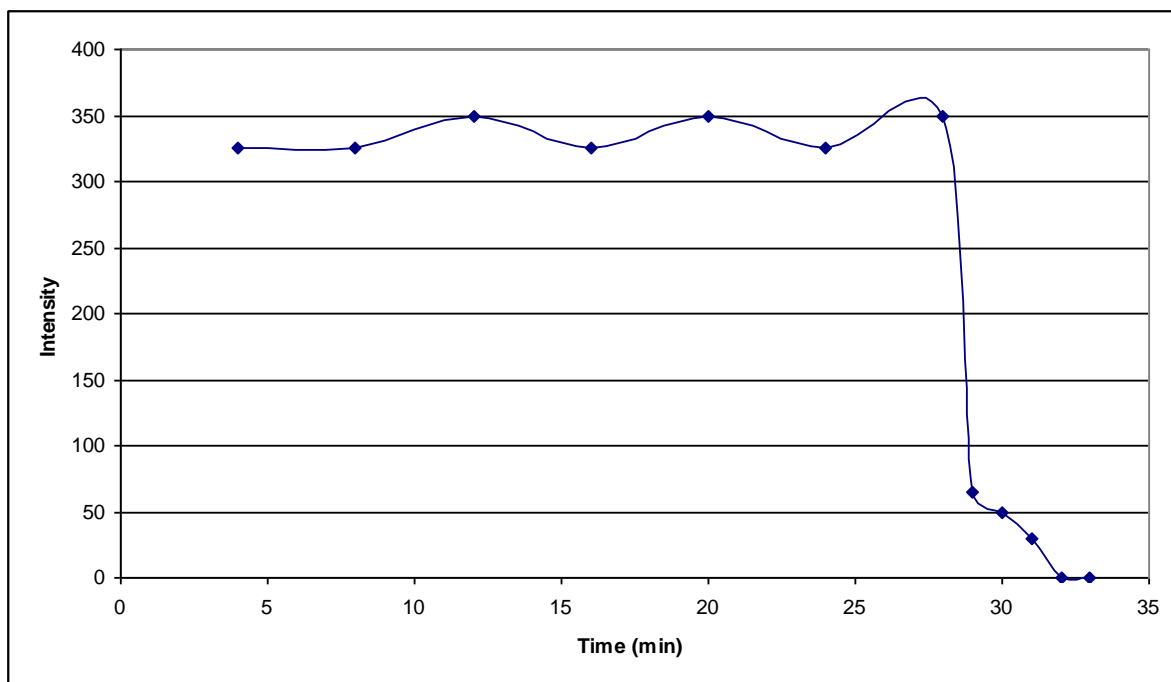
However, rather than monitor the single frequency, full spectra were recorded at each data point to ensure no impurity or other polymorph was developing.



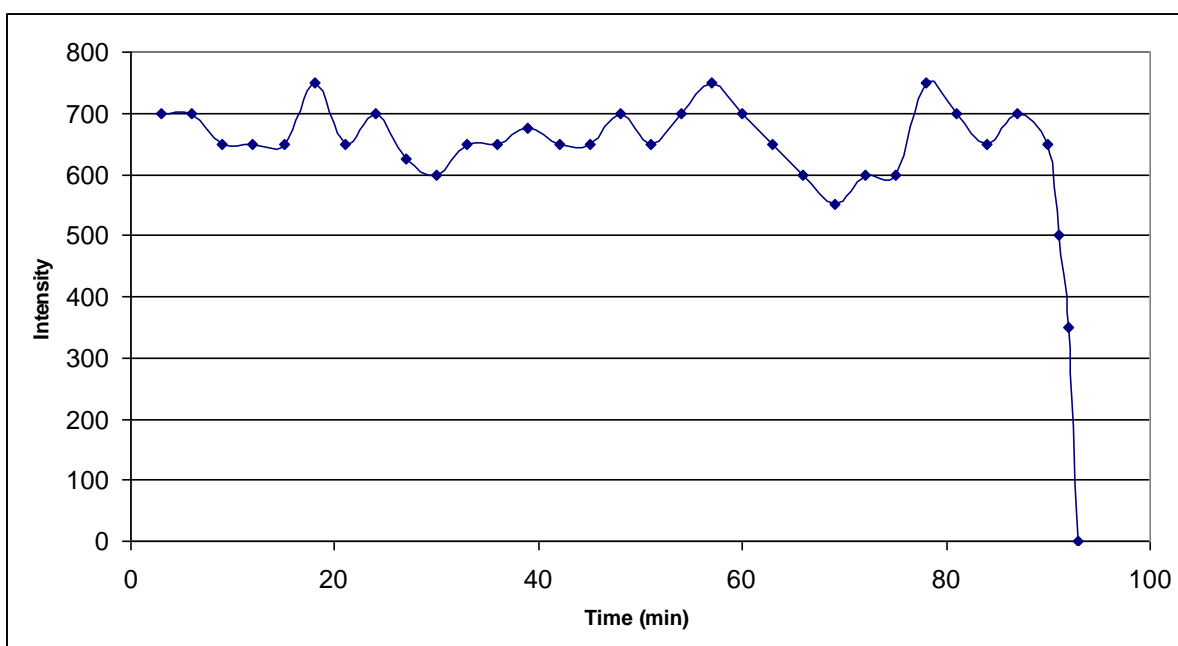
**Figure 4-9** Intensity of the  $\nu_1$  ( $1085\text{ cm}^{-1}$ ) peak against time; electrolyte held at  $-600\text{ mV}$  ( $\text{CaCl}_2$   $10\text{ mmol}$ ,  $\text{NaHCO}_3$   $20\text{ mmol}$ ), observed maxima thought to be point of optimal thickness for maximum enhancement

Figure 4-9 shows an example of the development of the  $1085\text{ cm}^{-1}$  peak with time. However, repeated experiments demonstrated that time taken for deposition and the degree of spectral enhancement varied significantly between experiments. A comparison of Raman intensity with that obtained from bulk powder analysis shows similar intensities suggesting no SERS enhancement and only bulk measurements. This does not support the thin film hypothesis. Following deposition the dissolution of the calcite was examined by switching the electrolyte flowing over the surface to UPW. No change in the intensity of the  $1085\text{ cm}^{-1}$  peak was measured over a period of several hrs following the switch.

Figure 4-10 and Figure 4-11 show two experiments in which dissolution with sulphuric acid was studied. In the first UPW was switched to  $0.01\text{M}$  acid after a period of 30 minutes, whereas the second involved a direct switch of the depositing solution to the acid. The dramatically different behaviour of the two experiments is illustrative of the inconsistent results this experimental strategy produced. In neither case was there any evidence to suggest that the SERS effect was being triggered at any point.



**Figure 4-10** Intensity of the  $\nu_1$  ( $1085\text{ cm}^{-1}$ ) peak against time; electrode held at  $-600\text{ mV}$ , electrolyte change from UPW to  $\text{H}_2\text{SO}_4$  ( $0.01\text{ M}$ ) after 28 minutes



**Figure 4-11** Intensity of the  $\nu_1$  ( $1085\text{ cm}^{-1}$ ) peak against time; electrode held at  $-600\text{ mV}$  ( $0.01\text{ M}$  sulphuric acid), after 90 minutes the concentration was increased to  $0.1\text{ M}$  resulting in dissolution

Images of the surface recorded through an optical microscope during and after deposition explain these inconsistencies (Figure 4-12). During deposition, small crystals were observed nucleating and growing over the surface. The Raman signal would depend upon whether in

any single experiment the laser focal point was on a growing particle or in an area encroached upon as the crystal grows.

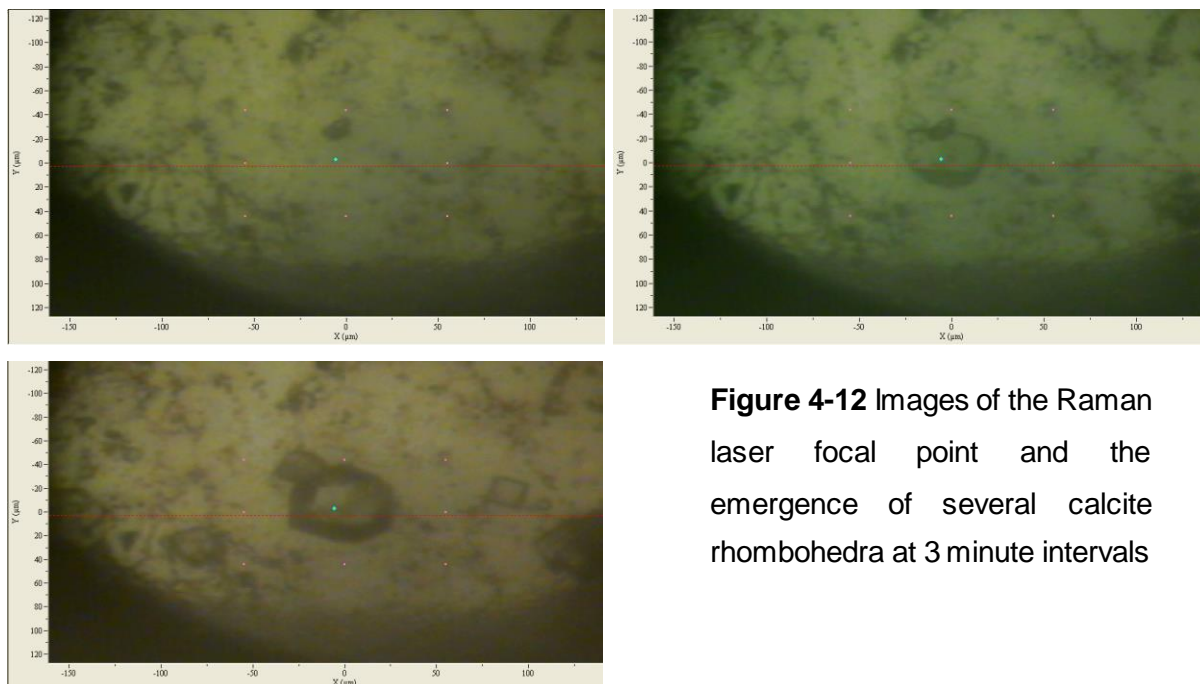


**Figure 4-12** Images of the Raman laser focal point and the emergence of several calcite rhombohedra at 3 minute intervals

Figure 4-12 shows the growth of calcium carbonate, the phase was confirmed with a very clear Raman spectrum of calcite (Figure 4-13). The optical images show the inconsistencies described due to the nucleation and growth of individual crystals over the surface and the dependency on of the position of the focal point of the laser. Furthermore, the low Raman intensity observed in Figure 4-13 highlights the absence of the SERS effect.

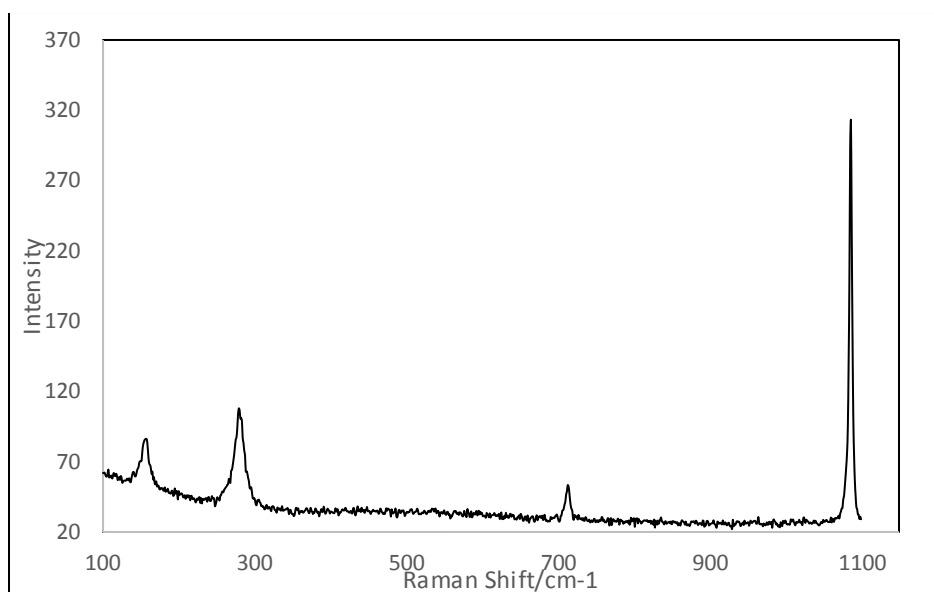


**Figure 4-13** Raman spectrum of calcite rhombohedra observed growing under the optical microscope in Figure 4-12

The following experiments were conducted with a slight variation of procedure from above. Without the Raman laser on, a reduction potential was applied and the surface of the electrode was monitored through the optical microscope. Crystals were observed nucleating and growing, the laser was then focused over the centre of a crystal and a spectrum was taken to identify its polymorph. The electrolyte was changed to a dilute acid and the time resolved process was again implemented to track the particle dissolution. The growth of a vaterite flower can clearly be seen in (Figure 4-15), and the observed rise in intensity over time can be attributed to the growth of the crystal coming into the field of focus of the laser. The vaterite lattice vibrations are seen at 107, 122, 209, 266 and 303  $\text{cm}^{-1}$  as well as the  $\nu_1$  symmetric stretch (1075 and 1091  $\text{cm}^{-1}$ ) and the  $\nu_4$  in-plane bending (740 and 750  $\text{cm}^{-1}$ ). With the use of elevated temperatures it was also possible to produce aragonite, however only minor phases were achieved with the dominating morphology being calcite.

The data suggests that the experimental protocol of carbonate growth in the flow cell was not successfully synthesising thin films with a demonstrable SERS enhancement. Subsequent studies will therefore consider the synthesis of  $\text{Au}@\text{CaCO}_3$  nanoparticles deposited onto the electrode; this will enable fine tuning of layer thickness prior to the study of dissolution and circumventing this issue.

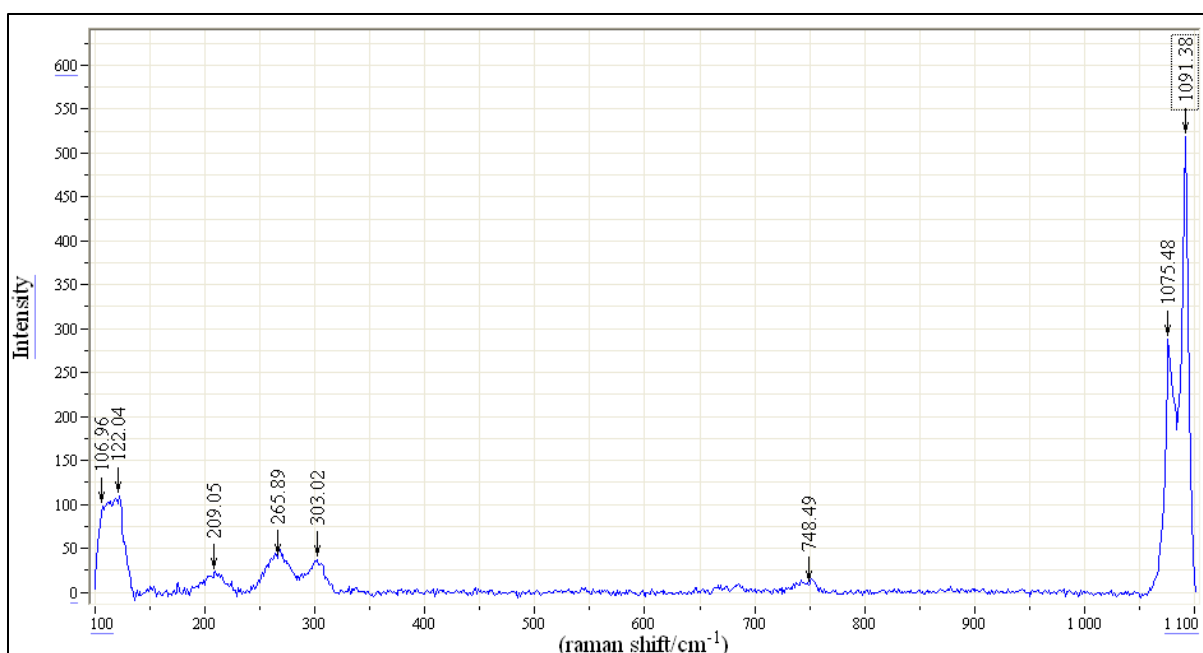


**Figure 4-14** Raman spectra of electrochemically deposited vaterite flower

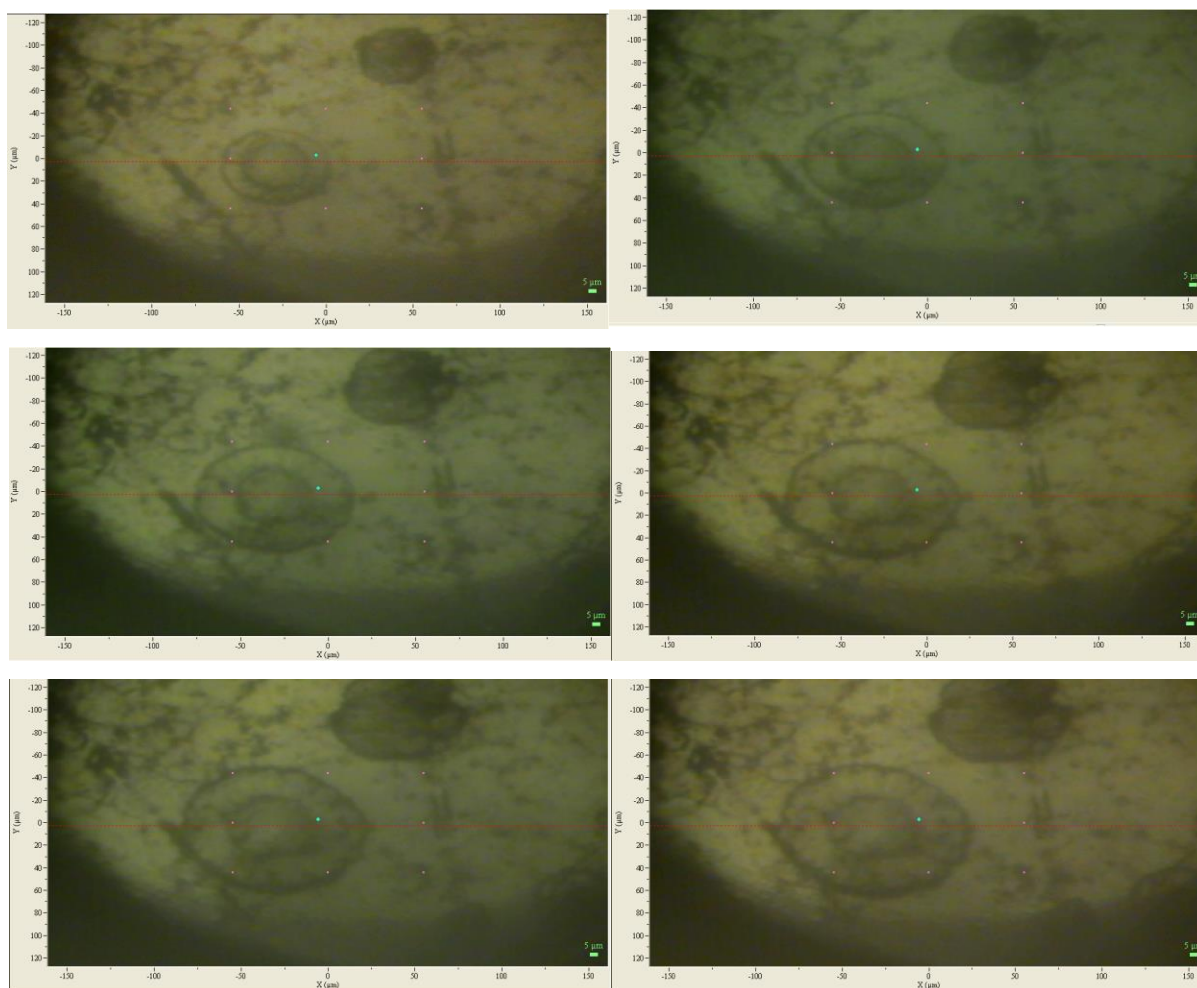


**Figure 4-15** Sequence of images showing growth of a vaterite flower

## 4.2 Nanoparticle Synthesis and Coating

### 4.2.1 Citrate Stabilised Gold Nanoparticles

Citrate stabilised gold nanoparticles were utilised for the ease of synthesis and pronounced SERS enhancement effect. Maximum SERS enhancement for such gold nanoparticles is found at around 50 nm [24-26]. The size of synthesised particles was confirmed using UV-Vis spectroscopy and the known correlation between size and surface plasmon frequency [24, 27]. The maximum absorbance observed in Figure 4-16 at 530 nm, is indicative of 50 nm sized particles and this was confirmed by TEM, Figure 4-17 which also shows the particles are predominantly round, but with a number of more elongated particles. Note, that for particle size counts it is always the longest length across a particle which was measured, hence the slightly higher than expected size distribution. It was noted that gold nanoparticles made in this way have been used extensively for SERS measurements and it was not until this analysis that the non-spherical nature of these particles was realised. Since this finding a variation of

the synthesis was found leading to much more spherical particles with a narrower size distribution.

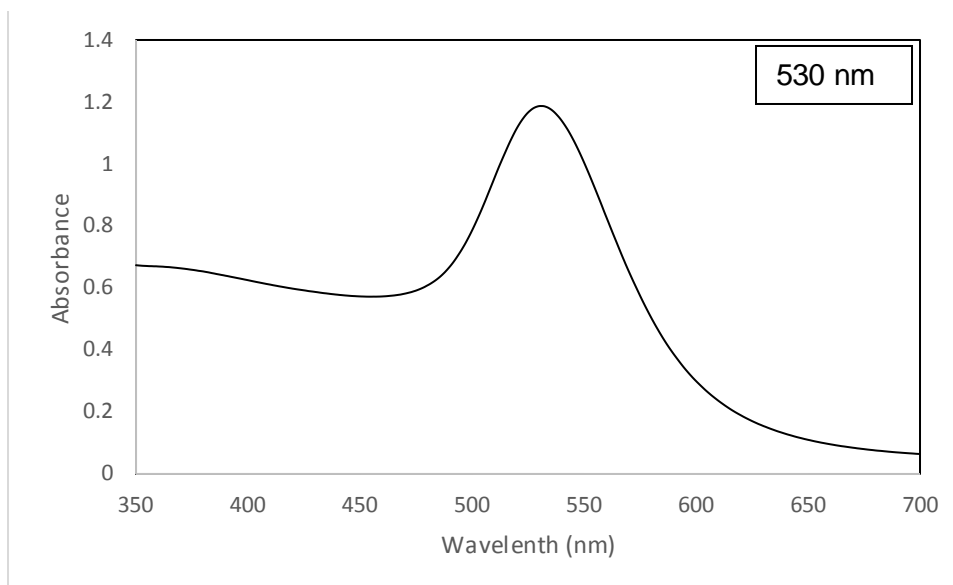


**Figure 4-16** UV-Vis spectrum of citrate stabilised gold nanoparticles

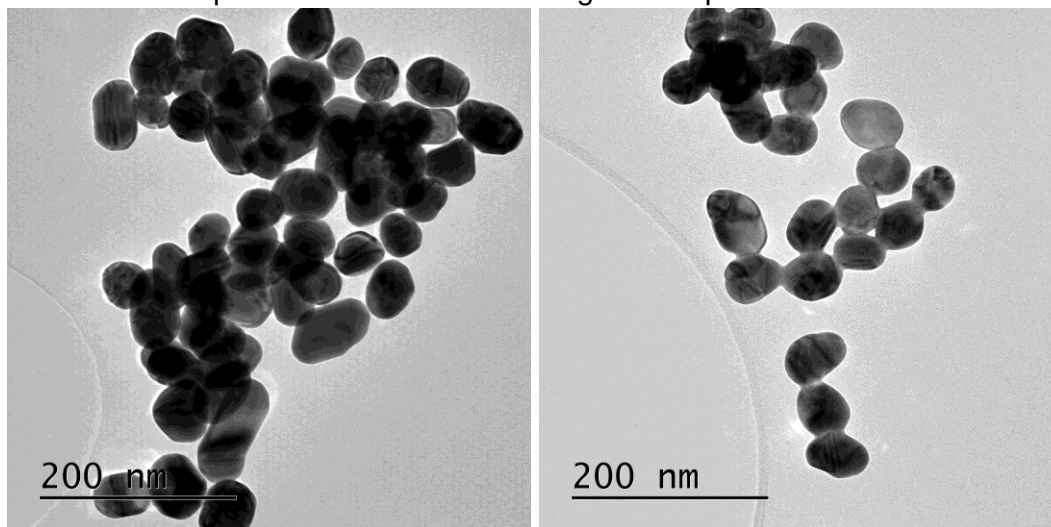


**Figure 4-17** TEM images of citrate stabilised gold nanoparticles

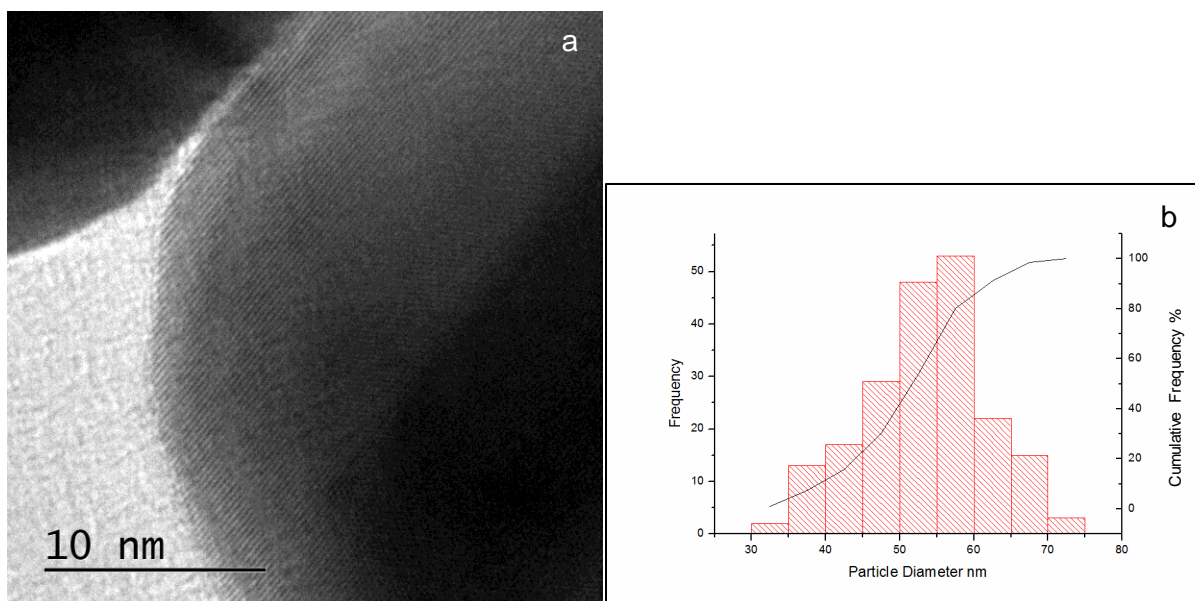


**Figure 4-18** a) TEM image of single gold nanoparticle revealing the lattice spacing and b) the particle size distribution

A high magnification image of a single gold particle in Figure 4-18 shows the particle has a high degree of crystallinity. The lattice lines were measured and the atomic spacing calculated to be 2.27 Å, close to values found in the literature of 2.22 Å [28].

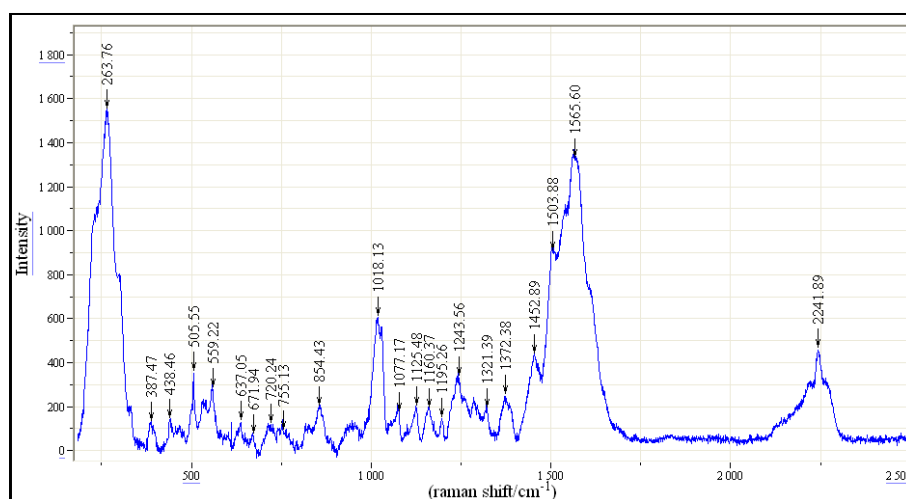


**Figure 4-19** Raman spectrum of citrate stabilised gold nanoparticles pre-deposited on a poly Pt working electrode

Citrate stabilised gold nanoparticles were analysed using SERS (Figure 4-19). Although the intensity does not appear very high here, this was expected as citrate was in low concentration, it is only physisorbed to the nanoparticle surface and due to the tridentate bonding the molecule is not perpendicular to the surface. The enhancing field effect of SERS is strongest when the analyte is perpendicular to the surface [29]. The broad intensity around

2240  $\text{cm}^{-1}$  is the combination of a sharp peak from a C-H stretching vibration and a broad peak from the O-H stretching vibration. The large broad intensity centred at 1566  $\text{cm}^{-1}$  is attributed to the  $\nu(\text{COO}^-)$ , its multiplicity is due to the different  $\text{CO}_2^-$  moieties of citrate, the reason for its width and strong intensity is due to the interaction with the gold surface. The group of medium intensity peaks from 1070-1380  $\text{cm}^{-1}$  are attributed to the various C-O out of plane vibrations. The sharp strong peak at 1018  $\text{cm}^{-1}$  is potentially the C-O stretching frequency of the tertiary alcohol. The many peaks observed from 550-950  $\text{cm}^{-1}$  are the various C-C stretching vibrations, the peaks below this are likely to be the C-O in-plane vibrations. Finally the large broad peak centred around 260  $\text{cm}^{-1}$  is probably not from the citrate but due to some hydroxide on the surface of the gold particle or underlying Pt electrode, hence the large intensity. These assignments agree with those found in the literature [30-32].

#### 4.2.1.1 Calcium Carbonate Deposition on Citrate Stabilised Gold Nanoparticles

The possibility of coating citrate stabilised gold nanoparticles using a standard literature method of exposing a solution containing  $\text{CaCl}_2$  to ammonium carbonate was investigated.

Calcium chloride (4.4 mg) was added to a solution of ~50 nm citrate stabilised gold nanoparticles (10 mL), before exposure to air or ammonium carbonate for 6hr. A droplet of the solution was pipetted onto a carbon adhesive slide, dried and analysed using SEM.

All experiments undertaken that involved the direct addition of calcium chloride powder to gold nanoparticle solutions, resulted in the aggregation of the citrate stabilised gold nanoparticles and the separate deposition of calcium carbonate in the form of calcite (Figure 4-20).

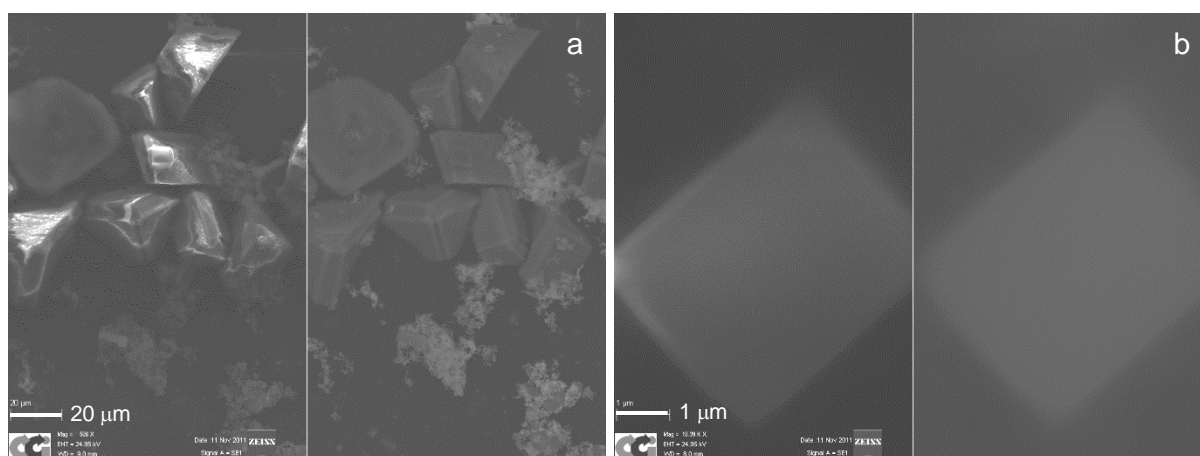


**Figure 4-20** SEM image of precipitate formed after addition of  $\text{CaCl}_2$  powder; a) exposed to ammonium carbonate, b) exposed to air.

Samples were exposed to ammonium carbonate or air. As expected the samples exposed to ammonium carbonate resulted in greater calcium carbonate deposits than those exposed to air in which only small numbers of small calcite rhombohedra were observed (Figure 4-20 b)).

#### 4.2.1.2 Addition of Nanoparticles to Solution of Calcium Chloride

Citrate stabilised gold nanoparticles ( $5 \text{ cm}^3$ ) were pipetted under the surface of a solution of calcium chloride ( $10 \text{ mmol}$ ,  $10 \text{ cm}^3$ ), before the solution was exposed to ammonium carbonate. A droplet was collected after 1, 6 and 48 hr exposure times. The droplet was pipetted onto a carbon slide and dried for SEM analysis. It was again observed that the addition of calcium chloride caused the gradual colour change of the solution from red to purple. After 48 hr the solution had become almost completely clear.

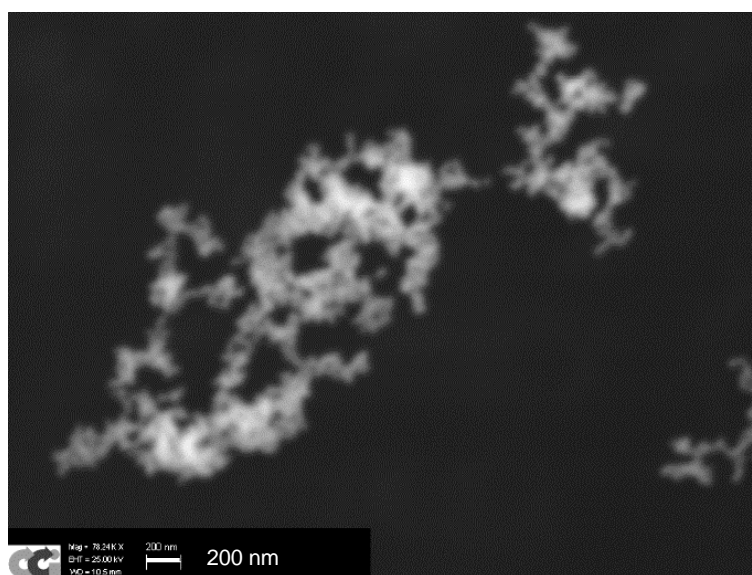


**Figure 4-21** SEM image of a cluster of aggregated gold nanoparticles 1 hr after injection into calcium chloride solution

In Figure 4-21 a cluster of nanoparticles are observed after 1 hr exposure, the stability of these particles has again been affected by the addition of calcium chloride. The SEM was almost able to resolve these individual nanoparticles.

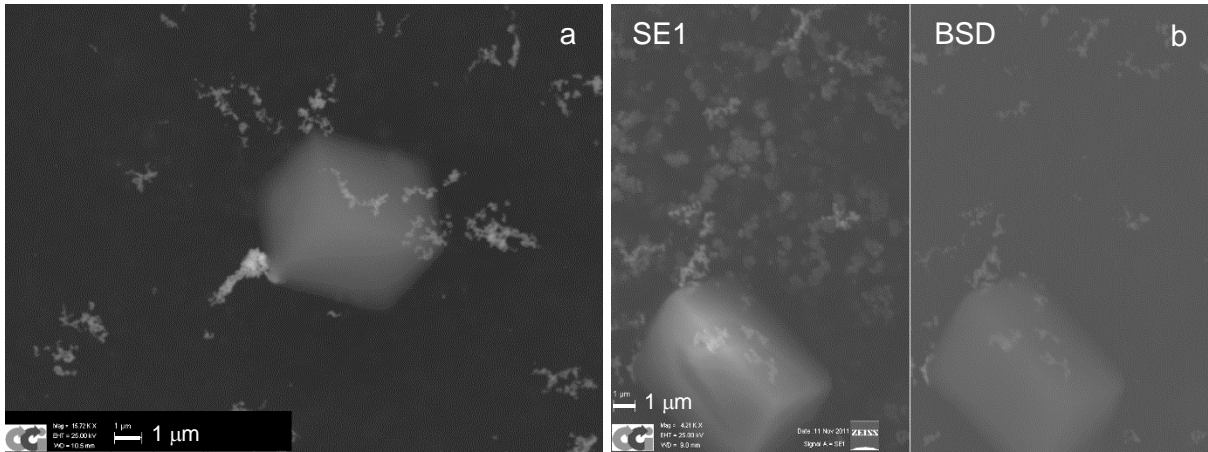


**Figure 4-22** SEM images of sample solution 1 hr after exposure to ammonium carbonate

Very few clusters of nanoparticles were observed after 1 hr (Figure 4-22), this shows that most are still well solvated in the sample solution, the presence of a few small rhombohedra of calcite are observed. In Figure 4-22 b) the comparison between the two detector images shows that the nanoparticles are present on the surface of the precipitated crystal. Further in Figure 4-22 b) it can be seen in the SE1 detector image that some clusters are visible which appear similar to the nanoparticles but do not appear in the BSD image. These clusters are a feature of the carbon adhesive SEM slide and highlight that very high resolution images are possible with this SEM, the resolution limit of this machine is in the region of 30-50 nm.

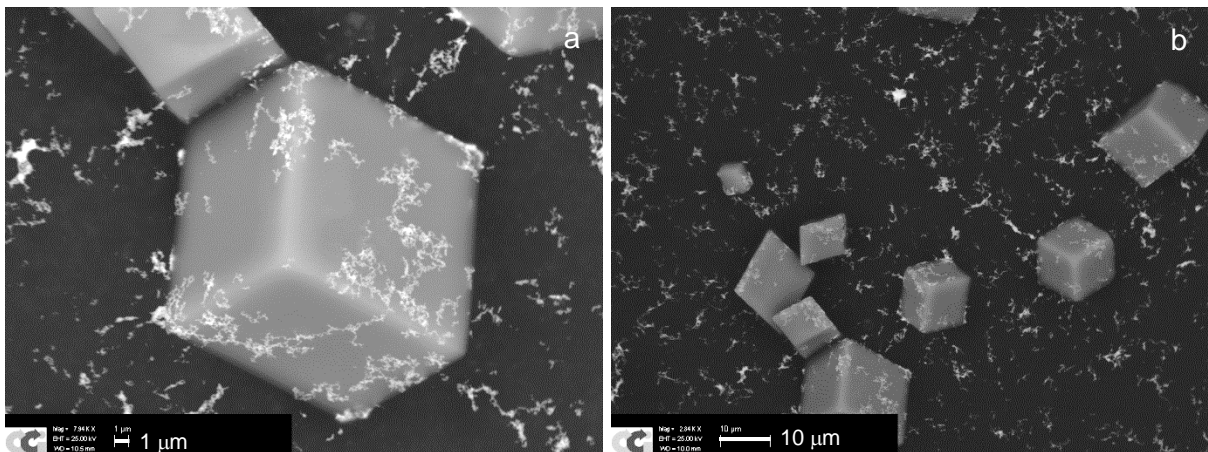


**Figure 4-23** SEM image of sample solution after 6 hrs exposure to ammonium carbonate; a) high magnification of calcite rhombohedra and b) lower magnification revealing multiple crystals

After 6 hrs exposure to ammonium carbonate, many rhombohedra of calcite are observed (Figure 4-23). There does not seem to be any influence from the surface or the gold nanoparticles on the calcite rhombohedra. The crystals are of various sizes indicating that

there is continual nucleation and growth of crystals. The crystals also do not appear to be experiencing any epitaxial growth from the surface as the rhombohedra are growing with different facets in contact with the surface. The nanoparticles appear to have adhered to the surface of the calcite crystals. Whether the particles adhered to the surface before or after dropping out of the solution is unclear. Further the nanoparticles may have simply deposited onto the calcite crystals as they aggregated and deposited.

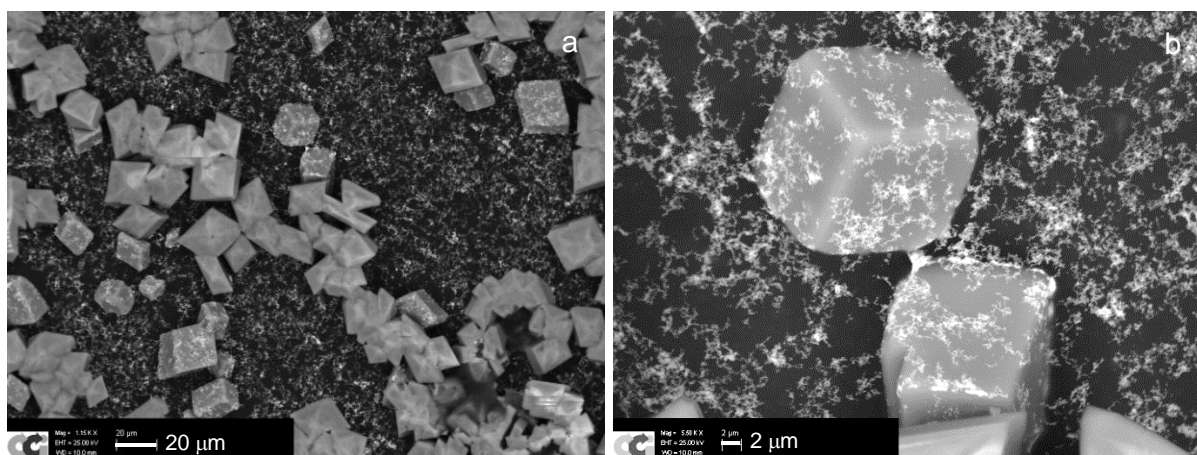


**Figure 4-24** SEM images after 48 hr exposure to ammonium carbonate; a) low magnification calcite and vaterite and b) high magnification of nanoparticle covered calcite

After 48 hrs it was seen in Figure 4-24 that more nanoparticles aggregated and precipitated from the solutions, also covering the calcite rhombohedra to a greater extent. Interestingly after 48 hrs what is likely vaterite has also formed. One of the more stable morphologies of vaterite is that of the octahedral form seen here [1], vaterite becomes a more favourable precipitate at lower concentrations of calcium [10, 13], hence here after a period of time has passed enough calcite has precipitated that vaterite becomes the dominant precipitate. The apparent preferential coating of gold on the calcite over vaterite is likely due to the order of precipitation: the calcite rhombohedra first precipitated followed by the nanoparticles and lastly the vaterite crystals. The presence of vaterite is attributed to the concentration difference with respect to available calcium ions, or more specifically the ratio of calcium and carbonate ions [3].

It can be deduced from the above coating attempts using citrate stabilised gold nanoparticles that the citrate is not great enough at stabilising the nanoparticles. The addition of calcium chloride was enough to destabilise the charge stabilised gold nanoparticles. The increase in the calcium chloride concentration has increased the ionic strength neutralising the charge repulsion and hence aggregation has occurred. This was similar to that observed for the experiments where calcium chloride was directly added to gold nanoparticle solutions. The

combination of these experimental findings indicates the charge stabilisation of citrate stabilised gold nanoparticles is inadequate for the applications required and stronger stabilising agents must be explored.

## 4.2.2 Thiol Stabilised Gold Nanoparticles

Thiols used were chosen for the greater ability to stabilise the gold nanoparticles and likely chemisorb to the nanoparticle through the sulphur moiety rather than physisorb as is the case for citrate. Thiol stabilised particles were produced via a simple exchange reaction with citrate stabilised particles (Chapter 3.3.2). The nanoparticle solutions were initially analysed with UV-Vis and Raman spectroscopy, later coupled with TEM analysis. Citrate was exchanged with mercaptosuccinic acid, p-mercaptophenol, p-mercaptophenylboronic (p-MPB) acid and p-mercaptobenzoic (p-MB) acid.

### 4.2.2.1 Analysis of p-Mercaptophenylboronic Acid

After the exchange reaction had taken place it was observed that the solution had changed colour from red to purple, this indicated some change to the energy of the surface plasmons. A UV-Vis spectrum of this sample (Figure 4-25) reveals that the particles maximum absorbance has changed by roughly 10 nm from 540 to 550 nm, which, using the same correlation as before would indicate that the particles had grown from around 50 to 80 nm in diameter. However, the correlation relies on the surface plasmon energies for nanoparticles stabilised by citrate rather than the p-MPB acid.

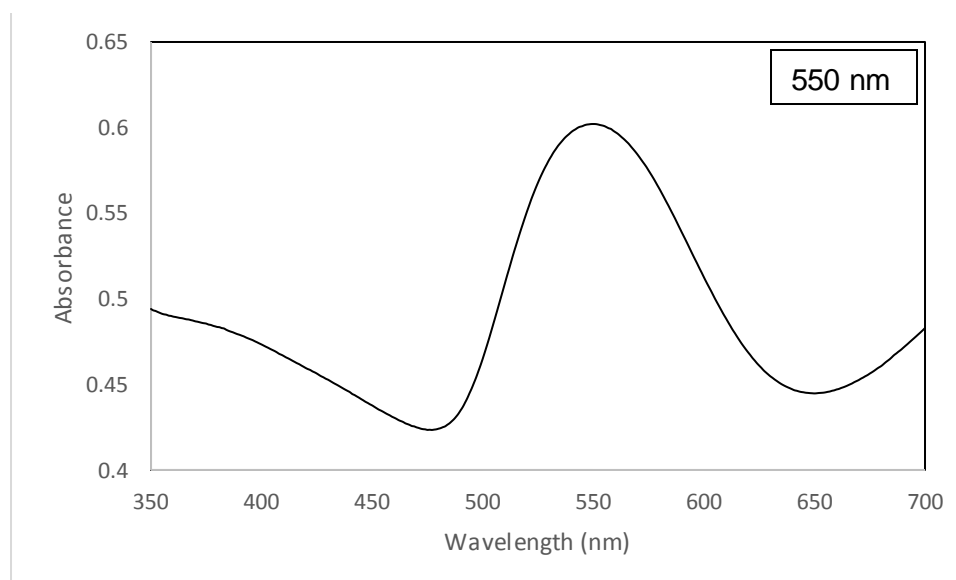


**Figure 4-25** UV-Vis spectrum of p-mercaptophenylboronic acid

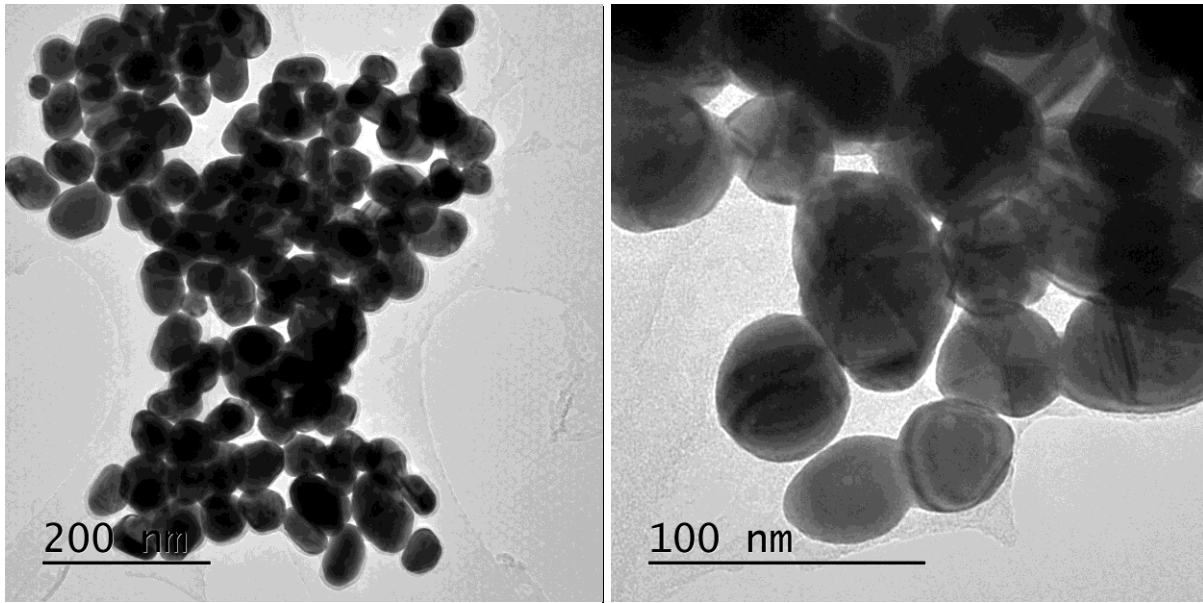


**Figure 4-26** TEM images of various areas of the sample slide

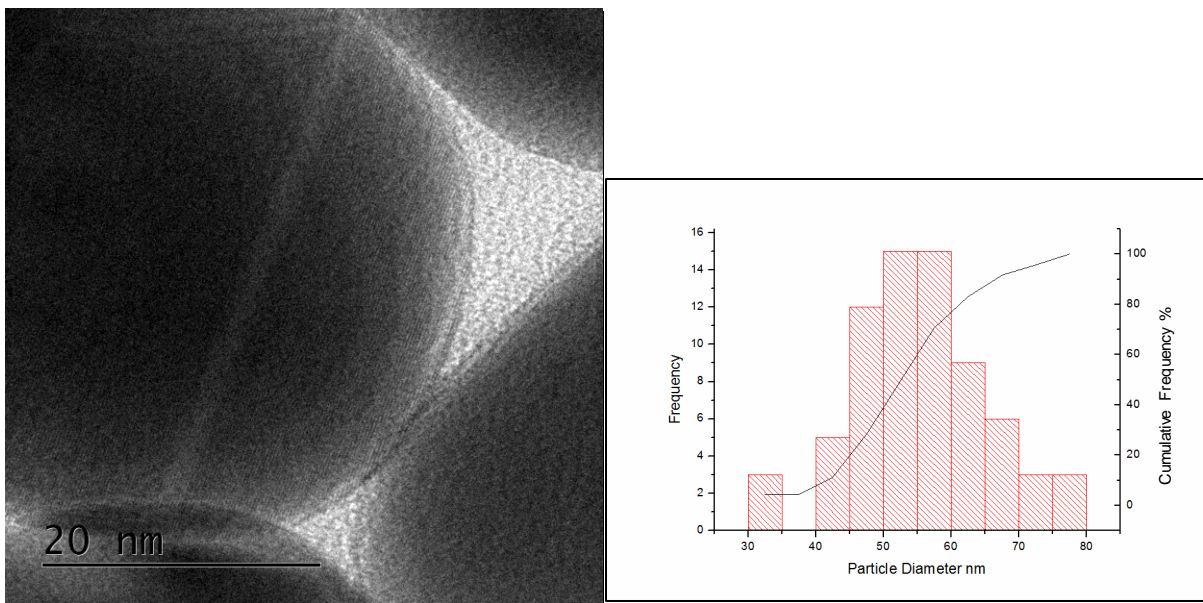


**Figure 4-27** a) High magnification TEM of single particle showing lattice fringes and b) size distribution of nanoparticles

TEM data in Figure 4-26 and 4-27 b) show that the nanoparticles retain the same size distribution indicating that the exchange process has had minimal impact with little sign of aggregation. Long range order is still observed in the p-MPB acid nanoparticles (Figure 4-27) with lattice fringes visible. Figure 4-28 demonstrates that the citrate has been successfully exchanged for p-MPB acid. The Raman intensity has risen significantly, indicating that the SERS enhancement is greater for this stabilising agent. The band observed at  $1069\text{ cm}^{-1}$  is the C-S vibrational mode and its intensity is pronounced due to the SERS field effect [33]. The

strong bands at 1566 and 1586  $\text{cm}^{-1}$  are the C-C ring modes, again these are pronounced due to the proximity to the surface. The strength of the latter two peaks suggest that the thiol is perpendicular to the surface, [29]. This spectrum is consistent for p-MPB acid and full assignment of the bands can be found at [33, 34].

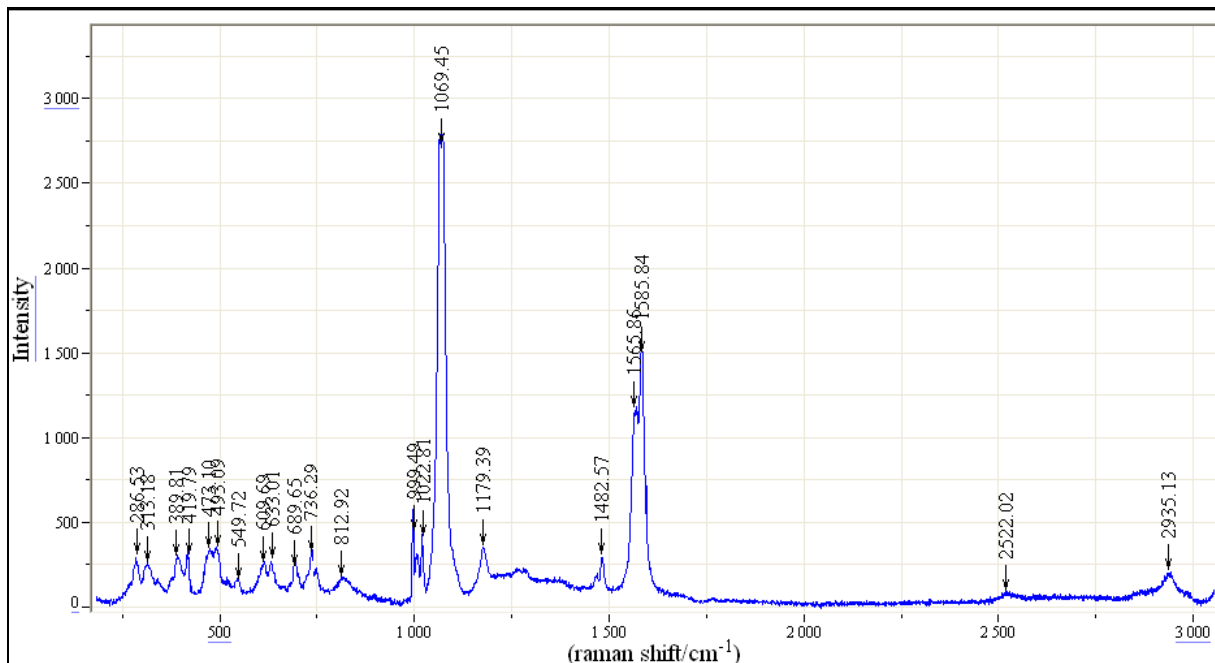


**Figure 4-28** Raman spectrum of gold nanoparticles after exchange of citrate for p-mercaptophenylboronic acid

#### 4.2.2.2 Analysis of p-Mercaptobenzoic Acid

In contrast to the situation with the p-MPB acid stabiliser, for p-MB acid, the UV-Vis spectrum shows little change to the wavelength of maximum absorbance. However there is a large shoulder at  $\sim 575$  nm.

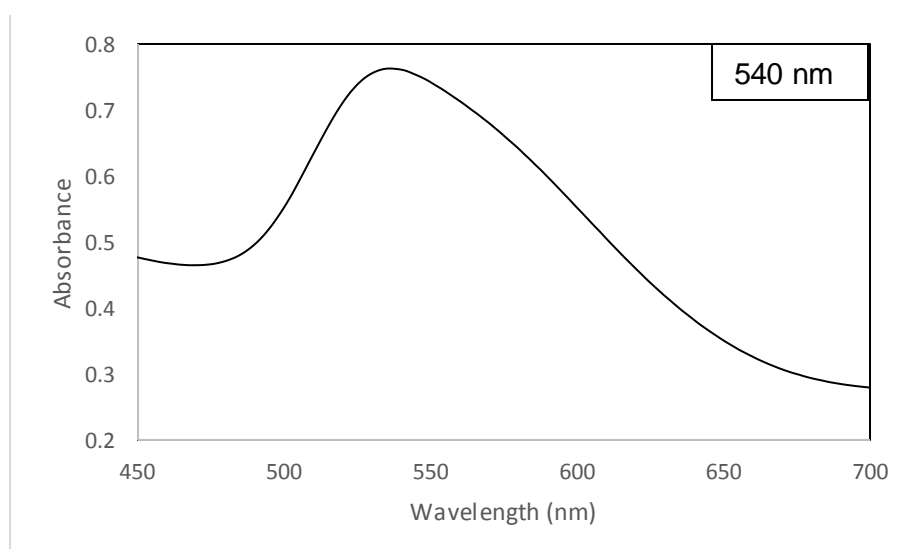


**Figure 4-29** UV-Vis spectrum of p-mercaptobenzoic acid stabilised gold nanoparticles

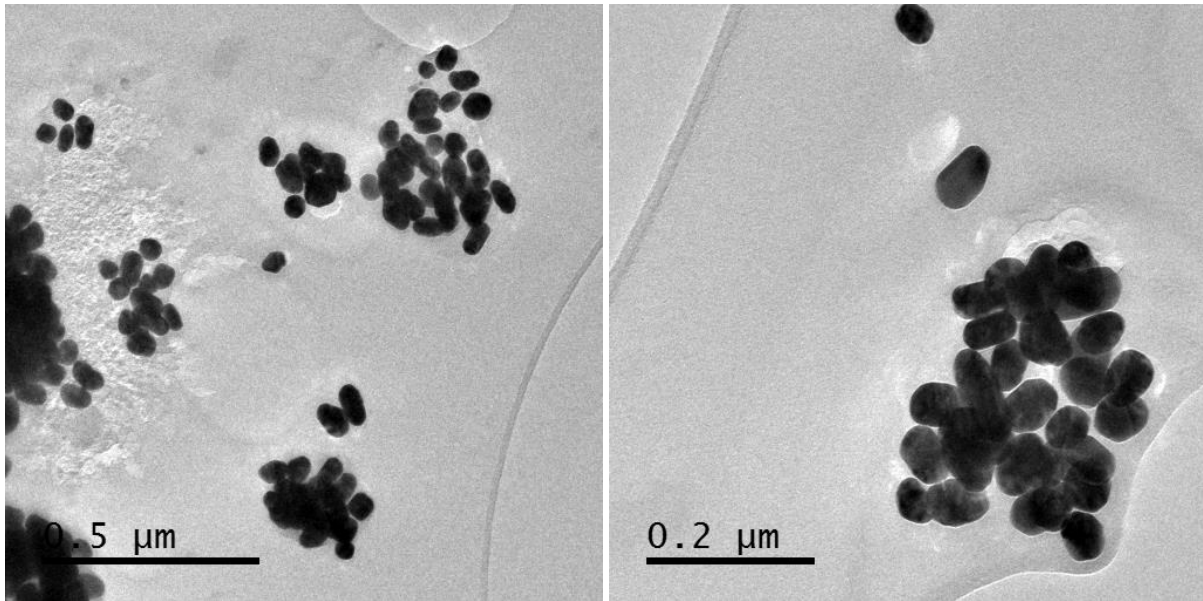


**Figure 4-30** TEM images from various areas of sample slide of p-mercaptopbenzoic acid stabilised particles

TEM images (Figure 4-30) again show that there are a large number of roughly 50 nm diameter spherical particles, but that a significant number of elongated particles again exist.

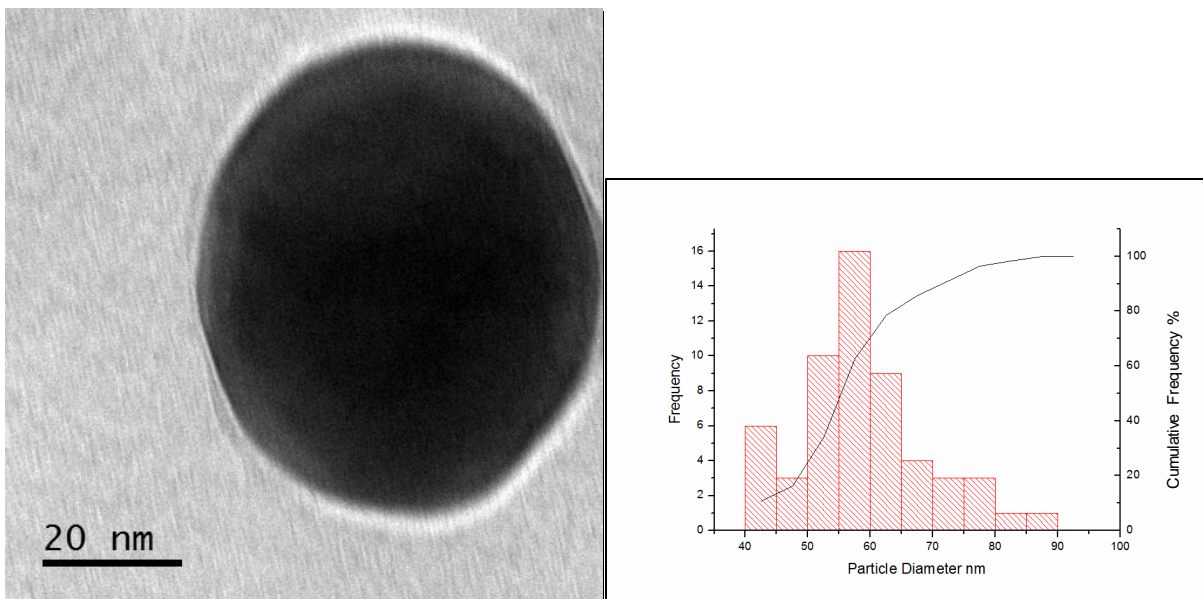


**Figure 4-31** a) TEM image of single nanoparticle and b) size distribution of p-MB acid stabilised nanoparticles

The size distribution of these particles is slightly broader overall (Figure 4-31 b)) than previously observed, however the number of particles in the range 50-60 nm is greater, with a narrower distribution about the desired size. The observed broadening is likely not the reason for the broad UV-Vis spectrum as it would be expected that the smaller particles (40

nm) make up a larger quantity than those over 70 nm, and hence if the UV-Vis was representative of the size distribution it should be seen to have a large shoulder at wavelengths lower than 540 nm. It was not possible to obtain lattice fringes due to a technical difficulty with the TEM rather than there being an issue with the nanoparticles themselves. This is highlighted by the blurring in a net diagonal direction across the image (Figure 4-31 a)).

—

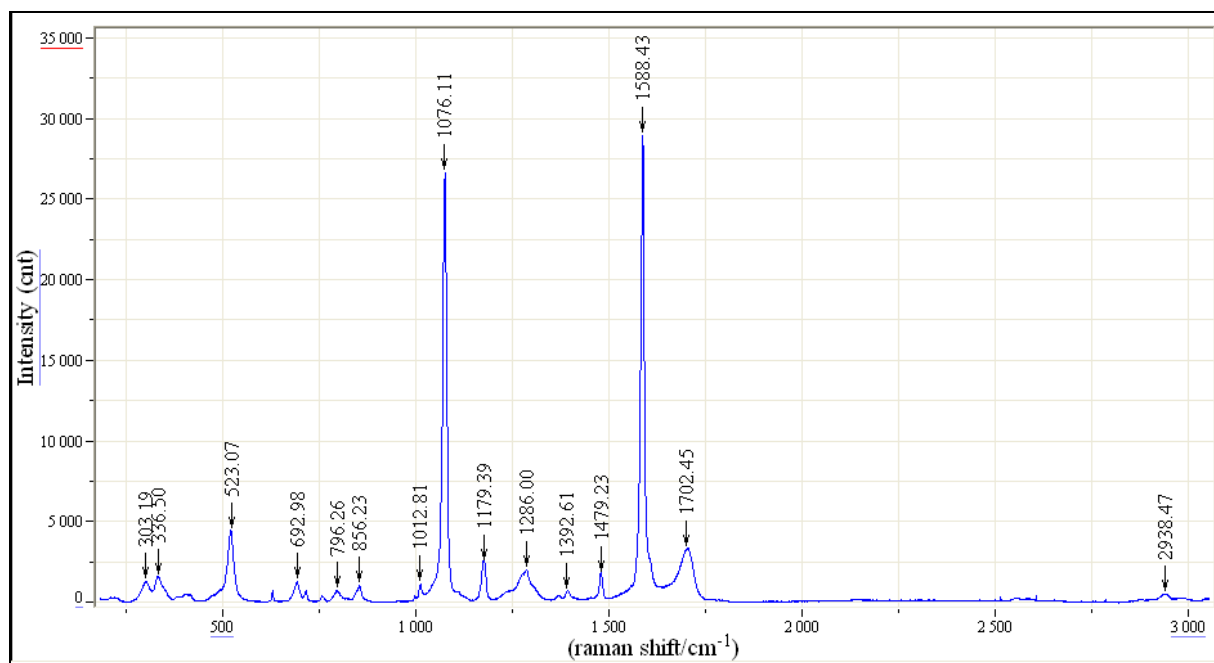


**Figure 4-32** Raman spectra of gold nanoparticles after exchange of citrate for p-mercaptobenzoic acid

The Raman spectrum of p-MB acid exchanged particles (Figure 4-32) is interesting for a number of reasons. Firstly it is seen that the maximum intensity is very high >30,000 counts indicating for the first time that a strong SERS enhancement is experienced. The strong band at 1588  $\text{cm}^{-1}$  is due to the C-C ring stretch and C-H asymmetric in-plane bending. The strong band at 1076  $\text{cm}^{-1}$  is the aromatic ring breathing, C-H symmetric stretching and C-S stretching modes [35-38]. The remaining peaks are indicative of p-MB acid and there is no evidence of citrate remaining [30, 32, 36, 37]. Most interestingly it has been shown, on a similar system but using Ag nanoparticles, that the relative intensity and presence of certain bands shows whether the p-MB acid is perpendicular to the surface or at an angle and further is able to show if the carboxylic acid is involved in the surface stabilisation [39]. It was shown that at pH values similar to that used here (>10 pH) the carboxylic acid was deprotonated and involved with surface bonding, leading the p-MB acid to be at an angle to the surface. The strong band at 1587  $\text{cm}^{-1}$  is due to vibrations of the aromatic ring, if the molecule were not perpendicular

to the surface this band would be much weaker [29]. The absence of a band at  $1417\text{ cm}^{-1}$  representative of the  $\nu_s(\text{COO}^-)$  mode, shows that the carboxylic acid is not bonding to the surface. No strong bands are observed at  $1318$  and  $1710\text{ cm}^{-1}$  for the COOH vibrational modes, suggesting that most of the p-MB acid present is deprotonated. Finally the absence of strong broad bands at  $2580$  and  $916\text{ cm}^{-1}$  shows no  $\nu(\text{S-H})$  or  $\delta(\text{S-H})$  are present indicating that the molecule is indeed bonding to the gold surface through the sulphur moiety. In contrast to the analogous Ag-p-MB system, no evidence for the involvement of the carboxylic acid is observed. This can be accounted for by the higher binding affinity of Au-S than Ag-S allowing it to out compete the carboxylic acid bonding.

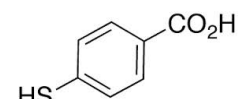
### 4.2.3 Coating of Thiol Stabilised Gold Nanoparticles

#### 4.2.3.1 Coating of Nanoparticles via Exposure to Ammonium Carbonate

Thiol stabilised gold nanoparticles ( $5\text{ cm}^3$ ) were added to a solution of calcium chloride ( $10\text{ mmol}$ ,  $10\text{ cm}^3$ ) before being exposed to ammonium carbonate in a closed desiccator ( $120\text{ min}$ ). An adhesive carbon SEM slide was placed in the bottom of the reaction vessel to collect precipitates. Raman analysis was attempted on multiple SEM slides and direct deposition of the sample solution however no signal was seen for any analyte, this was attributed to the weak Raman signal, small size of the particles and low concentrations.

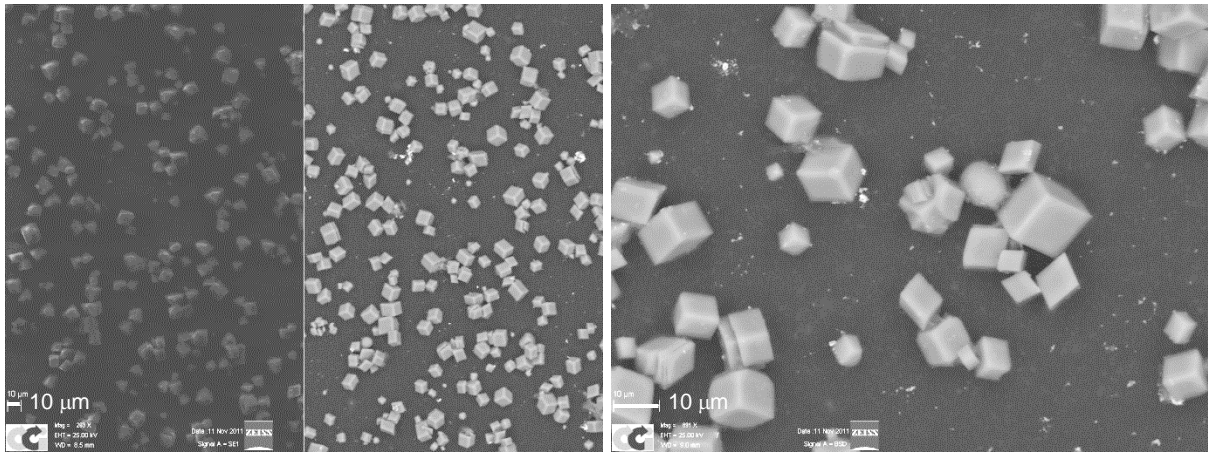
##### 4.2.3.1.1 *P-mercaptobenzoic acid stabilised gold nanoparticles*

Figure 4-34 shows that when compared to that of a one hr exposure using citrate (Figure 4-23), far fewer nanoparticles are observed on the slide, showing that the nanoparticles have not destabilised due to the addition of calcium chloride. The p-



**Figure 4-33**  
P-mercaptobenzoic acid

mercaptobenzoic (pMB) acid stabilised nanoparticles have remained more stable, seen here by only a minor presence in the analysed sample, further the particles which can be seen are present in much smaller clusters further supporting the greater stability as they have not aggregated to the same degree. Some calcium carbonate has precipitated in the form of calcite, inferred by the characteristic rhombohedra. The calcite particles are of a great variety in size and some more interesting shapes are observed. It is observed here that multifaceted, likely calcite rhombohedra are observed. The presence of the thiol stabilised nanoparticles seems to encourage the deposition of these unusual calcite particles. It can be seen from the higher magnification BSD image (Figure 4-34 b)) that bright spots due to gold nanoparticles are observed on the multifaceted deposits. A noticeable variation in the brightness of the nanoparticle spots is attributed to some of them being subsurface, as the BSD detector has a penetration depth of about a micron, this would be consistent with the nanoparticles causing the multifaceted nucleation.



**Figure 4-34** SEM images of pMB acid samples after 2 hrs exposure to ammonium carbonate a) low magnification; left SE1, right BSD and b) high magnification BSD image

#### 4.2.3.1.2 *P-mercaptophenol stabilised gold nanoparticles*

Similarly p-mercaptophenol (pMP) stabilised particles facilitate the deposition of multifaceted calcite particles (Figure 4-36). Again, although it was seen that nanoparticles deposited onto the analysis sides for all samples, there were far fewer and in smaller clusters than the comparable citrate stabilised particle coatings. Many multifaceted particles are observed (Figure 4-36), both larger and smaller particles of interesting shape are observed with further evidence of the inclusion of the gold nanoparticles in the deposits, seen as the brighter areas in the BSD detector images.

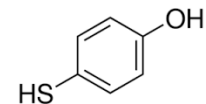


**Figure 4-35**  
P-mercaptophenol

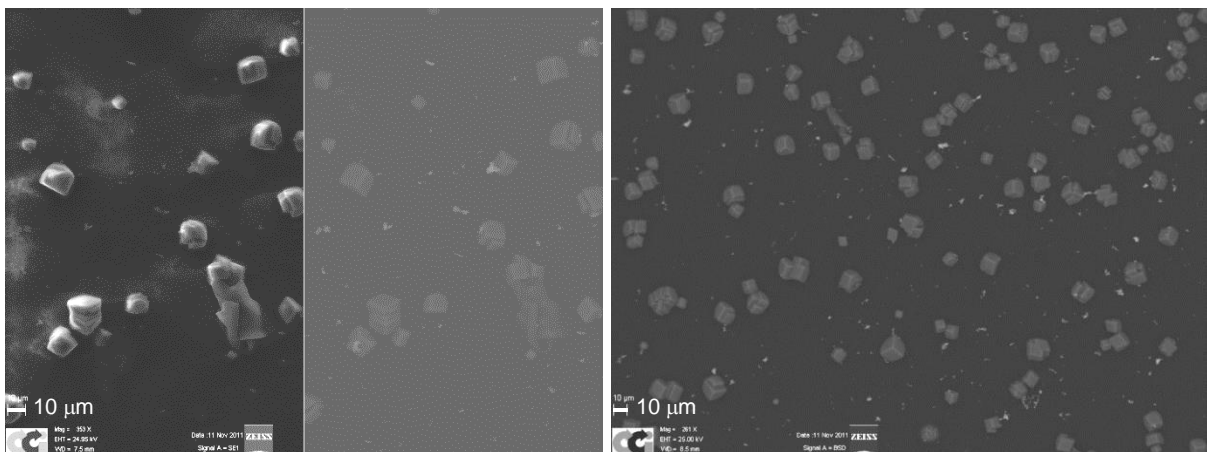


**Figure 4-36** SEM images of pMP samples after 2 hrs exposure to ammonium carbonate a) high magnification left SE1, right BSD and b) low magnification BSD image

#### 4.2.3.1.3 P-mercaptophenylboronic acid stabilised gold nanoparticles

P-mercaptophenylboronic (pMPB) acid stabilised nanoparticles have facilitated the nucleation of interesting morphologies of calcite (Figure 4-38). The number and degree of multifaceted particles was very high with pMPB acid, many nanoparticles can be observed in the BSD images included in the subsurface structure of the particles.

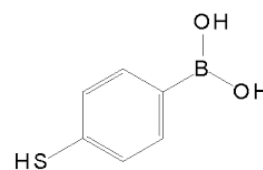


**Figure 4-37**  
p-mercaptophenylboronic

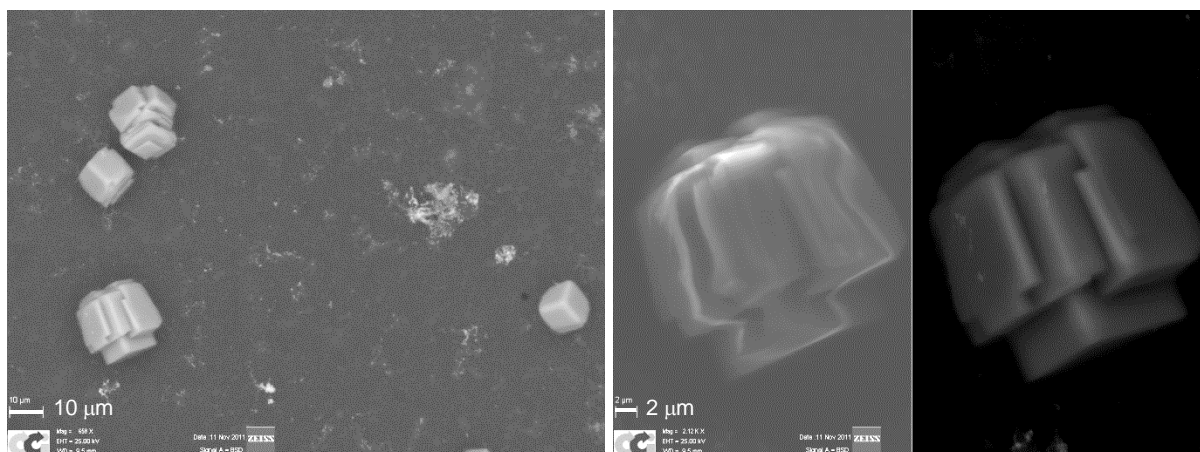


**Figure 4-38** SEM images of pMPB acid samples after exposure to ammonium carbonate a) low magnification BSD and b) high magnification left SE1, right BSD image

These images show great potential, with many multinucleated particles of varying size, Figure 4-39 b) shows a very small particle with numerous nanoparticles seeds within. The presence of small multinucleated particles after a 2 hr exposure time, highlights the stability of the nanoparticles in solution upon addition of calcium chloride. The nanoparticles are still stable in solution after this time and able to continue to nucleate and grow new calcium carbonate particles.

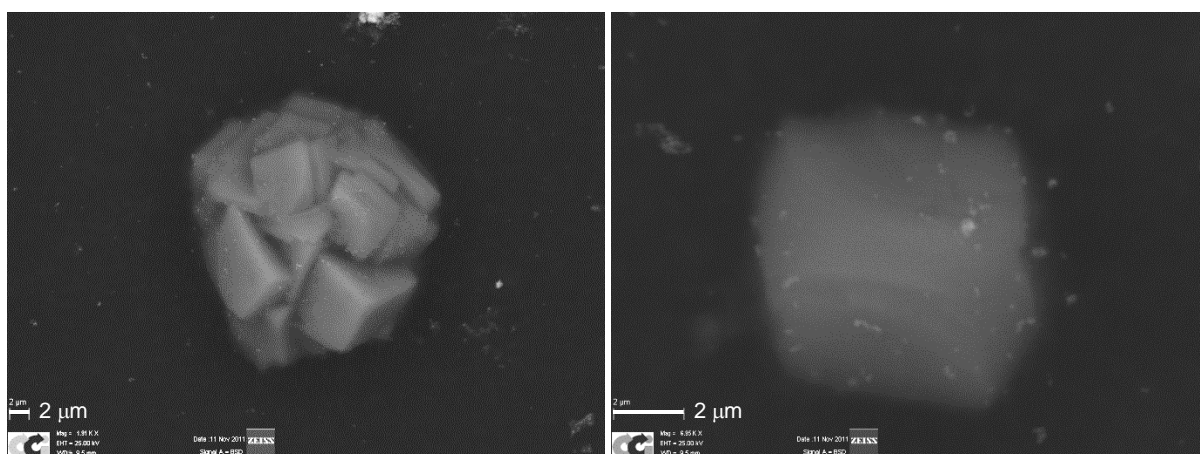


**Figure 4-39** SEM BSD images of pMPB acid samples after 2 hrs exposure to ammonium carbonate a) large multinucleated particle and b) small multinucleated particle

#### 4.2.3.1.4 Mercaptosuccinic acid stabilised gold nanoparticles

Mercaptosuccinic (MS) acid also facilitated the nucleation of interesting morphologies of what is thought to be calcite. MS acid appears to facilitate more spherical calcium carbonate particles (Figure 4-41), whereas all the previous thiols have led to more cubic multifaceted particles. However MS acid does not appear to be as stable in solution upon addition of the calcium chloride, evident by the higher concentration of aggregated and precipitated nanoparticles present on the SEM slide. This was echoed during nanoparticle exchange reactions with this stabilising agent. It was often observed that the nanoparticles had not formed and agglomeration and precipitation had occurred.

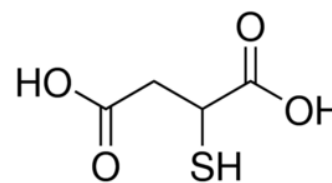


**Figure 4-40**  
Mercaptosuccinic acid

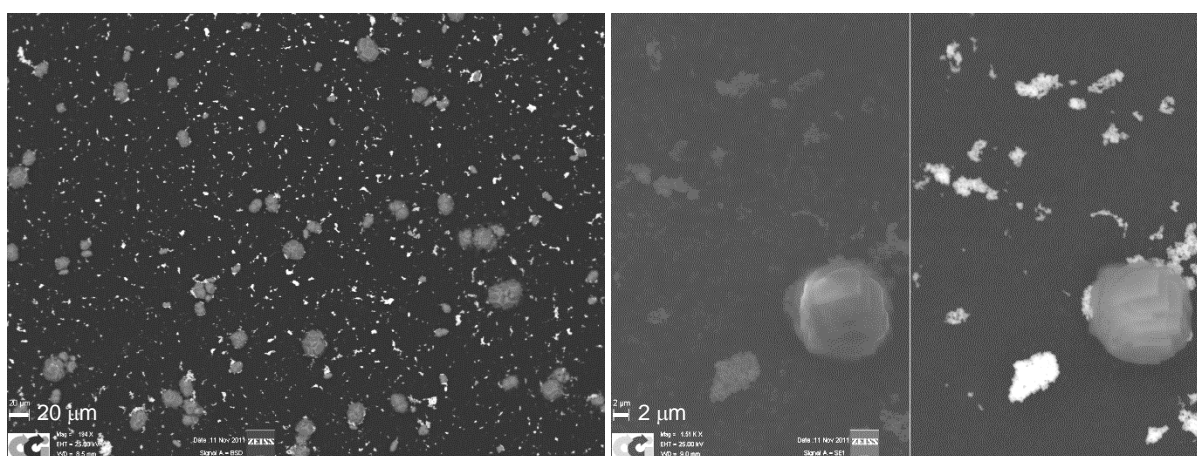


**Figure 4-41** SEM images of MS acid samples after 2 hrs exposure to ammonium carbonate a) low magnification BSD and b) high magnification left SE1, right BSD

It was clear from the set of experiments conducted that the linear thiols not only stabilise the gold colloid more strongly than citrate, they also facilitate the directed nucleation and growth of calcium carbonate. The linear thiols showed great stability with little bulk deposition of colloid on the SEM slides, further the presence of either hydroxyl or carboxylic acid moieties lead to nucleation and growth of unusual morphologies of calcium carbonate. The MS acid being the only non-aromatic linear thiol was expected to be a weaker stabilising agent, although it still showed great ability for the inclusion in nucleation and growth of interesting morphologies of calcium carbonate with its more unique ability to form more spherical deposits.

Thiol stabilised nanoparticles clearly influence the growth of calcium carbonate and hence are likely candidates for successful core-shell synthesis.

#### 4.2.3.2 Investigation of the Effect of Ca Concentration Variation in the Presence of pMPB Acid Stabilised Au Nanoparticles

The ability to control the polymorph of calcium carbonate by altering the Ca/CO<sub>3</sub> ratio was investigated. The amount of ammonium carbonate used during coating attempts was always in excess. The concentration of calcium chloride was varied systematically from 1 to 10 mmol in order to explore its effect on the polymorphism of the resulting carbonate. It has been reported previously that lower calcium concentrations would lead to the deposition of vaterite rather than calcite [6, 10, 13]. Due to the great colloidal stability and the presence of the highest number of multifaceted particles pMPB acid was used for the investigation into the effect of calcium concentration.

##### 4.2.3.2.1 Gold nanoparticles (5 cm<sup>3</sup>) added to calcium chloride (10 cm<sup>3</sup>, 1 mmol)

###### 4.2.3.2.1.1 Ammonium carbonate exposure: 1 hr

After exposure to ammonium carbonate for 1 hr a few small spheres of calcium carbonate were observed, it was assumed at the time that these were of vaterite due to the spherical morphology (Figure 4-42) [10], however simple calcium carbonate hydrates can also form spherules such as those observed here [40]. All of the particles observed in these samples were of similar size (2-3 μm) and had a very high density of nanoparticles, both adhered to the surface and present in the subsurface region, indicated by the presence of bright areas and less bright areas respectively. The number of nanoparticles present on these particles far exceeded the number present over the rest of the SEM slide, this supports the notion that these particles have been preferentially coated rather than simply bulk deposition of the nanoparticles over the whole sample area.

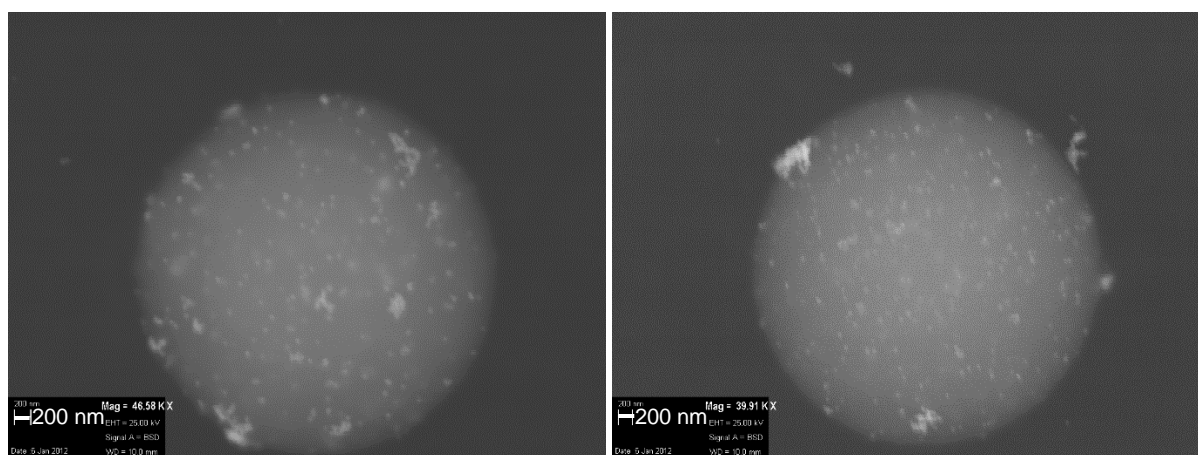


**Figure 4-42** SEM images of 1 mmol samples exposed for 1 hr to ammonium carbonate

Elemental analysis of the spheres (Figure 4-43 a)) reveals that they are composed largely of calcium and oxygen, with a significant amount of gold also present, as would be expected for a calcium carbonate sphere coated with gold nanoparticles. (The strong carbon signal is due to the glassy carbon support).

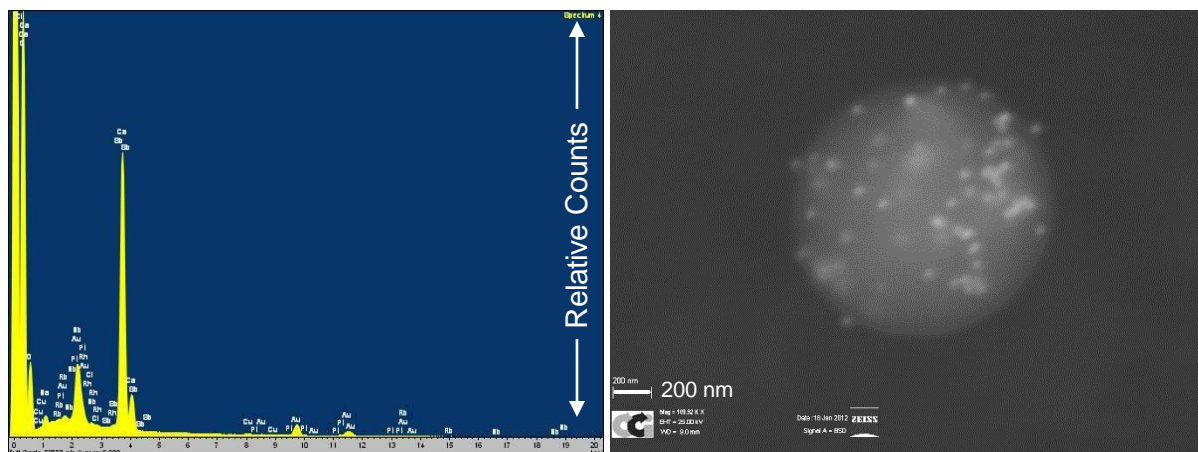


**Figure 4-43** a) EDX spectrum of a spherule and b) example of small spherules observed

#### 4.2.3.2.1.2 Ammonium carbonate exposure: 3 hrs

Exposure to the ammonium carbonate for three hrs results in more small spherules with diameters ranging from  $>1 - 3$  microns (Figure 4-44 a)), Elemental analysis supports the formation of calcium carbonate with Ca, O and Au appearing in the data (Figure 4-45). All the spheres of all sizes have a higher density of nanoparticles over the surface than the background, supporting the preference for nanoparticle inclusion on and in these calcium carbonate deposits.

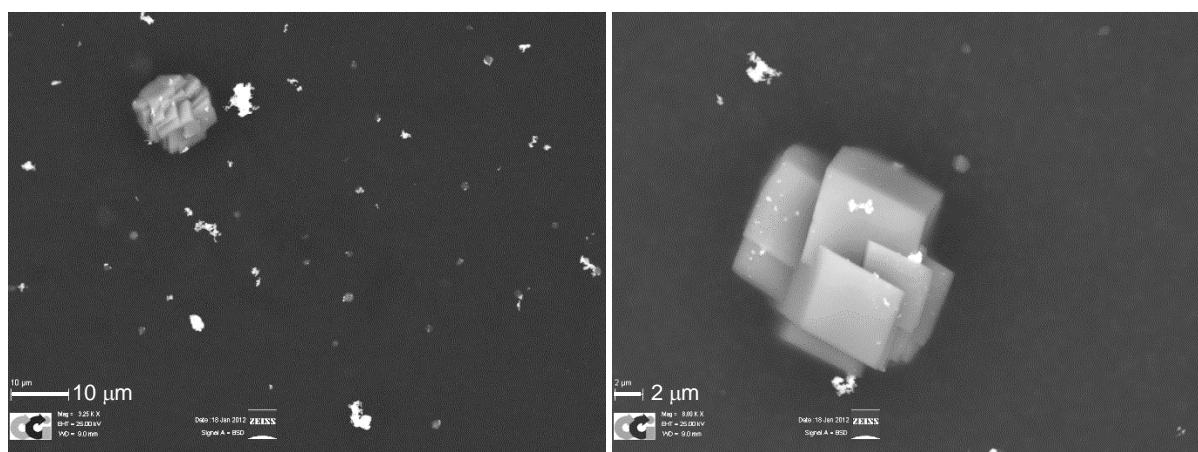


**Figure 4-44** SEM BSD images of samples after 3 hrs exposure to ammonium carbonate a) low magnification and b) high magnification

As well as many small spherules of calcium carbonate a number of larger ( $\sim 10 \mu\text{m}$ ) multinucleated particles are observed (Figure 4-44). These larger deposits appear to have

nanoparticles both on the surface and subsurface. Furthermore, on the right hand side of the deposit observed in Figure 4-44 b) a hemisphere is present on the surface of the multinucleated calcite particle. This could point to the formation of spherules prior to the formation of the multinucleated particles.

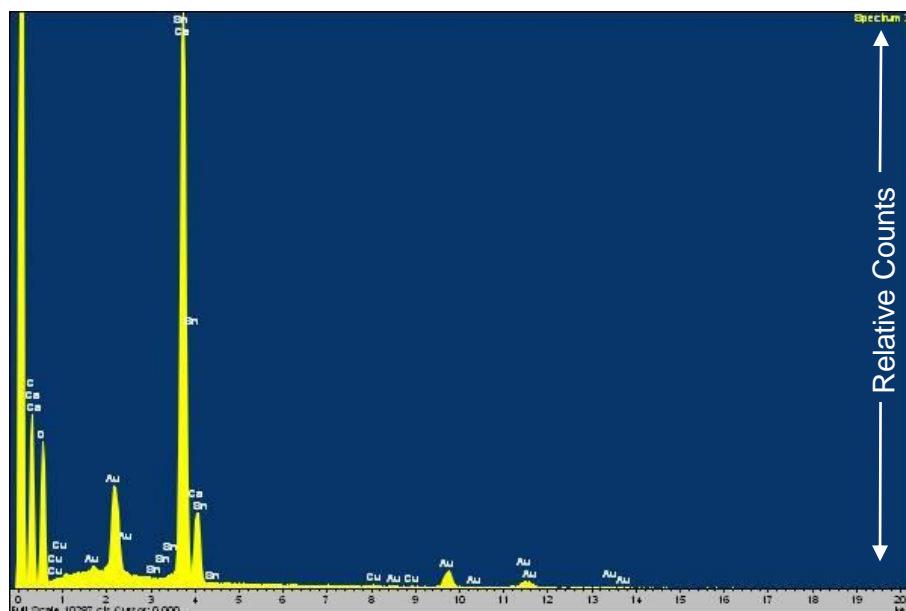


**Figure 4-45** EDX spectrum of a 1 mmol sample after 3 hrs exposure to ammonium carbonate

#### 4.2.3.2.2 Gold nanoparticles ( $5 \text{ cm}^3$ ) added to calcium chloride ( $10 \text{ cm}^3$ , 2 mmol)

##### 4.2.3.2.2.1 Ammonium carbonate exposure: 1 hr

For samples of a slightly higher concentration of 2 mmol, calcite particles are observed after one hr exposure to ammonium carbonate. Spherules are again observed, whether they are of vaterite or a calcium carbonate hydrate is unclear, however the preference for nanoparticles to adhere to these particles is again evident. Figure 4-46 b) clearly presents a spherule and a calcite rhombohedra, from this image it is clear that there are more nanoparticles adhered to the surface of the spherule than the calcite particle or the background. Whether the nanoparticles stabilise the formation of these particles or are attracted to the surface post growth is not clear, but they are observed on the surface even when particles are very small <1 micron (Figure 4-43 b) & 4-47a)) which would point to them being integrated into the particles during growth and would point to the nanoparticles stabilising the growth of these particles.

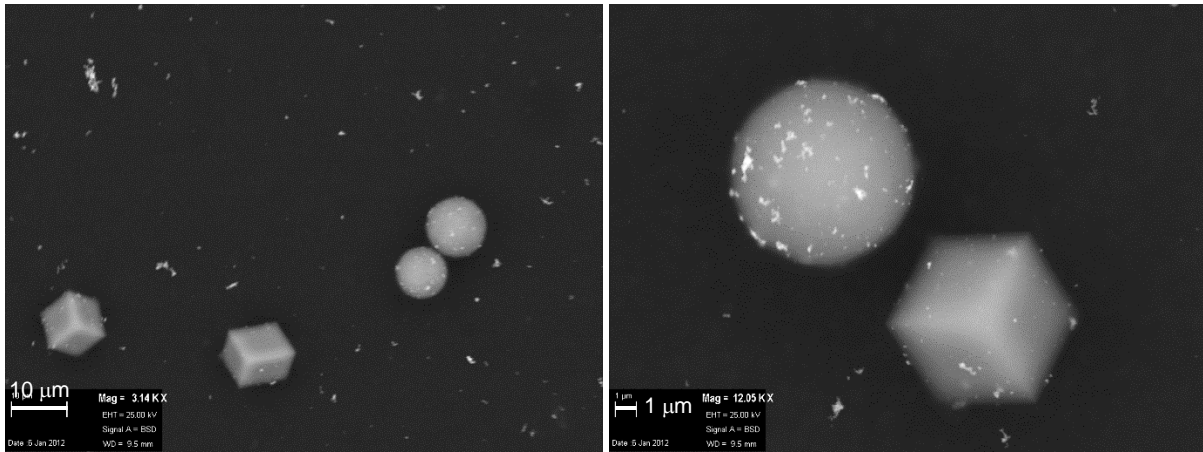


**Figure 4-46** SEM BSD images of 2 mmol samples exposed for 1 hr to ammonium carbonate

Elemental analysis of a single spherule highlights the presence of Ca, O and Au supporting the formation of calcium carbonate with gold nanoparticles present (Figure 4-47 b)).

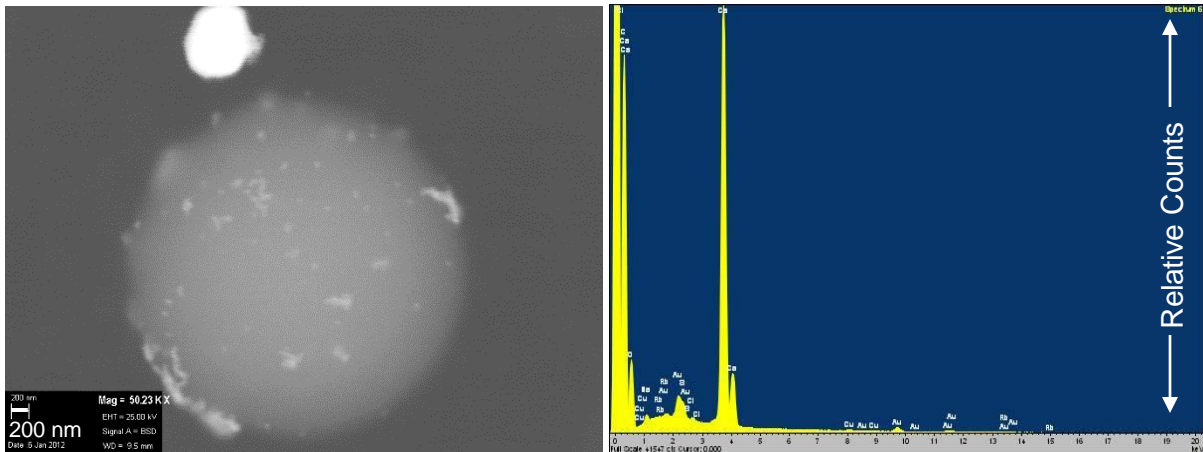


**Figure 4-47** a) SEM BSD image of spherule and b) EDX spectrum of spherule

#### 4.2.3.2.2.2 Ammonium carbonate exposure: 2 hrs

As in the case of the lower calcium concentration, the greater the duration of exposure to ammonium carbonate the larger the extent of further growth of spherules. A small number of calcite rhombohedra are also observed under these conditions but, the prevalence of nanoparticles on these deposits was minimal (Figure 4-48 a)). Elemental analysis has shown evidence of Ca, O and Au (Figure 4-48 b)).

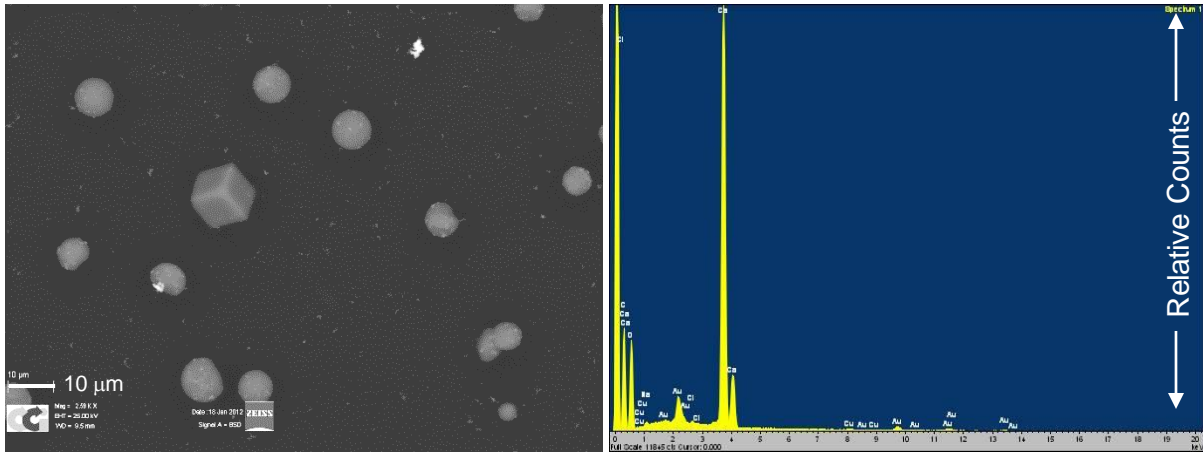


**Figure 4-48** a) SEM BSD image of a 2 mmol sample exposed to ammonium carbonate for 2 hrs and b) EDX spectrum of a spherule

#### 4.2.3.2.2.3 Ammonium carbonate exposure: 3 hrs

Increasing the exposure time further leads to a higher density of nanoparticle covered spherules.

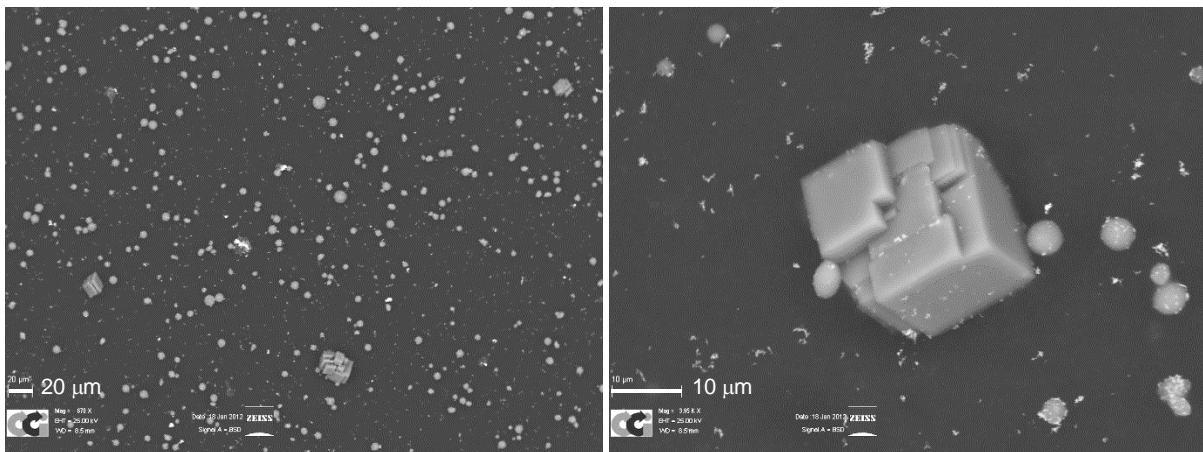
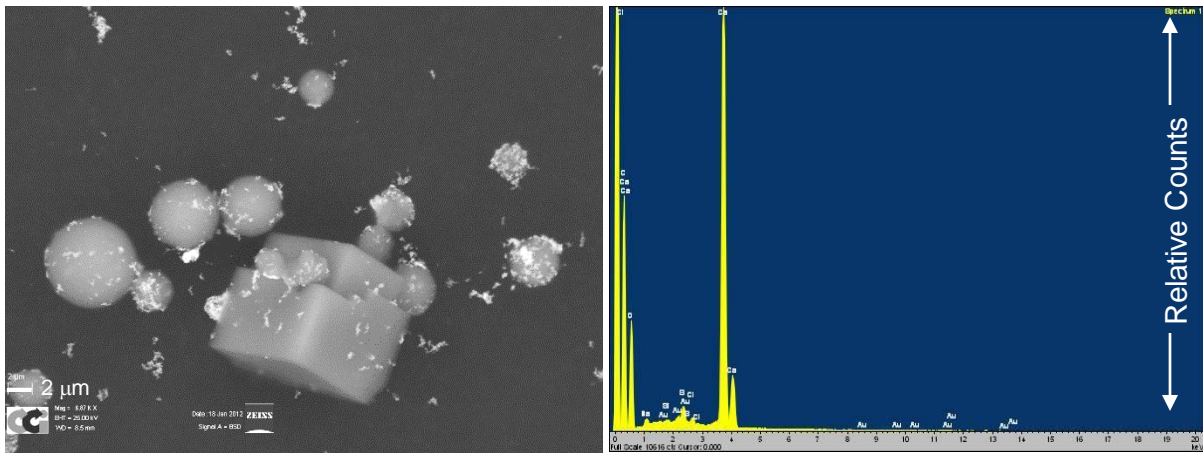


**Figure 4-49** SEM BSD images of samples exposed to ammonium carbonate for 3 hrs, a) low magnification and b) high magnification

As well as a high density of small spherules, a small number of ~1 micron sized calcite rhombohedra are also observed (Figure 4-49 a)). More interestingly a small number of large 10-20 micron sized multinucleated calcite rhombohedra are now observed (Figure 4-49b)). Some of the multinucleated calcite deposits are observed with nanoparticle covered spherules on the surface; some spherules are adhered to the surface while maintaining spherical shape, whereas others are observed as hemispheres on the surface. This points to the nanoparticle covered spherules being involved with the growth of these multinucleated macro sized calcite particles. Elemental analysis of the calcite particle in figure 4-50 a) shows the presence of Ca, O and Au (Figure 4-50 b)), the Au signal is lower as the analysis was performed on a spot on the surface where no Au was visible. The presence of Au in the spectrum either highlights

subsurface nanoparticles, or surface nanoparticles from the surrounding sample as the focal point of this EDX spectrometer is about a 1 micron square.



Again it is observed that spherules present have a much higher concentration of gold nanoparticles than the calcite rhombohedra present or the back ground of samples (Figure 4-52 a)). Elemental analysis confirmed the presence of Ca, O and Au (Figure 4-52), analysis was obtained from the centre of the spherule in Figure 4-52 a).

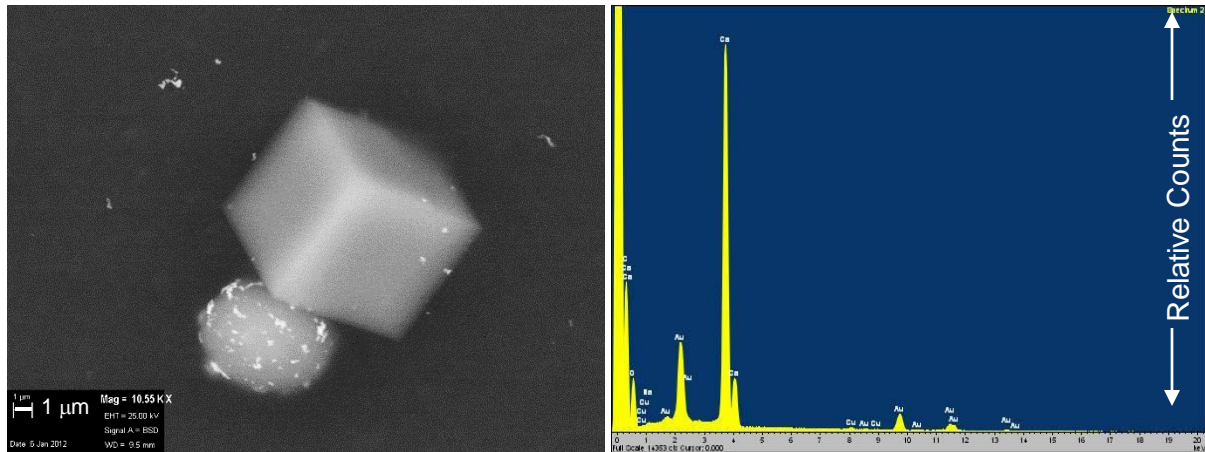


**Figure 4-52** a) SEM BSD image of a 3 mmol sample exposed to ammonium carbonate 1 hrs and b) EDX spectrum of spherule

#### 4.2.3.2.3.2 Ammonium carbonate exposure: 2 hrs

Exposure to ammonium carbonate for two hrs increases the size of the calcite rhombohedra but there is no change in the relative concentrations of gold nanoparticles on the different shaped carbonate particles with a continued presence of nanoparticle covered spherules. Elemental analysis of the calcite rhombohedra shows the presence of Ca and O, with no presence of Au. The analysis was performed on the surface of a large calcite particle, the lack of any Au shows that it is likely there are no nanoparticles within these well-formed calcite rhombohedra.

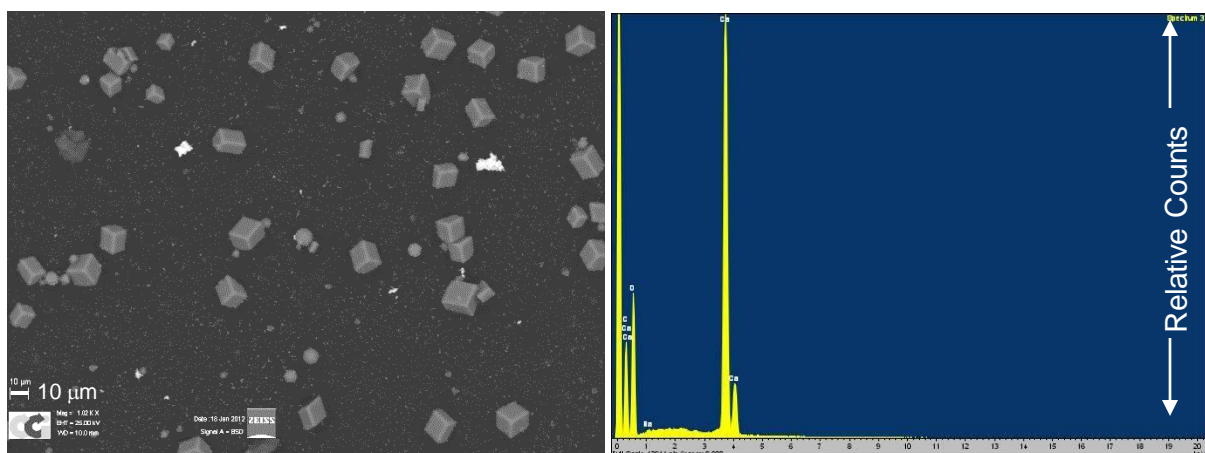


**Figure 4-53** a) SEM BSD image of calcite dominant deposition and b) EDX spectrum of calcite rhombohedra

#### 4.2.3.2.3.3 Ammonium carbonate exposure: 3 hrs

After three hrs exposure to ammonium carbonate, Figure 4-53 shows that the dominant morphology of the carbonate particles has switched to the spheres characteristic of vaterite over the calcite rhombohedra.

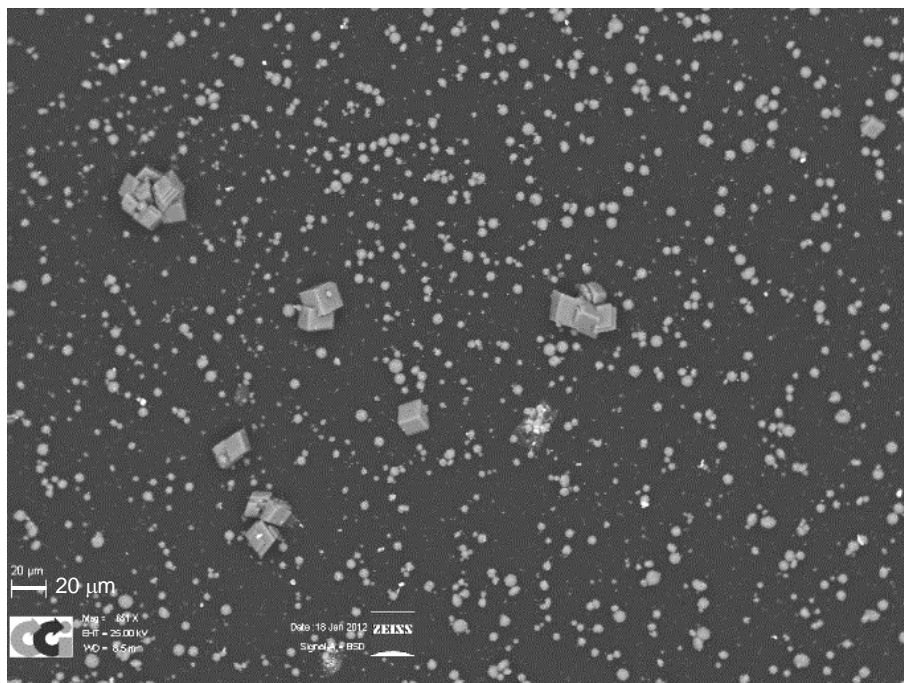


**Figure 4-53** SEM BSD image highlighting the large number of spherules and presence of large multinucleated calcite particles

A number of the large multinucleated calcite particles are also observed. Spherules can be seen on these particles and as hemispheres on the surface again pointing to this as the likely growth mechanism for the multinucleated calcite particles. Elemental analysis from the surface of one of the multinucleated deposits shows Ca, O and a small amount of Au present (Figure 4-54 b)). It is interesting to note that the perfectly formed calcite rhombohedra are much less often seen with nanoparticles either on or appearing subsurface. This further supports the idea of the vaterite spherules being involved in the growth of the multinucleated particles due to the presence of a higher number of nanoparticles. If these larger multinucleated particles were simply disordered calcite rhombohedra it would be expected that the number of nanoparticles should be similar to that seen on the small calcite rhombohedra, whereas they are more akin to the concentration seen on the vaterite spherules, suggesting these spherical particles are acting as the seed for these interesting particles.

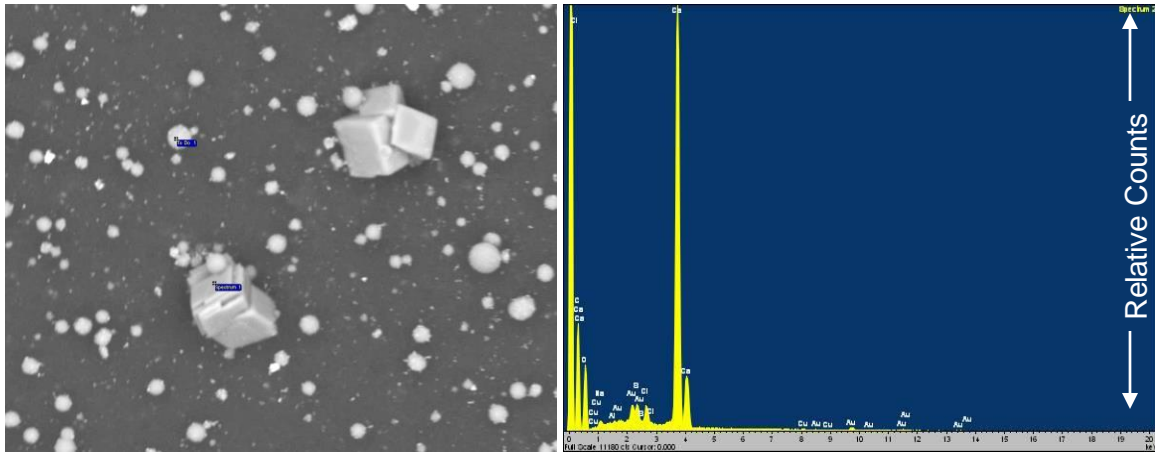


**Figure 4-54** a) SEM BSD image and b) EDX spectrum of multinucleated particle

#### 4.2.3.2.4 Gold nanoparticles (5 cm<sup>3</sup>) added to calcium chloride (10 cm<sup>3</sup>, 4 mmol)

##### 4.2.3.2.4.1 Ammonium carbonate exposure: 1 hr

At 4 mmol calcite is now the dominant form observed (Figure 4-55), as expected from the continued increase in calcium concentration. Vaterite spherules are still present on the surface but at much lower concentrations than before.

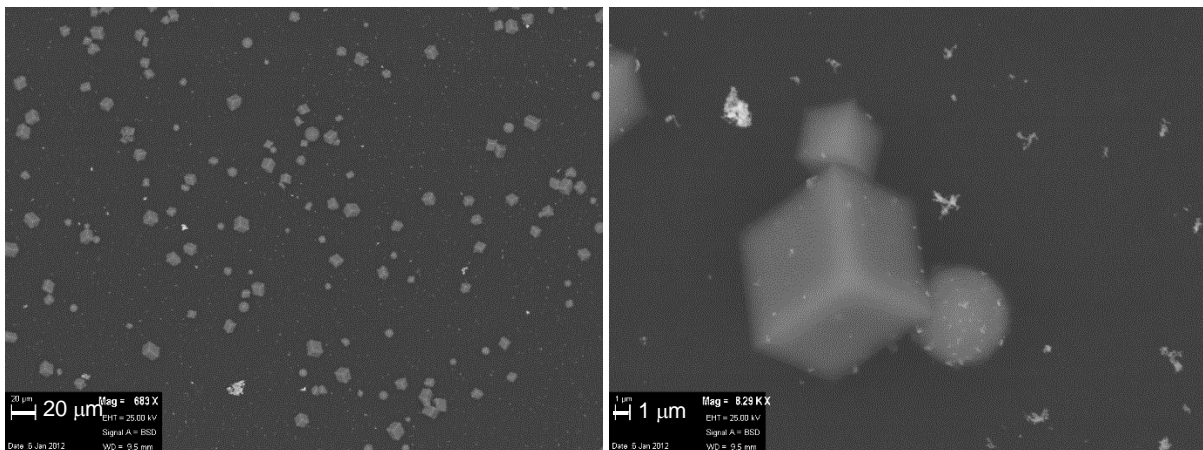


**Figure 4-55** SEM BSD image showing calcite dominant deposition

It is still observed that the vaterite particles present have a higher concentration of gold nanoparticles associated with them, although some rhombohedra of calcite can also be seen with gold nanoparticles, this may be due to the lack of available vaterite for the gold nanoparticles to adhere to, it is also observed that a slightly higher amount of nanoparticles have precipitated from the bulk colloid and appear over the surface. It is likely that the continued increase in calcium chloride concentration may be destabilising the nanoparticles.

#### 4.2.3.2.4.2 Ammonium carbonate exposure: 2 hrs

Exposure to ammonium carbonate for 2 hrs shows calcite rhombohedra as the main deposits observed. There are also more aggregated nanoparticles precipitated from the bulk solution. The few vaterite spherules which exist have a higher concentration of gold nanoparticles on the surface compared to the calcite rhombohedra or the back ground (Figure 4-56). Some interesting polymorphism is observed, rather than discrete particles as previously observed, now calcite rhombohedra appear to conjugate in an unusual manner, Figure 4-56 b) highlights an example of such particles. Close inspection of these deposits show that the calcite rhombohedra appear to be linked together with another phase of calcium carbonate, but the exact polymorph cannot be determined from the present data.

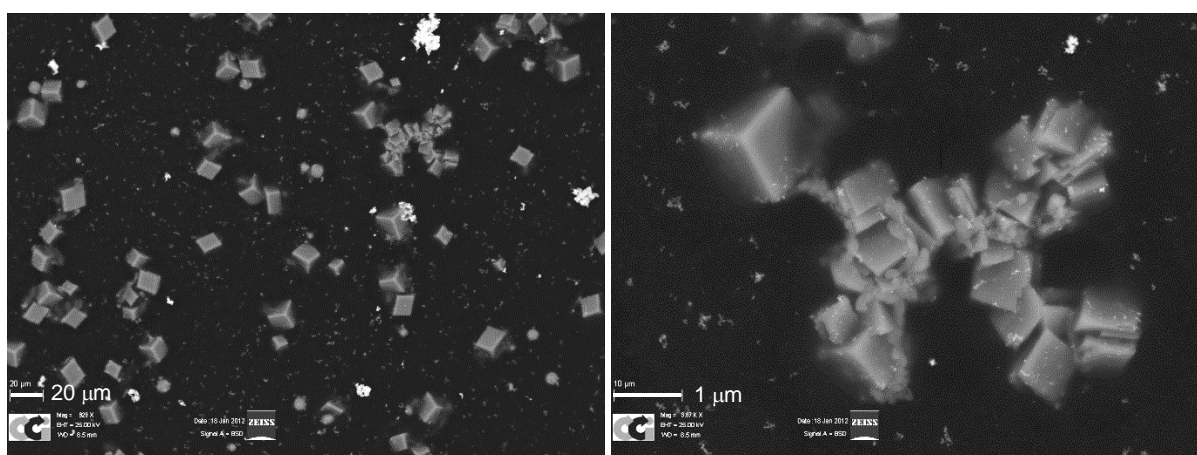


Figure 4-56 SEM BSD images of calcite dominant deposits with interesting polymorphism

Elemental analysis shows evidence of Ca, O and Au as expected. Na and Cl are also evident (Figure 4-57) arising from the calcium chloride used as the calcium source and the NaOH used to control the pH of the colloid to ensure the acidic thiol remained soluble.

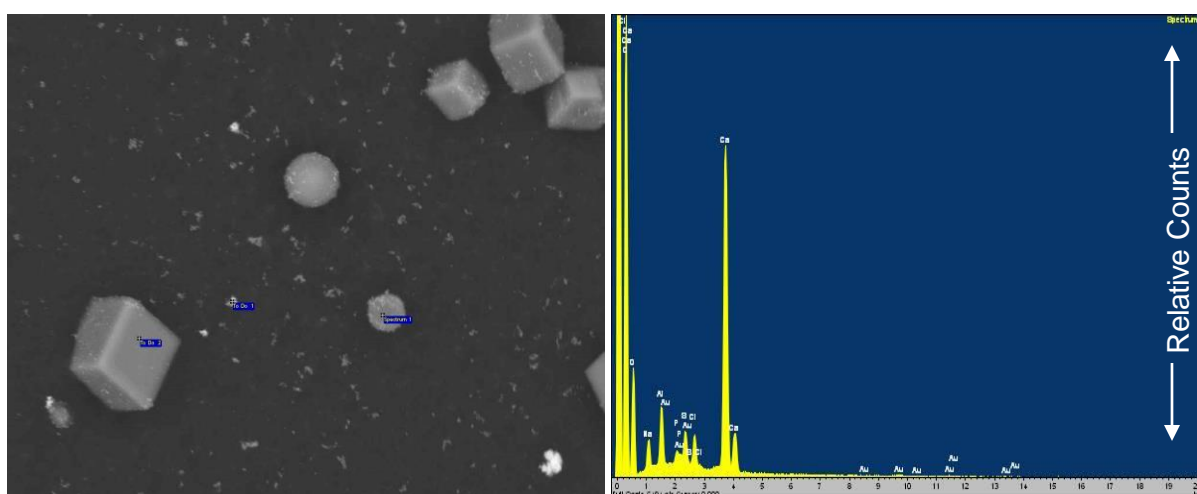
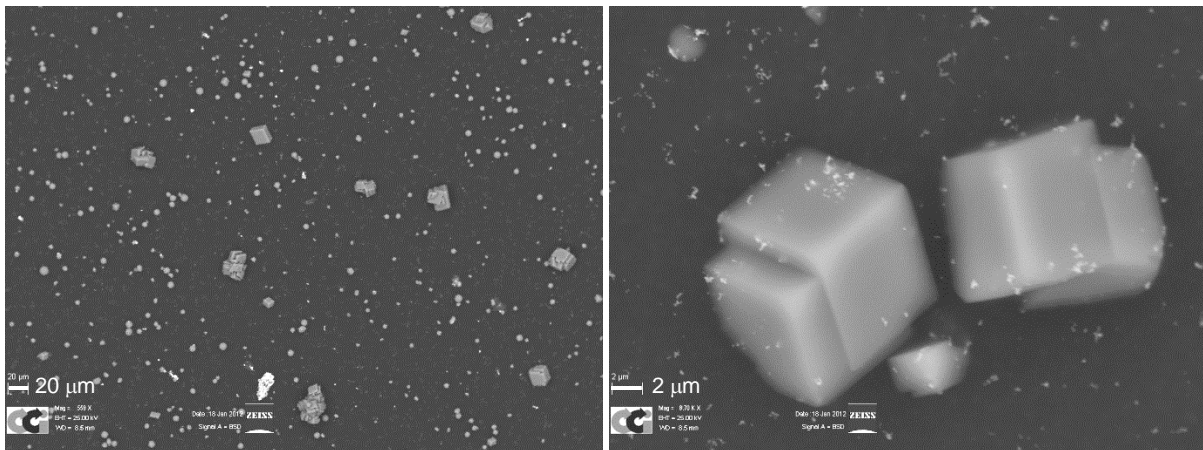


Figure 4-57 a) SEM BSD image of calcite rhombohedra, blue boxes denote where spectra were obtained and b) EDX spectrum of calcite rhombohedra

#### 4.2.3.2.4.3 Ammonium carbonate exposure: 3 hrs

After three hrs exposure at this concentration of calcium chloride vaterite spherules were again the more dominant feature. The high number of vaterite spherules all appear to have significant coverage of gold nanoparticles, further there are numerous multinucleated calcite particles with a high number of nanoparticles adhered to the surface, this would again point to the vaterite spherules being the seed for the growth of these calcite morphologies.



**Figure 4-58** SEM BSD image a) low magnification and b) high magnification of multinucleated calcite

Elemental analysis shows the presence of Ca, O and Au. Na and Cl are also visible in minor quantities (Figure 4-59 b)) as discussed above.

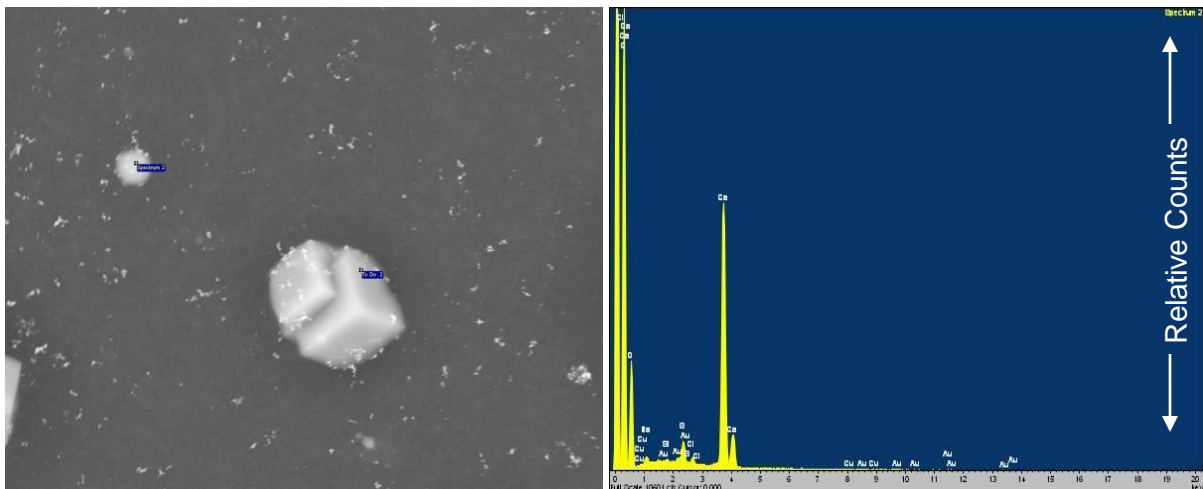


**Figure 4-59** a) SEM BSD image and b) EDX spectrum of multinucleated calcite

#### 4.2.3.2.5 Gold nanoparticles (5 cm<sup>3</sup>) added to calcium chloride (10 cm<sup>3</sup>, 5 mmol)

##### 4.2.3.2.5.1 Ammonium carbonate exposure: 1 hr

At this higher calcium chloride concentration the number of calcite rhombohedra increased and vaterite spherules are now almost non-existent (Figure 4-60). More interestingly some of the vaterite spherules appear to have numerous small rhombohedra on the surface. Figure 4-60 b) shows one example.

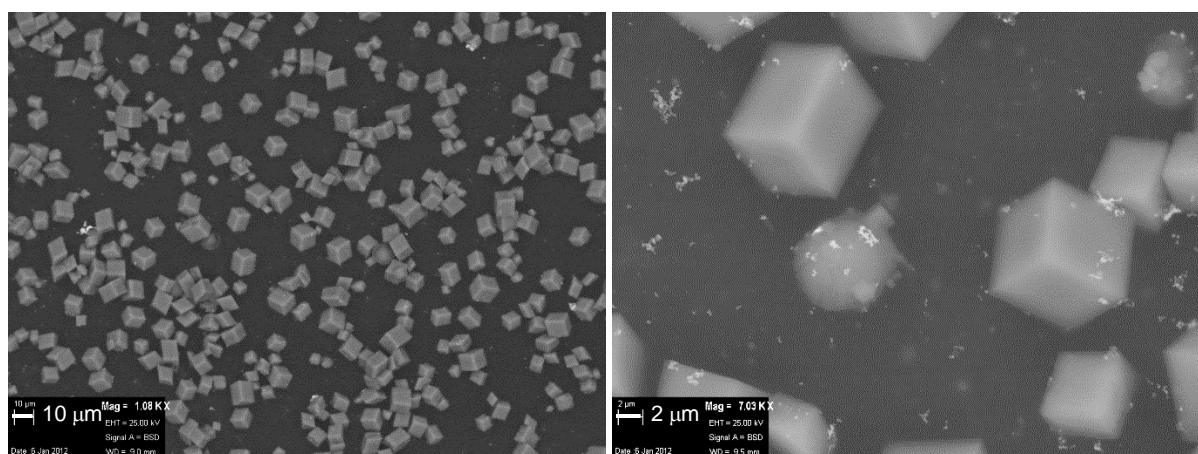


**Figure 4-60** SEM BSD image of samples exposed to ammonium carbonate 1 hr

Elemental analysis of the rhombohedra on the surface of the vaterite spherule in Figure 4-61 a) shows that Ca and O are present but no gold, the latter's absence was expected as the rhombohedra do not appear to have gold nanoparticles on them. Furthermore the absence of Na or Cl rules out NaCl and confirms the assignment of these features to calcium carbonate (Figure 4-61 b)). This example of the growth of calcite rhombohedra on the surface of a vaterite spherule is further evidence that the vaterite spherules are acting as seeds for the growth of the multifaceted calcite particles.

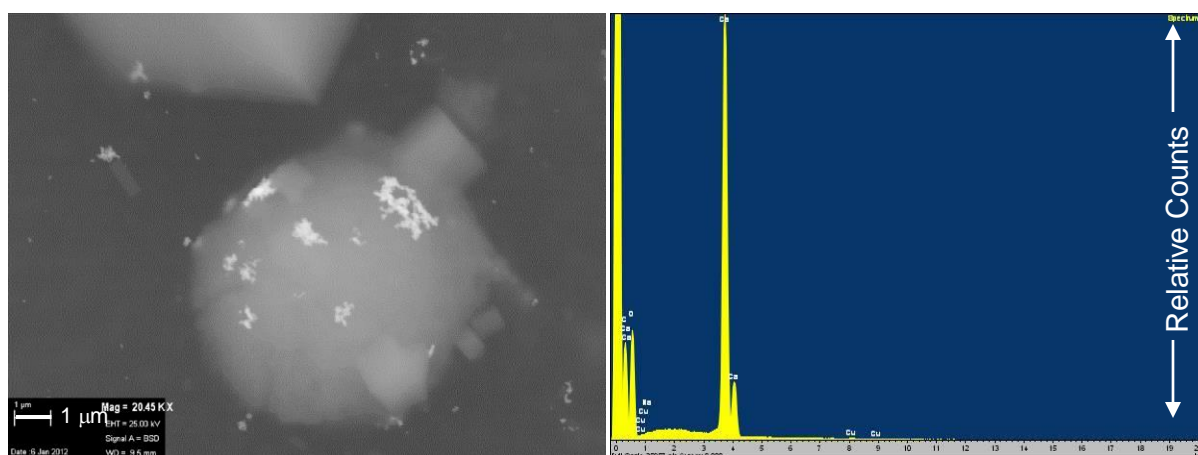


**Figure 4-61** a) SEM BSD image of vaterite spherule and b) EDX spectrum of rhombohedra on surface of vaterite spherule

#### 4.2.3.2.5.2 Ammonium carbonate exposure: 2 hrs

After 2 hr exposures, the number and size of calcite rhombohedra increased further and very few vaterite spherules or multinucleated particles were observed. It is noted that as the number of vaterite spherules decreases so too do the number of multinucleated calcite rhombohedra; further evidence that the gold nanoparticle coated vaterite spherules are responsible for the formation of the multinucleated calcite deposits.

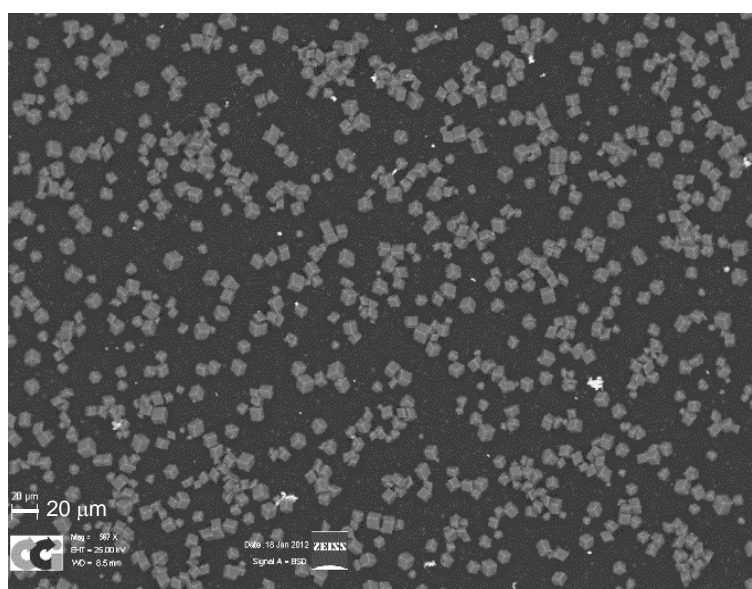


**Figure 4-62** SEM BSD image of calcite dominant precipitate

Elemental analysis was performed in distinct areas, firstly on the surface of simple calcite rhombohedra (Figure 4-63 a)) where the presence of Ca and O was evident with no trace of Au. Secondly on nanoparticle clusters (Figure 4-63 b)), where Au is observed. Trace amount of both Ca and O are observed along with the Au, perhaps this could point to the formation of core-shell particles, however it is also likely that the EDX is picking up these elements from the surrounding sample.

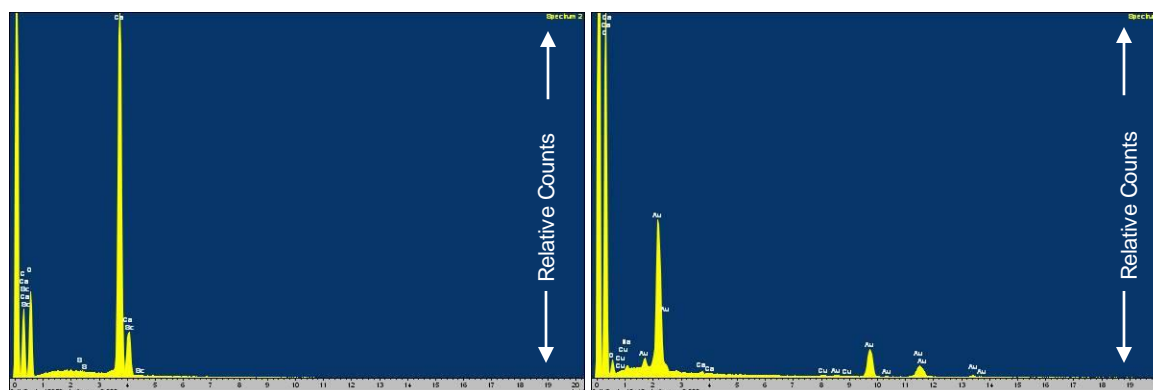


**Figure 4-63** EDX spectrums of a) calcite rhombohedra and b) gold nanoparticle cluster

#### 4.2.3.2.5.3 Ammonium carbonate exposure: 3 hrs

After exposing for 3 hr there exists about an equal mix of vaterite and calcite, this points to the dominance of vaterite after 3 hrs exposure again. Although at this calcium concentration there are more calcite rhombohedra than in the 3 or 4 mmol solutions after 3 hrs, it would be expected that calcite should become more dominant with higher concentrations, but the observed switch after 3 hrs exposure is a very interesting result. The vaterite spherules again have a high concentration of nanoparticles over the surface, however with this high concentration, long exposure time, many of the nanoparticles have aggregated and precipitated from the bulk, making the determination of the preferential coating ambiguous.

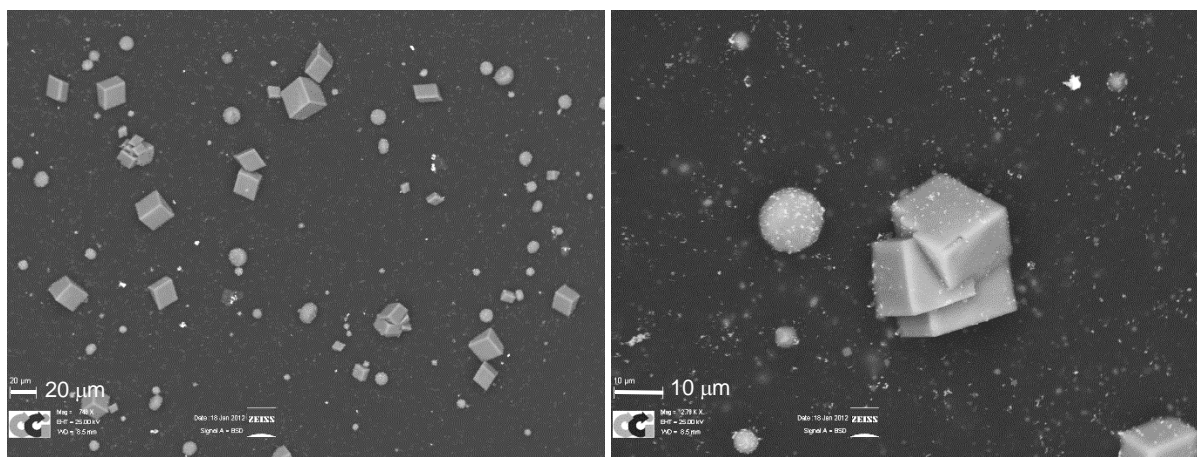


**Figure 4-64** SEM BSD images from 3 hr exposures

#### 4.2.3.2.6 Gold nanoparticles ( $5 \text{ cm}^3$ ) added to calcium chloride ( $10 \text{ cm}^3$ , 6 mmol)

##### 4.2.3.2.6.1 Ammonium carbonate exposure: 1 hr

After one hr exposure the precipitated carbonate is dominated by simple rhombohedra of calcite. Figure 4-65 a) shows an example of a spherule of vaterite with a calcite rhombohedra growing on the surface, further evidence that the vaterite spherules act as seeds for the formation of multinucleated calcite particles. Elemental analysis of the rhombohedra seen in Figure 4-65 a) shows the presence of Ca and O. No Au, Na or Cl are present ruling out the presence of NaCl as the source of this growth.

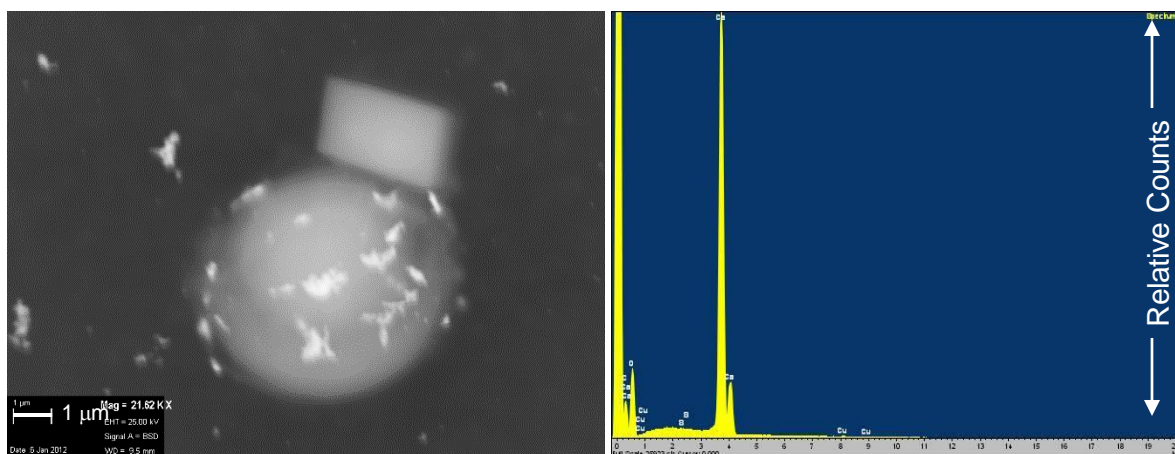


**Figure 4-65** a) SEM BSD image of growing multinucleated particle and b) EDX spectrum of rhombohedra

Due to the high concentration of calcium present, further experiments carried out at 7,8,9 and 10 mmol were only exposed to the ammonium carbonate for 1 hr. In all cases a large number of calcite rhombohedra were observed with very few vaterite spherules present, no multinucleated calcite particles and little deposition of gold nanoparticles.

#### Discussion

It has been shown that as the concentration of calcium chloride increases, essentially changing the  $\text{Ca}/\text{CO}_3$  ratio in favour of calcium, the dominant precipitate changes from vaterite to calcite. This is in accordance to that predicted in the literature [10, 41]. We have also observed the preferential coating of vaterite spherules with gold nanoparticles, these coated particles have been seen to act as seeds for the growth of multifaceted calcite rhombohedra and the continued growth of these interesting calcite polymorphs has also been attributed to the continued inclusion of the nanoparticle coated spherules. It is not known whether the vaterite spherules undergo a phase change to calcite, or whether the calcite rhombohedra are growing on the surface of the vaterite spherules. XRD of these particles would reveal if a mixture of phases or a single phase were present, which would point toward which mechanism for growth was occurring.

It is clear that the thiol stabilised gold nanoparticles are influencing the deposition of calcium carbonate, suggesting that the thiol stabilised nanoparticles are good potential candidates for the successful core-shell synthesis with polymorphism controlled with the variation of the calcium concentration. However, even at the lowest concentration and the shortest times of exposure the observed particles are in the micron range, thus for core-shell synthesis another route may need to be sought for coating which reduces the exposure time.

#### 4.2.3.3 Initial Coating of Thiol Stabilised Particles by the Bubbling Method

The production of core-shell nanoparticles was attempted using the bubbling method [6]. For all of the following experiments p-MPB acid stabilised gold nanoparticles ( $5 \text{ cm}^3$ ) were added to a solution of calcium chloride ( $10 \text{ cm}^3$ ,  $10 \text{ mmol}$ ) and bubbled with high purity  $\text{CO}_2$  for varying lengths of time. SEM analysis was carried out on slides which had been immersed in the solution prior to bubbling.

##### 4.2.3.3.1 Bubbled with high purity $\text{CO}_2$ (5 min)

After bubbling for 5 minutes the sample showed no precipitation of discrete particles of calcium carbonate, however a few clusters of Au-nanoparticles were apparent in the BSD images (Figure 4-66). This finding indicates that no bulk precipitation had yet occurred but some nanoparticles had precipitated from the bulk colloid. This finding could point to the production of core-shell type particles, as the formation of a calcium carbonate shell would likely cause the nanoparticles to become less soluble and make precipitation more likely.

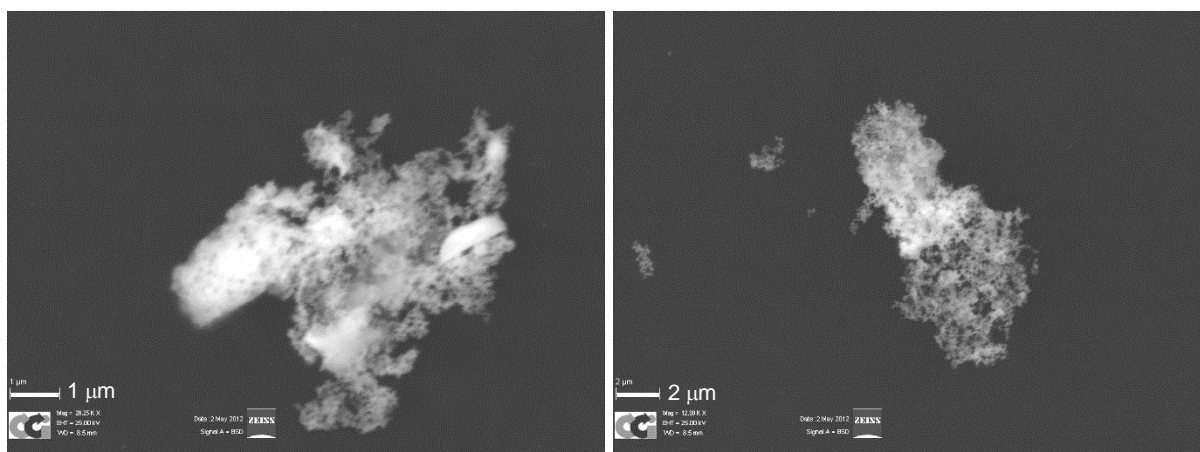


**Figure 4-66** SEM BSD images of observed gold nanoparticle clusters

##### 4.2.3.3.2 Bubbled with high purity $\text{CO}_2$ (30 min)

Similarly after 30 minutes very little precipitate was observed (Figure 4-67), more clusters of nanoparticles were present compared to the 5 minute bubbling samples. A few unidentified deposits were observed, likely contamination during drying and before analysis or some amorphous calcium carbonate phase.

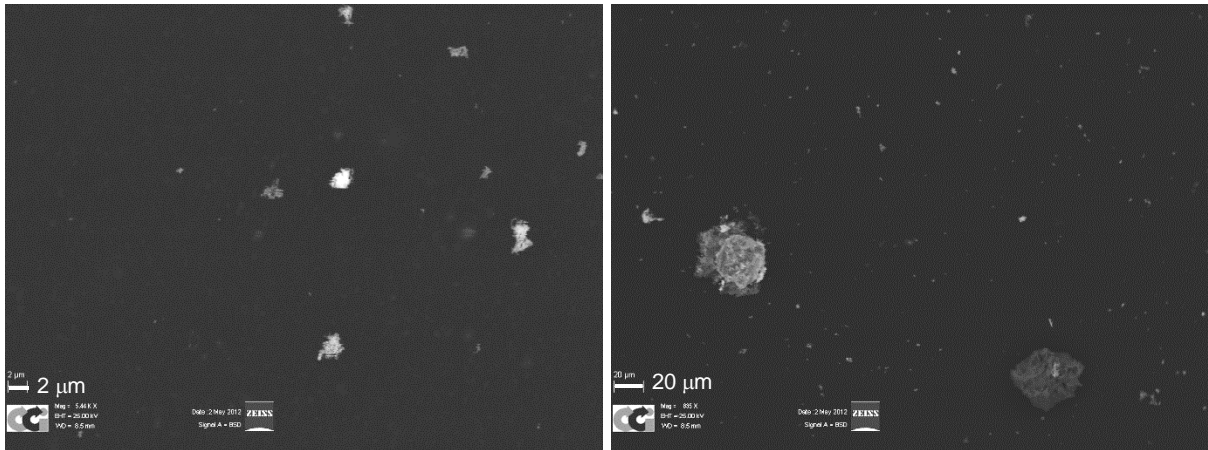


**Figure 4-67** SEM BSD images of observed gold nanoparticle clusters

#### *4.2.3.3.3 Bubbled with high purity CO<sub>2</sub> (60 min)*

After 1 hr some small rhombohedra had precipitated attributed to calcite based on the shape (Figure 4-68). These particles contained gold nanoparticles visible as brighter spots, apparent in the BSD images (Figure 4-68 b)). It was observed that a few small spherules were present in the sample as well as sporadic multinucleated calcite rhombohedra. By this point if core-shell particles were present then they would probably be coated to a greater degree than is desired, however this has highlighted that short bubbling times with CO<sub>2</sub> may yield the sought after core-shell particles.

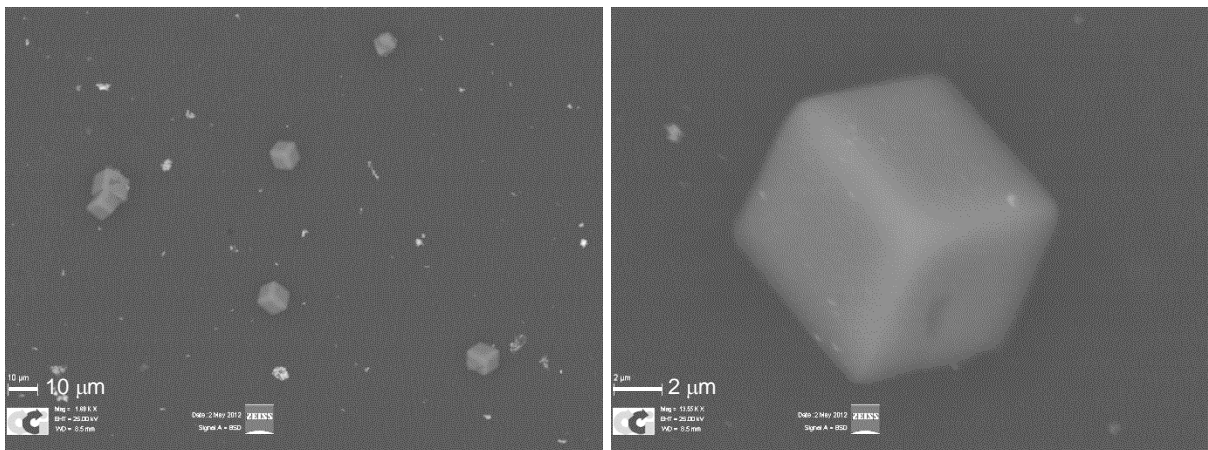


**Figure 4-68** SEM BSD images of gold nanoparticle clusters and small calcite deposits

#### *4.2.3.3.4 Bubbled with high purity CO<sub>2</sub> (150 min)*

After 2.5 hrs more calcite rhombohedra are present over the sample surfaces. Vaterite spherules are also present, however the preference of Au-nanoparticles to adhere to the surface is not seen and instead more precipitated Au-nanoparticles are observed. This may suggest

that the nanoparticles have precipitated due to the presence of a calcium carbonate coating, this would explain why they have precipitated and why they are not seen coating the vaterite particles as extensively as seen previously.

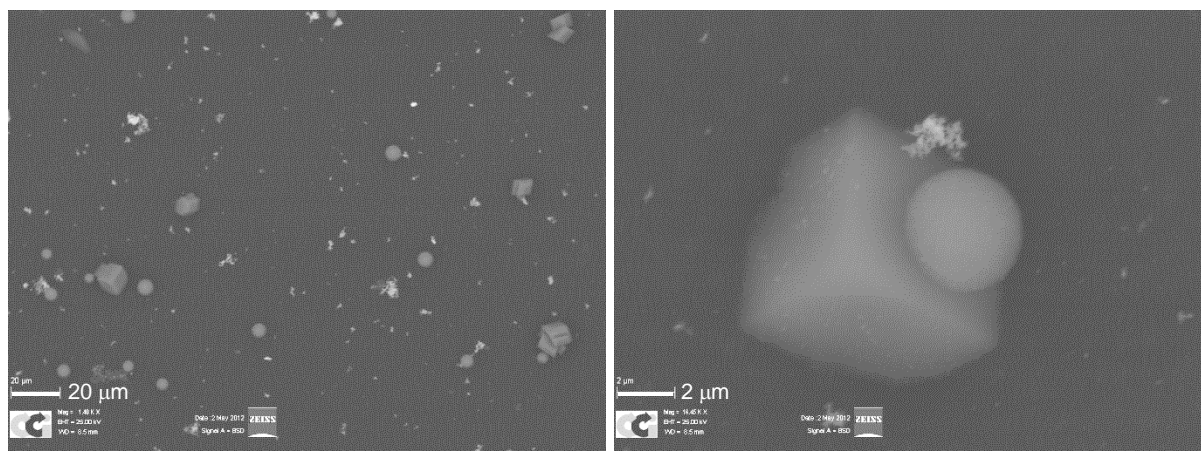


**Figure 4-69** SEM BSD images of precipitate and aggregated nanoparticles

#### 4.2.4 Synthesis of Gold@Carbonate Core Shell Nanoparticles

The combined coating attempts described above have highlighted potential stabilising agents and coating methods. These methods are now used with the aim of generating gold@carbonate core-shell nanoparticles with dimensions suitable for SERS measurements (i.e. Au diameter ~ 50nm).

Gold nanoparticles (5 cm<sup>3</sup>) stabilised with the three thiols (p-MP, p-MB acid and p-MPB acid) were added to calcium chloride solution (10 cm<sup>3</sup>, 10 mmol) and bubbled with high purity CO<sub>2</sub>. The samples were characterised by TEM and Raman spectroscopy. Unlike the SEM analysis this involved pipetting the solutions directly onto a TEM slide and drying.

Results from particle syntheses using the bubbling method of coating show very compelling results; with some variation of behaviour between particles. The left and right images of Figure 4-70 for example show some rather different coatings, the left image shows what appear to be towers or pillars of calcium carbonate attached to the surface of the nanoparticles, it can also be seen that there is some mosaicking of the background which suggests that a very thin film of calcium carbonate has formed on the slide during the evaporation of a droplet of the sample when being applied to the TEM slide for analysis.

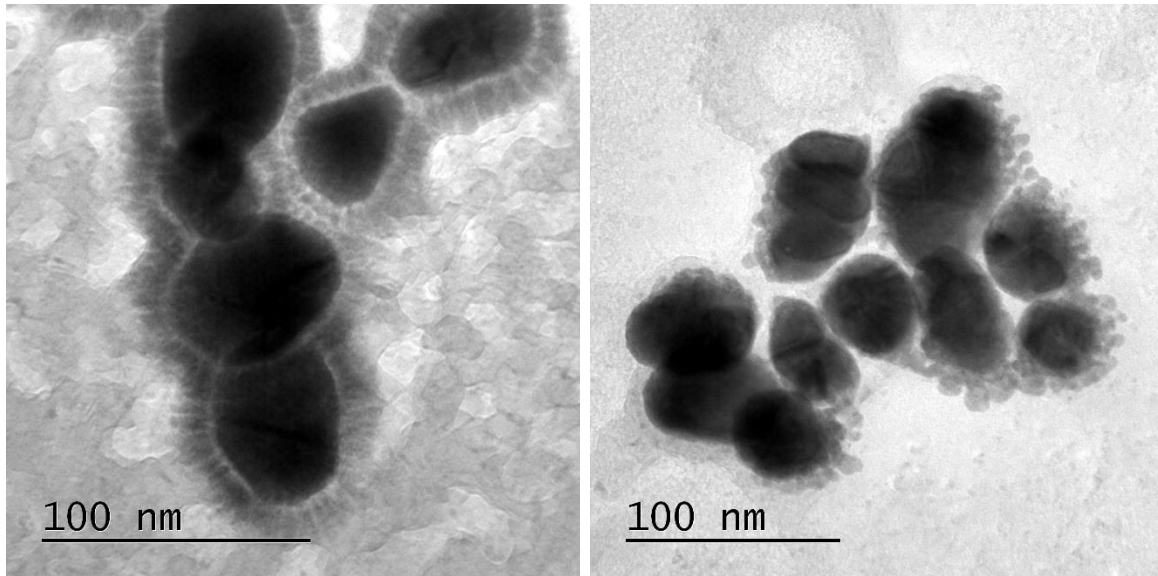


**Figure 4-70** TEM images of Au@CaCO<sub>3</sub> nanoparticles resulting from 5 mins bubbling with pMB acid stabilised gold nanoparticles

The excellent contrast between nanoparticle coating and the background is evidence that the coating is separate from the separate surface layer. Figure 4-70 b) shows some quite different coatings from those in a), with what appears to be small individual crystals of calcium carbonate attached to the surface of the gold nanoparticles. No particles/crystals of calcium carbonate are ever seen in the bulk or background of the sample suggesting that they have nucleated preferentially at the surface of the nanoparticles. This could be due to the carboxylic acid head (of the pMB acid thiol) stabilising Ca<sup>2+</sup> ions and hence favouring nucleation and growth in this area.

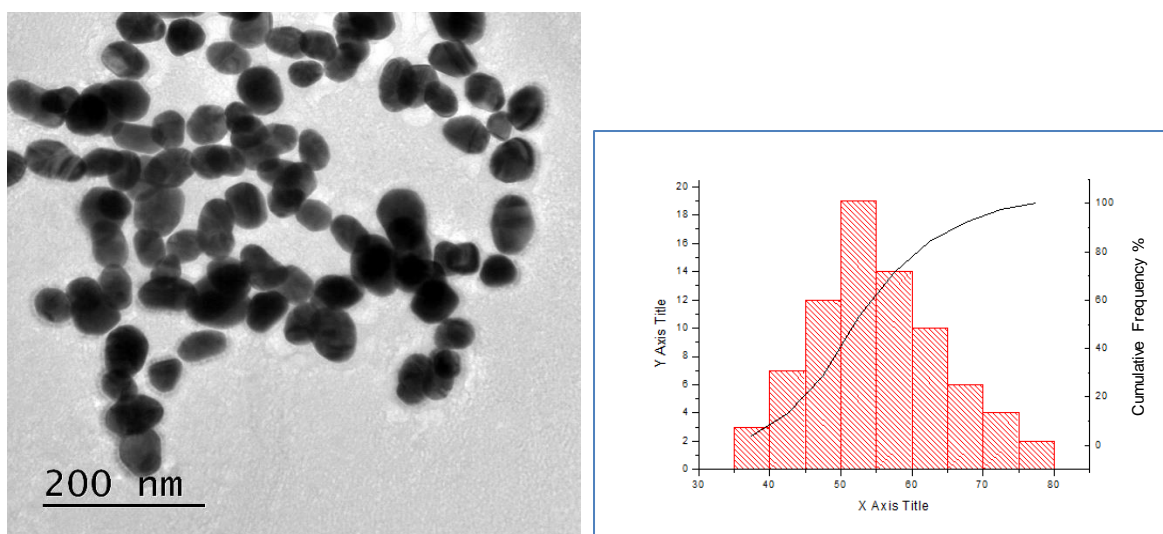


**Figure 4-71** a) TEM image of pMB stabilised Au@CaCO<sub>3</sub> nanoparticle cluster and b) particle size distribution

Figure 4-71 b) shows that the particle size distribution has not changed significantly when compared to that of the particles prior to coating, suggesting that nanoparticles were robust enough to undergo coating without any increase in particle size. Coatings for longer than 10 minutes resulted in the TEM slides being coated too heavily and it was not possible for the TEM to penetrate these samples.

In contrast Au-nanoparticles stabilised with pMPB acid showed no signs of coating after 5 or 10 minutes (Figure 4-72). From the preliminary results and observed directed crystallisation using pMPB acids stabilised Au-nanoparticles it was thought that these Au-nanoparticles would be the most likely to form core@shell nanoparticles. From the TEM analysis it is clear that the particles were coated with some form of shell, whether this is calcium carbonate is ambiguous as EDX analysis was not available.

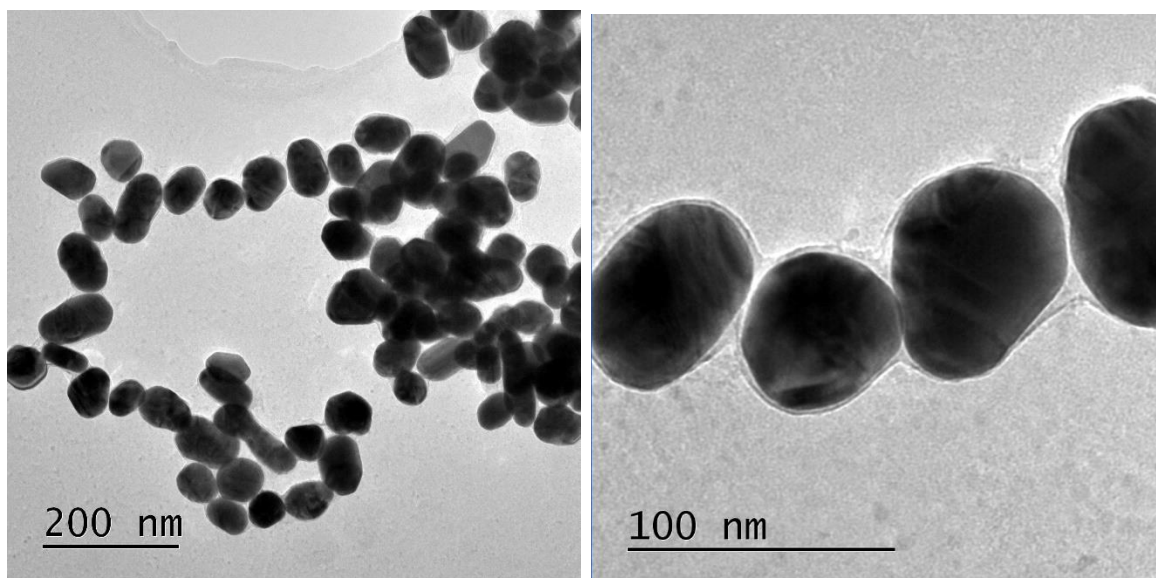


**Figure 4-72** TEM images of pMPB acid stabilised Au-nanoparticles after bubbling 10 mins

Core@shell nanoparticles were also observed forming with pMP stabilised Au-nanoparticles. Again a clear difference between the coating on the particles and the background mosaicking has been observed, further supporting the successful coating of the Au-nanoparticles.

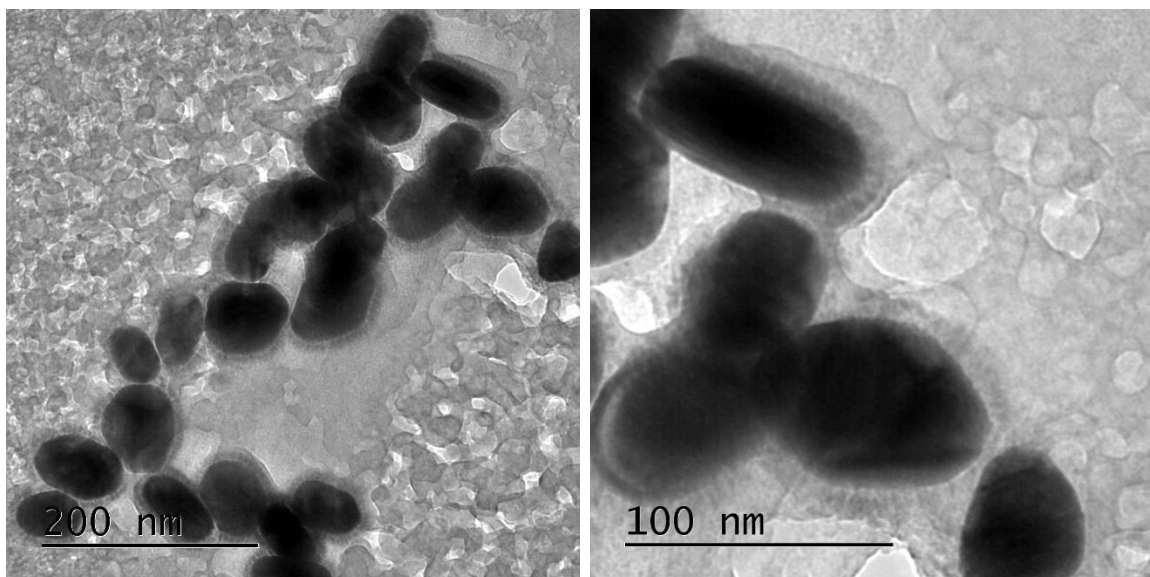


**Figure 4-73** TEM images of Au@CaCO<sub>3</sub> nanoparticles resulting from 5 mins bubbling with pMP stabilised gold nanoparticles

The shell observed in Figure 4-73 are of towers or pillars, similar to that seen with pMB acid stabilised Au-nanoparticles. These are very promising findings, although there was much background deposition seen as the mosaic affect, this was due to the relative excess of calcium chloride added (0.01 g). Finally, in future TEM imaging, it will be possible to gain EDX elemental analysis which is not a technique that has been available until now, this will enable the analysis of the coating and support the formation of calcium carbonate.

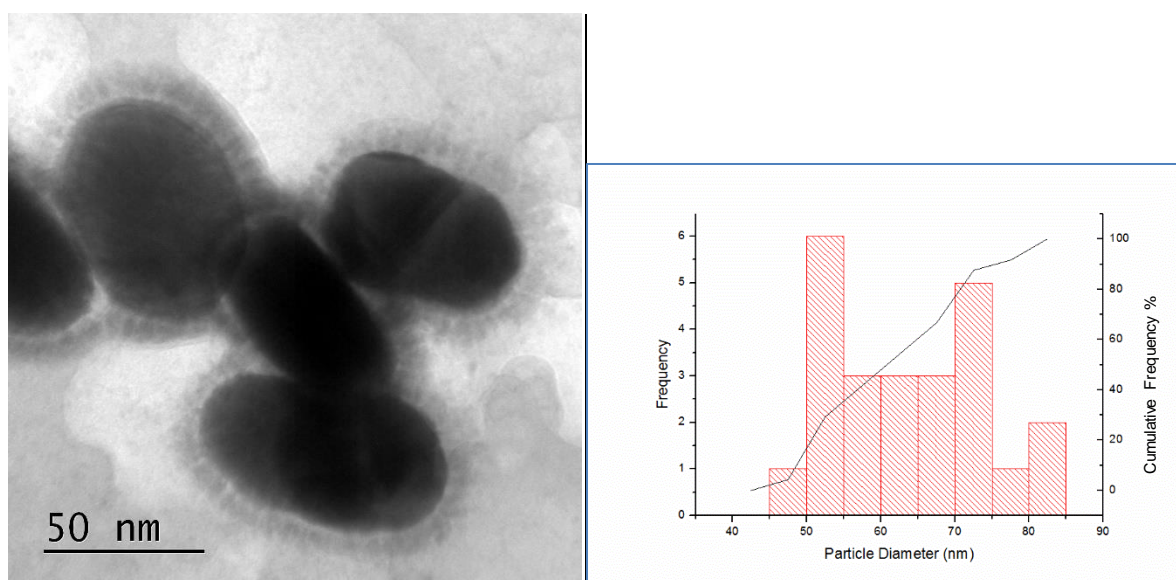


**Figure 4-74** TEM image of Au@CaCO<sub>3</sub> nanoparticles and b) nanoparticle size distribution

Analysis of all of these samples was attempted using SEM imaging and Raman spectrometry. SEM images obtained for these samples did not yield any useful information, due to the small

size of the particles being beyond the resolution capability of the instrument. Similarly the Raman spectra obtained gave no positive result, this was also expected as there is very little calcium carbonate present and hence below the detection limit of the apparatus. Nanoparticles of this size produce surface plasmons and so should give great spectral enhancement to any surrounding molecules, the penetration depth of the SERS effect will only extend for a few nm and hence the coatings present are too thick for the SERS effect to penetrate.

### 4.3 Discussion

Deposition of stable electrochemically produced calcium carbonate has been achieved and opens the doors for the study of how this will be affected by other stimuli (e.g. temperature or  $[Mg^{2+}]$ ). The deposition can be initiated by applying a reduction potential at the working electrode of  $\sim 1000$  mV, the reason for initiation of deposition is explained by the changes in pH near the electrode in accordance with that found by Gabrielli [18]. The solution composition can be altered to promote the desired polymorph. Attempts to follow the dissolution with Raman were possible by first locating deposited crystals through the optical microscope and using the Raman intensity to follow the dissolution, however all measurements were made following only bulk dissolution and the SERS effect was not observed to enable the monitoring of the very initial stages of dissolution. This investigation also found that the Au-nanoparticle coated Pt working electrode was not able to form the thin films which were expected from the 'rough' surface provided by the deposited Au-nanoparticles. Instead it was found that discrete calcium carbonate crystals were observed nucleating and growing.

A novel, facile, exchange of stabilising agents was employed for the successful exchange of citrate for a desired linear thiol. TEM analysis confirmed little change to the particle size distributions after exchange coupled with Raman analysis to confirm that the desired thiol had replaced citrate. These thiol stabilised Au-nanoparticles used in the preliminary attempts to form core@shell species, highlighting the thiols enhanced stability and ability to direct the crystallisation of calcium carbonate.

The thiol stabilised Au-nanoparticles were seen to preferentially coat vaterite spherules with little evidence for the inclusion of these nanoparticles in calcite deposits. It was observed that the vaterite spherules went through a transformation into calcite, this was as expected, however due to the inclusion of Au-nanoparticles the resulting calcite deposits were heavily disordered appearing as multinucleated calcite deposits. This change in expected morphology of calcite has been attributed to the inclusion of the Au-nanoparticles on the vaterite. Further the initial stages of multinucleated particle growth have been observed with the growth likely starting due to the formation of calcite rhombohedra upon the surface of vaterite spherules.

Vaterite spherules were observed being included in the growth of these multinucleated deposits as they become larger in size.

Thiol stabilised Au-nanoparticles were able to facilitate the formation of core@shell type nanoparticles, exhibiting interesting surface formations, pillar or towers and small spherical deposits. It is hoped that these core@shell nanoparticles will be used for future studies into the dissolution of calcium carbonate.

## References

1. de Leeuw, N.H. and S.C. Parker, *Surface structure and morphology of calcium carbonate polymorphs calcite, aragonite, and vaterite: An atomistic approach*. Journal of Physical Chemistry B, 1998. **102**(16): p. 2914-2922.
2. Carteret, C., et al., *Polymorphism Studied by Lattice Phonon Raman Spectroscopy and Statistical Mixture Analysis Method. Application to Calcium Carbonate Polymorphs during Batch Crystallization*. Crystal Growth & Design, 2009. **9**(2): p. 807-812.
3. Dandeu, A., et al., *Raman spectroscopy - A powerful tool for the quantitative determination of the composition of polymorph mixtures: Application to CaCO<sub>3</sub> polymorph mixtures*. Chemical Engineering & Technology, 2006. **29**(2): p. 221-225.
4. Burgess, K.M.N. and D.L. Bryce, *On the crystal structure of the vaterite polymorph of CaCO<sub>3</sub>: A calcium-43 solid-state NMR and computational assessment*. Solid state nuclear magnetic resonance, 2015. **65**: p. 75-83.
5. Dong, L.H., et al., *Free-standing crystalline CaCO<sub>3</sub> films composed of three-dimensional microstructures with different morphologies*. Journal of Crystal Growth, 2012. **343**(1): p. 86-94.
6. Han, Y.S., et al., *Factors affecting the phase and morphology of CaCO<sub>3</sub> prepared by a bubbling method*. Journal of the European Ceramic Society, 2006. **26**(4-5): p. 843-847.
7. Wang, J.W. and U. Becker, *Structure and carbonate orientation of vaterite (CaCO<sub>3</sub>)*. American Mineralogist, 2009. **94**(2-3): p. 380-386.
8. Bano, A.M., P.M. Rodger, and D. Quigley, *New Insight into the Stability of CaCO<sub>3</sub> Surfaces and Nanoparticles via Molecular Simulation*. Langmuir, 2014. **30**(25): p. 7513-7521.
9. Kitamura, M., *Crystallization and transformation mechanism of calcium carbonate polymorphs and the effect of magnesium ion*. Journal of Colloid and Interface Science, 2001. **236**(2): p. 318-327.
10. Kitamura, M., *Controlling factor of polymorphism in crystallization process*. Journal of Crystal Growth, 2002. **237**: p. 2205-2214.
11. Alimi, F., et al., *Influence of magnetic field on calcium carbonate precipitation*. Desalination, 2007. **206**(1-3): p. 163-168.
12. Alimi, F., et al., *Effect of magnetic water treatment on calcium carbonate precipitation: Influence of the pipe material*. Chemical Engineering and Processing, 2009. **48**(8): p. 1327-1332.
13. Devos, O., et al., *Nucleation-growth process of scale electrodeposition - Influence of the supersaturation*. Journal of the Electrochemical Society, 2003. **150**(7): p. C494-C501.
14. Devos, O., C. Gabrielli, and B. Tribollet, *Nucleation-growth process of scale electrodeposition - Influence of the mass transport*. Electrochimica Acta, 2006. **52**(1): p. 285-291.
15. Devos, O., et al., *Nucleation-growth process of scale electrodeposition - influence of the magnesium ions*. Journal of Crystal Growth, 2009. **311**(18): p. 4334-4342.

16. Gabrielli, C., et al., *Study of the electrochemical deposition of CaCO<sub>3</sub> by in situ Raman spectroscopy - I. Influence of the substrate.* Journal of the Electrochemical Society, 2003. **150**(7): p. C478-C484.
17. Tlili, M.M., et al., *Study of electrochemical deposition of CaCO<sub>3</sub> by in situ Raman spectroscopy - II. Influence of the solution composition.* Journal of the Electrochemical Society, 2003. **150**(7): p. C485-C493.
18. Tlili, M.M., et al., *Influence of the interfacial pH on electrochemical CaCO<sub>3</sub> precipitation.* Journal of the Electrochemical Society, 2003. **150**(11): p. C765-C771.
19. Gabrielli, C., et al., *In situ Raman spectroscopy applied to electrochemical scaling. Determination of the structure of vaterite.* Journal of Raman Spectroscopy, 2000. **31**(6): p. 497-501.
20. Kawano, J., et al., *Precipitation diagram of calcium carbonate polymorphs: its construction and significance.* Journal of Physics-Condensed Matter, 2009. **21**(42): p. 6.
21. Kuther, J. and W. Tremel, *Stabilization of aragonite on thiol-modified gold surfaces: effect of temperature.* Chemical Communications, 1997(21): p. 2029-2030.
22. Parker, J.E., et al., *A study of the aragonite-calcite transformation using Raman spectroscopy, synchrotron powder diffraction and scanning electron microscopy.* Crystengcomm, 2010. **12**(5): p. 1590-1599.
23. Socrates, G., *Infrared and Raman Characteristic Group Frequencies: Tables and Charts.* Third ed. 2001: John Wiley and Sons, Ltd. 347.
24. Bell, S.E.J. and M.R. McCourt, *SERS enhancement by aggregated Au colloids: effect of particle size.* Physical Chemistry Chemical Physics, 2009. **11**(34): p. 7455-7462.
25. Etchegoin, P., et al., *A novel amplification mechanism for surface enhanced Raman scattering.* Chemical Physics Letters, 2002. **366**(1-2): p. 115-121.
26. Freeman, R.G., et al., *Self-assembled metal colloid monolayers - an approach to sers substrates.* Science, 1995. **267**(5204): p. 1629-1632.
27. Haiss, W., et al., *Determination of size and concentration of gold nanoparticles from UV-Vis spectra.* Analytical Chemistry, 2007. **79**(11): p. 4215-4221.
28. Zhao, F. and Y. Yang, *Transmission electron microscope high magnification calibration.* Colloid Journal, 2010. **72**(3): p. 346-352.
29. Lombardi, J.R. and R.L. Birke, *A unified approach to surface-enhanced Raman spectroscopy.* Journal of Physical Chemistry C, 2008. **112**(14): p. 5605-5617.
30. Bell, S.E.J. and N.M.S. Sirimuthu, *Surface-enhanced Raman spectroscopy as a probe of competitive binding by anions to citrate-reduced silver colloids.* Journal of Physical Chemistry A, 2005. **109**(33): p. 7405-7410.
31. Grass, S., et al., *Quantitative Replacement of Citrate by Phosphane on Silver Nanoparticle Surfaces Monitored by Surface-Enhanced Raman Spectroscopy (SERS).* Journal of Nanoscience and Nanotechnology, 2015. **15**(2): p. 1591-1596.
32. Tada, H., J. Bronkema, and A.T. Bell, *Application of in situ surface-enhanced Raman spectroscopy (SERS) to the study of citrate oxidation on silica-supported silver nanoparticles.* Catalysis Letters, 2004. **92**(3-4): p. 93-99.
33. Sun, F., et al., *Sensitive and Fast Detection of Fructose in Complex Media via Symmetry Breaking and Signal Amplification Using Surface-Enhanced Raman Spectroscopy.* Analytical Chemistry, 2014. **86**(5): p. 2387-2394.
34. Sun, X.C., et al., *Functionalized aligned silver nanorod arrays for glucose sensing through surface enhanced Raman scattering.* RSC Advances, 2014. **4**(45): p. 23382-23388.
35. Jiang, L., et al., *Highly Reproducible Surface-Enhanced Raman Spectra on Semiconductor SnO<sub>2</sub> Octahedral Nanoparticles.* Chem Phys Chem, 2012. **13**(17): p. 3932-3936.
36. Michota, A. and J. Bukowska, *Surface-enhanced Raman scattering (SERS) of 4-mercaptobenzoic acid on silver and gold substrates.* Journal of Raman Spectroscopy, 2003. **34**(1): p. 21-25.

37. Yang, L.B., et al., *Adsorption study of 4-MBA on TiO<sub>2</sub> nanoparticles by surface-enhanced Raman spectroscopy*. Journal of Raman Spectroscopy, 2009. **40**(12): p. 2004-2008.
38. Suh, J.S. and J. Kim, *Three distinct geometries of surface-adsorbed carboxylate groups*. Journal of Raman Spectroscopy, 1998. **29**(2): p. 143-148.
39. Ho, C.H. and S. Lee, *SERS and DFT investigation of the adsorption behavior of 4-mercaptobenzoic acid on silver colloids*. Colloids and Surfaces a-Physicochemical and Engineering Aspects, 2015. **474**: p. 29-35.
40. Tlili, M.M., et al., *Characterization of CaCO<sub>3</sub> hydrates by micro-Raman spectroscopy*. Journal of Raman Spectroscopy, 2002. **33**(1): p. 10-16.
41. Wolthers, M., et al., *Calcite growth kinetics: Modeling the effect of solution stoichiometry*. Geochimica Et Cosmochimica Acta, 2012. **77**: p. 121-134.

# Chapter 5 Epitaxial Growth of Calcium Carbonate on Gold Single Crystals

---

## 5.1 Introduction

Nanoparticles are often described by the shape they exhibit, for example, sphere, rod, tube etc. However when particles are produced on the nanoscale the shapes they form are not this simple. The surface of a spherical nanoparticle is not homogeneous and is in fact made up of different single crystal surfaces. A simple spherical nanoparticle of an fcc metal, such as gold, comprises of large (111) and (100) facets linked together with small (110) facets (Figure 5-1).

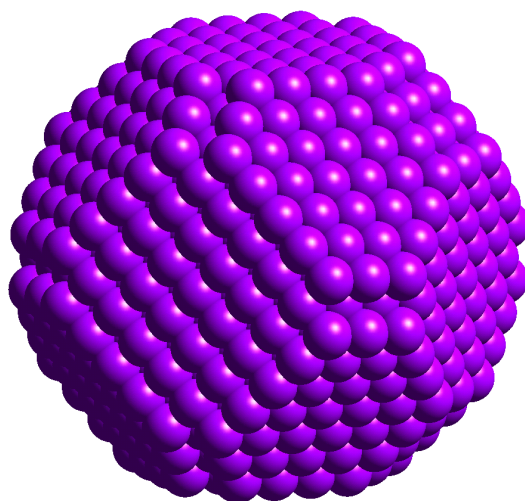


**Figure 5-1** Diagram of facets expressed by an fcc metal nanoparticle (Au, Ag, Cu, Pd, Pt, Ni)

Each of the three basal planes (Figure 5-2) expressed by such a nanoparticle have differing atomic arrangements, the different atom structure leads to the surface possessing different surface electronic structure, this differing electronic structure leads to the single crystal surfaces behaving quite differently toward the same reaction or conditions. Therefore the study of single crystal surfaces leads to the better understanding of how reactions take place on the surface of nanoparticles, and by knowing which surfaces react more favourably for a given reaction a nanoparticle can be tuned, by changing its shape, to express more of the desired surface [1].

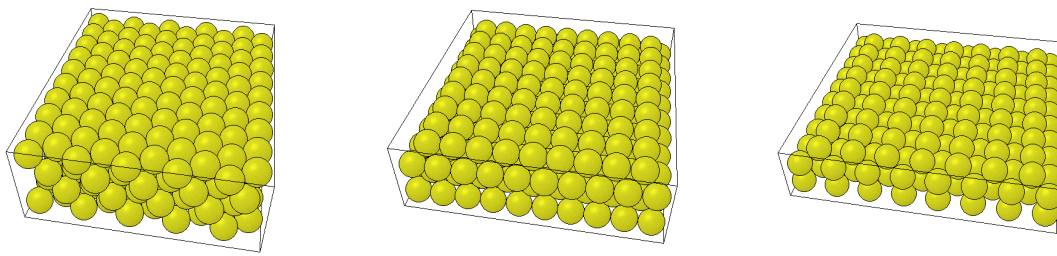


**Figure 5-2** Diagram of the surface structure of fcc basal planes, a) (111), b) (100) and c) (110)

Gold single crystal surfaces undergo reconstruction to reduce surface energy at room temperature, for example, the close packed Au(111) reconstructs to the well-known  $(22 \times \sqrt{3})$  reconstruction often labelled as the 'herringbone' structure. There is a uniaxial compression of the topmost layer of Au atoms, the compression occurs along one of the  $[\bar{1}10]$  directions. This compression results in the observed  $(22 \times \sqrt{3})$  reconstruction whereby 23 atoms of the top layer compress to fit over 22 atoms of the second layer. It is this compression that pushes the Au atoms sideways along the  $[\bar{1}\bar{1}]$  direction causing more hcp stacking structure. At the boundaries between fcc and hcp stacking, atoms are forced to form a ridge (Figure 6-17). On large reconstructed Au(111) surfaces the ridges can express different orientations due to the presence of a 3 fold symmetry, each orientation is of equal probability and hence at domain boundaries there can be a  $120^\circ$  change in orientation. This usually occurs about every 280 Å. Figure 5-3 shows an example of the long range reconstruction known as the herringbone structure [2].

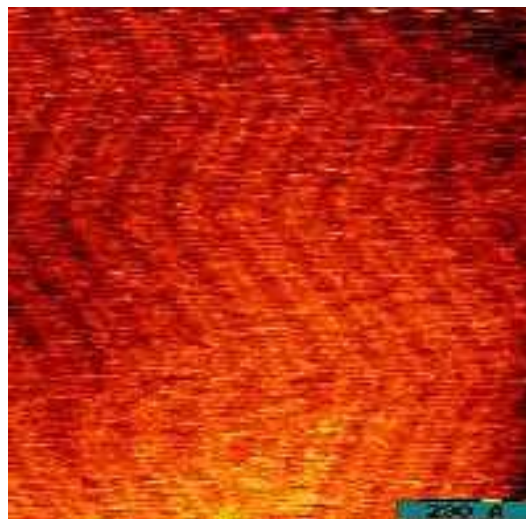
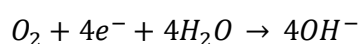


**Figure 5-3** STM image of the reconstructed Au(111) surface showcasing the 'herringbone' structure, reprinted from [3]

Much work has been presented on the directed growth of calcium carbonate using self-assembled monolayers (SAM) of linear thiols on single crystal metal surfaces. This was one of the reasons that thiol stabilised gold nanoparticles were used for the synthesis of Au@carbonate nanostructures previously described. Kuther et al. and Lee et al. have both produced comprehensive studies of these interfaces; Kuther found that longer chain thiols gave more ordered deposition while shorter chain thiols led to more disordered deposition [4]. Lee et al [2001], used the SAM to probe the amorphous calcium carbonate (ACC) to anhydrous calcium carbonate transformation, showing that the shorter chain thiols promote the formation of ACC before transformation to the anhydrous calcite [5, 6], this highlights the difficulty in replicating biomineralisation processes. Both Kuther and Lee have investigated the deposition of calcium carbonate on clean metal single crystals finding no evidence of epitaxial growth. However these findings were obtained from large single crystal wafers which may not have the same degree of atomic 'flatness' as the single crystal beads used herein. Further, the deposition in these cases was performed without the presence of a reduction potential [4-11].

Teghidet et al. employed reduction potentials to initiate the deposition of calcium carbonate on clean Au and Ag(111) single crystals [12]. When a reducing potential is applied of a certain magnitude (-1000 mV Au and -1400 mV Ag) dissolved oxygen in the solution is reduced at the electrode surface, this process forms an ordered layer of surface hydroxides and raises the pH a few units near the electrode surface [13]. The local pH change encourages calcium carbonate to deposit and the subsequent deposition occurs in an ordered epitaxial manner.



When deposition occurs it is the calcium ions which form the first layer which is thought to start the formation of calcium carbonate. The aim of the work described here is to further Teghidet's work on clean Au(*h.k.l*) single crystals, exploring the other basal planes. This will feedback useful information for future core@shell synthetic work.

## 5.2 Preliminary Investigations on Au(*h,k,l*)

A series of reference experiments were conducted to ensure the validity of subsequent investigations of epitaxial growth on gold single crystals.

### 5.2.1 Deposition in the Absence of an Applied Potential

A solution of dissolved calcium carbonate ( $300 \text{ mgL}^{-1}$ ) was flowed over the surface of the single crystal (30 min) in the absence of an applied reduction potential to ascertain whether any bulk deposition independent of the reduction potential was likely to occur. Figure 5-4 and 5-5 shows aragonite particles (identified by their characteristic crystalline shape) adhered to the Au(111) crystal surface, these may have precipitated from the electrolyte solution.

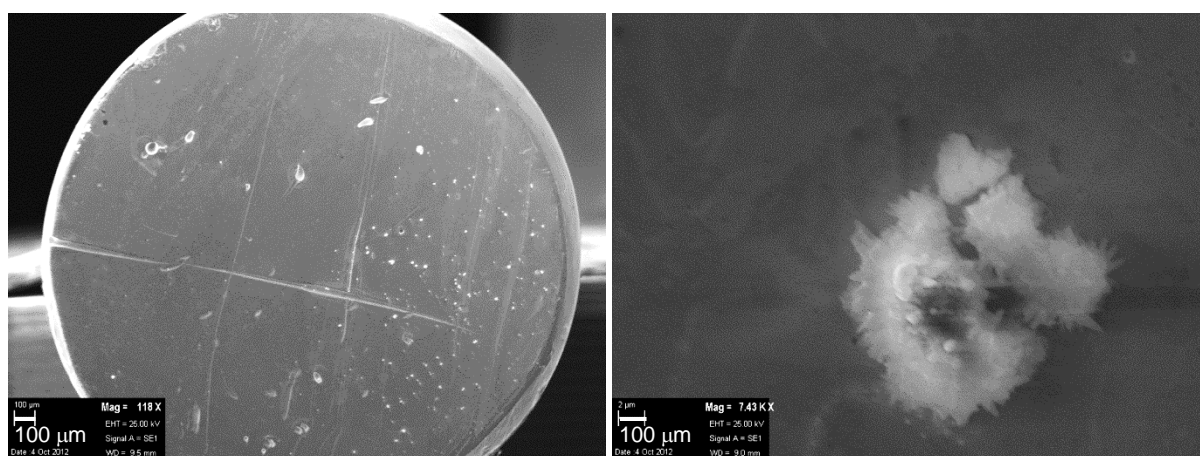


**Figure 5-4** SEM images of a) coated Au(111) crystal and b) aragonite particle

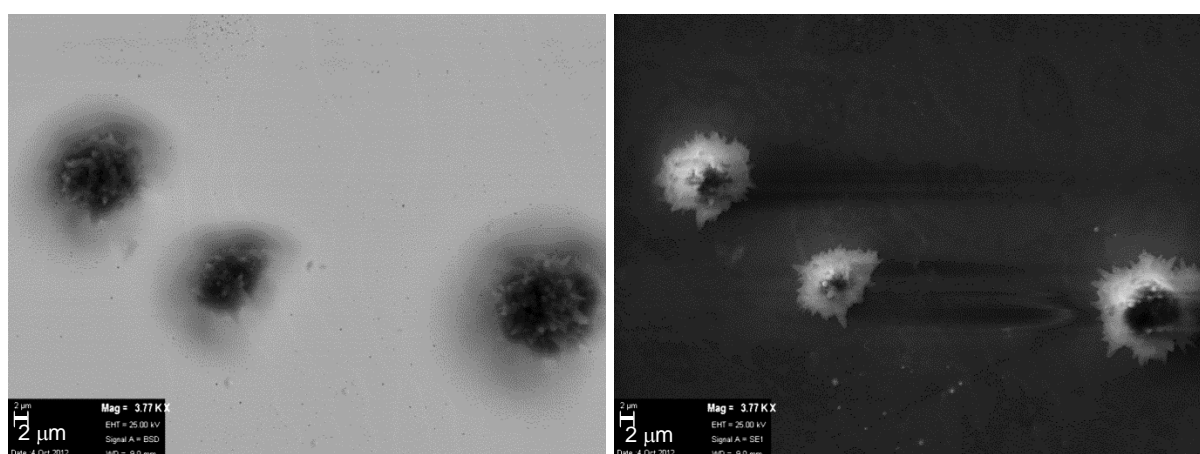


**Figure 5-5** SEM image of aragonite particles on the Au(111) surface, a) backscatter detector (BSD) image and b) secondary electron (SE1) image

However, the formation of aragonite typically only occurs at elevated temperatures (>40 °C), and so it is more likely, due to the insolubility of calcium carbonate, that these are undissolved aragonite particles stemming from the stock powder. Figure 5-6 shows images of stock calcium carbonate powder which shows very close similarity to those observed above. Further, without any external stimuli, particularly heat, it would be likely that any precipitated calcium carbonate would form calcite, the more stable polymorph.

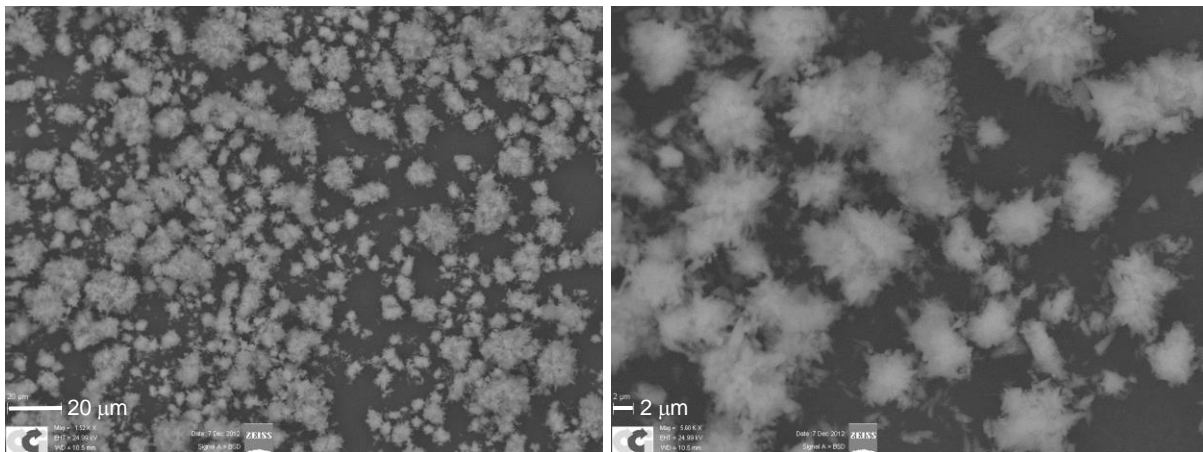


**Figure 5-6** SEM images of stock precipitated calcium carbonate.

One interesting finding that has been observed when taking SEM images of the single crystal surfaces, is that the imperfections of the crystals can clearly be seen. Figure 6-4 a) shows a particular crystal that has a number of deep scratches in its surface and asymmetrical punch holes can also be seen. These asymmetrical imperfections are attributed to the previous use of this crystal for STM studies and hence are likely due to tip-surface crash incidents. The larger scratches are not due to the STM as these scratches are on the macro scale and would require a rather serious incident; instead they are more likely to have occurred during previous preparative work.

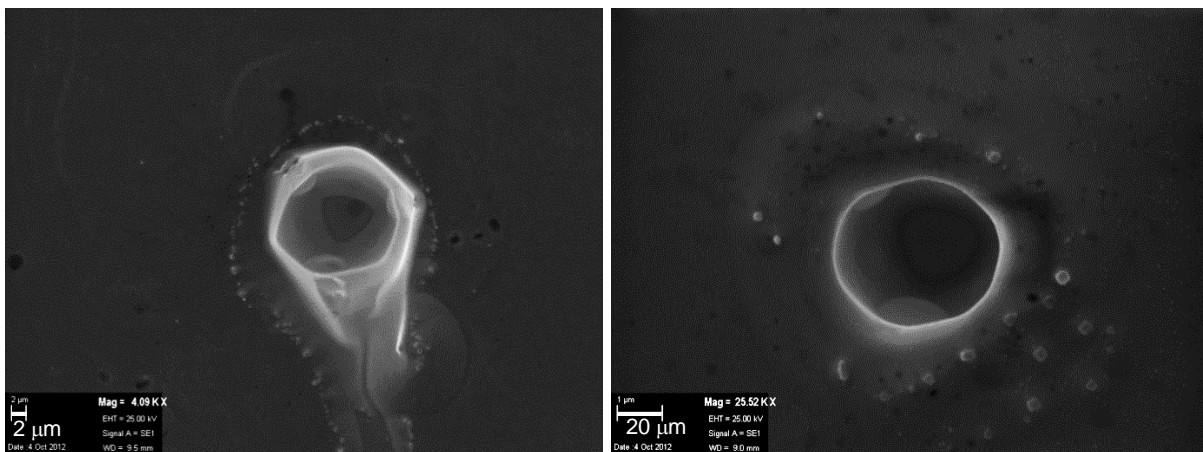


**Figure 5-7** SEM SE1 image of unknown surface structures

Figure 5-7 shows some form of large feature on the surface, probably another example of a punch hole created by an STM tip, with some smaller particles around the outside. The smaller particles are either amorphous calcium carbonate or small spherules of vaterite, however due to their small size and occurrence, reliable Raman or EDX was not viable.

### 5.2.2 Ultra-Pure Water (-1000 mV, 10 mins)

Ultra-pure water was flowed over the single crystal surface in the absence of any calcium carbonate but with an applied reduction potential to assure that no contaminants were depositing from the UPW or as a result of the applied reduction potential, as expected no peaks were observed in the Raman spectrum prior to SEM.

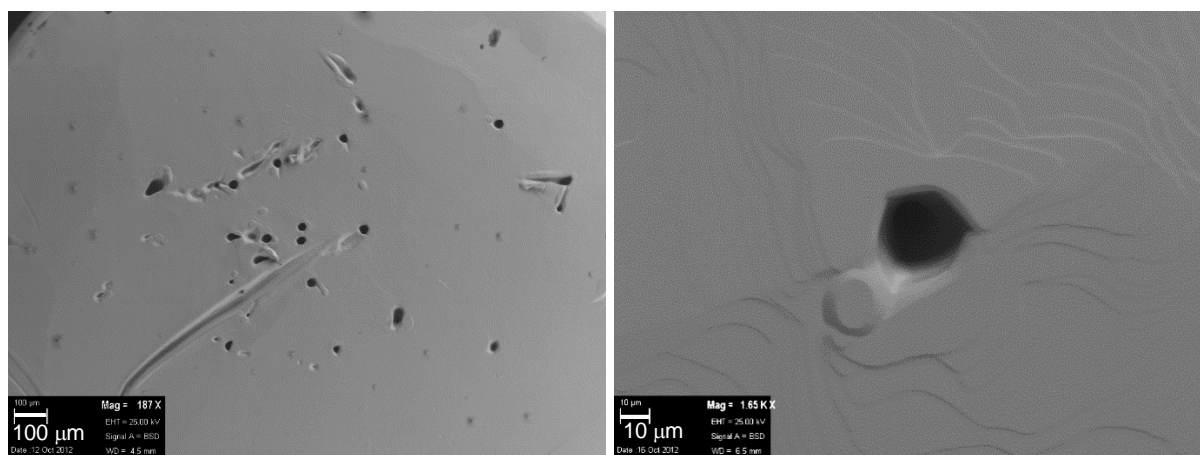


**Figure 5-8** SEM images of Au(111) crystal surface

Figure 5-8 shows the imperfections of another gold coated Pt(111) single crystal used in these experiments, again scratches and holes are visible on the surface, again attributed to the prior use for STM investigations. After in depth scanning of the single crystal surface no deposition of any kind was observed, as expected from the Raman spectrum obtained prior to imaging. Of interest are the terraces and steps visible in the SEM, although it was not expected that steps would be visible it can be confirmed that these are real features as the whole surface is stepped in a net direction (Figure 5-9), this would have occurred during the single crystal preparation, specifically the laser calibrated grinding/polishing to expose the desired surface.

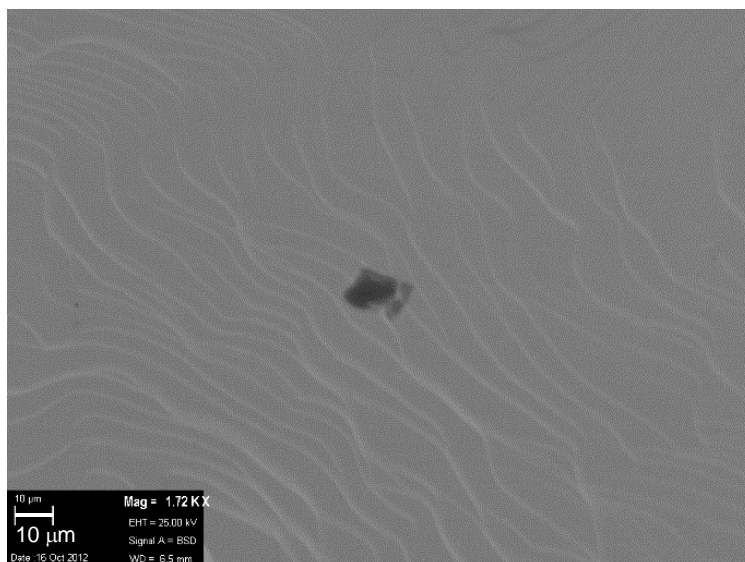
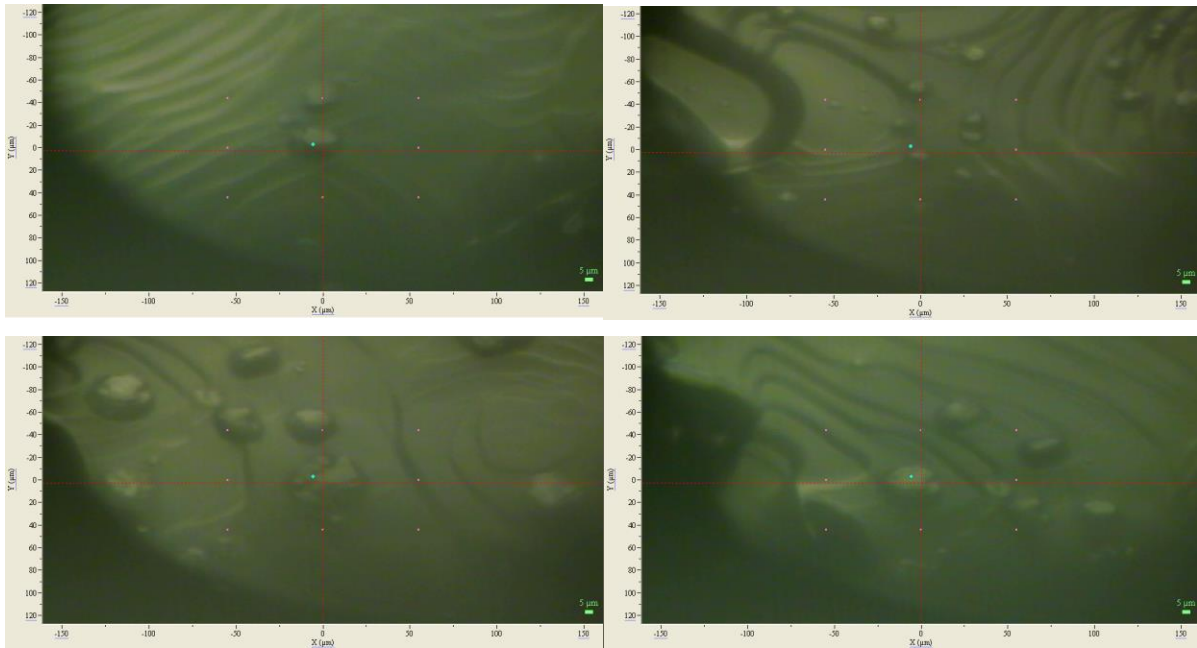


**Figure 5-9** SEM BSD image of the Au(111) single crystal surface

### 5.3 Epitaxial Growth on Au(111)

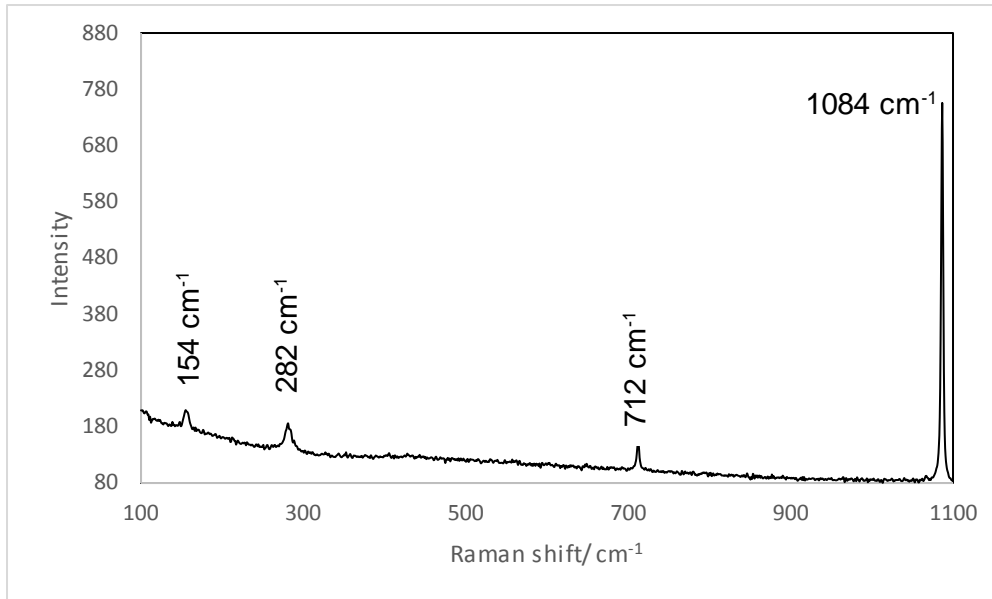
A solution of  $\text{CaCO}_3$  (3 mM) was acidified with  $\text{CO}_2$  gas bubbling (<7.2 pH) to prevent bulk deposition occurring and flowed over the electrode surface. Initially deposition was performed at -1000 mV (5 or 10 mins) to see if similar results were observed to those reported by Teghidet [12], before deposition at -1400 mV and -400 mV.

The single crystal surface was observed through the optical microscope so that crystals could be located for Raman analysis. SEM analysis was also essential as the optical microscope was not sufficient for the determination of crystal polymorphism and orientation.



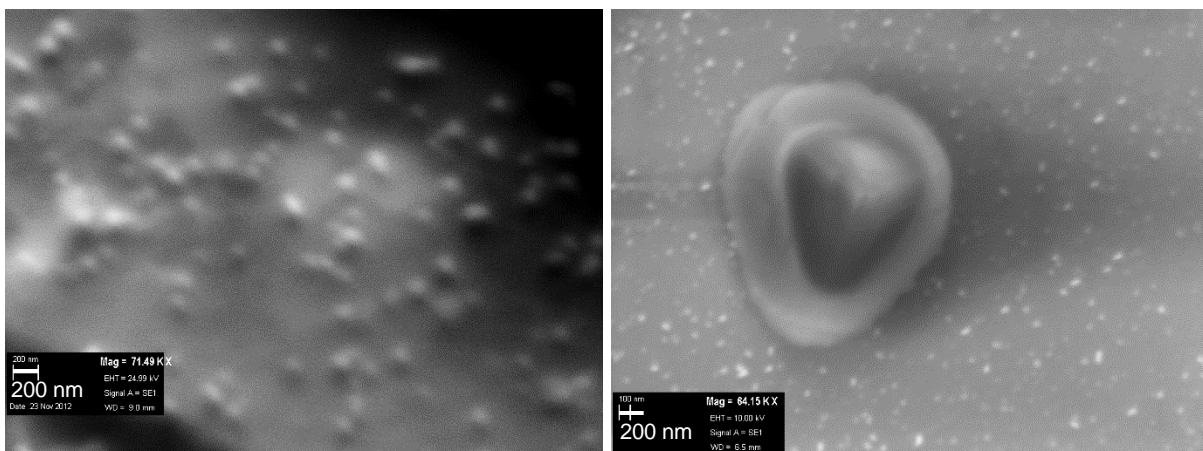
**Figure 5-10** Optical microscope images of calcium carbonate deposits, a) and b) are after 5 min, c) and d) after 10 mins deposition time at -1000 mV

Figure 5-10 shows optical images of calcium carbonate deposits, images a) & b) both have smaller and fewer particles than images c) & d) as expected due to the difference in deposition times. The Raman spectra for all of these particles were similar and an example is shown in Figure 5-11. A strong, sharp band at  $1084\text{ cm}^{-1}$  and a smaller sharp band at  $712\text{ cm}^{-1}$  can be assigned to the internal carbonate vibrations  $\nu_1$  and  $\nu_4$  respectively. Bands were also observed in the fingerprint Raman region at  $282$  and  $154\text{ cm}^{-1}$ . These lattice vibrations are indicative of the presence of the calcite polymorph. There was no evidence of band broadening or the presence of shoulder peaks indicating that the deposits were of pure calcite and no evidence of other polymorphs were observed.



**Figure 5-11** Raman spectrum of calcite particle from Figure 5-10 a)

After 5 minute depositions a small number of particles were observed in the optical microscope, the resulting SEM images (Figure 5-12 and 5-13) show a blanket covering of small spherical deposits. These are likely amorphous calcium carbonate (Figure 5-12 a)) inferred from there spherical shape and small size [14, 15]. Larger particles are also observed over the electrode surface, these larger particles are the calcite particles detected in the Raman analysis. In a similar way to those observed by Teghidet the calcite rhombohedra are all growing from the surface in an epitaxial manner with the calcite  $[10\bar{1}]$  face in contact with the surface. No other polymorphs of calcium carbonate were observed over the single crystals, and all of the calcite particles expressed this type of growth pattern supporting the epitaxial nature of this growth.



**Figure 5-12** SEM SE1 images of the Au(111) crystal surface after 5 minute depositions

Of particular interest is the presence of a band around all of the growing calcite particles; examples can be seen in Figure 5-12 b) and 5-13. When anhydrous calcium carbonate has been formed previously it was seen that it was at the expense of surrounding amorphous phase, supporting the ACC to anhydrous calcium carbonate growth mechanism. The depletion of surrounding ACC has also been documented by Lee [5]. However the depletion of surrounding amorphous phase it not observed, therefore if the ACC to anhydrous phase mechanism is to hold true, it is likely that the band observed around the growing particles is ACC. This is an excellent visual example of the transformation of ACC to anhydrous calcite.

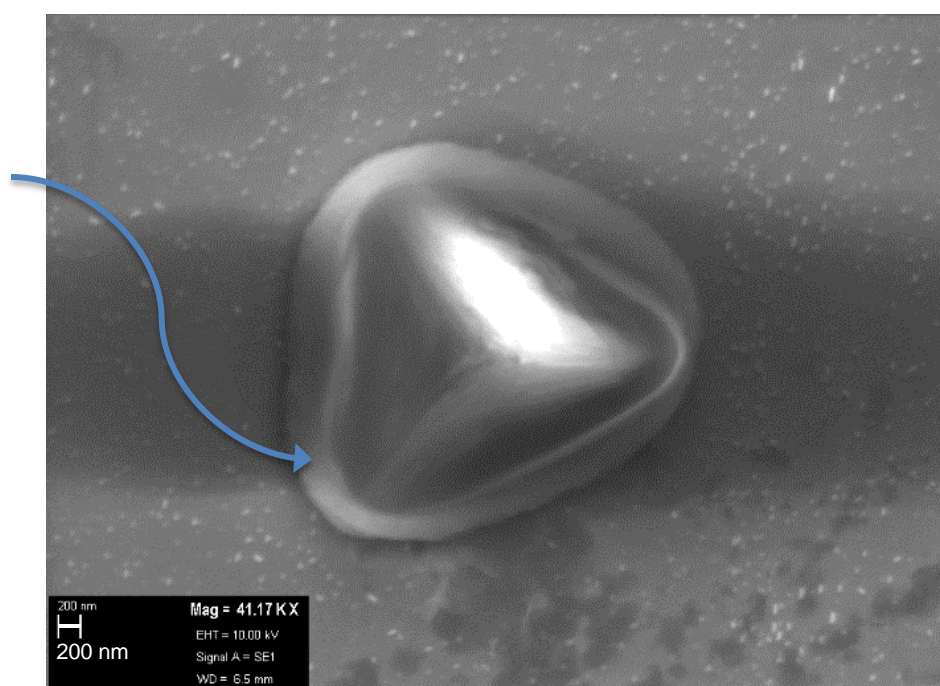


**Figure 5-13** SEM SE1 image of particle after 5 min deposition at -1000 mV, blue arrow highlighting the proposed hydrated precursor

Longer deposition times led to a much higher coverage of calcite particles. Although the larger particles become more disordered as they grow away from the surface, it is still evident that they are growing in an epitaxial manor with the calcite  $[10\bar{1}1]$  face in contact with the gold single crystal surface (Figure 5-14). A large range of sizes of calcite particles are observed highlighting that the continued application of a reduction potential is promoting continued nucleation of calcite particles on the electrode surface.

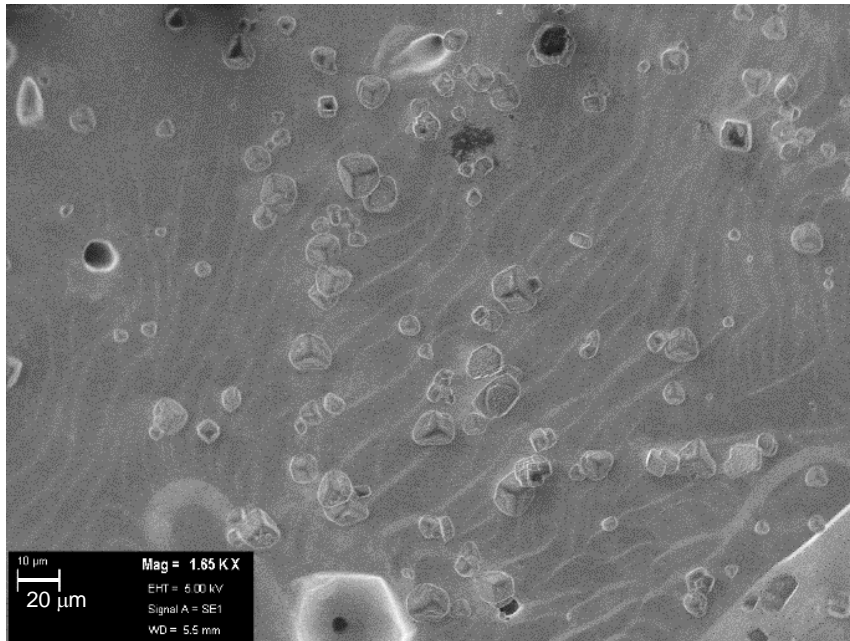
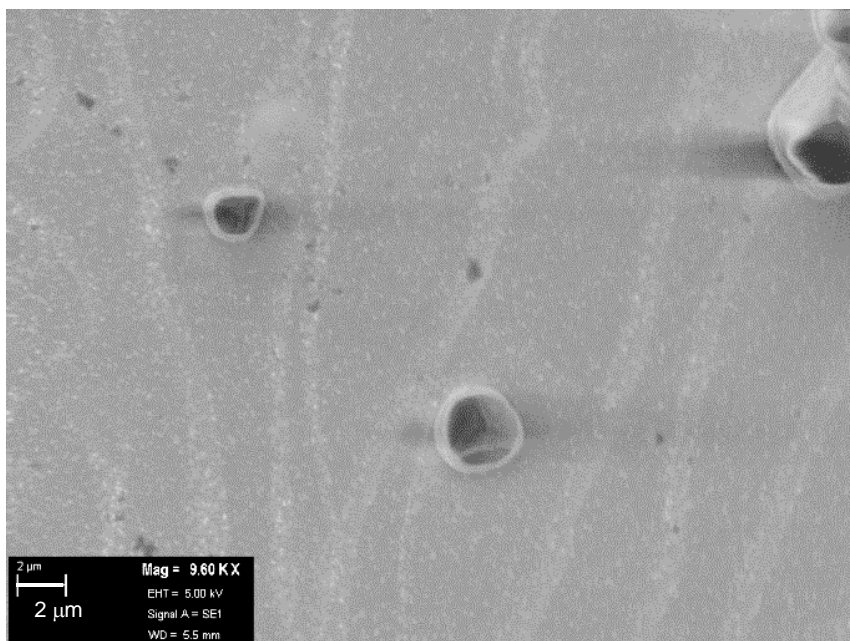


Figure 5-14 SEM SE1 image of calcite deposited at -1000 mV after 10 mins

The larger particles which have finished their rapid nucleation and growth do not have signs of an amorphous band around the outside (Figure 5-14), whereas the observed smaller particles still possess the small band around the edge of the growing particle (Figure 5-15). This further supports the amorphous nature of the observed band. This also suggests that although the calcite is growing epitaxially from the gold single crystal it is still progressing through an ACC to crystalline mechanism.



**Figure 5-15** SEM SE1 image of small growing calcite particles after 10 mins deposition time at -1000 mV

When depositions were carried out at -1400 mV no epitaxial growth was observed, this supports that found by Teghidet. Figure 5-16 a) shows that the only deposits observed, which are that of the undissolved stock calcium carbonate are in the form of aragonite. The aragonite particles have adhered to the surface due to electrostatic interaction upon drying of the electrode before SEM analysis took place.

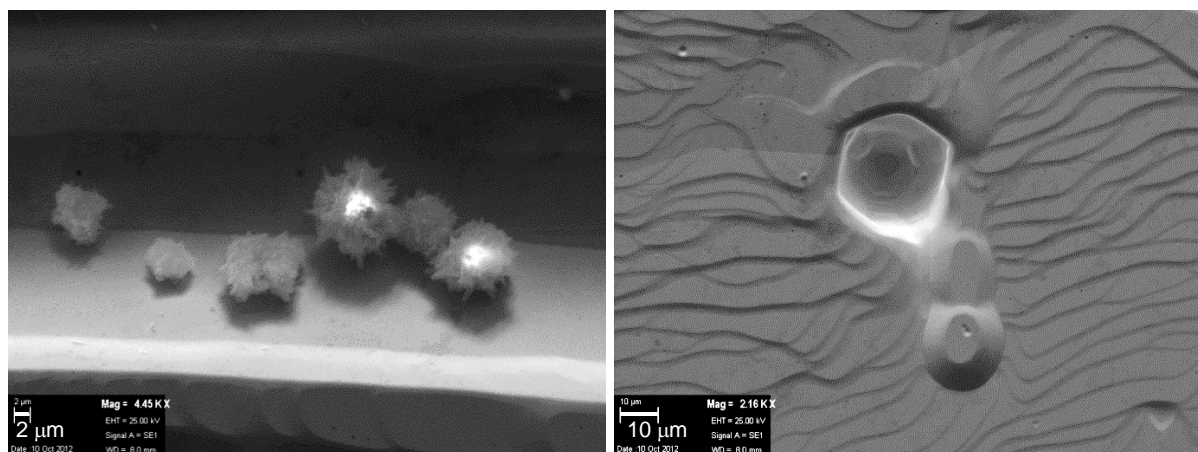


**Figure 5-16** SEM SE1 images of deposits after 5 min at -1400 mV

Figure 5-16 b) also reveals again what is thought to be steps along the single crystal surface, as was seen previously in the production of a clean CV for this crystal that peaks appear showing that (111)x(111) and (110)x(111) steps are present in this crystal. This further supports the epitaxial coating of the gold as the platinum steps are still present.

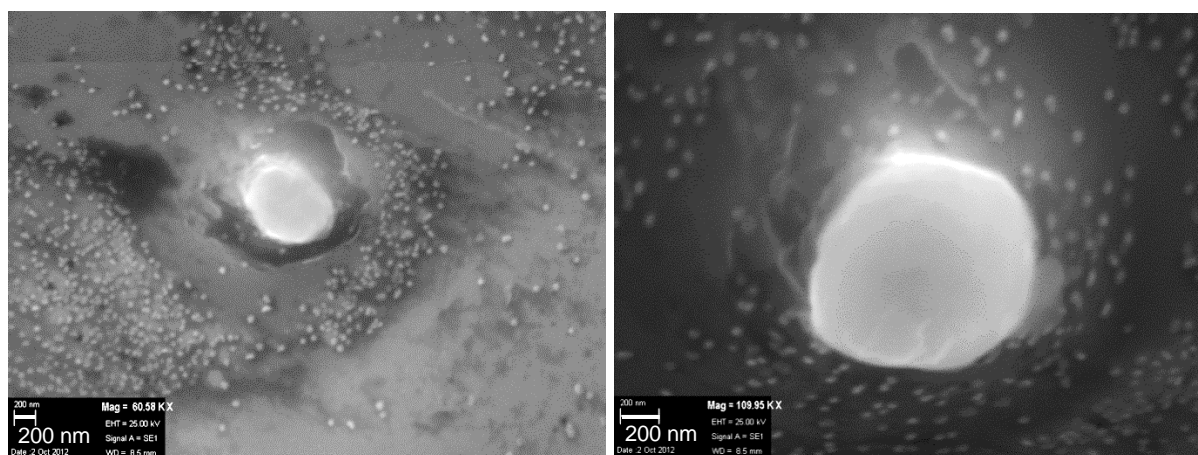


**Figure 5-17** SEM SE1 images of deposits after 10 min at -1400 mV

After 10 minute depositions at -1400 mV a blanket covering of very small (< 5 nm) near spherical particles were observed for all depositions, these are again attributed to the presence of amorphous calcium carbonate and examples of these can be seen in Figure 5-17. No clear deposits of calcite or any other anhydrous polymorph were observed, however a

few larger near spherical deposits were observed, these are attributed to amorphous calcium carbonate, however due to their low coverage and relatively small size they were not observed in the optical microscope and no Raman spectra were obtained. At -1400 mV water is reduced leading to the formation of hydrogen bubbles on the surface of the electrode, this rapid formation of bubbles over the surface could be the reason that no epitaxial calcium carbonate growth is observed at this potential.

Depositions were carried out at -400 mV, Figure 5-18 and 5-19 show examples of epitaxial growth observed at this potential. Figure 5-18 shows images of calcite particles after 5 minutes, the epitaxial growth with the calcite  $[10\bar{1}\bar{1}]$  face in contact with the single crystal surface is again apparent. At this potential it appears the  $[1014]$  face of calcite is more disordered than those deposited at -1000 mV, however the pyramidal shape is still apparent.

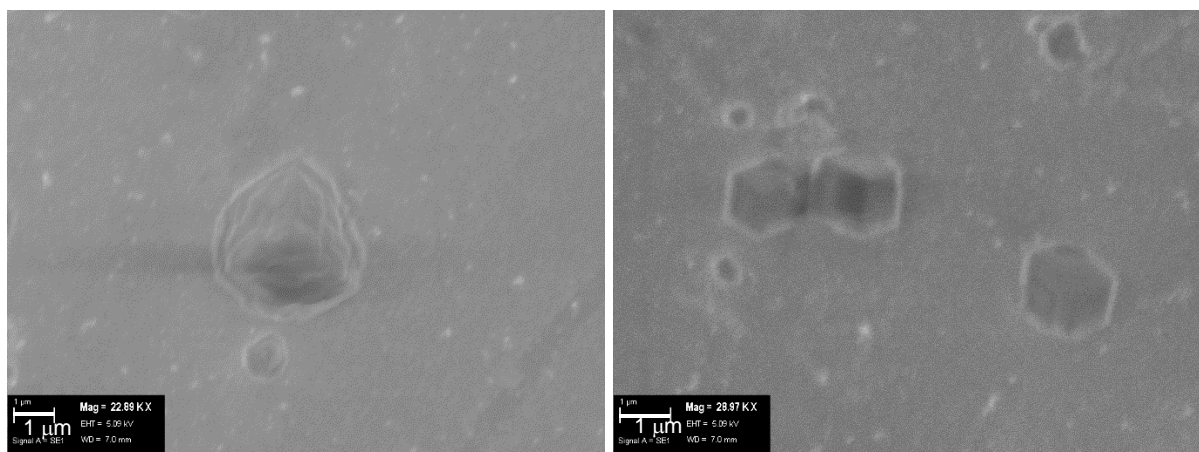


**Figure 5-18** SEM SE1 images of deposits after 5 min at -400 mV

After longer deposition times (Figure 5-19) it is still clear that the calcite particles are growing epitaxially with the  $[10\bar{1}\bar{1}]$  face in contact with the single crystal surface however these particles have become particularly disordered as they have grown larger and further from the surface and the influence of the epitaxy.

The epitaxial growth observed at this reduction potential is of particular interest as it is in contrast to that predicted by Teghidet. It was thought that the epitaxial growth occurred due to the local electrode pH being lowered and the presence of surface hydroxides, both due to the reduction of oxygen at the potential applied. This encourages the deposition by the stabilisation of the first Ca layer. This 'accelerated scaling method' first introduced by Gabrielli [13] and used by Teghidet [12] should only have this effect on reduction potentials around -1000 mV. However at -400 mV the reduction of oxygen does not occur and hence the observed epitaxy cannot be attributed to this. A possible explanation for the observed epitaxial growth at -400 mV is the formation of oxalate from dissolved  $\text{CO}_2$ . The electrolyte, acidified

with CO<sub>2</sub>, would be rich in this species which may be directing the deposition of ordered calcium carbonate, perhaps through an interaction between the oxalate and calcium ions preceding the formation of calcium carbonate.

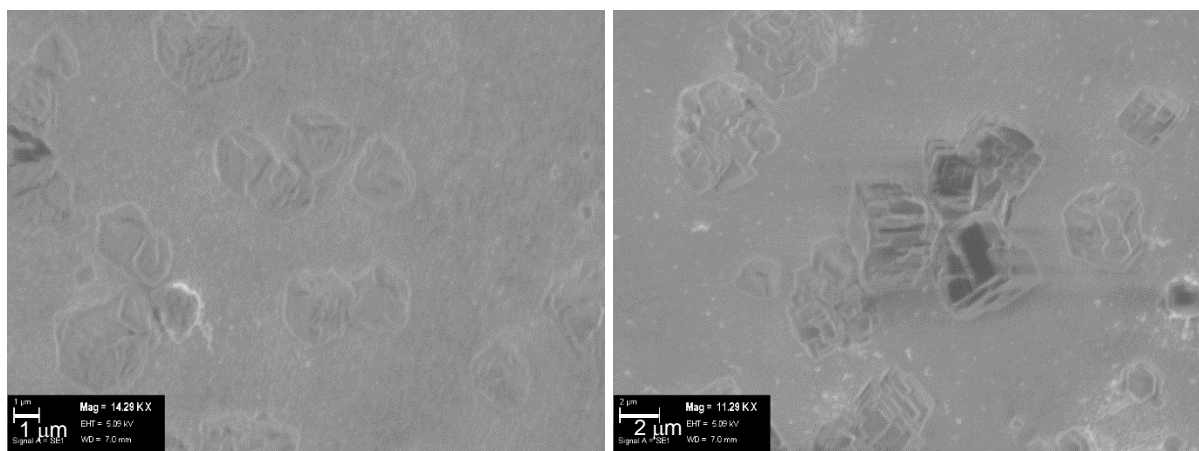


**Figure 5-19** SEM SE1 image of deposits after 10 min at -400 mV

### 5.3 Epitaxial Growth on Au(110)

As before, a solution of CaCO<sub>3</sub> (3 mM) was acidified with CO<sub>2</sub> gas bubbling (<7.2 pH) to prevent bulk deposition occurring and flowed over the electrode surface. Depositions were performed at -1400, -1000 and -400 mV. As expected no epitaxial growth was observed at -1400 mV attributed to the production of H<sub>2</sub> bubbles at the electrode surface. Interestingly at -1000 mV there was also no observed deposition.

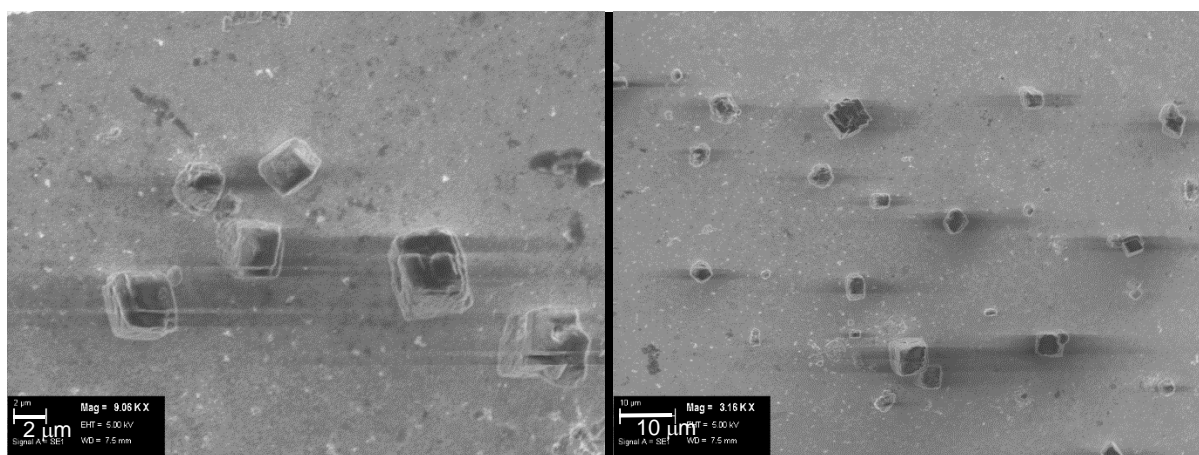


**Figure 5-20** SEM SE1 image of calcite deposits after 10 min at -400 mV

Depositions performed at -400 mV revealed epitaxial growth of calcite, more interestingly all of the calcite particles grew with the calcite [1014] face in contact with the surface, this is in contrast to that seen for the Au(111) where particles grew with the calcite [010] face in contact

with the single crystal surface. After 10 minute depositions, particles had grown larger and more disordered but still with the [1014] face in contact with the surface (Figure 5-20), there were also many smaller particles observed, illustrating that the reduction potential was continuously facilitating the nucleation of calcite particles (Figure 5-21). Amorphous calcium carbonate could again be seen covering the entire surface, however there was no evidence of the amorphous band surrounding the small growth crystals that was previously seen for particles with the [10 $\bar{1}$ ] face in contact with the surface.

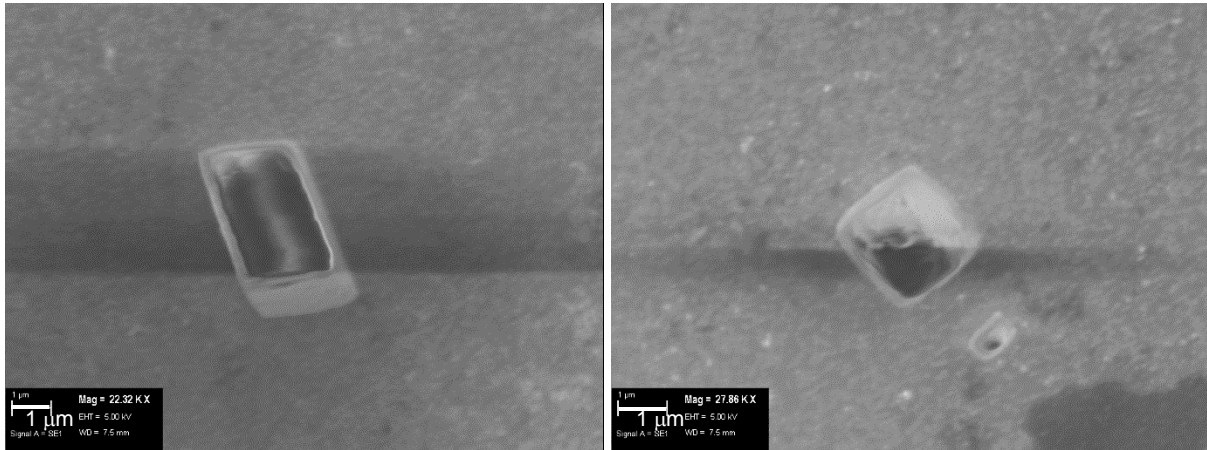


**Figure 5-21** SEM SE1 image of calcite deposits after 10 min at -400 mV

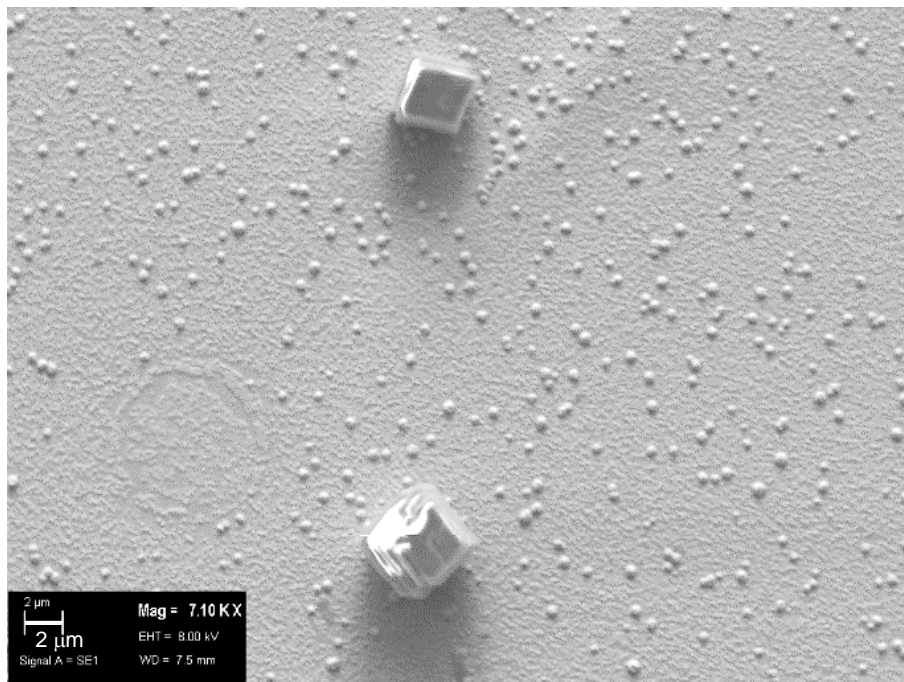


**Figure 5-22** SEM SE1 image of calcite deposits after 10 min at -400 mV

When depositions were performed for the shorter 5 minute period, far less calcite appeared on the surface than for those deposited on the analogous Au(111) surfaces; further, the depletion of the surrounding amorphous layer was observed for the growth of these particles. Figure 6-23 shows examples of very small calcite rhombohedra with the [1014] growth face in contact with the surface and the presence of the ring of depleted amorphous phase similar to that seen by Lee [5].

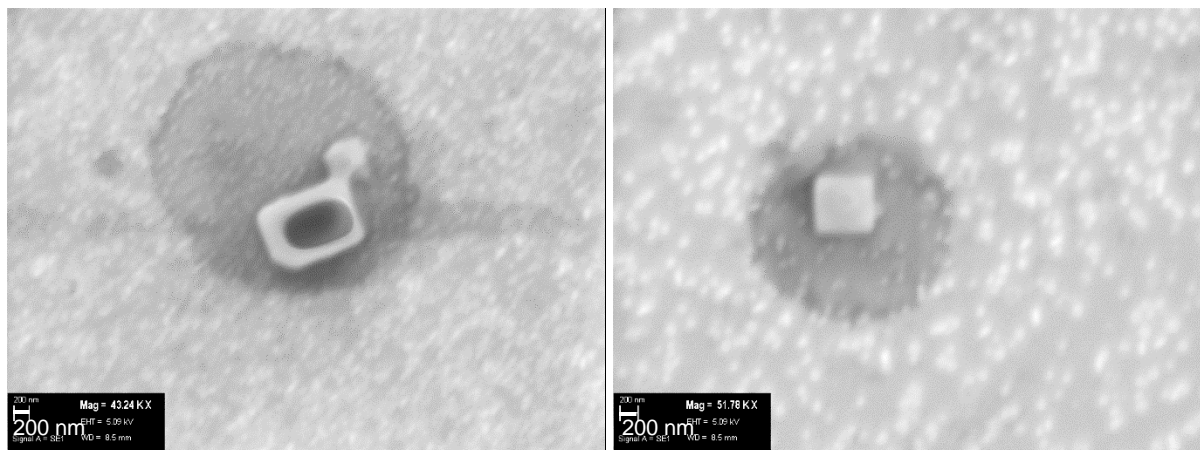


**Figure 5-21** SEM SE1 image of calcite deposits after 5 min deposition at -400 mV

## 5.4 Epitaxial Growth on Au(100)

Depositions on the Au(100) crystal were performed at reducing potentials of -1000 and -1400 mV however no precipitate was observed. Precipitates were only observed at -400 mV (Figure 5-24 and 5-25). It was observed that amorphous calcium carbonate was covering the single crystal surfaces with the similar small particles previously observed. There were also some larger amorphous deposits visible however no epitaxial growth was observed on any Au(100) surface.

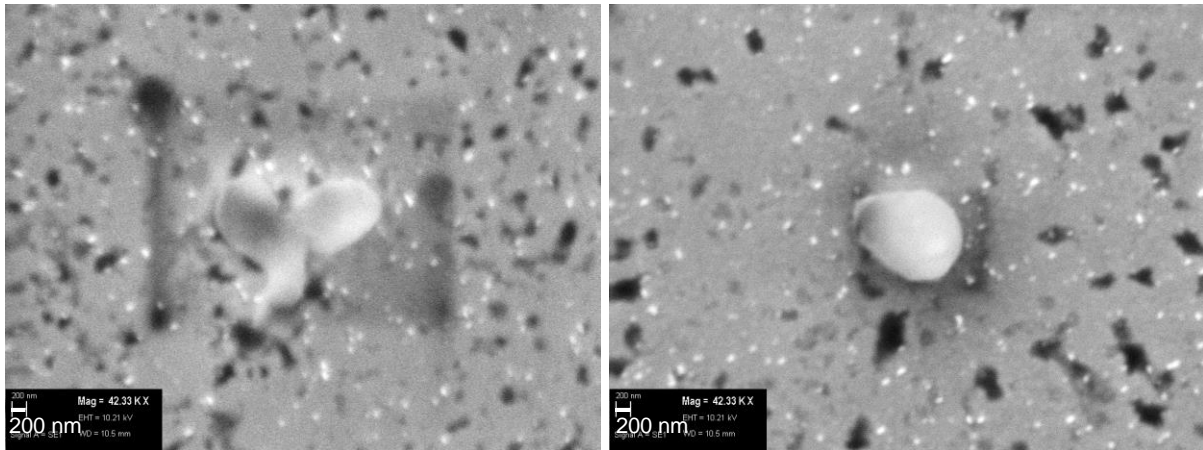


**Figure 5-24** SEM SE1 image of Au(100) surface after 10 min deposition at -400 mV

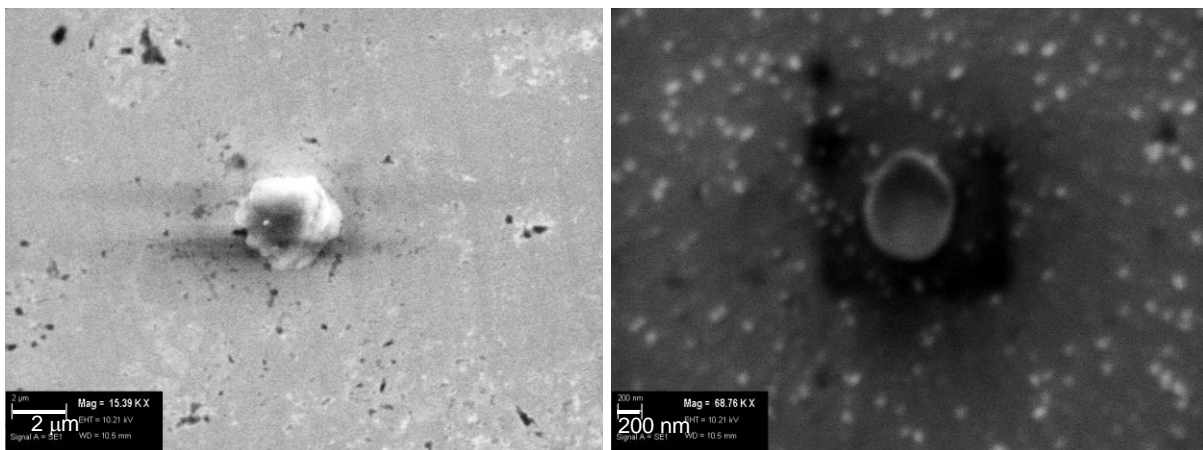


**Figure 5-25** SEM SE1 image of deposits after 10 min deposition at -400 mV

## 5.5 Discussion

The successful epitaxial growth has been controlled and monitored on the Au(111) and Au(110) surfaces. In agreement with that found by Teghidet we have observed the formation of calcite on the Au(111) with the calcite  $[10\bar{1}]$  face in contact with the gold surface. This was performed at -1000 mV, the potential at which dissolved oxygen is reduced to form surface hydroxides, also raising the local pH. The raised pH facilitates the precipitation of calcium carbonate and the ordered surface directs the deposition of epitaxial calcite. When a calcium layer is deposited over the Au(111) there is excellent parameter matching with that of the calcite  $[10\bar{1}]$ , the Au/Au distance of  $a=0.499$  nm and that of calcium  $a=0.498$  nm which explains the favourable epitaxy observed (Figure 5-26) [12].

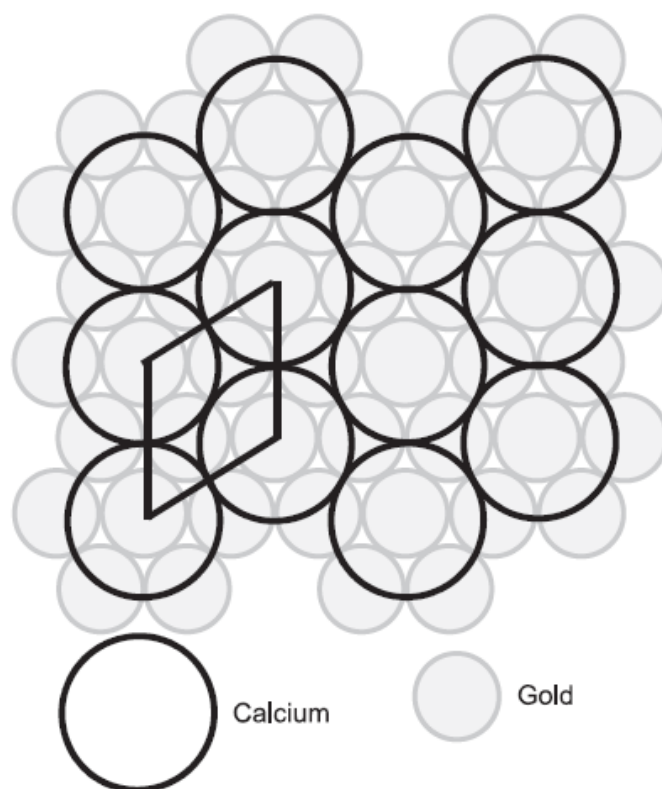


**Figure 5-26** Schematic of the epitaxial relationship between calcite and Au(111) surface [12].

At reduction potentials higher than -1000 mV dissolved oxygen will not form hydroxides at the surface and hence the formation of epitaxial calcite at -400 mV cannot be explained with this hypothesis. However at -400 mV dissolved  $\text{CO}_2$  forms oxalic acid, which is likely to be in the form of oxalate. Surface oxalate may be acting in a similar way to that of the hydroxide species, raising the local pH to encourage calcium carbonate precipitation and directing the epitaxial growth.

On the Au(110) surface no epitaxial growth is observed at -1000 mV although surface hydroxides are still likely to be produced however the surface structure of the Au(110) may not allow an ordered layer of hydroxides to influence the epitaxial growth due to the larger inter-atomic distances (0.816 nm). At -400 mV where oxalate is formed, epitaxial growth is once again observed, we hypothesise that the oxalate molecule is able to bridge the rows of atoms on the Au(110) surface giving an ordered matrix capable of the epitaxial formation of calcite, likely via an initial calcium oxalate surface layer before the calcite [1014] growth proceeds.

The Au(100) surface showed no epitaxial growth at any of the reduction potentials investigated. This may provide an explanation for the difficulty in forming core@shell nanomaterials using spherical gold nanoparticles. The nanoparticle surface is predicted to be

made up almost entirely of Au(111) and Au(100) surfaces. Since the epitaxial growth of calcium carbonate only occurs readily on one of these surfaces a complete coating is very difficult. Our conclusion is that further syntheses should be investigated whereby nanomaterials for carbonate coating are produced expressing more of the Au(111) and Au(110) faces while minimising the influence of the Au(100). Further investigation into other single crystal surfaces is also desirable to better understand the relationship between the epitaxial and non-epitaxial growth observed on the basal planes.

## References

1. Cao, G., *Nanostructures & Nanomaterials: Synthesis, Properties & Applications*. 2004, London: Imperial College Press. 433.
2. Reinert, F. and G. Nicolay, *Influence of the herringbone reconstruction on the surface electronic structure of Au(111)*. Applied Physics a-Materials Science & Processing, 2004. **78**(6): p. 817-821.
3. Starke, U. *STM examples of application [Online]*. 2012 20-07-15]; Available from: <http://www2.fkf.mpg.de/ga/research/stmtutor/stmex.html>.
4. Kuther, J., et al., *Templated growth of calcite, vaterite and aragonite crystals on self-assembled monolayers of substituted alkylthiols on gold*. Journal of Materials Chemistry, 1998. **8**(3): p. 641-650.
5. Lee, J.R.I., et al., *Structural development of mercaptophenol self-assembled monolayers and the overlying mineral phase during templated CaCO<sub>3</sub> crystallization from a transient amorphous film*. Journal of the American Chemical Society, 2007. **129**(34): p. 10370-10381.
6. Lee, S.W., K.B. Lee, and S. Bin Park, *A new approach to the synthesis of functional thin films: Hierarchical synthesis of CaCO<sub>3</sub> thin films and their transformation into patterned metal thin films*. Micron, 2009. **40**(7): p. 737-742.
7. Lee, I., et al., *Nanoparticle directed crystallization of calcium carbonate*. Advanced Materials, 2001. **13**(21): p. 1617.
8. Lee, K., et al., *Self-assembly of amorphous calcium carbonate microlens arrays*. Nature Communications, 2012. **3**: p. 7.
9. Kuang, M., D.Y. Wang, and H. Mohwald, *Fabrication of Au@CaCO<sub>3</sub> nanoparticles by in situ mineralization in hydrogel microspheres*. Chemistry of Materials, 2006. **18**(5): p. 1073-1075.
10. Kuther, J., et al., *Mercaptophenol-protected gold colloids as nuclei for the crystallization of inorganic minerals: Templated crystallization on curved surfaces*. Chemistry of Materials, 1999. **11**(5): p. 1317-1325.
11. Kuther, J. and W. Tremel, *Stabilization of aragonite on thiol-modified gold surfaces: effect of temperature*. Chemical Communications, 1997(21): p. 2029-2030.
12. Teghidet, H., et al., *Calcite epitaxy on Au and Ag (111)*. Journal of Crystal Growth, 2011. **331**(1): p. 72-77.
13. Gabrielli, C., et al., *Nucleation and growth of calcium carbonate by an electrochemical scaling process*. Journal of Crystal Growth, 1999. **200**(1-2): p. 236-250.
14. Huang, F.Z., et al., *Controlled deposition and transformation of amorphous calcium carbonate thin films*. Crystal Research and Technology, 2009. **44**(8): p. 818-822.
15. Tlili, M.M., et al., *Characterization of CaCO<sub>3</sub> hydrates by micro-Raman spectroscopy*. Journal of Raman Spectroscopy, 2002. **33**(1): p. 10-16.

# Chapter 6 Carbonate Formation On Au(111) Under UHV Conditions

---

## 6.1 Introduction

Ultra high vacuum (UHV) systems are utilised for the ability to study reactions occurring on the atomic and single molecule level. Using XPS and STM in a high vacuum system, the effect from any contaminants is minimised and it is possible to study the formation and reaction of extremely small quantities, XPS analysis can detect accurately the quantity and binding energies and hence chemical states of surface species down to fractions of a monolayer coverage.

The formation and reaction of calcium carbonate on an Au(111) single crystal under UHV conditions was studied to compliment the electrochemical work performed on Au(*h,k,l*) single crystals and for further information for the synthesis of core@shell type nanostructures. To form calcium carbonate under UHV conditions, first an evaporator would coat the Au(111) with metallic calcium followed by the exposure to CO<sub>2</sub> or CO<sub>2</sub>/O<sub>2</sub> mixtures to form the desired surface species.

Extensive attempts were made to deposit calcium, however no calcium was ever seen on the Au(111) surface after evaporation procedures. This was investigated thoroughly and it was concluded that the calcium was oxidising before the system was pumped down to high vacuum pressures or during the bakeout procedure and hence when the subsequent evaporation was attempted, the calcium had already oxidised preventing any deposition. No other means for calcium coating was available at the time, however a SAES caesium getter was available and as well as allowing an investigation of any other sources of error in the calcium deposition experiments it also provided a means of studying carbonate (Cs<sub>2</sub>CO<sub>3</sub>) formation on gold alloy surfaces albeit with a different metal than initially desired.

Classically Au is known to be an inert metal, large scale single crystals of the nature used here can be considered in this way. The doping of noble metals and metal oxides with alkali metals is a large area of research, with applications ranging from catalysis [1] to semiconductor production [2]. Here we focus on the doping of gold single crystals with caesium. When gold is coated with caesium it can form an alloy, it is unlikely to form a semiconductor in this case as the bulk gold crystal will always be the dominant contribution, for semiconductor properties to prevail the CsAu compound must be synthesised in a 50/50 ratio with a structure similar to that of CsCl [3].

Investigations have been conducted by Carley et al. of the reaction of CO<sub>2</sub>, O<sub>2</sub> and CO/O<sub>2</sub> mixtures at the interface of Cs doped Au(100) and Cu(110) surfaces. It was found that CO<sub>3</sub> species and various oxide species formed, at high CO/O<sub>2</sub> ratios the CO<sub>3</sub> species and a peroxy species dominated [4]. In this investigation we are exposing the Cs doped Au(111) surface to CO<sub>2</sub> and CO<sub>2</sub>/O<sub>2</sub> mixtures in the hope of forming carbonate dominant surfaces. Analogous investigations on the Cs doped Cu(110) surfaces have highlighted that doping of the surface increases the reactivity to CO<sub>2</sub> forming surface caesium carbonate species [5].

Carley's work focused on the effect of alloying in the case of high Cs coverages, the formation of an alloy is inferred from the emergence of Au<sup>+</sup> peaks in the Au 4f region. Upon formation of surface oxide or caesium carbonate species the Au<sup>+</sup> peaks disappear indicating that the formation of surface species has caused the dealloying of the CsAu [4, 6].

Here we are investigating the formation of surface species in the presence of low coverages of caesium on the Au(111) surface, investigating the presence of alloying and the activation of the surface towards CO<sub>2</sub> forming caesium carbonate and the subsequent thermal stability of the surface species formed.

## **6.2 Clean Au Surface, Stability of Clean Surface, Effect of CO<sub>2</sub> Exposure**

To ensure that no reaction occurred between CO<sub>2</sub> and the clean Au(111) surface, initial experiments focussed on the effect of exposure of CO<sub>2</sub> to a clean Au(111) single crystal. The Au(111) single crystal was cleaned by cycles of sputtering with Ar (2.5 x10<sup>-5</sup> mbar, 8-10 mA, 15 min) and annealing (500-600 °C), before the chamber was filled with CO<sub>2</sub> (1x10<sup>-6</sup> mbar, 10 min/30 min, 600/1800 L).

The XPS analysis reveals that the clean gold surface was not entirely cleaned of Cs, this is likely due to the high anneal temperature (~500-600 °C) drawing Cs from the bulk sample to the surface, however the Cs concentration was calculated to be just 0.025 ML coverage (Figure 6.1). The bulk gold signal does not change throughout and the Au 4f 7/2 is centred at 84.0 eV.

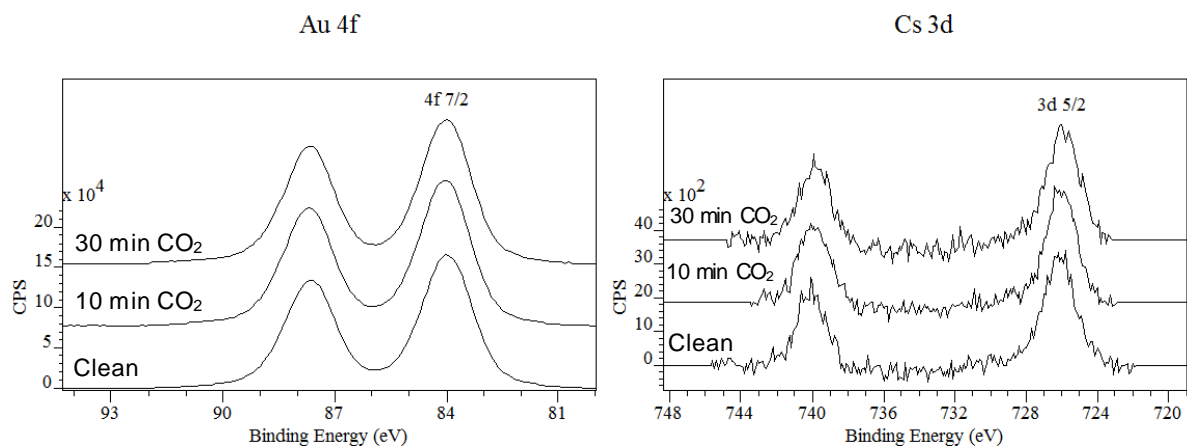


**Figure 6-1** XP spectra of Clean and CO<sub>2</sub> exposed Au(111) a) Au 4f region and b) Cs 3d region

It is observed in the O region that a small peak is present, the peak remains unchanged throughout the exposures and is hence not attributed to the CO<sub>2</sub> exposure. With a measured binding energy of 530.5 eV it is consistent with the presence of a Cs<sub>2</sub>O<sub>4</sub> species, further the coverage was calculated to be 0.035 ML coverage which would also support the formation of this oxide, therefore this peak is attributed to the presence of a caesium oxide.

Although this surface is not completely clean of impurities (Cs and O), what is apparent is that there is no change seen in any region observed after the exposure to CO<sub>2</sub>, therefore as expected it is concluded that the CO<sub>2</sub> does not interact with the gold, and hence that further studies can conclude than any carbon species generated on the surface after exposure to CO<sub>2</sub> are associated with the Cs.

The binding energy of Cs was found to be 726.1 eV which is very close to that of literature measurements of 726.4 eV, this can confidently be assigned to metallic Cs; any ionic form of Cs is at least 2 eV to a higher binding energy.

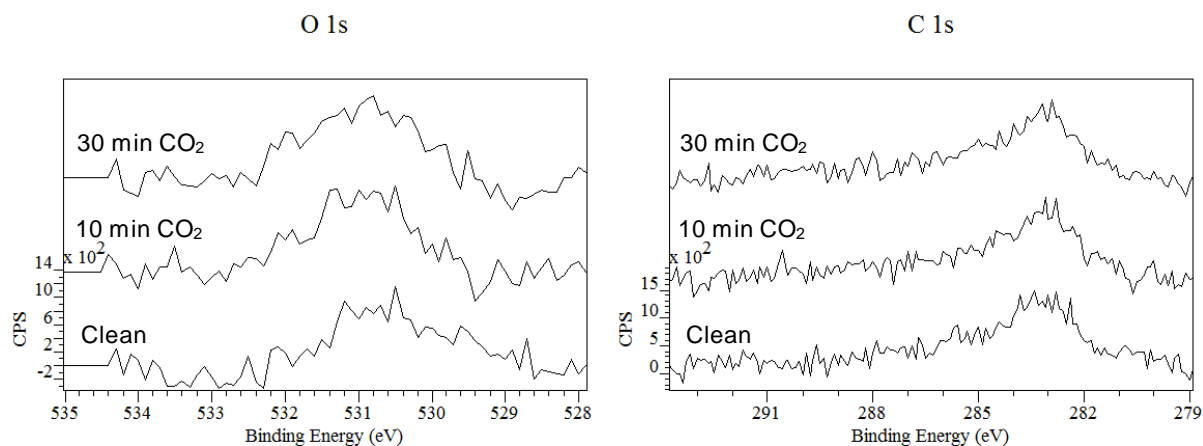


**Figure 6-2** XP spectra of Clean and CO<sub>2</sub> exposed Au(111) a) O 1s region and b) C 1s region

No peaks are seen in the carbon region which is the clearest indicator that the CO<sub>2</sub> is not interacting with the surface, the peak intensity observed here around 283 eV is due to an Al  $k\beta$  satellite peak of the Au 4d 5/2 due to the non-monochromatic X-ray source and not a carbide peak; the feature is not affected by exposure to CO<sub>2</sub>. This peak is seen in all spectra except for instances where an intense carbon peak causes a significant decrease in the scale of the vertical axis. It will not be discussed further.

## 6.3 Calibration of Cs Coating and Stability of Cs Layer in Vacuum

### 6.3.1 Caesium Coating Calibration

A calibration for the coating of caesium was performed; the Au(111) sample was coated with Cs from a SAES getter, the sample was then analysed using XPS to calculate the coverage, this process was repeated and the resulting calibration graph can be seen in Figure 6-3. It should be noted that when the Cs getter was left for longer periods than the incremental steps used for calibration, more Cs was released from the getter due to higher temperatures from prolonged current running through the getter, thus the calibration was only for estimation purposes. It was found that after 5 minutes 1.094 ML had been deposited. A further complication is that as the getter ages it releases more Cs in a shorter period of time. In all the experiments reported here dosing conditions are only guides however Cs concentrations have been accurately determined using XPS.

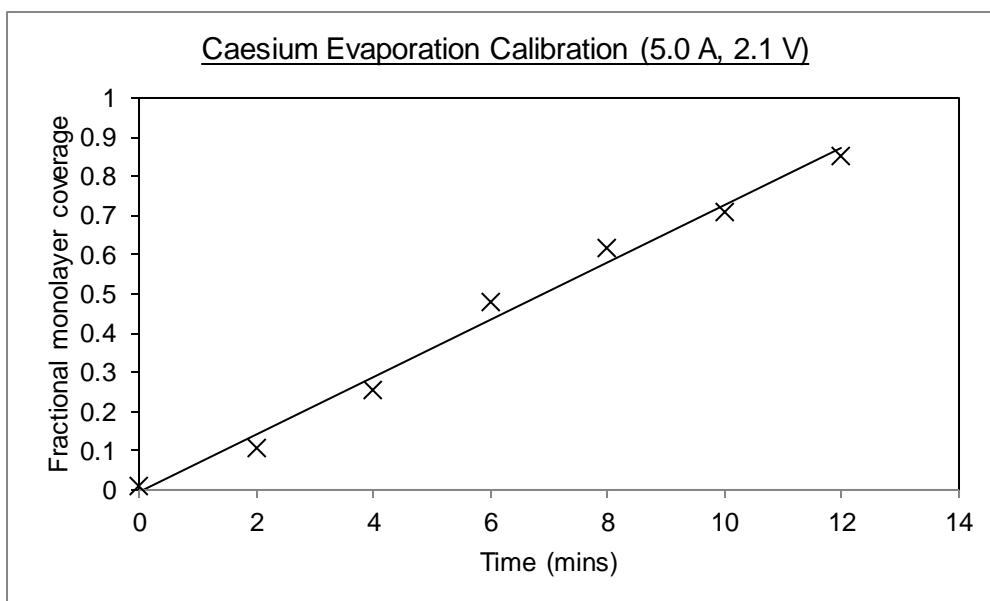


**Figure 6-3** Calibration for the coating of caesium on Au(111)

### 6.2.2 Caesium Stability in Vacuum

Caesium was deposited on the Au(111) single crystal (1.5 min, 5.0A, 2.1 V) and an XP spectrum recorded, the sample was then left under vacuum ( $1 \times 10^{-9}$ , 12 hrs).

XPS analysis revealed that the freshly coated surface contained 0.89 ML of Cs, the time taken to run this analysis was nearly 60 min and therefore the XPS analysis of the 'fresh' Cs layer is of the surface after ~60 min left under vacuum. The sample was then left under vacuum for 12 hrs. A subsequent XPS analysis revealed that after this time the sample has collected much residual oxide from the chamber. Interestingly after this period the coverage of Cs increased significantly from 0.89 to 1.35 ML.

After 12 hrs, carbon at 0.1 ML coverage and O at 1.1 ML coverage are observed. This high ratio of O/C suggests that there is a mixture of caesium oxide and  $\text{CO}_x$  species. The binding energy of the C species of 289.5 eV is very close to literature values of 289.3 eV for  $\text{Cs}_2\text{CO}_3$ . The O region binding energy of 531.2 eV matches exactly to that of literature values for  $\text{Cs}_2\text{CO}_3$ , however the O:C ratio indicates that this cannot be attributed to carbonate formation alone and other surface oxides must be present.

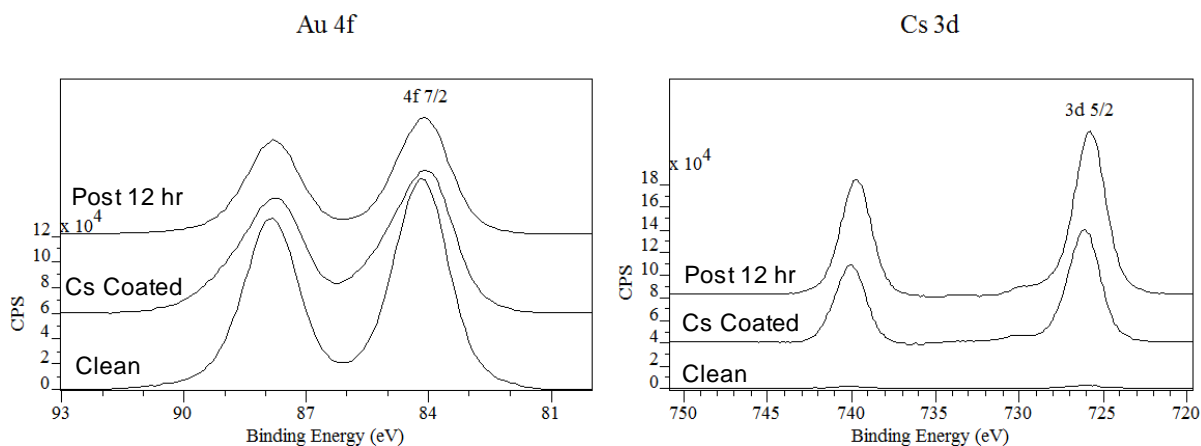


**Figure 6-4** XPS spectra of clean and Cs coated samples a) Au 4f region and b) Cs 3d region

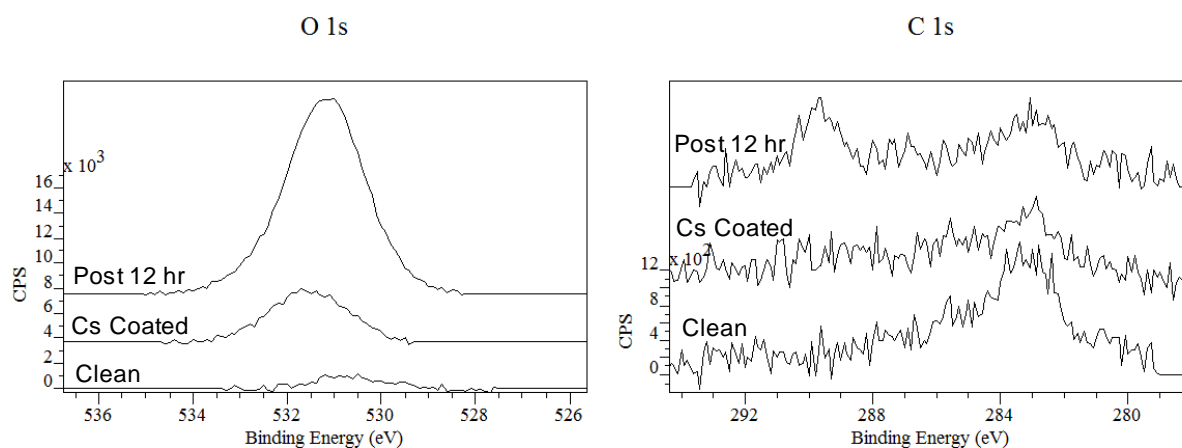


**Figure 6-5** XPS spectra of clean and Cs coated samples a) O 1s region and b) C 1s region

The Au 4f spectrum recorded of the freshly coated surface shows a very distinct asymmetry to higher binding energy which by the curve fitting in Figure 6.6 is shown to be consistent with the emergence of an  $\text{Au}^+$  species. The XPS spectra after 12 hrs when there is a high surface coverage of caesium oxide shows that this Au species no longer exists. This suggests that the freshly coated surface is forming the CsAu alloy reported by Carley et al.; when the surface oxides form it is accompanied by a dealloying of the Cs from the gold surface in favour of the more stable surface oxide. The increase in Cs coverage is also accompanied by a shifting of the Cs binding energy. The initial binding energy for Cs on the clean surface is 725.8 eV, upon coating with further Cs the binding energy shifts up by 0.3 eV to 726.1 eV before reverting back to 725.8 eV after the oxide layer has formed.

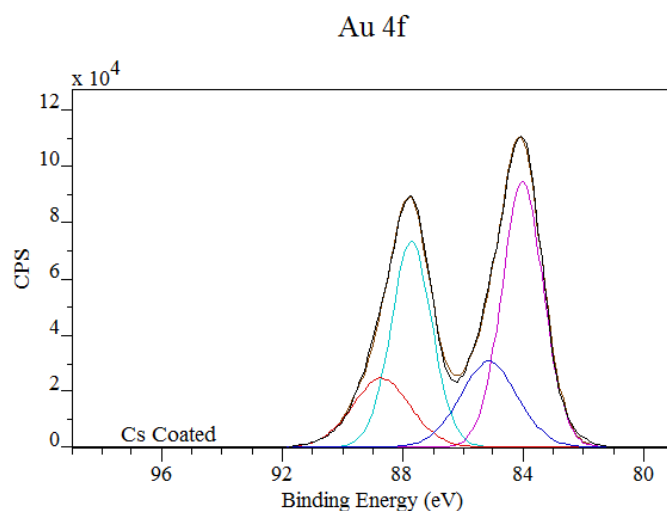


**Figure 6-6** XP spectrum of Au 4f region for the freshly coated Cs Au(111) surface

These experiments show that the freshly coated CsAu surface remains relatively free of contaminants for long enough for the subsequent exposures to CO<sub>2</sub>, however that freshly coated samples are not stable enough to be left for extended periods between experimentation.

## 6.4 Investigating Alloy Formation on Cs Coated Au(111) Surface

To investigate the presence of alloying and its effect on the formation of Cs<sub>2</sub>CO<sub>3</sub>, experiments were conducted whereby the deposition of Cs followed by exposure to CO<sub>2</sub> gas was performed on three different surfaces: a freshly sputtered surface, which should exhibit the highest degree of disorder; a partially annealed surface (~300 °C) and an annealed surface (~600 °C). In each case the surface was coated with Cs (5.0 A, 2.1 V, 1 min), and exposed to CO<sub>2</sub> (1x10<sup>-6</sup> torr, 10 min, 600 L).

### 6.4.1 Sputtered Surface

The clean sputtered Au(111) surface shows no trace of caesium, and as a result of the absence of Cs, there is no trace of any surface oxides. XPS analysis of the sample after Cs deposition shows the lowest level of surface Cs for any analogous deposition conditions with the surface coverage calculated to be 0.61 ML. Interestingly, once the coated surface was exposed to CO<sub>2</sub> there was no increase in Cs concentration, maintaining a 0.61 ML coverage and no shift in binding energy (Figure 6-7). This suggests that there has been no change to the surface Cs in response to the exposure of CO<sub>2</sub>, this is supported by the O and C region analysis.

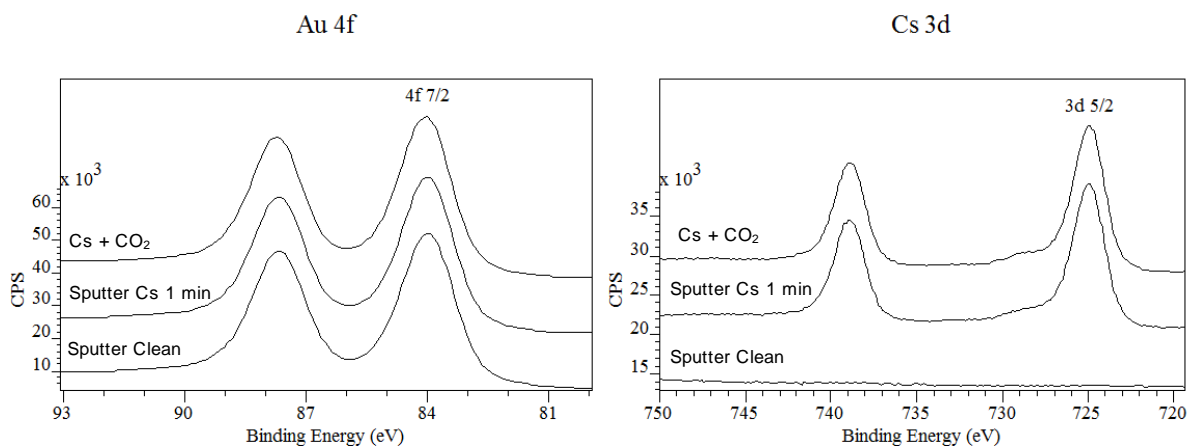


**Figure 6-7** XPS spectra of sputtered only surfaces a) Au 4f region and b) Cs 3d region

After deposition of Cs, peaks appeared in the O and C region; the binding energy of the peak observed in the O region is 530.5 eV indicative of caesium oxide formation, the surface coverage is calculated to be 0.30 ML. After exposure to CO<sub>2</sub> the O peak remains unchanged, both the binding energy and coverage remaining at 530.5 eV and 0.32 ML respectively. Similarly in the C region a very small peak is observed after the coating with Cs, which again remains unchanged upon exposure to CO<sub>2</sub> (Figure 6-8). The O/C ratio is calculated to be 4/1 pointing to the formation of caesium oxide and some CO<sub>x</sub> species.

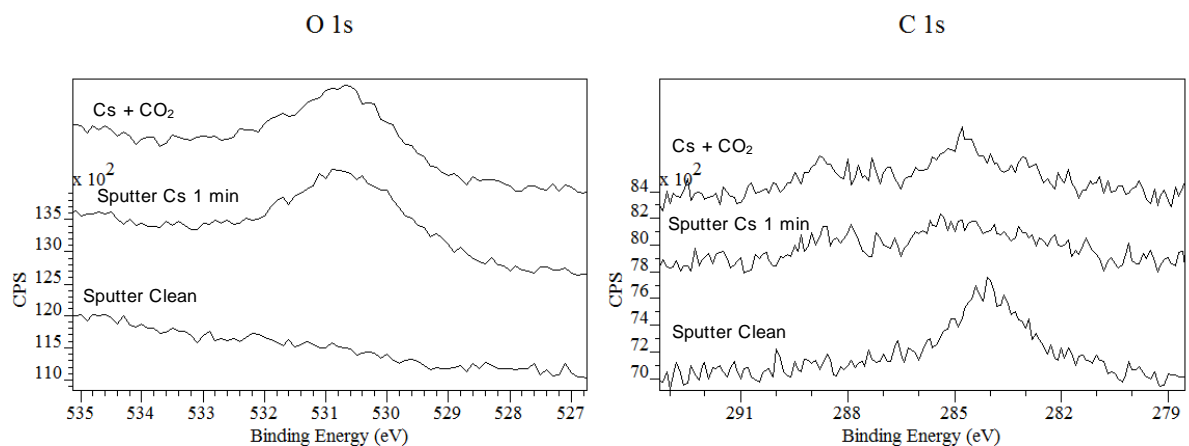


**Figure 6-8** XPS spectra of sputtered only surfaces a) O 1s region and b) C 1s region

### 6.4.2 Partially Annealed Surface

The clean partially annealed surface has some residual Cs present, although the coverage is calculated to be negligible 0.006 ML, there are no associated O or C peaks appearing in the XPS analysis. After deposition of Cs the surface coverage is calculated to be 0.72 ML, upon exposure to CO<sub>2</sub> this remains at 0.72 ML (Figure 6-9). It is interesting to note that on the partially annealed surface, the binding energy of the Cs changes upon exposure to CO<sub>2</sub>

indicating some change in the Cs metal character, the binding energy has shifted -0.3 eV, indicating minor changes in the metal structure of the Cs. This may be due to the initial formation of a CsAu alloy and upon exposure to CO<sub>2</sub> dealloying has occurred in favour of the more stable caesium oxide and caesium carbonate surface species.

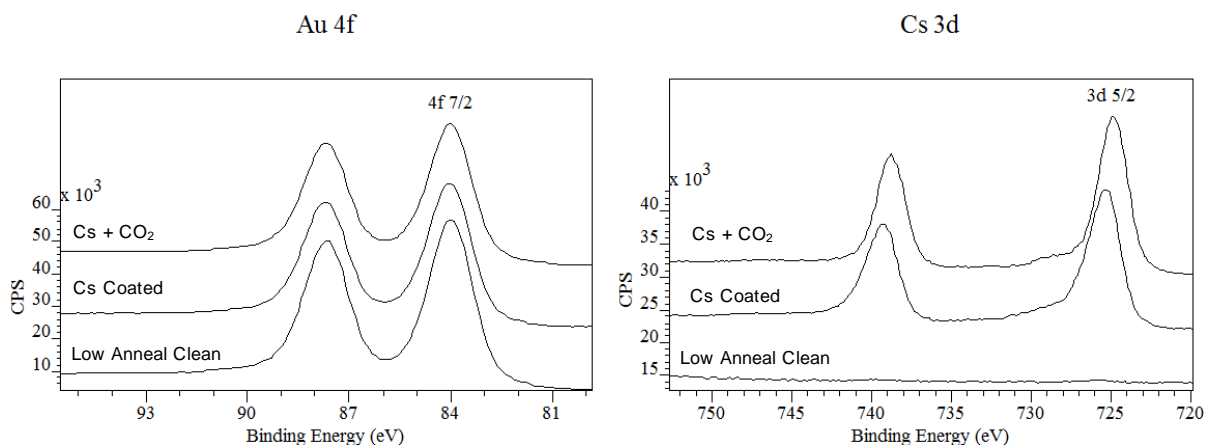


**Figure 6-9** XPS spectra of partially annealed surfaces a) Au 4f region and b) Cs 3d region

The O region shows there to be surface oxides after deposition of Cs, this rises after exposure to CO<sub>2</sub> along with the appearance of a peak in the C region (Figure 6-10). The coverage of O after the deposition of Cs is calculated to be 0.37 ML rising to 0.52 ML after the exposure to CO<sub>2</sub>. This is accompanied by a change in the O binding energy from 529.7 to 530.5 eV. Cs is able to form numerous different surface oxides and this indicates a change from one surface oxide to another upon exposure to CO<sub>2</sub> [7]. The peak that emerges in the carbon region has a binding energy of 288.6 eV which is low for carbonate formation, this could indicate the presence of other CO<sub>x</sub> species such as CO, CO<sub>2(ads)</sub> or C<sub>2</sub>O<sub>4</sub><sup>2-</sup>. The O/C ratio is 1.4/1, based upon the calculated monolayer coverage (Equation 2-35). Although this ratio is much lower than the expected 3/1 expected for carbonate formation, it is worth noting that the ratio of O/C can appear much lower in XPS calculations than that expected for carbonate [8]. However, in this case the ratio is beyond the lower estimate expected for carbonate. The unusual stoichiometry and lower than expected binding energies for both the O and C regions could indicate oxalate formation, which has been proposed as a surface intermediate during reactions of CO<sub>2</sub> on metal surfaces. However, this would imply the formation of a C-C bond and further evidence (ideally vibrational) would be needed to support this assignment.

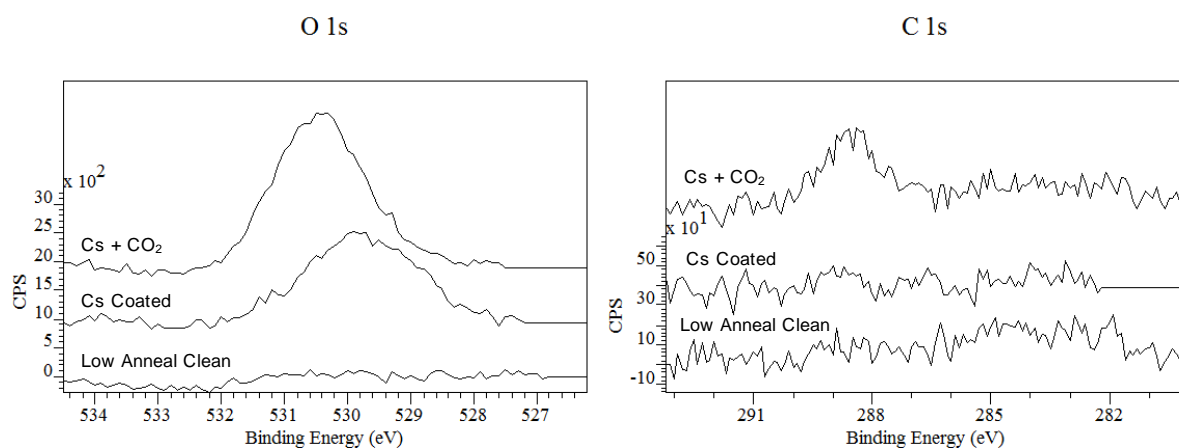


**Figure 6-10** O 1s and C1s XP spectra of partially annealed surfaces after deposition of Cs and exposure to CO<sub>2</sub>.

### 6.5.3 Annealed Surface

The clean and annealed surface has a higher coverage of residual Cs, calculated to be 0.02 ML, than that of the partially annealed surface, supporting the annealing procedure drawing more Cs from the bulk to the surface (Figure 6-11). There is also some residual oxide peak observed in the O region, calculated at a coverage of 0.07 ML and with a binding energy of 530.2 eV. The binding energy is in the region expected for carbonate or caesium oxide, however there is no occurrence of C in the XPS analysis of the clean sample, therefore this is attributed to the presence of surface caesium oxide species.

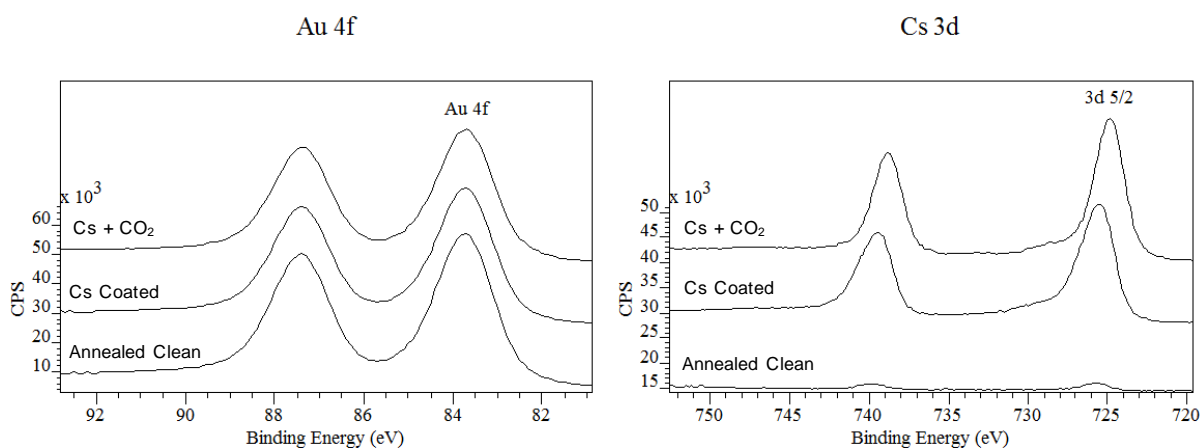


**Figure 6-11** XP spectra of annealed surfaces a) Au 4f region and b) Cs 3d region

In the Cs region a shift is again seen between the freshly coated and CO<sub>2</sub> exposed surfaces, further the observed shift is greater than that of the partially annealed surface with a shift of -0.8 eV. The coverage of Cs also increases between the freshly coated and CO<sub>2</sub> exposed surfaces, with calculated coverages of 0.8 ML and 0.92 ML respectively. This increase in

coverage is greater than that observed for the partially annealed surface. This shift in binding energy and coverage increase upon exposure to CO<sub>2</sub> is attributed to the initial formation of a CsAu alloy, before the formation of surface caesium carbonate upon exposure to CO<sub>2</sub> and the subsequent dealloying of the surface.

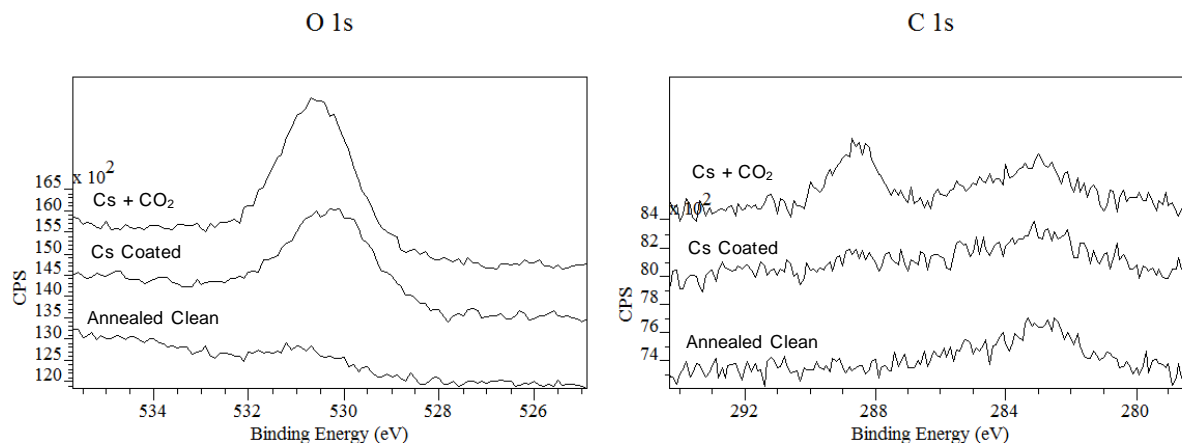


**Figure 6-12** XPS spectra of annealed surfaces a) O 1s region and b) C 1s region

The O region shows that there is a shift from 530.2 to 530.6 eV upon exposure to CO<sub>2</sub>, a significant peak in the C region also develops upon exposure to CO<sub>2</sub> confirming the presence of surface CO<sub>x</sub> species. The O/C ratio of the freshly coated surface is calculated to be 4.8/1, this indicates that there is likely caesium oxide and some CO<sub>x</sub> species present. Upon exposure to CO<sub>2</sub> this ratio changes to 2.35/1, this ratio is consistent with that seen in the literature with XP studies of surface carbonate formation [8]. The binding energies are within the range for that expected for carbonate in both the O and C region [9]. Caesium carbonate formation was not conclusively identified on the partially annealed surface, however it is on the annealed surface. This is attributed to the higher surface order of the annealed surface, and higher Cs coverage.

## 6.5 Formation of Cs<sub>2</sub>CO<sub>3</sub> on Au(111)

Cs (5.0 A, 2.1 V, 6 min) was deposited on a clean Au(111) single crystal and the sample then exposed to CO<sub>2</sub> (1x10<sup>-6</sup> torr, 10 min, 600 L), STM analysis was performed after each procedure.

The O and C region remained clear suggesting very low contamination for the clean Au(111) surface (Figure 6-14), this is explained due to the negligible residual caesium, calculated to be >0.03 ML (Figure 6-13 b)).

After the Cs deposition, its coverage was calculated to be 0.44 ML with the caesium possessing a binding energy of 725.8 eV. Upon exposure to CO<sub>2</sub> the caesium coverage increased to 0.53 ML, accompanied by a shift in binding energy of -0.5 eV to 725.3 eV.

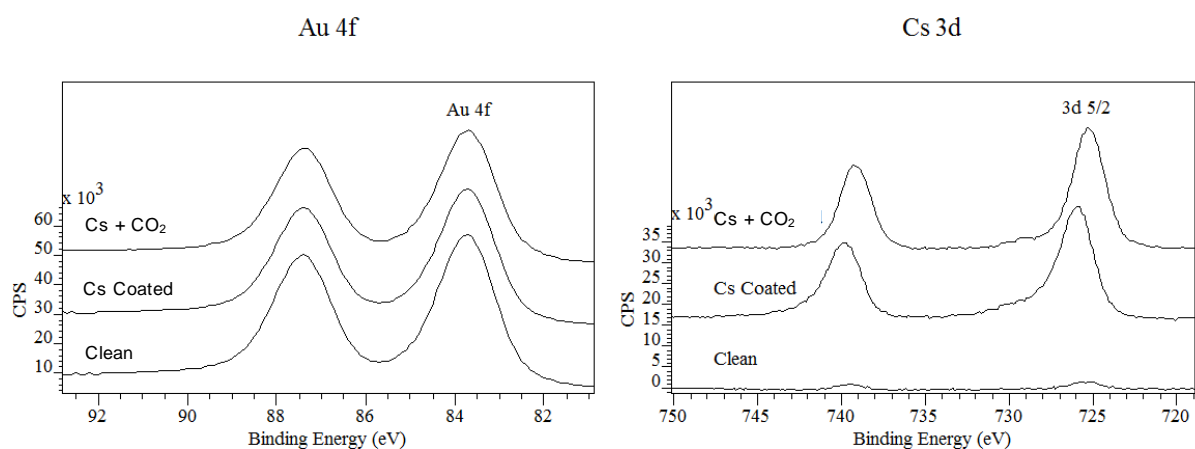


**Figure 6-13** XPS spectra of caesium carbonate formation a) Au 4f region and b) Cs 3d region

The O region (Figure 6-14 a)) remains clear of O species in the clean sample, upon deposition of Cs a small peak is observed at 530.9 eV with a surface coverage of 0.08 ML, there is no accompanying peak in the C region (Figure 6-14 b)) and hence this is attributed to the formation of a caesium oxide species. After the surface has been exposed to CO<sub>2</sub> a large peak is observed in the O region, shifted 0.2 eV to 531.1 eV, this binding energy suggests the presence of a carbonate or oxide species. The C region post CO<sub>2</sub> exposure possess a significant peak with binding energy of 288.5 eV this is slightly lower than the literature value for Cs<sub>2</sub>CO<sub>3</sub> however the influence of the gold surface may be causing this shift in observed binding energy, and the value is well within the range for carbonates [9]. The O/C ratio is 2.98/1 which confirms the likely surface species as being that of Cs<sub>2</sub>CO<sub>3</sub>.

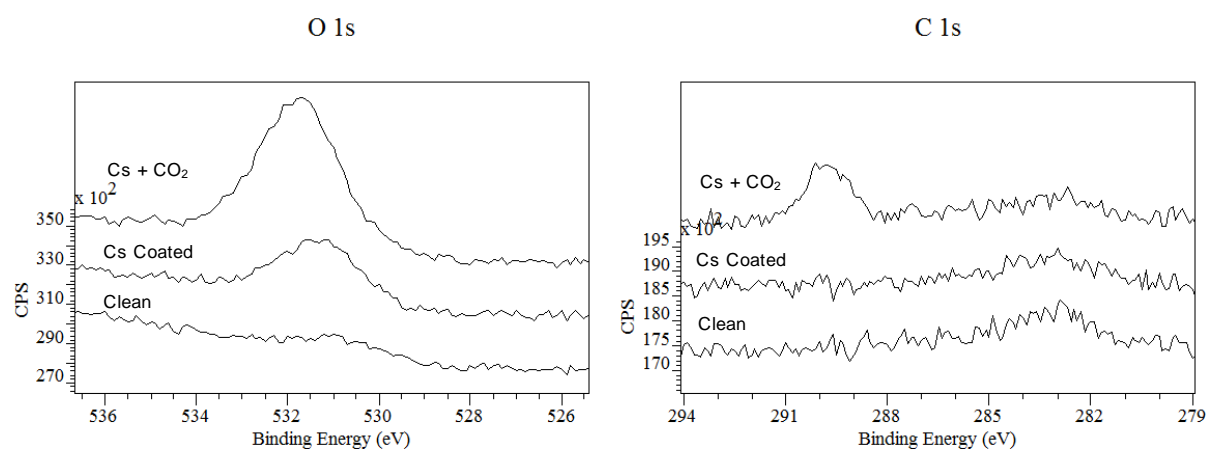


**Figure 6-14** XPS spectra of caesium carbonate formation a) O 1s region and b) C 1s region

Figure 6-15 shows the STM analysis of the clean gold surface, good resolution is observed with the presence of many large terraces and steps.

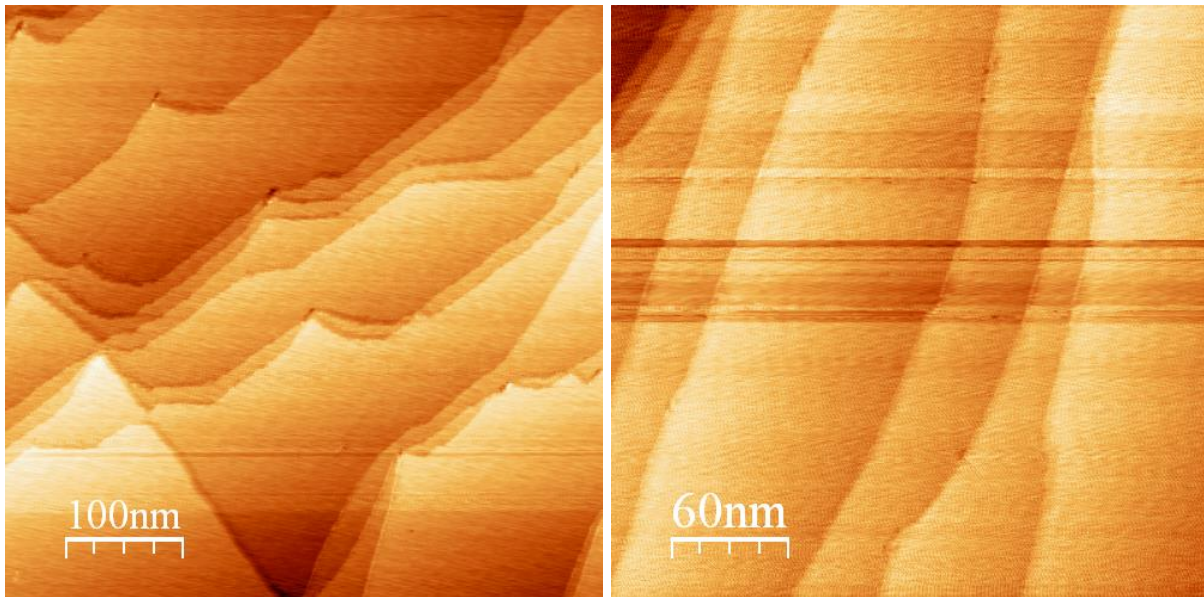


**Figure 6-15** STM images of the clean Au(111) surface

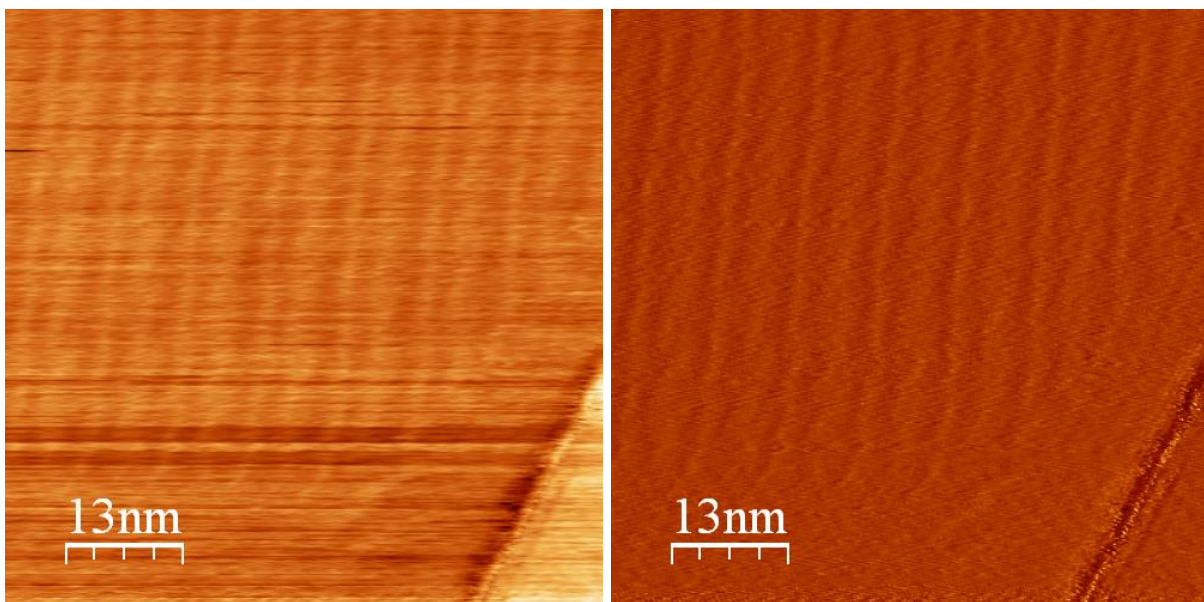


**Figure 6-16** STM images of the surface reconstruction of the clean Au(111) surface

Figure 6-16 shows high resolution STM images of the Au(111) surface. This surface undergoes a reconstruction ( $22\times\sqrt{3}$ ), leading to the well-known herringbone structure discussed previously (Chapter 5.1). Gold has an fcc crystal structure, the surface however undergoes a reconstruction to reduce surface energy, with a contraction along the [110] direction leading surface Au atoms to be pushed sideways along the [111] direction, this causes the Au atoms to express a more hcp stacking structure, at the domain boundaries

with the atoms forming ridges; it is these ridges which are visible in Figure 6-16. To show that the observed ridges are not an artefact of the STM analysis two images are presented one recorded in the forward (Figure 6-16 a)) and one in the backward direction (Figure 6-16 b)). If this were an artefact of the STM analysis the observed diagonal tendency of the ridges would appear in mirror image, however they remain in the same direction and hence are due to a true surface structure. STM analysis was performed at room temperature and hence the Au surface atoms are relatively mobile such that atomic resolution is not possible. Figure 6-17 shows an STM image of the Au(111) surface taken at 80 K from reference [9], this low temperature image reveals not only the ridges seen in Figure 6-16, but also the individual atoms and the observed displacement at the domain boundaries where the ridges occur.

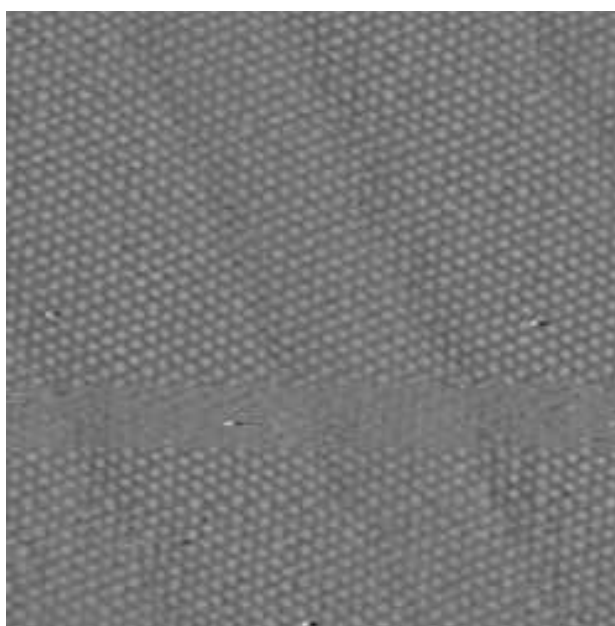


**Figure 6-17** STM image of a low temperature Au(111) surface reprinted from [10]

STM analysis of the surface revealed that after Cs deposition (0.43 ML) the ordered surface is no longer visible (Figure 6-18), this is attributed to the inclusion of Cs into the Au surface. This is in agreement with similar studies on the Ag(110) surface [11], and that the Cs and Au atoms are highly mobile in the alloyed state, preventing higher resolution in the STM.

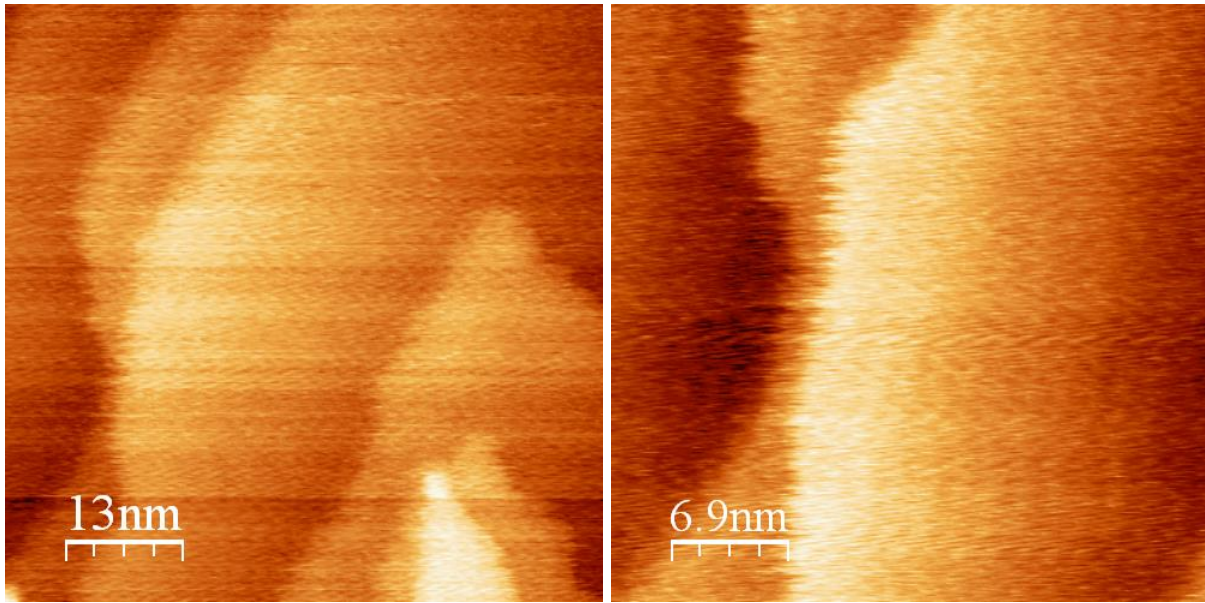


**Figure 6-18** STM images of the Cs coated Au(111) surface

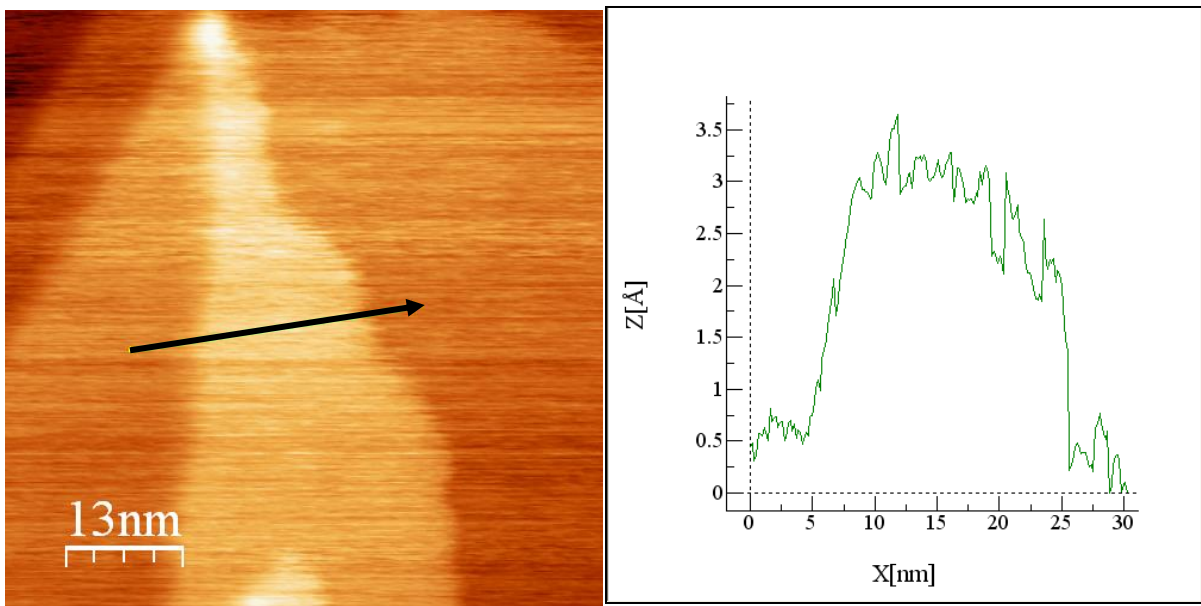


**Figure 6-19** a) STM image of the Cs coated Au(111) surface and b) Z direction cross section analysis

Figure 6-19 a) shows a terrace on the Cs coated Au(111) surface, the height of the terrace is measured in 6-19 b) to be  $\sim 2.5 \text{ \AA}$ , the atomic diameter of metallic Au is  $2.88 \text{ \AA}$ , the small discrepancy in the atomic diameter can be explained by the surface contraction of the Au surface. If this terrace were formed purely of Cs the expected height would be  $\sim 5.2 \text{ \AA}$  which is significantly higher than that observed here. Further if caesium atoms were on top of the Au surface large  $5 \text{ \AA}$  protrusions would be observed, this therefore supports the inclusion of the Cs in the Au surface forming an alloy.

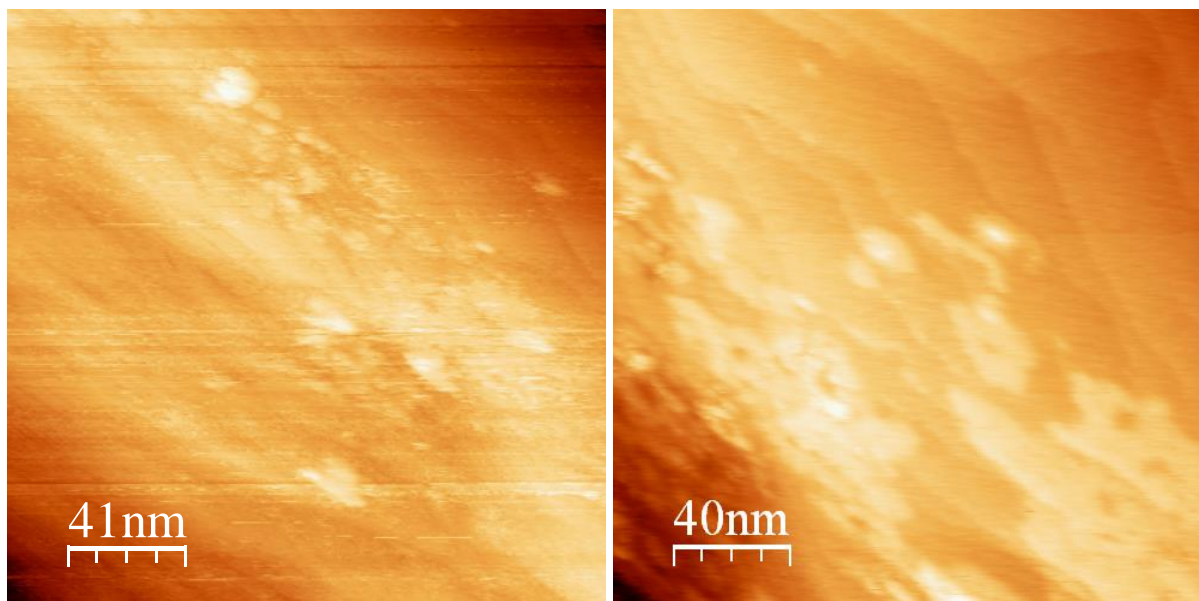


**Figure 6-21** STM image of  $\text{Cs}_2\text{CO}_3$  islands on the Au(111) surface

Figure 6-21 shows images obtained after Cs coating and exposure to  $\text{CO}_2$ , steps and large terraces of the Au(111) surface are still visible, most interesting is the creation of large islands which have formed over the surface. Although there is no clear long range order of these islands, what can be seen in the lower right quartile of Figure 6-21 b) is that the Au(111) step edge boundaries can still be seen, this shows that the islands have formed in an ordered manner over the Au as they are still expressing the Au structure below. The XPS analysis (Figure 6-13 and 6-14) supports the formation of  $\text{Cs}_2\text{CO}_3$  with roughly a  $\sim 0.5$  ML coverage.

The combination of XPS and STM analysis has shown that an initial CsAu alloy is forming upon deposition of Cs on the clean Au(111) surface. When this alloy is exposed to  $\text{CO}_2$  the more stable  $\text{Cs}_2\text{CO}_3$  forms, causing dealloying of the surface, further drawing Cs from the sub-surface and forming large island structures.

## 6.6 Thermal Stability of Caesium Carbonate

The thermal stability of surface  $\text{Cs}_2\text{CO}_3$  was investigated; initially the clean Au(111) surface was coated with Cs, then exposed to  $\text{CO}_2$  to form the caesium carbonate. The samples were then heated (100-500  $^\circ\text{C}$ ) and analysed using XPS.

### 6.6.1 Caesium Carbonate Formation and Thermal Stability at ~1 ML Coverage

The clean Au(111) surface was exposed to Cs (5.0 A, 2.1 V, 1 min) before exposure to CO<sub>2</sub> (1x10<sup>-6</sup> torr, 10 min, 600 L).

The XPS analysis of the Cs region of the clean Au(111) surface (Figure 6-22 b)) shows a very small signal for Cs, with a negligible residual coverage calculated to >0.03 ML, subsequently there is no residual C or O visible in the regions for this sample (Figure 6-24).

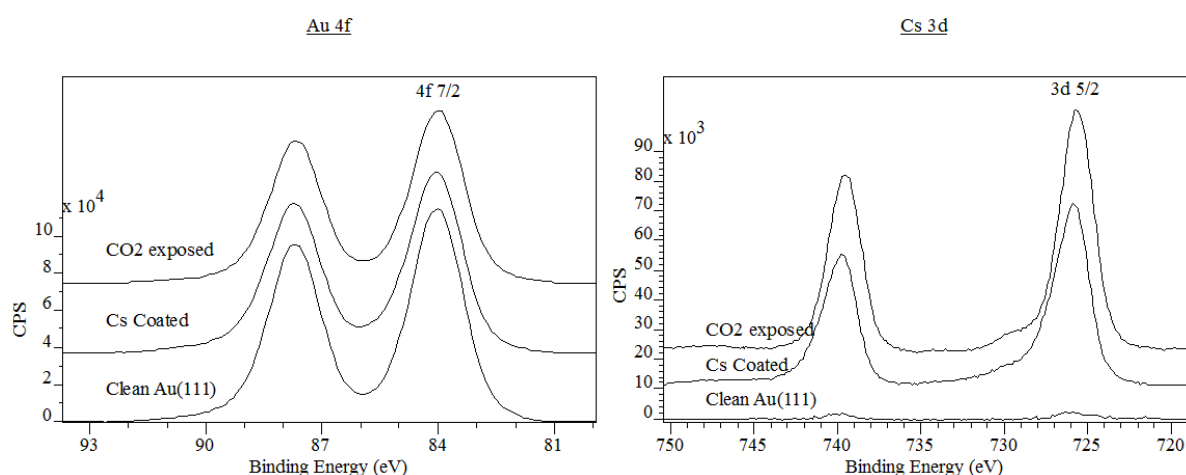


**Figure 6-22** XP spectra of clean, Cs coated and CO<sub>2</sub> exposed surfaces a) Au 4f region and b) Cs 3d region

The Cs region after deposition shows a large Cs peak with a binding energy of 726.0 eV for which the coverage was calculated to be 0.92 ML. After exposure to CO<sub>2</sub> the Cs binding energy has shifted by -0.3 eV to 725.7 eV and the Cs coverage has increased to 1.11 ML, now attributed to the formation of large surface island structures of Cs<sub>2</sub>CO<sub>3</sub>.

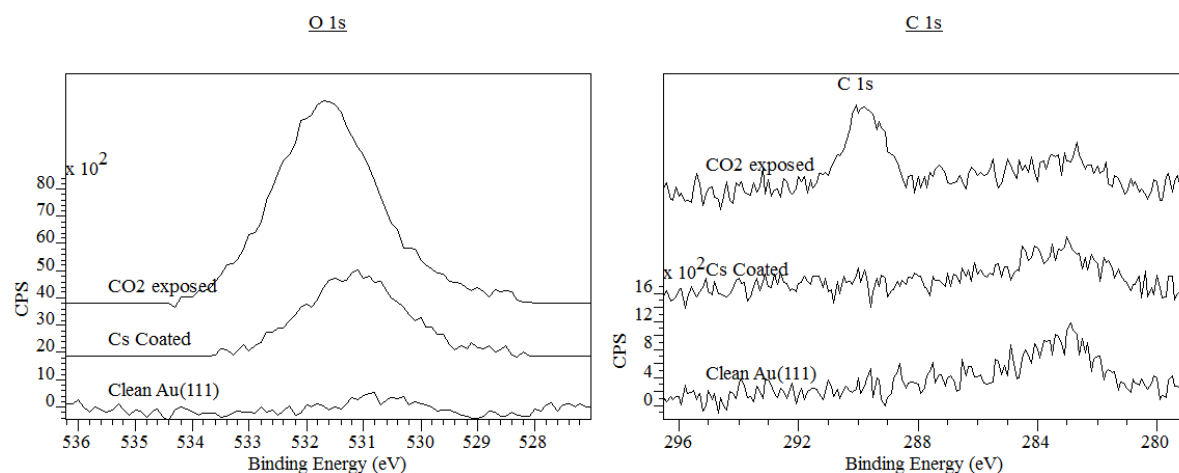


**Figure 6-23** XP spectra of clean, Cs coated and CO<sub>2</sub> exposed surfaces

The O and C region support the formation of  $\text{Cs}_2\text{CO}_3$ : After the deposition of Cs it can be seen that a peak appears in the O region, with a binding energy of 531.1 eV this is in the range for carbonates and oxides, the C region however remains clear of any peak, supporting the formation of surface caesium oxide species. Once the surface has been exposed to  $\text{CO}_2$  the O peak is now centred at 531.7 eV more akin to the expected binding energy for carbonates. This is accompanied by the appearance of a peak in the C region at 289.8 eV, the O/C ratio is calculated to be 2.3/1 which again supports the formation of  $\text{Cs}_2\text{CO}_3$ .

The sample was then heated (100, 200, 300 and 400 °C, 10 min) and monitored with XPS (Figure 6-24 and 6-25). The Cs, C and O region all show a similar trend in binding energy shift. The binding energies initially rise at 100 °C before slowly, incrementally lowering at each higher temperature. After the final heating step to 400 °C there is still a significant amount of  $\text{Cs}_2\text{CO}_3$  on the surface but the Cs coverage has dropped from 1.11 ML to 0.67 ML. Similarly the C and O coverage has reduced from 0.31 – 0.19 ML and 0.71 – 0.46 ML respectively, the O/C ratio has remained at that expected for carbonate formation, fluctuating from 2.3/1 to 2.5/1.

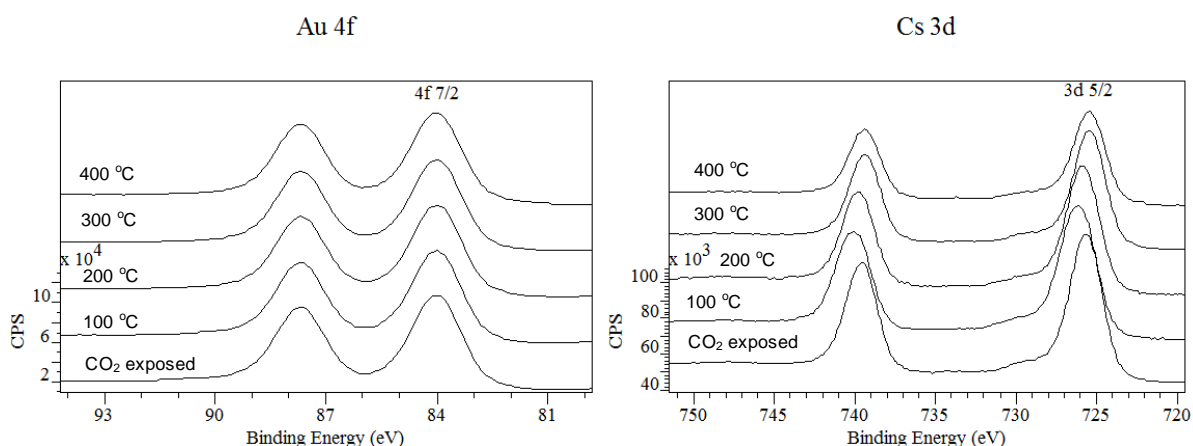


**Figure 6-24** XP spectra of heated samples a) Au 4f region and b) Cs 3d region

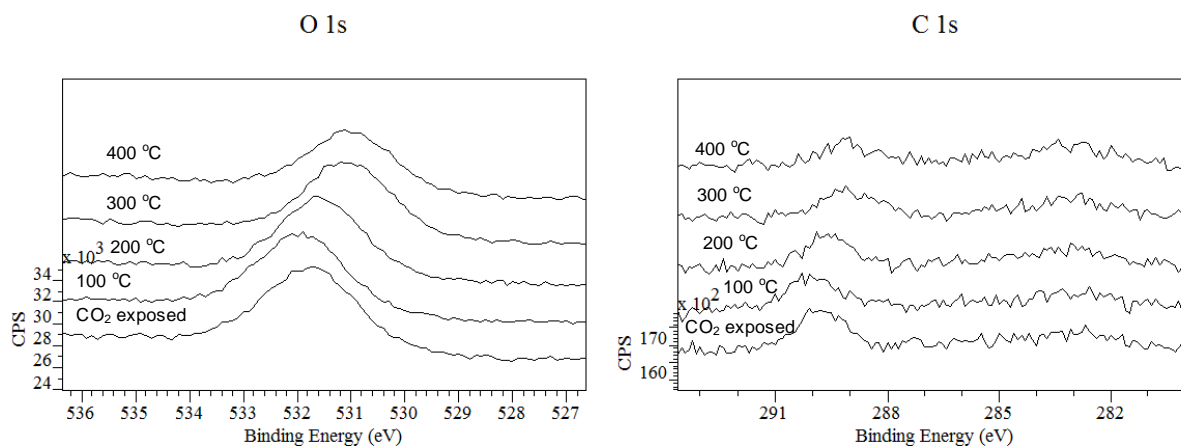


**Figure 6-25** XPS spectra of heated samples a) O 1s region and b) C 1s region

A similar set of experiments were run to those above but involving heating the surface further to 500 °C. The clean Au(111) surface was coated with Cs (5.0 A, 2.1 V, 1 min) and exposed to CO<sub>2</sub> (1x10<sup>-6</sup> torr, 10 min, 600 L).

The XPS analysis again supports the formation of caesium oxide formation upon deposition of caesium, the Cs surface coverage was 0.89 ML very close to that obtained above. The subsequent exposure to CO<sub>2</sub> again resulted in an observed shift in the Cs binding energy and increase in coverage from 0.89 – 0.92 ML (Figure 6-26).

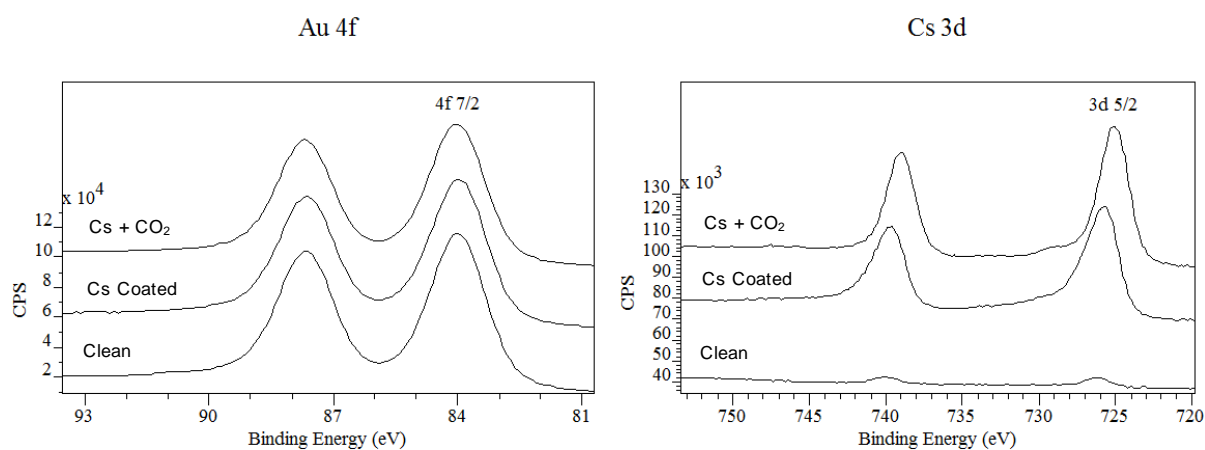


**Figure 6-26** XPS spectra of the clean, Cs coated and CO<sub>2</sub> exposed surfaces a) Au 4f region and b) Cs 3d region

The O and C regions again support the formation of caesium oxide after deposition of Cs and the formation of caesium carbonate after exposure to CO<sub>2</sub> (Figure 6-27). The O/C ratio is calculated to be 2.25/1 very close to that obtained above and indicating the formation of

caesium carbonate. The binding energy for O was measured at 530.8 eV and the C region at 289.0 eV which supports the assignment to carbonate formation.

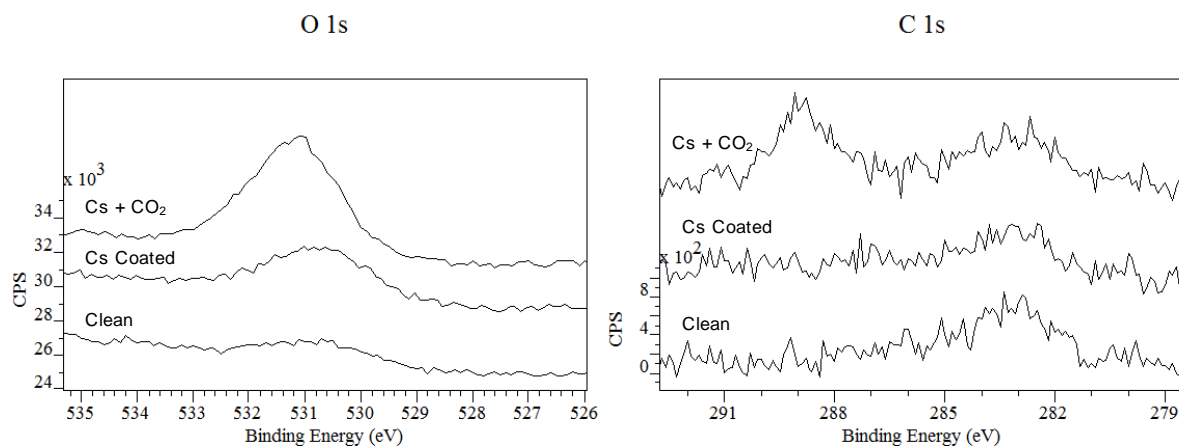


**Figure 6-27** XP spectra of the clean, Cs coated and CO<sub>2</sub> exposures surfaces a) O 1s region and b) C 1s region

The surface was then heated, this time to a higher temperature of 500 °C (Figure 6-28 and 6-29). What is immediately evident is that at 500 °C the caesium carbonate has decomposed leaving the surface, there is no peak observed in the C region after this heating cycle, the O has reduced considerably and the Cs has also reduced. Of particular interest here is that once the carbonate has decomposed the binding energy for the Cs shifts considerably back to that observed in the clean (residual) and freshly coated Cs samples.

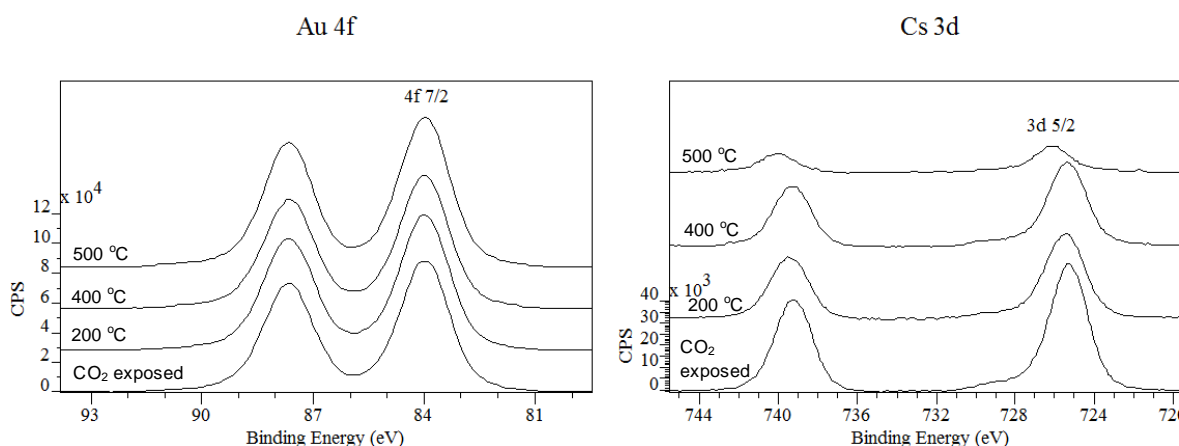


**Figure 6-28** XP spectra of heated surfaces a) Au 4f region and b) Cs 3d region

As before when the sample was heated the Cs binding energy initially shifted to a higher binding energy between 100 and 200 °C, before gradually lowering upon further heating.

However when the sample is heated to 500 °C a sudden drop in the coverage is observed along with a shift to higher binding energy. The O region shows a gradual reduction in coverage as does the C region, again at 500 °C the O region has become very weak and there is no peak in the C region.

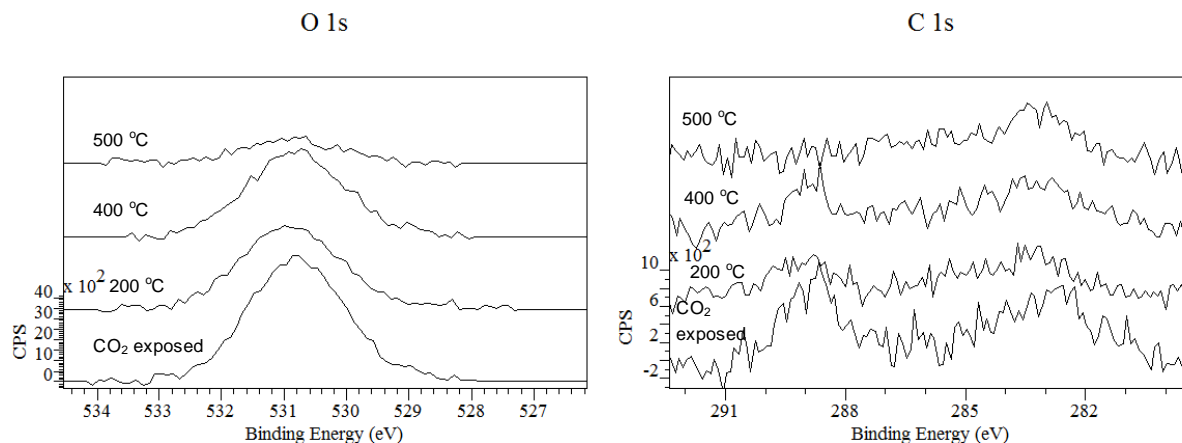


**Figure 6-29** XP spectra of heated surfaces a) O 1s region and b) C 1s region

When the Cs region of the clean Au(111) surface is compared to that of the sample which has been heated to 500 °C it can be seen that the binding energies are the same.

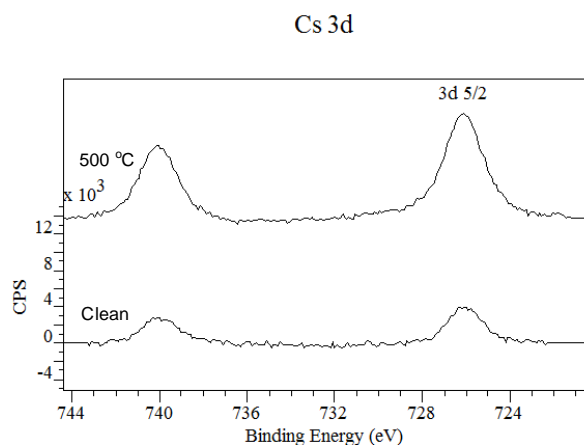


**Figure 6-30** XP spectra of the Cs region for the Clean Au(111) surface and the surface post heating to 500 °C

The trends observed here for the Cs, O and C region binding energies of the heated samples are of particular interest. Upon formation of caesium carbonate there is a change in the observed binding energy accompanied by an increase in the coverage, which is attributed to the dealloying of the surface upon exposure to CO<sub>2</sub> and formation of islands of caesium carbonate. When the samples are heated there is a tendency toward higher binding energies for Cs, O and C up to 200 °C. After this temperature, the binding energy trend reverses and lowers until 500 °C is reached at which point the caesium carbonate has

decomposed. Caesium metal possesses plasmon resonances, highlighted by the fine structure in the XP spectrums at a slightly higher binding energy to the main 3d 5/2 or 3d 3/2 peaks. When islands of Cs form, the collective plasmon resonances of the caesium will change: an increase in island size being associated with a lowering of the energy of the surface plasmon which would cause an apparent increase of the binding energy of the peak. When the sample is heated to 200 °C the islands increase in size, with an accompanied increase in the observed binding energy, this explains the trend in binding energy observed simultaneously in the Cs, O and C regions. When the temperature is raised higher than 200 °C the caesium carbonate decomposes and thus the islands reduce in size, raising the energy of the surface plasmon and lowering the observed binding energy for all 3 regions.

### **6.6.2 Caesium Carbonate Formation and Thermal Stability at ~2 ML Coverage**

To test whether the observed trends in binding energy are linked to the caesium surface plasmon resonances, similar experiments were undertaken at a higher coverage of caesium. If the proposed trend is correct when a higher coverage of caesium is initially applied larger islands will be able to form, lowering the energy of the surface plasmon resonance and causing the same trend seen before but with a larger binding energy shift.

The clean Au(111) surface was coated with Cs (5.0 A, 2.1 V, 1.5 min) and exposed to CO<sub>2</sub> (1x10<sup>-6</sup> torr, 10 min, 600 L). The clean Au(111) surface had only residual Cs, measured at a coverage of 0.05 ML. After the deposition of Cs the coverage was calculated to be 1.2 ML, the O region for the freshly coated sample showed a significant coverage of 0.18 ML attributed to the much higher surface coverage of Cs. After the exposure to CO<sub>2</sub> the Cs coverage increases from 1.2 – 2.0 ML, there is a small shift in the binding energy from 725.8 – 725.6 eV. This is a smaller shift than for any of the previous experiments where ~1 ML was deposited, this could be attributed to the difference in surface plasmon resonance for this higher coating.

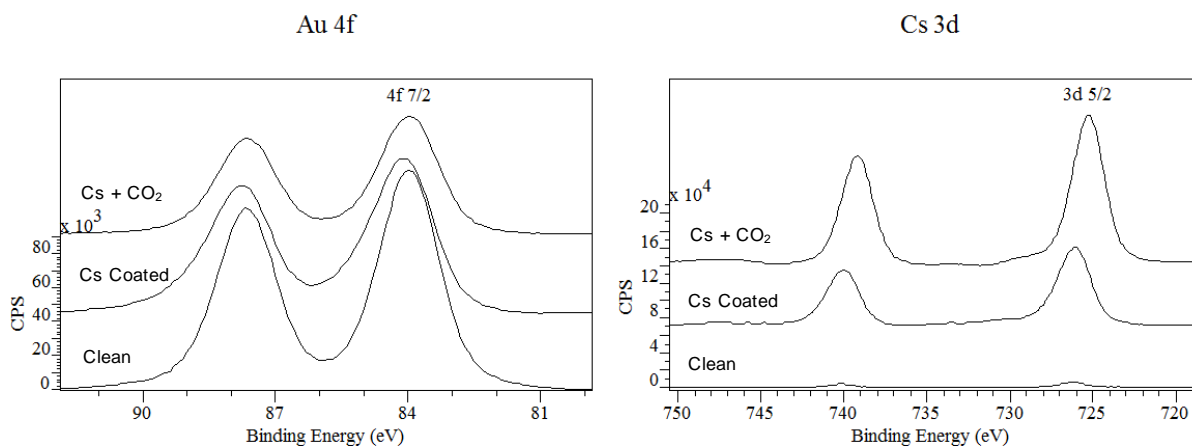


**Figure 6-31** XP spectra of clean, Cs coated and CO<sub>2</sub> exposed surfaces a) Au 4f region and b) Cs 3d region

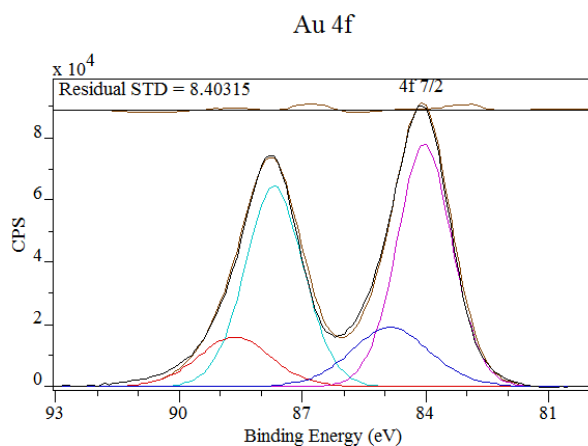


**Figure 6-32** XP spectrum of the Au 4f region for the 2 ML Cs coated Au(111)

The O and C region support the formation of caesium carbonate with a shift in the O binding energy from 531.1 – 531.8 eV, this shift is attributed to the change from caesium oxide to caesium carbonate. It is interesting to note that these binding energies are slightly higher than those previously seen for both the oxide and carbonate. The C region reveals the presence of a peak at 289.2 eV which is that expected for carbonate albeit slightly higher than those previously observed here. The O/C ratio is calculated to be 2.7/1 which further supports the formation of caesium carbonate.

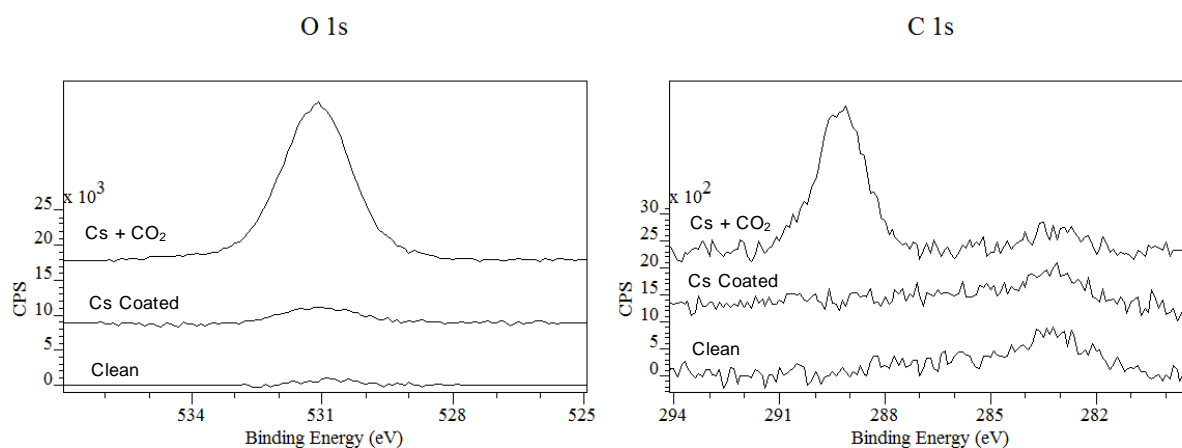


**Figure 6-33** XP spectra of clean, Cs coated and CO<sub>2</sub> exposed surfaces a) O 1s region and b) C 1s region

The sample was then heated (100, 200, 300 and 400 °C, 10 min) and XPS analysis was performed (Figure 6-34 and 6-36). The Cs, C and O region all show a similar trend in binding energy shift. The binding energies initially rise to 200 °C before slowly, incrementally lowering at each higher temperature. After the final heating there is still a significant amount of Cs<sub>2</sub>CO<sub>3</sub> on the surface, but the Cs coverage has dropped from 2.0 ML to 0.99 ML. Similarly both the C and O coverages have reduced, from 0.71 to 0.34 ML and 2.04 to 0.83 ML respectively, the O/C ratio has remained at that expected for carbonate formation, fluctuating from 2.8/1 to 2.4/1.

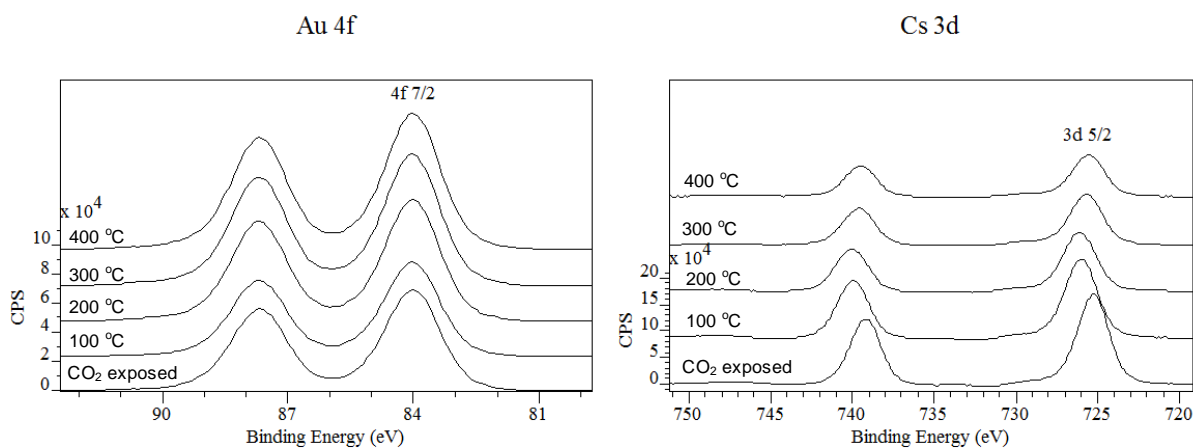


**Figure 6-34** XP spectra of heated surfaces a) Au 4f region and b) Cs 3d region

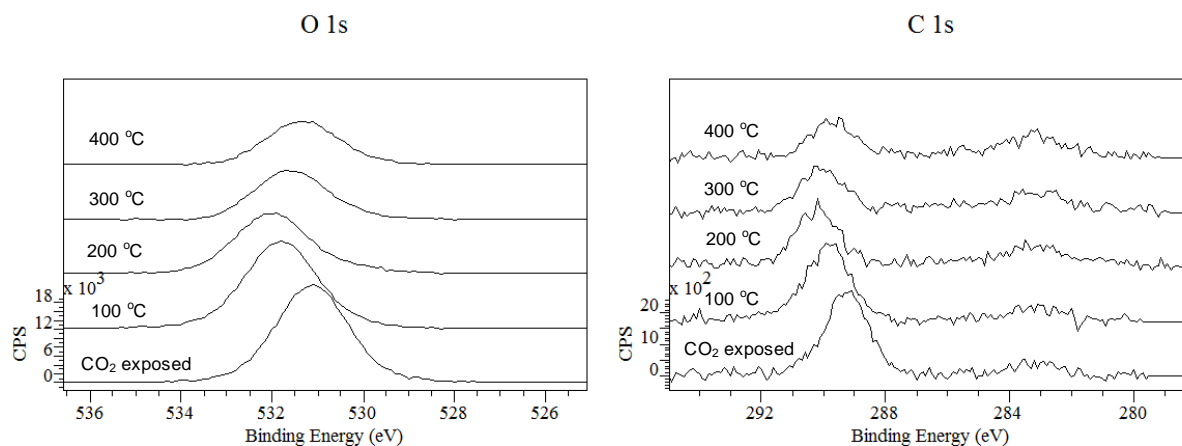


**Figure 6-35** XP spectra of heated surfaces a) O 1s region and b) C 1s region

When the binding energy shift here is compared to that of the heated samples of  $\text{Cs}_2\text{CO}_3$  formed on the 1 ML system, it can be seen that there is a considerably larger shift to more positive binding energies in this system. The Cs shift on the 1 ML system was 0.52 eV and on the 2 ML system was measured at 0.94 eV. Similar larger shifts are also observed in the O region of 0.23 and 0.98 eV and C region of 0.34 and 1.00 eV for the 1 ML and 2 ML systems respectively. This supports the presence of a lower energy surface plasmon resonance due to the larger islands, resulting from the higher concentration of caesium.

## 6.7 Exposure of CsAu Surface to a 1:1 $\text{CO}_2 / \text{O}_2$ Mixture

Initial experiments were also performed to investigate the effect of a 1:1 mixture of  $\text{CO}_2/\text{O}_2$  gas on the formation of  $\text{Cs}_2\text{CO}_3$ . Initially, 0.5 ML of Cs was investigated, the clean Au(111) sample was coated with Cs (5.0 A, 2.1 V, 0.5 min) and exposed to  $\text{CO}_2/\text{O}_2$  ( $1 \times 10^{-6}$  torr, 10 min, 600 L), followed by  $\text{CO}_2$  ( $1 \times 10^{-6}$  torr, 10 min, 600 L).

The XPS analysis of the Cs region (Figure 6-36 b)) of the clean Au(111) reveals residual Cs coverage of  $>0.01$  ML. No peaks appear in the O and C region (Figure 6-37), this is attributed to the very low concentration of Cs, further this shows that the mixture of  $\text{CO}_2/\text{O}_2$  has no preference for reaction on the clean Au(111) surface.

The Cs region reveals that after deposition of Cs the surface coverage was calculated at just 0.11 ML. Upon exposure to  $\text{CO}_2/\text{O}_2$  there was a slight increase in the measured Cs peak area, however the calculated coverage was still 0.11 ML which was not expected from the previous results that have been observed. The O and C regions reveal that after exposure to  $\text{CO}_2/\text{O}_2$  and  $\text{CO}_2$  there has been no species formed on the surface. This is attributed to the very low coverage of Cs.

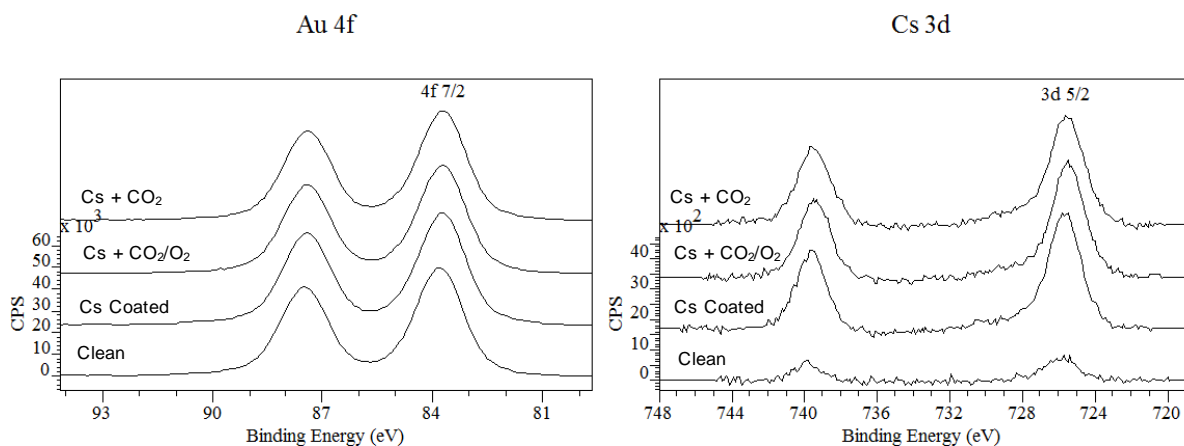


**Figure 6-36** XP spectra of Cs coated surfaces exposed to CO<sub>2</sub>/O<sub>2</sub> and CO<sub>2</sub> a) Au 4f region and b) Cs 3d region

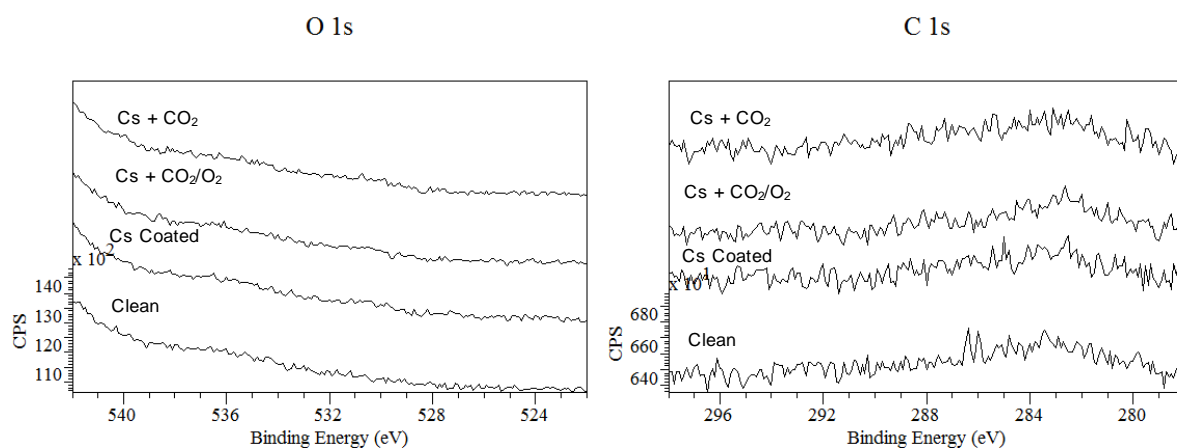


**Figure 6-37** XP spectra of Cs coated surfaces exposed to CO<sub>2</sub>/O<sub>2</sub> and CO<sub>2</sub> a) Au 4f region and b) Cs 3d region

Of particular interest here is the absence of any surface species upon gas exposure, this shows that the surface concentration of Cs is too low to form large enough islands to support the formation of caesium carbonate or caesium oxide and that the Cs on the surface is remaining alloyed with the Au.

## 6.8 Discussion

There was no reaction observed between the clean Au(111) surface after exposure to CO<sub>2</sub>, this was as expected and in agreement with previous studies [4-6]. The O region revealed a small peak at a binding energy of 530.5 eV and a minor coverage of 0.035 ML which is attributed to the formation of caesium oxide due to the residual caesium on the clean

surface. Further, after exposure to CO<sub>2</sub> no discernible peaks appear in the C region which is the best indication for the absence of any reaction to the gas.

Formation of a CsAu alloy at a Cs coverage of ~1 ML was confirmed by the emergence of a shoulder in the Au 4f region, assigned to a Au<sup>+</sup> species, this was in agreement to that found in the literature for the formation of CsAu alloys [4]. This freshly coated surface possesses a modest peak in the O region at 531.5 eV, which is attributed to the formation of caesium oxide. After the sample had been left in the chamber for 12 hrs the O region peak had grown substantially and was measured at 1.1 ML, accompanied by a small peak in the C region. This indicated the formation a small amount of caesium carbonate and high coverage of caesium oxides. This highlighted the need for efficient experimentation as the highly reactive alloy surface only remained clean of contaminants for a few hrs even under the ultra high vacuum conditions (1x10<sup>-9</sup> torr).

Investigations performed on annealed, partially annealed and sputtered only surfaces revealed that the formation of CsAu alloy and its subsequent reaction to gaseous CO<sub>2</sub> is significantly different for the three surfaces. It was shown that the annealed surface had the most surface Cs, followed by the partially annealed and lastly the sputtered only surface for the same coating conditions. Upon exposure to CO<sub>2</sub> the three surfaces again reacted very differently, the annealed surface saw the largest increase in Cs coverage after exposure to CO<sub>2</sub> accompanied with the largest shift in Cs binding energy, dealloying of the AuCs surface and highest coverage of caesium carbonate. The partially annealed surface saw a similar trend to the annealed surface but to a lesser extent and the sputtered only surface saw no change upon exposure to CO<sub>2</sub> and no carbonate formation.

The formation of Cs<sub>2</sub>CO<sub>3</sub> on a clean annealed Au(111) surface was followed with both XPS and STM analysis. These experiments showed that near atomic resolution was obtained for the clean annealed surface, inferred by the presence of the ridges described above indicative of the (22x√3) reconstruction. After the surface had been coated with Cs, the ridges were no longer visible in the STM indicating a change to the surface structure, this was attributed to the formation of a CsAu alloy, confirmed by XPS analysis of this surface, where the Au 4f region indicated the formation of Au<sup>+</sup> species. Once the surface has been exposed to CO<sub>2</sub>, XPS analysis supported the formation of Cs<sub>2</sub>CO<sub>3</sub> accompanied with the dealloying of the surface evidenced by the disappearance of the Au<sup>+</sup> shoulder in the Au 4f region. STM analysis of this surface showed the formation of large islands over the Au(111) surface supporting the formation of Cs<sub>2</sub>CO<sub>3</sub> islands at the expense of the CsAu alloy.

These results can be rationalised in terms of the adsorption environments available to the Cs atoms when they impact the gold surface. The annealed surface possesses the highest degree of crystallinity, the partially annealed surface will have more defects and the sputtered only surface the highest degree of disorder. During Cs coating, when Cs atoms interact with the surface they can be expected to be most mobile on the annealed surface, less mobile on the partially annealed surface and least mobile on the sputtered only surface where the abundance of high energy sites are likely to trap the Cs atoms. We can speculate therefore that the caesium on the annealed surface is most able to form islands and also that the high energy sites available in the sputtered surface prevent the formation of a subsurface Cs. This would account for the observation that exposure of Cs at the annealed surface to CO<sub>2</sub> results in much larger increases in Cs coverage than the other two surfaces; the more stable Cs<sub>2</sub>CO<sub>3</sub> results in a dealloying of the CsAu surface in. This is seen to a lesser extent on the partially annealed surface. On the sputtered only surface the Cs atoms at the high energy sputtered sites are more stable. It is interesting that the Cs atoms adsorbed at the sputtered surface do not react with CO<sub>2</sub> to form carbonate. This could be because of the additional stability of these sites. An alternative model is that the immobility of the Cs atoms prevents the formation of Cs islands at the sputtered surface and that the formation of caesium carbonate on the Cs/Au surface depends on a critical Cs island size. We cannot distinguish between either model with the present data.

### 6.8.1 Effect of heating

Caesium carbonate was formed on an annealed Au(111) surface with a Cs coverage of ~1 ML, the increase in Cs coverage upon formation of the caesium carbonate was again seen in conjunction with the dealloying of the surface in favour of the formation of islands of caesium carbonate. Upon heating, binding energy shifts were observed in the Cs, O and C regions. We attribute these shifts to the formation of larger islands before the decomposition of caesium carbonate from the surface. This was confirmed when an analogous investigation on a surface possessing higher Cs coverage revealed that similar trends in the Cs, O and C region were observed with larger shifts in the binding energies. This can be attributed to changes in the electronic structure of the caesium plasmon resonances associated with changes in the islands sizes. It was not possible to confirm whether the caesium carbonate was decomposing by desorption of caesium oxide and CO<sub>2</sub> or further dissolution of Cs into the bulk gold. Mass spectrometry investigations would reveal the nature of the decomposition process. However, it is observed that when the decomposition occurs, some surface oxides remain, while the Cs coverage reduces. Another hypothesis is that carbon dioxide is desorbing from the surface leaving surface oxides and the Cs is being drawn back into the sub-surface Au(111) crystal accompanied with alloy formation again. When the area

of the Au 4f region was examined the reduction in caesium coverage should be accompanied with an increase in the Au area. However as the caesium coverage reduces it was observed that the Au area remained constant. This would indicate that desorption of carbon dioxide and realloying of the CsAu is the likely decomposition mechanism. It also explains why it was hard to produce very clean Au(111) surfaces after many experiments involving Cs had been conducted on the crystal, further it would explain the slow reduction in the Au 4f area throughout the investigations.

Initial investigations into the reaction of the CsAu surface with gaseous mixtures of CO<sub>2</sub>/O<sub>2</sub> did not form any surface species, we attribute this to the low surface coverage of Cs. However, this has highlighted that there must exist a threshold surface concentration of Cs before island formation and reaction to CO<sub>2</sub> becomes more favourable than remaining in the CsAu alloy state.

## References

1. Mross, W.D., *Alkali Doping In Heterogeneous Catalysis*. Catalysis Reviews-Science and Engineering, 1983. **25**(4): p. 591-637.
2. Wertheim, G.K., et al., *Surface-Properties Of The Semiconductor CsAu*. Surface Science, 1995. **330**(1): p. 27-33.
3. Erdinc, B., F. Soyalp, and H. Akkus, *First-principles investigation of structural, electronic, optical and dynamical properties in CsAu*. Central European Journal of Physics, 2011. **9**(5): p. 1315-1320.
4. Carley, A.F., M.W. Roberts, and A.K. Santra, *Interaction of oxygen and carbon monoxide with CsAu surfaces*. Journal of Physical Chemistry B, 1997. **101**(48): p. 9978-9983.
5. Carley, A.F., et al., *Reactivity and structural aspects of cesium and oxygen states at Cu(110) surfaces: An XPS and STM investigation*. Journal of Physical Chemistry B, 2004. **108**(38): p. 14518-14526.
6. Carley, A.F., P.R. Davies, and M.W. Roberts, *Activation of oxygen at metal surfaces*. Philosophical Transactions of the Royal Society a-Mathematical Physical and Engineering Sciences, 2005. **363**(1829): p. 829-846.
7. Burt, M.G. and V. Heine, *Theory of work-function of cesium suboxides and cesium films*. Journal of Physics C-Solid State Physics, 1978. **11**(5): p. 961-968.
8. Freund, H.J. and M.W. Roberts, *Surface chemistry of carbon dioxide*. Surface Science Reports, 1996. **25**(8): p. 225-273.
9. Wanger, C. D., et al., *Handbook of X-ray Photoelectron Spectroscopy*. 1992, 6509 Flyer Cloud Drive, Eden Prairie, Minnesota 55344: Perkin-Elmer Corporation.
10. Starke, U. *STM examples of application [Online]*. 2012 20-07-15; Available from: <http://www2.fkf.mpg.de/ga/research/stmtutor/stmex.html>.
11. Guo, X.C. and R.J. Madix, *Adsorption of oxygen and carbon dioxide on cesium-reconstructed Ag(110) surface*. Surface Science, 2004. **550**(1-3): p. 81-92.

# Chapter 7 Conclusions

---

The deposition and dissolution of calcium carbonate is of great environmental importance, the analysis of its composition in sediments can be used as a proxy for paleoceanographers, gleaning useful information about past oceanic conditions. The oceanic environment changes in response to changes in the global climate, such as temperature and atmospheric CO<sub>2</sub> concentrations. Therefore looking at how the oceanic environment has changed in the past in response to global climatic changes, it is possible to predict how this will affect the environment and oceanic environment in the future. However considerable uncertainty surrounds the deposition and dissolution of calcium carbonate especially in oceanic environments where local salinity and high pressure can have a significant impact on the rates of deposition and dissolution.

For these reasons the research described in this thesis aimed to develop an *in-situ* probe using gold nanoparticles for their ability to enhance Raman spectroscopy. As part of the work electrochemical potentials were employed to deposit controlled phases of calcium carbonate, to study the rates of calcium carbonate deposition and dissolution to better understand the factors effecting these rates.

Initially, citrate stabilised gold nanoparticles were employed for their SERS activity and calcium carbonate was electrochemically deposited over them. It was hoped that uniform thin films of calcium carbonate would be deposited with fine control over the polymorphism of calcium carbonate and the SERS enhancement would greatly enhance the subsequent spectra. Although it was not possible to form the desired thin films it was possible to reliably deposit polymorphically pure calcium carbonate (calcite) by altering the composition of the electrolyte and applying reduction potentials. The nucleation and growth of discrete particles was observed and the subsequent dissolution was followed using Raman spectroscopy which revealed bulk dissolution was being observed.

To enable the study of dissolution using Raman spectroscopy with the presence of SERS enhancement, core@shell Au@calcium carbonate nanoparticles were synthesised. It was found that citrate stabilised gold nanoparticles were not stable enough to form such structures. It was postulated that linear carboxylic acid terminated thiol stabilised gold nanoparticles would be both stable enough to support a calcium carbonate shell and that the carboxylic acid would be directing in the formation of calcium carbonate. A novel, facile, exchange of stabilising agents was employed for the exchange of citrate for the desired linear thiol.

The linear thiol stabilised Au-nanoparticles showed interesting interactions with the vaterite polymorph as well as directing the formation of novel multinucleated calcite particles during the transformation from vaterite to calcite due to the initial inclusion of the gold nanoparticles on the surface of vaterite spherules. The synthesis of core@shell Au@calcium carbonate type nanoparticles, possessing interesting surface structures, were also formed. It is hoped that these particles will enable future studies into the dissolution of calcium carbonate followed by SERS.

Spherical gold nanoparticles are not homogenous and are made up of discrete single crystal surfaces. The (111) and (100) surfaces made up the majority of the spheres' surfaces, with only very small (110) facets linking the (111) facets together. The reactivity on each of these single crystal surfaces will be slightly different and hence investigations were performed to better understand the nature of calcium carbonate deposition on each of these surfaces. This would complement the previous work on core@shell nanoparticle synthesis revealing how nanoparticles may be tuned to promote the coating of calcium carbonate.

Epitaxial growth of calcium carbonate was found on both the Au(111) and Au(110) surfaces. The reduction potential and surface structure both played important roles in the epitaxial formation of calcium carbonate. The reduction potential formed either hydroxyl or oxalate species at the surface raising the local pH and changing the equilibrium in favour of calcium carbonate deposition from solution. Due to the ordered single crystal surfaces the reduced species on the surface formed an ordered matrix which then directed the epitaxial growth of calcium carbonate.

There was no epitaxial growth observed for the formation of calcium carbonate on the Au(100) surface. This finding suggests that the spherical nanoparticles which have large Au(100) facets may not be the ideal shape for the deposition of calcium carbonate. It would be of great interest to perform more epitaxial growth investigations using different electrolyte compositions, known to favour vaterite or aragonite formation, to explore the epitaxial growth of these polymorphs on the Au(*h,k,l*) basal planes. It would also be of interest to synthesise gold nanoparticles of different shapes, some bearing larger Au(100) facets, and others minimising the Au(100) facets to see if the coating of calcium carbonate was facilitated on nanoparticles with minimal Au(100) facets which would support this hypothesis.

UHV systems were employed for the study of calcium carbonate formation and reactivity on the Au(111) single crystal. Extensive attempts were made to coat calcium however difficulties were experienced with the coating apparatus and hence surface studies for the formation and reactivity of calcium carbonate were investigated. The investigation into the formation and

reactivity of caesium, CsAu alloy formation and  $\text{Cs}_2\text{CO}_3$  formation on the Au(111) surface complimented similar studies on different metal single crystals.

It was observed that when the Au(111) surface was coated with Cs, a CsAu alloy formed. Subsequent exposure to  $\text{CO}_2$  formed caesium carbonate on the Au(111) surface. It was seen through STM studies accompanied with XPS analysis that the formation of caesium carbonate caused the CsAu alloyed surface to dealloy. The dealloying was accompanied with the formation of islands seen in the STM and attributed to that of the caesium carbonate species.

The formation of caesium carbonate was dependent upon the crystallinity of the Au(111) surface: An investigation on surfaces which had not been annealed or had been annealed to different temperatures, revealed that caesium carbonate only formed on the annealed surfaces, and formed to a greater degree on the higher temperature annealed surface. This was attributed to the presence of high energy defect sites on the un-annealed surface which effectively trap the Cs atoms preventing movement on the surface. The annealed surfaces with fewer defect sites showed a much greater propensity for penetration of the Cs into the subsurface region and for the formation of islands which subsequently reacted with  $\text{CO}_2$  to form caesium carbonate at the expense of the CsAu alloy.

Investigations into the stability of the caesium carbonate were performed by heating the surface and monitoring the decomposition of caesium carbonate from the surface. An interesting binding energy shift trend was observed which was more pronounced on surfaces with higher Cs surface coverages. This trend was attributed to the formation of islands of different sizes; higher surface coverages of Cs allowed for larger islands to form. Caesium possess surface plasmon resonances and hence changes in the size of the Cs islands caused changes in the surface plasmon resonance energy effecting the binding energy and explaining the observed trends seen in binding energy.

In future, we would like to investigate the effect of surface coverage of caesium on caesium carbonate formation, it was observed that at very low concentrations the Cs was not reactive to  $\text{CO}_2$ . To find the point at which activation to  $\text{CO}_2$  occurs would be very desirable, as well as further investigating the effect of mixtures of gases on carbonate formation. Finally it is hoped that new apparatus for the successful coating of calcium could be found and pave the way for UHV investigations into the formation of calcium carbonate on a range of gold single crystals.